# Darstellung und Charakterisierung von $MoS_2$ Cokatalysatoren für die $H_2$-Entwicklung

Dissertation zur Erlangung des Doktorgrades der Mathematisch-Naturwissenschaftlichen Fakultät der Christian-Albrechts-Universität zu Kiel

vorgelegt von

**John Djamil**

Kiel, 2015

Erster Gutachter: Prof. Dr. Wolfgang Bensch

Zweiter Gutachter: Prof. Dr. Christian Näther

Tag der mündlichen Prüfung: 05.10.2015

Zum Druck genehmigt: 05.10.2015

Prof. Dr. W. J. Duschl, Dekan

# Abkürzungsverzeichnis

| | |
|---|---|
| $\Delta G$ | Änderung der Gibbs-Energie |
| $B_0$ | magnetische Flussdichte |
| BE | Bindungsenergie |
| C-[…] | Kohlenstoff-[…] |
| Cr-[…] | Chrom-[…] |
| EDTA | Ethylendiamintetraessigsäure |
| H-[…] | Wasserstoff-[…] |
| I | Stromstärke |
| M-H | Metall-Wasserstoff |
| Mo-[…] | Molybdän-[…] |
| N-[…] | Stickstoff-[…] |
| O-[…] | Sauerstoff-[…] |
| P-[…] | Phosphor-[…] |
| P | Leistung (Power) |
| Ph | Phenyl |
| Pt-[…] | Platin-[…] |
| S-[…] | Schwefel-[…] |
| T | Temperatur |
| U | Spannung |

# Zusammenfassung

Die lichtgetriebene Darstellung von $H_2$ stellt als Alternative zu Rohöl und Kernenergie eines der richtungsweisenden Forschungsgebiete im Bereich erneuerbarer Energien dar. Dafür erfolgen Untersuchungen und Entwicklungen von Fotokatalysatoren, an deren Oberfläche durch Lichtabsorption Protonen zu $H_2$ reduziert werden. Durch den Einsatz von Cokatalysatoren kann die Aktivität fotokatalytischer Systeme verbessert werden, da einerseits eine effizientere Ladungstrennung gewährleistet wird und andererseits zusätzlich katalytisch aktive Zentren zur Verfügung gestellt werden.

In dieser Arbeit wurden Cokatalysatoren auf Basis von $MoS_2$ hergestellt, charakterisiert und hinsichtlich der fotokatalytischen $H_2$-Entwicklung untersucht. Die Herstellung erfolgte einerseits über den thermischen Abbau von Tetraalkyl-Ammoniumthiomolybdaten mit verschiedenen Kettenlängen des organischen Kations und andererseits durch die mechanische Behandlung von kristallinem $MoS_2$, so dass Proben sowohl mit unterschiedlicher chemischer Zusammensetzung als auch unterschiedlichen strukturellen Eigenschaften erhalten wurden. Dadurch sollten Zusammenhänge zwischen chemischer Zusammensetzung, mikrostrukturellen Eigenschaften und der fotokatalytischen Aktivität besser verstanden werden. Bei beiden Syntheserouten resultierten nanopartikuläre Molybdänsulfide. Bei der zuerst genannten Syntheseroute wurden kohlenstoffhaltige Molybdänsulfid-Nanokomposite erhalten, welche sich je nach Kettenlänge des Eduktes in dem C- und S-Gehalt und in den Partikelgrößen (Stapelhöhe und Schichtlängen) unterscheiden. Zusätzlich wurde bei der thermischen Zersetzung von $(Ph_4P)_2MoS_4$ ein Kompositmaterial gebildet, welches einen signifikant vergrößerten Interschichtabstand zwischen den $MoS_2$-Schichten aufweist. Eine Erklärung für das Auftreten dieser strukturellen Eigenschaft konnte mit der Einlagerung von *in situ* gebildeten $Ph_3PS$- und $(Ph_4P)_2S$-Molekülen zwischen den $MoS_2$-Schichten erbracht werden. Während sich die $(Ph_4P)_2S$-Moleküle ‚frei' in den van der Waals Lücken aufhalten, sind die $Ph_3PS$-Moleküle über Mo-S-Bindungen an die $MoS_2$-Schichten gebunden. Bei der mechanischen Behandlung von kristallinem $MoS_2$ resultierten in Abhängigkeit von der Behandlungsdauer unterschiedlich große $MoS_2$-Nanopartikel bei gleich bleibender chemischer Zusammensetzung. Mit zunehmender Behandlungszeit nahm

die Zahl gestapelter $MoS_2$-Schichten in einem deutlicheren Maß ab als die Schichtlänge, so dass das Aspektverhältnis zunimmt und daher die Partikelform beeinflusst wird.

Alle nanopartikulären Cokatalysatoren haben sich als effizientere Materialien für die lichtgetriebene $H_2$-Entwicklung herausgestellt als kristallines $MoS_2$. Kohlenstoff als zusätzliche Komponente verbessert die Elektronenleitfähigkeit und unterdrückt Rekombinationsprozesse, so dass über angrenzende Grenzflächen zu $MoS_2$ die Bildung von $H_2$ verbessert wird. Die strukturellen Eigenschaften der Teilchen belegen den positiven Einfluss der $MoS_2$-Kanten auf die $H_2$-Entwicklung. Zusätzlich wurde die Bedeutung der Partikelform auf die fotokatalytische Aktivität deutlich.

Fotokatalytische Untersuchungen an neuartigen Übergangsmetallsulfiden und –oxiden für die Darstellung von $H_2$ hat eine Reihe von viel versprechenden Materialien hervorgebracht.

# Abstract

As a suitable alternative to fossil fuels and nuclear energy light induced generation of $H_2$ represents a trend-setting research area in the field of regenerative energy. Therefore photocatalysts, which provide surface sites for light driven reduction of protons to $H_2$, are being investigated and developed. Enhancement of photocatalytic systems can be achieved by the usage of cocatalysts, which simplify charge separation and provide additional catalytic active sites as well.

In the present work cocatalysts based on $MoS_2$ were synthesized, characterized and investigated for photocatalytic $H_2$ generation. $MoS_2$ cocatalysts were synthesized by thermal decomposition of tetraalkyl ammonium thiomolybdates with varying carbon content in the organic cation and by mechanical treatment of bulk $MoS_2$ respectively. Hence, samples with differing chemical composition as well as structural properties were obtained. Based on these findings relations between chemical composition, microstructural properties and photocatalytic activity were supposed to reveal. Nanoparticulate molybdenum sulfides resulted in both synthetic routes. Thermal decomposition of tetraalkyl ammonium thiomolybdates yielded in carbon containing molybdenum sulfide nanocomposites, in which carbon and sulfur content and the crystallite size as well varied with the carbon amount in the precursor. Additionally a composite with a significant enlarged interlayer distance between the $MoS_2$ layers was obtained by thermal decomposition of $(Ph_4P)_2MoS_4$. Such interlayer expansion could be explained by an insertion of *in situ* generated $Ph_3PS$- and $(Ph_4P)_2S$-molecules between the $MoS_2$ layers. While $Ph_3PS$-molecules were bonded through Mo-S-bonds to the $MoS_2$ layers, $(Ph_4P)_2S$-molecules remained free in rotation between $MoS_2$ sheets. The mechanical treatment of bulk $MoS_2$ resulted in different-sized $MoS_2$ nanoparticles as a function of milling time but with the same chemical composition. In doing so, the $MoS_2$ stacking was reduced more rapidly than the slab length, yielding in increasing aspects ratios and thus affecting the particle shape.

All nanosized cocatalysts exceeded bulk $MoS_2$ in light driven hydrogen generation. The enhancement of $H_2$ generation on $MoS_2$ was achieved by addition of carbon, improving the electron conductivity and suppressing recombination processes. The positive influence of $MoS_2$ edge sites on $H_2$ generation was proofed by structural

properties of the cocatalysts. Additionally, the importance of the particle shape on photocatalytic properties was demonstrated.

Photocatalytic investigations on novel transition metal sulfides and –oxides for $H_2$ evolution yielded in a rash of promising materials.

## Inhaltsverzeichnis

# 1 Einleitung

## 1.1 Fotokatalytische $H_2$-Entwicklung

### 1.1.1 Einleitung

Die Bereitstellung von Energie ist und wird noch in einem deutlicheren Ausmaß ein Schlüsselelement für die weltweite industrielle, ökonomische und soziale Entwicklung spielen. 2008 betrug der globale Energiebedarf etwa 533 EJ. Dieser soll nach aktuellen Berechnungen um 1.1 %/a steigen, so dass die weltweite Energienachfrage im Jahre 2035 voraussichtlich bei etwa 812 EJ liegen wird.[1,2] Gründe dafür sind u.a. das stetige Bevölkerungswachstum, die Urbanisierung besonders in Entwicklungsländern, die Modernisierung, stetig zunehmende Industrialisierung, zunehmende Mobilität und ein erwartetes Einkommenswachstum. Neben der wesentlichen Frage, ob der durch die genannten Gründe steigende Energiebedarf überhaupt gedeckt werden kann, spielt auch die Herkunft der Energie eine wichtige Rolle. Derzeit werden etwa 83 % des globalen Energiebedarfs von nicht erneuerbaren Energiequellen, namentlich den fossilen Brennstoffen und der Kernenergie gedeckt (Abb. 1).[3,4] Die Verwendung von Kern- und fossiler Energie wird von einer Reihe an Problemen begleitet. So stellt die Entsorgung des Atommülls bei der Nutzung von Atomkraftwerken eine große Schwierigkeit dar. Gravierende Unfälle verursacht durch technische Mängel oder menschliches Versagen wie auf Three Miles Island, in Tschernobyl oder Fukushima haben das enorme Gefährdungspotential dieser Form der Energieerzeugung eindrücklich demonstriert. Der Großteil (80.3 %) der weltweiten Energie wird von fossilen Brennstoffen, wie Kohle, Erdöl und Erdgas gedeckt. Auch diese Art der Energieerzeugung ist nicht völlig nebenwirkungsfrei und birgt viele Risiken. V.a. die Nutzung von Erdöl ist mit Problemen behaftet. Da Erdöl global nicht gleichmäßig verteilt vorkommt, können die Förderländer Druck auf Wirtschaft und Politik ausüben. Die Folgen sind sprunghafte Preisentwicklungen und geopolitische Spannungen. Die Verwendung von fossilen Brennstoffen wird zusätzlich durch die damit verbundene Freisetzung von Schadstoffen wie Kohlenstoffdioxid ($CO_2$), Stickoxiden und Schwefeloxiden von schwerwiegenden Folgen begleitet, wie z.B. die globale Erderwärmung, die Bildung von saurem Regen und Smog, was zu Gesundheitsrisiken und Umweltverschmutzung führt. Zudem sind fossile Brennstoffe zeitlich begrenzt verfügbar und somit endlich, was ein Ausweichen auf alternative Energieerzeugung erfordert.

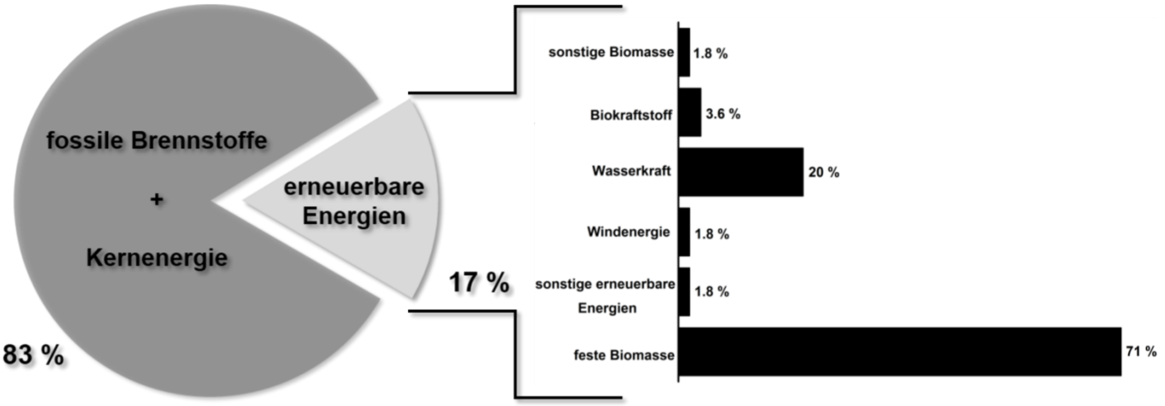

**Abb. 1: Zusammensetzung des globalen Energieverbrauchs 2010. Adaptiert von Referenz [3].**

Ein viel versprechender Lösungsansatz stellt die Nutzung so genannter erneuerbarer Energien dar. Darunter werden Energiequellen verstanden, die nach Zeitmaßstäben des Menschen unendlich lange zur Verfügung stehen. Dazu gehören die Solarstrahlung, die Erdwärme und die Gezeitenkraft. Entweder werden diese direkt genutzt oder aber indirekt als Biomasse, Umgebungswärme, Wasserkraft, Windenergie oder Wellenenergie (Abb. 1).[3] Insbesondere solare Energienutzung stellt einen attraktiven Lösungsansatz der Energieversorgung dar. Pro Jahr empfängt die Erde etwa $3.9 \times 10^6$ EJ Sonnenenergie.[2] Ein Vergleich mit dem globalen Energiebedarf von 2009 zeigt, dass in etwa 1 h auf die Erde so viel Sonnenenergie einfällt, wie die Menschheit in einem Jahr nutzt. Davon beträgt der sichtbare Anteil der auftreffenden Strahlung ($380 > \lambda > 780$ nm) etwa 48 % und der UV-Vis-Anteil ($1 > \lambda > 380$ nm) etwa 4 %. Die Sonnenenergie kann mit Hilfe von photovoltaischen Zellen direkt in elektrische Energie umgewandelt werden. Aus diesem Grund stellt die Photovoltaik mit Wachstumsraten von 35-40 %/a einer der am schnellsten wachsenden Technologien dar.[5] Trotz der bereits jahrelangen Nutzung photovoltaischer Zellen in der Raumfahrt, leistet die Photovoltaik noch keinen entscheiden Beitrag bei der globalen Energieversorgung aufgrund der noch zu niedrigen Effizienzen bzw. der hohen Kosten der Solarenergiemodule.[5] Allgemeine Probleme dieser Energiequellen sind häufig die periodische bzw. unterbrochene Energieproduktion aufgrund von Jahres-, Tageszeiten, generell Wetterbedingungen und der geografischen Lage. Zurzeit erfolgt die Energieumwandlung meistens in elektrische Energie. Diese kann jedoch nur schwierig bzw. aufwendig als solches gespeichert werden, sondern muss entweder sofort verbraucht oder in eine andere Form umgewandelt werden. Durch geeignete Energiespeicher könnte eine kontinuierliche Energielieferung gewährleistet werden, so dass beispielsweise überschüssige Energie, welche in der Nacht produziert wurde, für den Tagesverbrauch zur Verfügung gestellt werden kann. Wasserstoff ($H_2$) repräsentiert einen effektiven, nachhaltigen und sauberen Energieträger, in welchem die Energie in der chemischen Bindung enthalten ist. Die Energiefreisetzung kann durch die Reaktion mit Sauerstoff ($O_2$) zu Wasser in der so genannten Brennstoffzelle erfolgen.[6] Bei diesem Prozess wird die chemische Energie direkt in elektrische Energie umgewandelt mit Wasser als Nebenprodukt. Diese Energieumwandlung stellt daher eine saubere und gezielt freisetzbare Bereitstellung von Energie dar. Die Bedeutung von $H_2$ ist enorm z.B. in der Industrie, wo es u.a. in Ölraffinerien (44 %), für die Herstellung von Ammoniak ($NH_3$) (38 %) und auch für die Herstellung von Methanol, Aminen und Wasserstoffperoxid unabdingbar ist.[7] Die vielseitige und v.a. mengentechnisch enorme Nutzung von $H_2$ erfordert daher eine kostengünstige, umweltfreundliche und effiziente Herstellung des Gases. $H_2$ kommt auf der Erde nur in sehr geringem Maß molekular vor, so dass die Gewinnung durch chemische Umwandlungsprozesse aus Kohlenwasserstoffen, Alkoholen oder Wasser erfolgt. Derzeit stammt der Großteil des $H_2$ aus der Dampfreformierung (etwa 90 %). Dabei handelt es sich um einen heterogenen katalytischen, endothermen Prozess, in welchem $H_2$ aus Methan und der damit verbundenen Freisetzung von $CO_2$ erzeugt wird (Gl. 1).[8] Der hohe Energieaufwand und die Umweltbelastung machen diesen Prozess langfristig unattraktiv.

$$CH_{4(g)} + 2H_2O_{(g)} \rightleftharpoons 4H_{2(g)} + CO_{2(g)},\ \Delta G^0 = +131\ \text{kJ/mol} \qquad (1)$$

In geringen Mengen (4 %) wird $H_2$ alternativ durch die Elektrolyse von Wasser produziert. Bei diesem Verfahren handelt es sich ebenfalls um einen endothermen Vorgang. Das Wasser wird stöchiometrisch zu $H_2$ reduziert und zu $O_2$ oxidiert (Gl. 2).[9]

$$2H_2O_{(l)} \rightarrow 2H_{2(g)} + O_{2(g)},\ \Delta G^0 = +237\ \text{kJ/mol} \qquad (2)$$

Ein Blick auf die Zusammensetzung des globalen Energieverbrauchs zeigt, dass die Energiebereitstellung größtenteils durch fossile Brennstoffe erfolgt (Abb. 1). D.h. die elektrische Energie, die für die Elektrolyse von Wasser aufgebracht werden muss, stammt selbst von fossilen Brennstoffen. Die Herstellung eines sauberen Energieträgers erfolgt also unter Energieaufwand und Umweltbelastung. Aus diesem Grund sind alternative Herstellungsmöglichkeiten von $H_2$ unter Berücksichtigung sowohl der Umwelt als auch der Energiebilanz sehr von Interesse.

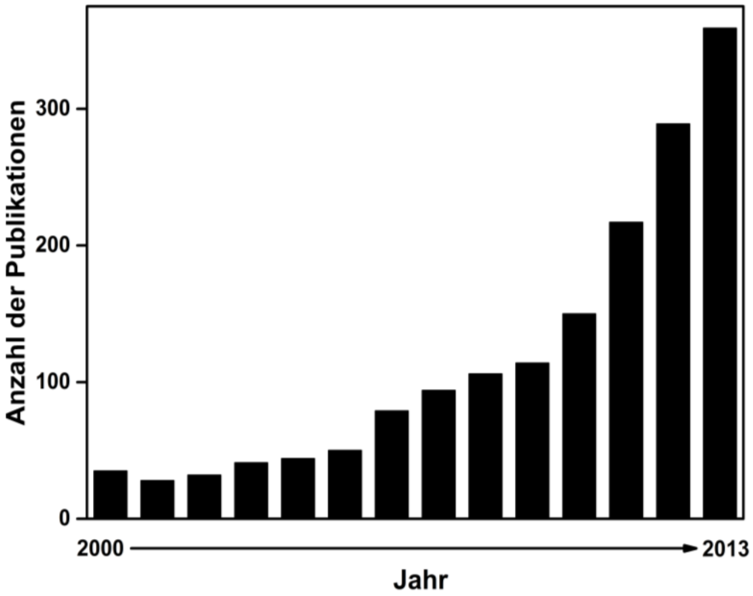

**Abb. 2: Anzahl der Publikationen in Abhängigkeit der vergangenen Jahre für den Suchbegriff 'water splitting' aus der Web of Science Datenbank (Stand: 15.10.2014).**

Eine viel versprechende alternative Produktionsmöglichkeit stellt die fotokatalytische $H_2$-Erzeugung dar. Das exponentiell-ähnliche Wachstum der Publikationsanzahl auf diesem Themengebiet verdeutlicht die Bedeutung dieses Forschungsgebietes (Abb. 2). Der Grundstein dafür wurde unmittelbar vor der Ölkrise 1973 gelegt, als Honda und Fujishima über die fotoelektrolytische Wasserspaltung berichteten.[10] In einem Setup bestehend aus einer $TiO_2$-Fotoanode, einer Pt-Gegenelektrode und einem Separator konnte durch Lichtanregung und einer geringen Spannung ein Fotostrom erzeugt werden, so dass $O_2$ und $H_2$ an der Anode und Kathode aus Wasser gebildet wurden (Abb. 3). Seit dieser Entdeckung sind viele Arbeiten und Entwicklungen auf dem Gebiet der lichtgetriebenen $H_2$-Entwicklung publiziert worden.[11–16] Nach aktuellem Wissensstand haben sich die verwendeten Materialien als nicht hinreichend effektiv bzw. zu kostenintensiv herausgestellt, so dass weiterführende Forschungen notwendig sind, um bessere und kostengünstige Materialien zu entwickeln bzw. zu entdecken. Erste Berechnungen deuten darauf hin, dass in 2050 ein Drittel des globalen Energiebedarfs mit fotokatalytisch erzeugtem $H_2$ gedeckt werden kann, wenn Solaranlagen mit einer Effizienz von 10 % ca. 1 % der weltweiten Wüstenflächen bedecken.[17]

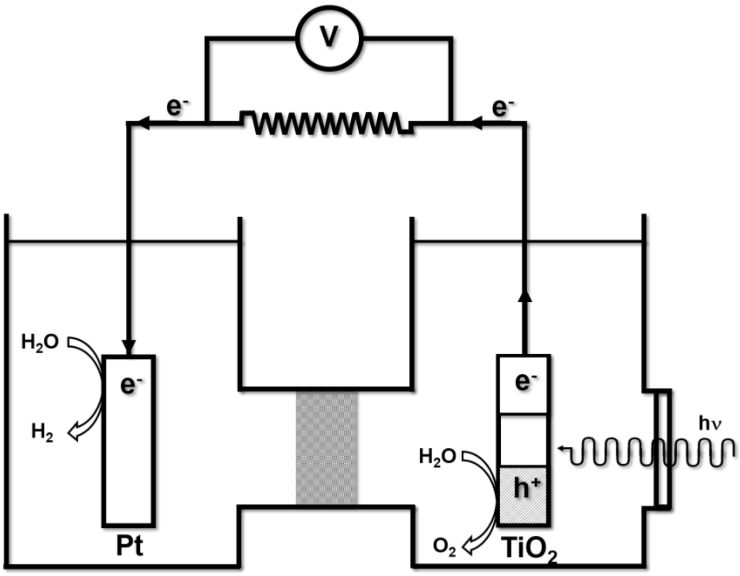

**Abb. 3: Fotoelektrolyse von Wasser zu $H_2$ und $O_2$ an Pt- und $TiO_2$-Elektroden. Adaptiert von Referenz [10].**

Als Vorbild der fotokatalytischen Spaltung von Wasser zu $H_2$ und $O_2$ dient die in der Natur ablaufende Fotosynthese in den Chloroplasten von Pflanzen, einigen Bakterien und Protisten.[18] Bei diesem Prozess werden unter Verwendung von Sonnenenergie Wasser und $CO_2$ zu Kohlenhydraten und $O_2$ umgesetzt (Gl. 3). Dabei lässt sich die Gesamtreaktion in die zwei Teilbereiche (sowohl funktionell als auch räumlich getrennt) Energieumwandlung und Substanzumwandlung unterteilen. Im erst genannten Bereich finden die Lichtreaktionen im fotochemischen Reaktionsbereich statt, während im letztgenannten die lichtunabhängigen Reaktionen im biochemischen Reaktionsbereich ablaufen. Bei der natürlichen Fotosynthese handelt es sich um einen endothermen Prozess mit einem Energiebedarf von $\Delta G^0 = +\ 2875$ kJ/mol (Gl. 3).

$$6CO_{2(l)} + 6H_2O_{(l)} \longrightarrow C_6H_{12}O_{6(s)} + 6O_{2(g)},\ \Delta G^0 = +2875\ \text{kJ/mol} \qquad (3)$$

### 1.1.2 Grundlagen der fotokatalytischen $H_2$-Entwicklung

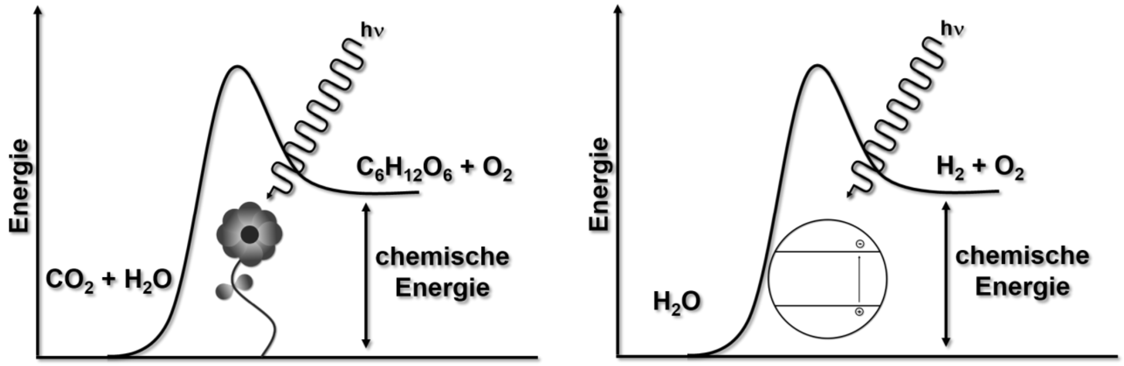

**Abb. 4: Energieschema der Fotosynthese (links) und der fotokatalytischen Wasserspaltung (rechts). Adaptiert von Referenz [11].**

Aufgrund vorhandener Analogien zur natürlichen Fotosynthese wird die fotokatalytische Wasserspaltung in $H_2$ und $O_2$ auch künstliche Fotosynthese genannt. Zum einen handelt es sich auch hier um eine endotherme Reaktion mit einem Energiebedarf von $\Delta G^0 = +\ 237$ kJ/mol (Gl. 2) und zum anderen wird ähnlich wie bei der natürlichen Fotosynthese die solare Energie in chemische Energie umgewandelt (Abb. 4). Fotokatalytische Reduktions- und Oxidationsreaktionen können mit Hilfe von Halbleitermaterialien realisiert werden. Halbleiter weisen eine elektronische Bandlücke auf, welche das Valenzband (VB) vom Leitungsband (LB) trennt. Die Elektronen können thermisch, elektrisch oder auch optisch vom VB in das LB angeregt werden. Bei diesem Prozess können z.B. durch Lichtanregung Elektronen-Loche Paare ($e^-/h^+$) gebildet werden, so genannte Exzitone, so dass die Wasserreduktion durch das Elektron im Leitungsband und die Wasseroxidation durch das Loch im Valenzband erfolgen können (Abb. 5). Die fotokatalytische Wasserspaltung lässt sich in drei wesentliche Schritte unterteilen, auf die im Folgenden näher eingegangen wird: Lichtabsorption und die damit verbundene Erzeugung der Exzitone, Ladungstrennung, in welcher die Ladungsträger an die Oberfläche transportiert werden und schließlich die katalytische Oberflächenreaktion.[11]

Die Lichtabsorption eines Halbleiters stellt den ersten Schritt der fotokatalytischen Wasserspaltung dar. Dabei bestimmt die energetische Größe der Bandlücke den Absorptionsbereich der elektromagnetischen Strahlung, welcher im so genannten Band Gap Engineering durch Variation der Teilchengröße oder das Einbringen von Fremdatomen bzw. Substitutionen im Kationen- und/oder Anionenteilgitter verändert werden kann. Beispielsweise bewirkt eine Verkleinerung der Bandlücke ein Lichtabsorptionsvermögen in einem größeren Wellenlängenbereich. Aus den Redoxpotentialen von $H^+/H_2$ und $O_2/H_2O$ muss ein geeigneter Halbleiter eine Bandlücke von mindestens 1.23 eV aufweisen (Abb. 5).

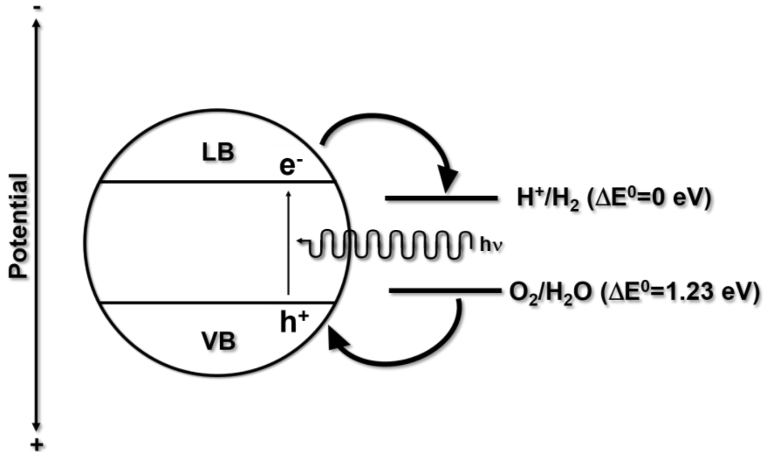

**Abb. 5: Fotokatalytische Wasserspaltung an Halbleitermaterialien. Adaptiert von Referenz [11].**

Für eine erfolgreiche Reaktion zu $H_2$ und $O_2$ aus Wasser müssen im zweiten Schritt die gebildeten Elektronen-Loch-Paare voneinander getrennt werden und an die Oberfläche wandern. Bei diesem Vorgang treten häufig Deaktivierungsprozesse auf, in welcher die Elektronen mit Löchern rekombinieren oder an Haftstellen eingefangen werden und daher nicht mehr für die Reaktionen zur Verfügung stehen. Die Rekombinationen können sowohl im Materialinneren als auch an der Oberfläche erfolgen. Eine effiziente Ladungstrennung und anschließende Diffusion an die Oberfläche wird besonders durch die Kristallstruktur, die Kristallinität und die Partikelgröße stark beeinflusst. Dabei wird die Anzahl von Defekten durch eine hohe Kristallinität reduziert, während durch Verkleinerung der Partikelgröße die Migrationszeit und der Weg der Ladungsträger verkürzt werden. Rekombinationen können auch durch die zusätzliche Verwendung von Cokatalysatoren unterdrückt werden. Diese können selber als Elektronenfänger agieren und Elektronen von dem Halbleiter einfangen.[19]

Im finalen Schritt erfolgt die Oberflächenreaktion des Katalysators zu $H_2$ (Reduktion) und $O_2$ (Oxidation). Dabei werden im Wesentlichen zwei Anforderungen an den Halbleiter gestellt: zum einen die Reduktion bzw. Oxidation zu H und O und zum anderen die Kombination der Oberflächenatome zu molekularem $H_2$ und $O_2$. Die

Reaktionsfolge an der Oberfläche ist am Bespiel der Reduktion mit folgenden Gleichungen beschreibbar.[20]

$$H^{+} + e^{-} + {}^{*} \rightarrow H^{*} \qquad (4)$$

$$2H^{*} \rightarrow H_2 \qquad (5a)$$

$$H^{+} + e^{-} + H^{*} \rightarrow H_2 \qquad (5b)$$

$$2H^{+} + 2e^{-} \rightarrow H_2 \qquad (6)$$

Das * bezeichnet dabei eine Stelle auf der Katalysatoroberfläche, so dass ein * eine freie Stelle und H* ein auf der Oberfläche adsorbiertes H-Atom darstellt. Zunächst werden die Protonen an der Oberfläche adsorbiert, wo sie anschließend zu H* reduziert werden, aber an der Oberfläche adsorbiert bleiben (Gl. 4). Die Bildung von molekularem $H_2$ kann entweder durch Reaktion zweier adsorbierter H-Atome (Gl. 5a) oder durch die Reaktion eines adsorbierten H-Atoms mit einem weiteren Proton und Elektron (Gl. 5b) erfolgen. Die Aktivität der katalytischen Oberfläche kann an Hand des so genannten Vulkandiagramms beurteilt werden (Abb. 6).[20–24] In diesem wird die Rate der $H_2$-Entwicklung (experimentelle Austauschstromdichte, $i_0$) als Funktion der M-H-Bindungsstärke (berechnete Energie für die H-Chemisorption an der Katalysatoroberfläche, $\Delta G_{H^*}$) verschiedener Übergangsmetalle aufgetragen. Aus dieser Auftragung wird deutlich, dass für eine optimale $H_2$-Ausbeute das H-Atom weder zu stark noch zu schwach an die Katalysatoroberfläche gebunden werden darf[25], also $\Delta G_{H^*} = 0$ sein sollte. Daher erschwert eine zu schwache M-H-Bindung die Reaktion der Gl. 4, während eine zu starke M-H-Bindung die Reaktionen der Gl. 5a und b verhindern können. Daraus ergibt sich die einem Vulkan ähnelnde Anordnung der Datenpunkte.

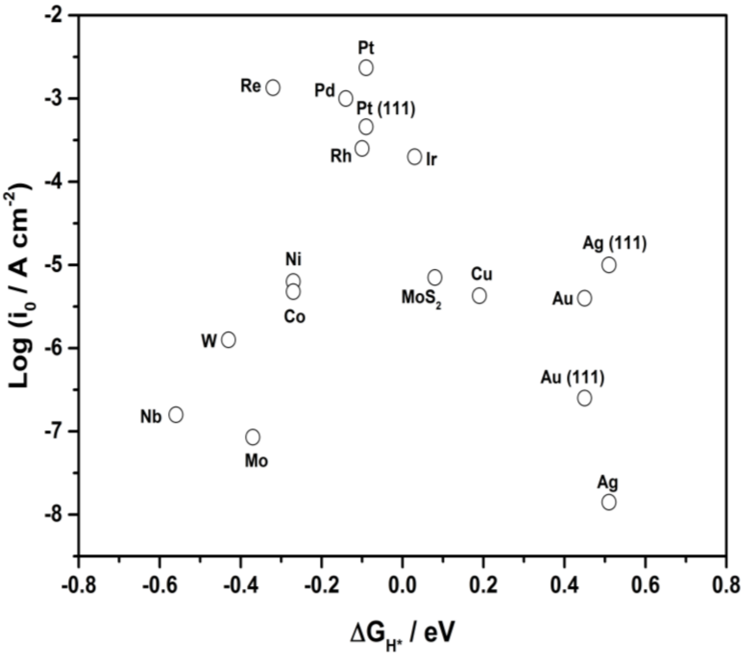

**Abb. 6: Vulkandiagramm (Austauschstromdichte gegen M-H-Bindungsenergie) verschiedener Metalle und $MoS_2$. Adaptiert von Referenzen [20–24].**

Eine weitere Voraussetzung für fotokatalytische Wasserspaltung stellt die energetische Lage der Bänder relativ zu dem Potential der Wasserspaltung dar. So können sich Halbleiter mit einer Bandlücke von ≥ 1.23 eV (= 1100 nm) als inaktive Materialien für die fotokatalytische Wasserspaltung herausstellen, da das Leitungsband positiver und das Valenzband negativer gegenüber von $H^+/H_2$ und $O_2/H_2O$ sind (Abb. 7). Eine Anpassung der energetischen Lage der Bänder an die Redoxpotentiale der Wasserreduktion und –oxidation kann durch das Band Gap Engineering erreicht werden, so dass diese Reaktionen ermöglicht werden können. Für eine erfolgreiche Oberflächenreaktion muss der fotoaktive Halbleiter geeignete aktive Stellen aufweisen. Sonst würden die fotogenerierten Elektronen und Löcher rekombinieren, da die Oberflächenreaktion zu langsam ist oder gar nicht abläuft. Durch die Beladung des aktiven Materials mit einem Cokatalysator können solche aktiven Stellen zur Verfügung gestellt werden. Die Verwendung von Cokatalysatoren spielt daher eine wichtige Rolle für fotokatalytische Reaktionen zur $H_2$-Generierung.[19] Einerseits begünstigen sie die Ladungstrennung durch Einfangen der Elektronen, so dass Deaktivierungsprozesse unterdrückt bzw. minimiert werden und andererseits stellen sie die aktiven Stellen für die katalytischen Reaktionen. Aus dem Vulkandiagramm (Abb. 6) wird deutlich, warum die häufigsten Vertreter der Cokatalysatoren aus der Gruppe der Pt-Metalle kommen (Ru, Rh, Pd, Os, Ir, Pt).

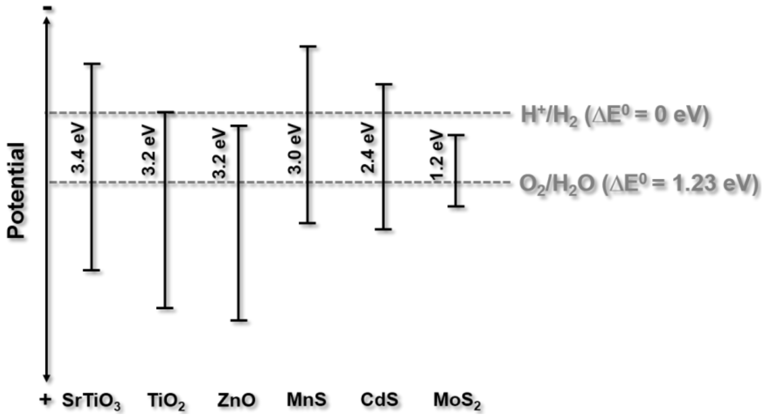

**Abb. 7: Berechnete Leitungs- und Valenzbandlagen für ausgewählte Halbleiter. Adaptiert von Referenz [26].**

Nicht alle Halbleiter, die die diskutierten Anforderungen erfüllen, eignen sich für die Zersetzung von Wasser zu $H_2$ und $O_2$. Besonders Übergangsmetallchalkogenide unterliegen häufig Zersetzungsreaktionen während fotochemischer Prozesse, der so genannten Fotokorrosion. Der bekannteste Vertreter eines fotokatalytisch aktiven Halbleitermaterials stellt Cadmiumsulfid (CdS) dar. Trotz der geeigneten elektronischen Bandlücke (sowohl Größe als auch Lage der Bänder) eignet sich dieser Halbleiter nicht für die fotokatalytische Wasserspaltung. Das Problem stellt die Oxidationsreaktion dar, in welcher CdS statt Wasser oxidiert wird (Gl. 7).[27]

$$CdS+2h^+ \longrightarrow Cd^{2+}+1/8S_8 \qquad (7)$$

### 1.1.3 Fotokatalytische $H_2$- und $O_2$-Entwicklung unter Verwendung von Hilfsreagenzien

Die Spaltung von Wasser stellt eine thermodynamisch und kinetisch anspruchsvolle Reaktion inklusive Mehrelektronenprozessen dar (Gl. 2). Für die Beurteilung von geeigneten Katalysatoren hat sich die Betrachtung der Halbseitenreaktionen bewährt (Gl. 6 und Gl. 8).

$$2H_2O+4h^+ \longrightarrow O_2+4H^+ \qquad (8)$$

Die Untersuchung dieser Reaktionen erfolgt in Anwesenheit zusätzlicher Elektronendonatoren (für die $H_2$-Entwicklung) bzw. –akzeptoren (für die $O_2$-Entwicklung). Als Elektronendonatoren werden häufig Alkohole oder Sulfid-Ionen eingesetzt, welche statt des Wassers irreversibel oxidiert werden und daher als Lochfänger dienen.[28,29] Durch diesen Prozess werden die Elektronen im Fotokatalysator angereichert, was zu der Ermöglichung bzw. Verbesserung der Bildung von $H_2$ führt. Elektronenakzeptoren verbessern die $O_2$-Entwicklung da diese statt Wasser reduziert werden und folglich Löcher in dem Halbleiter für die Oxidation zurückbleiben. Als Elektronenfänger werden oft $Ag^+$ und $Fe^{3+}$ verwendet.[30,31]

Weitere hilfreiche Zusätze für die fotokatalytische $H_2$-Entwicklung stellen Sensibilisatoren dar. Diese ermöglichen Reaktionen im sichtbaren Licht und werden eingesetzt, wenn sich die Bandlücke eines Halbleiters nicht im sichtbaren Bereich befindet. Die Lichtanregung des Sensibilisators führt zu dessen Oxidation, bei der Elektronen in das Leitungsband des Halbleiters übertragen werden, so dass Protonen anschließend zu $H_2$ reduziert werden können (Abb. 8). Dieser katalytische Prozess wird durch die Anwesenheit eines Elektronendonators (z.B. EDTA, Ascorbinsäure) aufrechterhalten, der den Sensibilisator wieder reduziert. Allerdings wird der Elektronendonator während der Reaktion irreversibel oxidiert, während sowohl Sensibilisator als auch Halbleiter unverändert aus der Reaktion gehen. Als Sensibilisatoren werden häufig organische Farbstoffmoleküle oder Übergangsmetallkomplexe verwendet.[32–34]

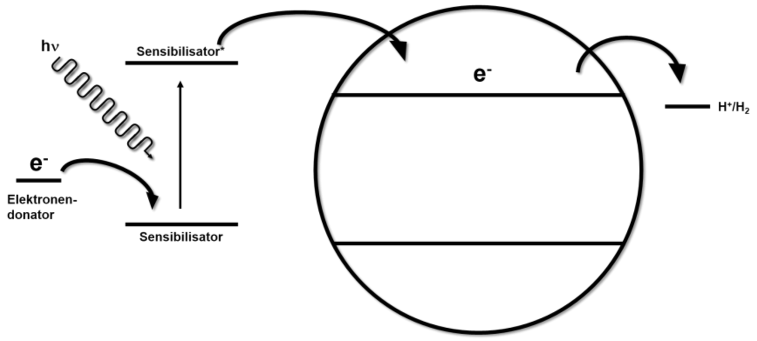

**Abb. 8: Schematische Darstellung der Sensibilisator gestützten $H_2$-Entwicklung. Adaptiert von Referenz [35].**

## 1.2 Molybdändisulfid

**Abb. 9: Molybdänit, entnommen aus Referenz [36].**

### 1.2.1 Eigenschaften

Molybdändisulfid, $MoS_2$, wurde von Carl Wilhelm Scheele erstmals in dem graublau-schimmernden Mineral Molybdänit Ende des 18. Jahrhunderts gefunden (Abb. 9).[37] Die größten Molybdänitvorkommen befinden sich in China, USA und in Südamerika.[38] Das Interesse an diesem Mineral nahm zu Beginn des 20. Jahrhunderts erheblich zu, nachdem die Herstellung von reinem Molybdän daraus in handelsüblichen Mengen möglich wurde. Eine der ersten Beschreibungen der Kristallstruktur von $MoS_2$ wurde von Roscoe Dickinson und Linus Pauling Anfang des 20 Jahrhunderts präsentiert.[39] Demnach besteht die Struktur von $MoS_2$ aus einer hexagonalen Schichtstruktur, welche aus kovalent gebundenen S-Mo-S-Schichten gebildet wird und die Schichten sind über van der Waals Wechselwirkungen aneinander gebunden (Abb. 10). Das Mo-Atom ist von sechs S-Atomen trigonal prismatisch umgeben und pro Elementarzelle sind zwei S-Mo-S-Einheiten enthalten. Daraus ergibt sich eine BcB/CbC Stapelfolge (Großbuchstaben stellen die Position der S-Ebenen und Kleinbuchstaben die der Mo-Ebenen dar). Die Struktur wird als 2H-$MoS_2$ (2: zwei Schichten pro Elementarzelle, H: hexagonale Symmetrie) bezeichnet und stellt den thermodynamisch stabilsten von drei Polytypen dar. Auch in 3R-$MoS_2$ (3: drei Schichten pro Elementarzelle, R: rhomboedrische Symmetrie) sind die Mo-Atome trigonal prismatisch umgeben mit dem Unterschied, dass drei S-

Mo-S-Einheiten pro Elementarzelle vorliegen und sich eine Stapelfolge von BcB/AbA/CaC ergibt (Abb. 10).[40] Im dritten Polytyp, 1T-$MoS_2$ (1: eine Schicht pro Elementarzelle, T: trigonale Symmetrie), liegt eine oktaedrische Koordination der Mo-Atome von sechs S-Atomen vor (Abb. 10). In der Elementarzelle liegt nur eine S-Mo-S-Einheit vor, so dass sich als Stapelfolge AbC ergibt.[41] Der schichtartige Aufbau von $MoS_2$ hat anisotrope Eigenschaften zur Folge. So ist der elektrische Widerstand parallel zu den Schichten um das 1000-fache größer als entlang der Schichten.[42]

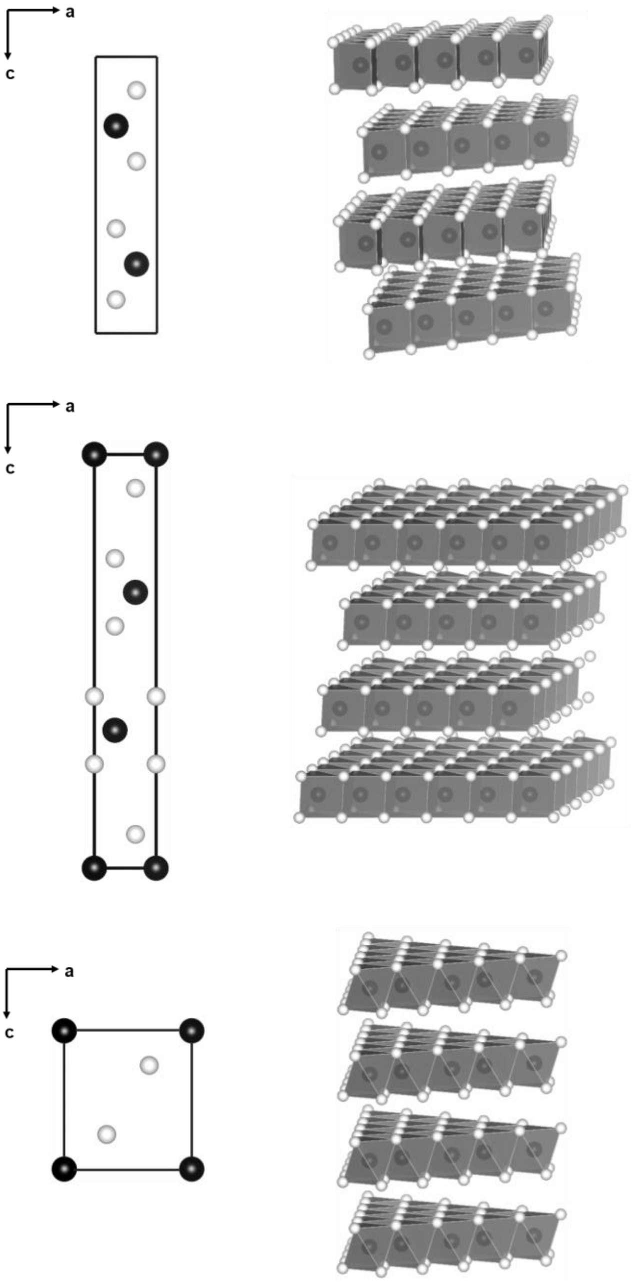

**Abb. 10: Elementarzelle (links) und strukturelles Modell entlang der c-Achse (rechts) von 2H- (oben), 3R- (mitte) und 1T-$MoS_2$ (unten). Schwarze bzw. farblose Symbole repräsentieren Mo- bzw. S-Atome.**

$MoS_2$ weist als Halbleiter eine direkte und indirekte Bandlücke von 1.74 eV bzw. 1.23 eV auf.[43] Während die Elektronenanregung im Volumenmaterial über die indirekte Bandlücke erfolgt, führt eine Verringerung der Anzahl gestapelter $MoS_2$-Schichten zu einem Übergang zur direkten Bandlücke.[44] Im Gegensatz zu anderen prominenten Übergangsmetallchalkogeniden, wie z.B. CdS, unterliegt $MoS_2$ nicht der Fotokorrosion. Der Grund für die Widerstandsfähigkeit gegenüber Fotokorrosion wird bei Analyse der Energiebänder deutlich (Abb. 11). Die Bandlücke liegt zwischen dem gefüllten $d_z{}^2$-Band und den leeren $d_{xy}$- und $d_x{}^2{}_{-y}{}^2$-Bändern von Molybdän. Eine geringfügige Hybridisierung zwischen dem Mo $d_z{}^2$-Zustand und dem $p_z$-Niveau von Schwefel bildet das energetische Valenzband-Maximum am $\Gamma$-Punkt der ersten Brillouin-Zone. Die Mo $d_{xy}$- und $d_x{}^2{}_{-y}{}^2$-Zustände sind mit den $p_x$- und $p_y$-Zuständen der S-Atome hybridisiert und stellen das energetische Leitungsband-Minimum dar. Da die Elektronen des $d_z{}^2$-Bandes nicht direkt zur chemischen Bindung zwischen Molybdän und Schwefel beitragen, führt der Übergang von d-Elektronen aus dem Valenzband in das Leitungsband (Energie zwischen 1.7 und 3 eV) nicht zum Bruch chemischer Bindungen. Dies ist für die hohe Stabilität gegen Fotokorrosion verantwortlich.[45] Eine andere Interpretation für die große Stabilität gegen Fotokorrosion wird auf einen antibindenden und bindenden Zustand zwischen dem Mo $d_z{}^2$ – und dem S $p_z$-Orbital zurückgeführt. Der bindende Zustand soll dabei 5 eV über dem $d_z{}^2$-Valenzband liegen und die große Energiedifferenz ist Resultat einer starken kovalenten Wechselwirkung zwischen dem Mo $d_z{}^2$- und dem S $p_z$-Orbital.[46] In CdS dagegen wird die Valenzbandkante von S p–Orbitalen ausgebildet, so dass der Schwefel in CdS während einer fotochemischen Reaktion für Oxidationsprozesse zugänglich ist.

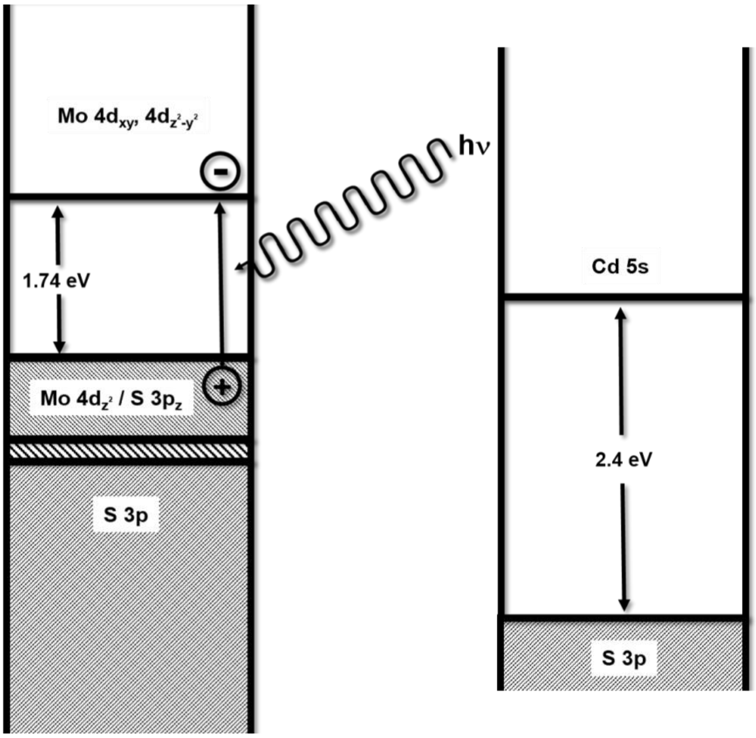

**Abb. 11: Schema der Energiebänder von $MoS_2$ (links) und CdS (rechts). Adaptiert von Referenzen [43,46,47].**

### 1.2.2 Synthese

Neben der Gewinnung aus Molybdänit kann $MoS_2$ auch auf alternativen Wegen präpariert werden. Sowohl die Behandlung von elementarem Molybdän als auch von den Molybdänoxiden ($MoO_2$ und $MoO_3$) mit elementarem Schwefel bei hohen Temperaturen oder in einem $H_2S$-Gasstrom bei niedrigeren Temperaturen führt zur Bildung von kristallinem 2H-$MoS_2$.[40,48,49] Die thermische Zersetzung von Ammoniumtetrathiomolybdat, $(NH_4)_2MoS_4$, in einem $H_2S$- oder $H_2S$/Inertgas-Strom ermöglicht die Herstellung von $MoS_2$ bei recht niedrigen Temperaturen.[50–53] $MoS_2$-Nanopartikel mit unterschiedlichen Morphologien, wie beispielsweise fullerennartige[54], schnurartige[55], blumenartige Partikel[56], Nanoscheiben[57], Nanobälle[57] und Nanotubes[58] lassen sich nach diversen Syntheserouten herstellen. Von technologischer Bedeutung ist die Herstellung von $MoS_2$-Filmen, welche durch Verfahren wie beispielsweise Sputtern oder chemische Beschichtung aus der Gasphase (CVD) erhalten werden können.[59–62] Besonders die Herstellung von graphenartigem, d.h. monolagigem $MoS_2$, ist von wissenschaftlichem Interesse.[63–67] $MoS_2$-Monoschichten lassen sich durch Delaminierung von $LiMoS_2$, welches durch Interkalation von $MoS_2$ mit n-Butyllithium hergestellt wird, oder durch Ultraschallbehandlung in geeigneten Lösungsmitteln herstellen. Die Delaminierung/Exfoliation von $LiMoS_2$ erfolgt in Wasser, was durch die große Hydratationsenthalpie von $Li^+$ hervorgerufen wird.[68] Die Erzeugung von $MoS_2$-Einzelschichten in geeigneten Lösungsmitteln, wie beispielsweise in *N*-methyl-pyrrolidon oder Alkohol-Wasser-Gemischen, erfolgt mit Ultraschallbehandlung von $MoS_2$.[67] Alternativ kann graphenartiges $MoS_2$ durch mechanisches Abtragen mit Klebeband erhalten werden.[69]

### 1.2.3 Anwendungen

Die Hauptanwendungsgebiete von $MoS_2$ sind Schmiermittel und Katalysatoren. Zusätzlich weist $MoS_2$ bereits viel versprechende Eigenschaften als Anodenmaterial für Li-Ionen-Batterien und als Transistor auf.[70–73] Die $MoS_2$-Schichten sind über die relativ schwachen van der Waals Wechselwirkungen gebunden, so dass sich die Schichten analog zum Graphit leicht gegeneinander verschieben lassen.[74,75] Aufgrund dieser tribologischen Eigenschaften wird $MoS_2$ als Schmiermittel in verschiedensten Bauteilen verwendet.[75] Als Katalysator wird promotiertes $MoS_2$ seit Dekaden bei der Hydrodesulfurierung (HDS) von Rohölfraktionen verwendet.[36,76] Bei der Entschwefelung werden schwefelhaltige Kohlenwasserstoffe in Anwesenheit von $H_2$ und $MoS_2$ als Katalysator zu $H_2S$ und einem entschwefelten Kohlenwasserstoff umgesetzt (Abb. 12).[77,78] Die Reaktion verläuft dabei exotherm bei höheren Temperaturen (zwischen 300 und 500 °C) und Drücken (1 – 10 MPa) ab.

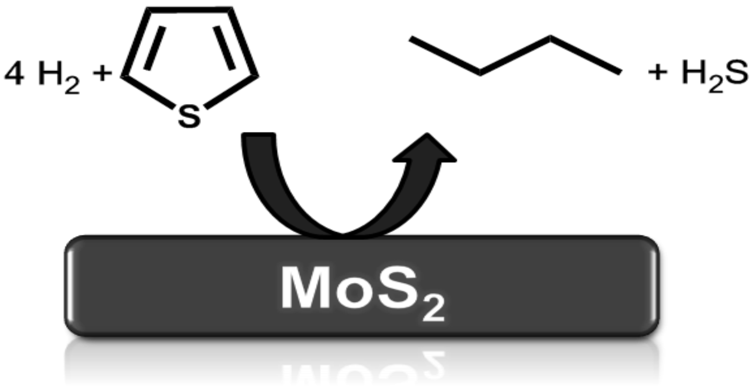

**Abb. 12: Schematischer Ablauf der HDS-Reaktion.**

Darüber hinaus wird $MoS_2$ als Fotokatalysator für den Abbau von organischen Substanzen[79,80] und für die $H_2$-Entwicklung, sei es fotokatalytisch als Cokatalysator oder auch elektrokatalytisch[71,81,82] untersucht. Gegenstand aktueller Diskussionen ist die Aufklärung der katalytisch-aktiven Zentren für die katalytische $H_2$-Entwicklung. Unterschiedliche Arbeitsgruppen konnten dabei durch quantenmechanische Berechnungen und auf Basis experimenteller Ergebnisse die Bedeutung der $MoS_2$-Kanten für die katalytische Reaktion nachweisen. $MoS_2$ wurde hinsichtlich der $H_2$-Aktivität als Funktion von $\Delta G_{H^*}$ untersucht (Abb. 6). Dabei wird deutlich, dass $MoS_2$ viele Metalle in der Austauschstromdichte übertrifft und sich nur den Pt-Metallen unterordnet.[23] Bei den Experimenten wurde festgestellt, dass sich die aktiven Zentren an den Kanten befinden, während die Basalflächen als ungeeignet für die $H_2$-Entwicklung eingestuft werden.[23,83] Theoretische Arbeiten und Rastertunnelmikroskopie-Studien haben die Anwesenheit von zwei unterschiedlichen Kanten in $MoS_2$ aufgezeigt, welche sich aus zwei verschiedenen Morphologien von $MoS_2$ ergeben.[84] Bei den Experimenten wurde elementares Molybdän unter unterschiedlichen Bedingungen zu $MoS_2$ umgesetzt. Die Reaktion in einer deutlich sulfidischen Atmosphäre ($H_2S:H_2 = 500$) führte zur Ausbildung von $MoS_2$-Dreiecken, während sich unter eher reduktiven, schwefelarmen Bedingungen ($H_2S:H_2 = 0.07$) $MoS_2$-Sechsecke ausbildeten (Abb. 13). Im Gegensatz zu den $MoS_2$-Dreiecken, bei welchen lediglich ein Kantentyp vorliegt, bilden sich bei den $MoS_2$-Sechsecken sowohl Mo- als auch S-Kanten aus. Die S-Addition an die Mo-Atome der Mo-Kante verläuft bis zu einer Belegung von 50 % exotherm ab, so dass die Mo-Kante vorzugsweise mit S-Atomen gesättigt ist.[85] Diese sulfidisierte Mo-Kante wurde mittels Dichtefunktionaltheorie (DFT) -Studien und experimentellen Untersuchungen als katalytisch aktives Zentrum für die $H_2$-Entwicklung identifiziert.[21,23,86] Bei den Experimenten konnte durch kontrolliertes Sintern das Verhältnis zwischen Basalfläche und der Mo-Kante variiert werden, so dass eine lineare Korrelation zwischen der Menge an produziertem $H_2$ und dem Anteil an Mo-Kanten hergestellt werden konnte. Die Ergebnisse der Untersuchungen an z.B. unterschiedlichen Morphologien der $MoS_2$-Kristallite, der Generierung katalytisch aktiver Stellen und die Widerstandsfähigkeit gegenüber Fotokorrosion demonstrieren, warum $MoS_2$ besonders als Cokatalysator für die lichtgetriebene $H_2$-Entwicklung eine wichtige Rolle spielt.[29,87,88,88–90]

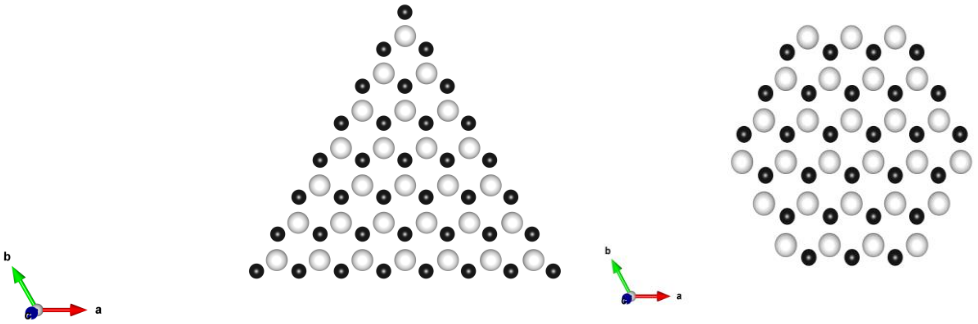

**Abb. 13: $MoS_2$-Dreieck (links) und –Sechseck (rechts) hergestellt unter verschiedenen Bedingungen. Schwarze bzw. farblose Symbole repräsentieren Mo-bzw. S-Atome. Adaptiert von Referenzen [84,91].**

# 2 Ziel

Die Wichtigkeit der Forschung und Entwicklung alternativer Energiegewinnungsmöglichkeiten wurde bereits im vorangegangenen Kapitel verdeutlicht und die fotokatalytische $H_2$-Erzeugung als potentielle Energieträgererzeugung dargestellt. Nicht selten werden Edelmetalle wie beispielsweise Platin als Cokatalysator in den fotokatalytischen Systemen verwendet. Eine intensiv diskutierte Alternative zu den seltenen und teuren Pt-Gruppemetallen stellt $MoS_2$ dar. Ziel der vorliegenden Arbeit ist die Synthese und Charakterisierung von neuartigen $MoS_2$ Cokatalysatoren. Dabei sollte sowohl die Rolle der chemischen Zusammensetzung als auch der Einfluss der strukturellen Eigenschaften auf die fotokatalytische Aktivität untersucht werden. Experimente mit C-haltigen $MoS_2$-basierten Kompositen haben bereits viel versprechende Verbesserungen in der lichtgetriebenen $H_2$-Entwicklung nachgewiesen. Die Aktivitätssteigerung durch C-Zusätze werden dem verbesserten Ladungstransfer, der Bereitstellung von einer größeren Anzahl an aktiven Zentren und der Unterdrückung von Rekombinationsprozessen zugeschrieben. Das Einbringen von Kohlenstoff in die Molybdänsulfide sollte in dieser Arbeit *in situ* durch den thermischen Abbau von unterschiedlichen C-haltigen Thiomolybdaten erfolgen. Bei den Untersuchungen stand die Rolle des C-Gehaltes auf die $H_2$-Entwicklung im Fokus der Arbeiten. Eine in der Literatur viel diskutierte Fragestellung stellt die Identifizierung der aktiven Zentren von (Co-)Katalysatoren dar. Daher haben sich bereits diverse Arbeitsgruppen mit dieser Fragestellung beschäftigt und dabei die Kanten von $MoS_2$ als aktives Zentrum angenommen. In dieser Arbeit sollten weitere Schritte zur Aufklärung der aktiven Zentren in $MoS_2$ durchgeführt werden, so dass durch Änderung der strukturellen Eigenschaften mögliche Korrelationen zur lichtgetriebenen $H_2$-Entwicklung aufgedeckt werden. Darüber hinaus sollten neuartige Übergangsmetallsulfide sowie auch –oxide hinsichtlich der fotokatalytischen $H_2$-Entwicklung untersucht werden.

# 3 Methoden

Die Anfertigung dieser Arbeit erfolgte mit Hilfe folgender analytischer Methoden (Tabelle 1).

**Tabelle 1: Auflistung der verwendeten Methoden.**

| Methode | Abkürzung | Gerät | Messbedingungen |
|---|---|---|---|
| Elementaranalyse | - | Eurovektor EuroEA Elemental Analyzer | Trägergas: He<br>$T_{Verbrennung}$ = 1010 °C<br>Wärmeleitzelle als Detektor |
| mittlere Infrarot-Spektroskopie | MIR | Bruker Alpha P | |
| ferne Infrarot-Spektroskopie | FIR | Bruker ISF66 FIR | Probe in KBr-Matrix |
| Resonanz Raman-Spektroskopie | - | Raman Dilor XY | $\lambda_{Anregung}$ = 514.5 nm<br>$P_{Laser}$ = 10 mW<br>Probe in KBr-Matrix |
| $N_2$-Gas Sorption | - | BEL Japan INC, BEL Sorp max | Probenvorbehandlung: über Nacht im Vakuum gelagert |
| Differenz-Thermoanalyse und Thermogravimetrie | DTA-TG | STA-409CD Netzsch | $N_2$-Gasstrom: 75 mL/min<br>Heizrate: 2 °C/min |
| Raster-Elektronenmikroskopie | REM | Philips ESEM XL 30 | U = 20 kV<br>I = 33 A |
| Festkörper Kernspin-resonanz-Spektroskopie | NMR | Bruker Advance III | $B_0 = 7$ T<br>Bruker 4 mm WVT MAS<br>4 mm $ZrO_2$ Kreisel |
| Röntgenpulverbeugung | XRD | STOE-P | Strahlungsquelle:<br>$CuK_{\alpha 1}$ = 1.54056 Å<br>Transmissionsgeometrie<br>Step, Steptime und $2\Theta$-Bereich variabel<br>PSD und Mythendetektor |
| Röntgenkleinwinkelstreuung | SAXS | Double Ganesha AIR (SAXSLAB, Denmark) | Strahlungsquelle: rotierende Cu-Anode, MicoMax 007HF, Rigaku Corporation, Japan |
| Transmissions-Elektronen-mikroskopie | TEM | Tecnai $G^2$-ST F30 | Strahlungsquelle: 200 kV Shottky FEG Gun |
| Röntgenphotoelektronenspektroskopie | XPS | - | Strahlungsquelle:<br>$AlK\alpha$ = 1486.6 eV, 14.5 kV, 35 mA<br>Ultra-Hochvakuum: $5 \times 10^{-10}$ mbar<br>Gammadata-Scienta SES 2002 Analysator |
| Gasmesssystem | - | Gasmess, MesSen Nord | - |
| Gaschromatographie | GC | 6890 Plus, Agilent | Trägergas: Ar<br>Säule: 5 Å Molsieb<br>Wärmeleitfähigkeitsdetektor |
| Lampe | - | LSB530, LOT | 300 W Xe-Bogenlampe<br>$\lambda$ > 420 nm cut-off Filter |

## 3.1 Röntgenkleinwinkelstreuung

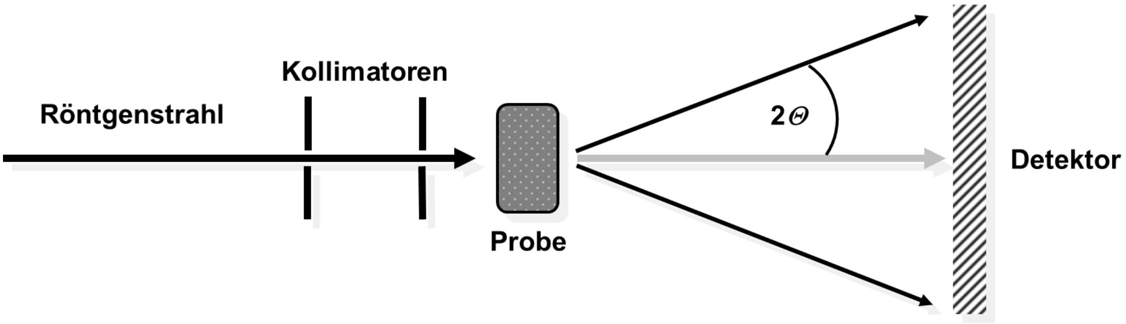

**Abb. 14: Schematisches Messprinzip der SAXS-Methode. Adaptiert von Referenz [92].**

SAXS-Untersuchungen werden i.d.R. an nanoskaligen Materialien in Dispersion/Lösung durchgeführt, um Form und Größe von Teilchen bzw. von deren Aggregaten zu bestimmen. Die Probe wird mit monochromatischen und parallelen Röntgenstrahlen bestrahlt und die elastische Streuung der Röntgenstrahlen an der Elektronendichte wird in einem kleinen Winkelbereich ($\leqq 2°$) in Transmission detektiert (Abb. 14). Die Streuintensität I(q) wird üblicherweise in Abhängigkeit des Streuvektors (q) dargestellt, dessen Zusammenhang aus Gl. 9 erkenntlich wird.

$$q=(4\pi\sin\Theta)/\lambda \qquad (9)$$

Da SAXS-Messungen sehr oft in Anwesenheit eines Lösungsmittels erfolgen und dabei eine zufällig orientierte Verteilung der Partikel zueinander vorliegt, ergibt sich eine radial-symmetrische Intensitätsverteilung. Der Elektronendichteunterschied zwischen Probe und Lösungsmittel ist von zentraler Bedeutung, was SAXS zu einer Kontrastmethode macht. Die Streukurve ergibt sich demnach aus der Differenz zwischen dem reinem Lösungsmittelsignal und der Probe im Lösungsmittel. Dabei wird das Streusignal mit steigendem Kontrast verstärkt. Die Streukurven lassen sich in verschiedene Regionen einteilen (Abb. 15). Aus der Guinier-Region lässt sich die Partikelgröße als Streumassenradius (Gyrationsradius) R bestimmen. Dafür wird der vordere Bereich der Streukurve mit $qR > 1$ betrachtet. An diese Region schließt sich die Porod-Region an, in welcher über den Exponenten x in $q^{-x}$ Rückschlüsse auf Partikelform und –oberfläche gezogen werden können. Detaillierte Beschreibungen zu dieser Charakterisierungsmethode sind in der Literatur enthalten.[93–95]

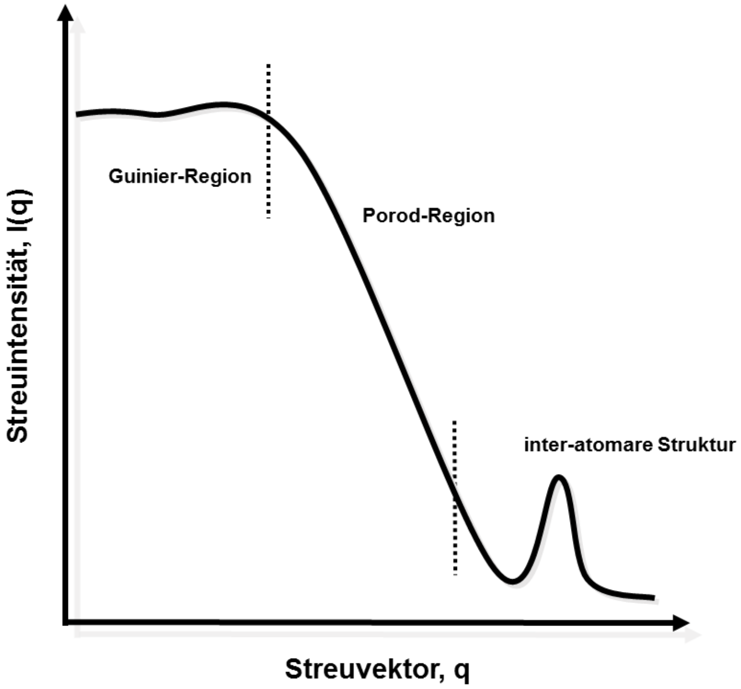

**Abb. 15: Streukurve als Funktion des Streuvektors inklusive der verschiedenen Regionen. Adaptiert von Referenz [96].**

## 3.2 Röntgenphotoelektronenspektroskopie

XPS ist eine oberflächensensitive Methode, die Aussagen über den chemischen Zustand und die quantitative Zusammensetzung einer Probe erlaubt. Diese Art der Spektroskopie beruht auf dem Fotoeffekt, bei welchem Elektronen durch kurzwelliges Licht aus einer Probenoberfläche in das Vakuum befördert werden. Dabei verlassen sie die Probenoberfläche mit einer kinetischen Energie (KE) abhängig von der Energie der einfallenden Strahlung ($h\nu$) und der Bindungsenergie (BE) der Elektronen in dem Material (Abb. 17). In vereinfachter Weise ergib sich Gl. 10, welche den Zusammenhang zwischen den drei Größen herstellt:

$$KE = h\nu - BE \qquad (10)$$

Die Messung der KE gibt daher direkt Auskunft über die BE, da $h\nu$ bekannt ist. Ein Blick auf den Atomaufbau zeigt, dass die BE elementspezifisch ist und jedes Element ein einmaliges XP-Spektrum aufweist. Rumpfelektronen weisen natürlich höhere BE als Valenzelektronen auf. Darüber hinaus hat die chemische Umgebung bzw. der Oxidationszustand einen Einfluss auf die BE. Bei XPS-Experimenten an Feststoffen werden die gemessenen BE in Bezug zur BE des elementaren Zustandes referenziert. Je elektropositiver ein Atom durch einen elektronegativeren Bindungspartner bzw. den Oxidationszustand wird, desto größer wird dessen BE sein, da die Elektronen stärker von dem Atomkern angezogen werden. Im Gegensatz dazu verschiebt sich die BE zu kleineren Werten, wenn ein elektropositiverer Bindungspartner vorhanden ist, da der Oxidationszustand negativer ist. So nimmt z.B. die BE des Cr-2p-Niveaus von 574.2 über 575.7 bis 579.6 eV für Cr(0) – Cr(III) Oxid – Cr(VI) Oxid zu.[97] XPS zählt zu den Nichtgrundzustandsspektroskopien. D.h. die gemessenen BE weichen von theoretischen Orbitalenergien ab, da diese Berechnungen für den Grundzustand durchgeführt werden. Die Photoelektronen können aus den s-, p-, d- und f-Orbitalen stammen. Spin-Bahn-Kopplungen führen zu einer Aufspaltung der p-, d- und f-Orbitale, also Orbitale mit $l > 0$ ($l$ = Bahndrehimpuls). Folglich werden für Fotoelektronen aus p-, d- und f-Orbitalen Dubletts beobachtet, während für s-Elektronen Singuletts im Spektrum vorhanden sind (Abb. 16).

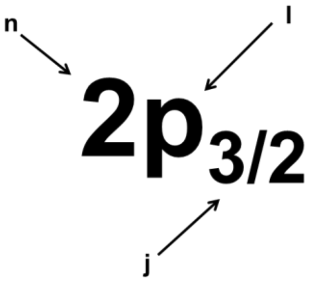

**Abb. 16: Zusammensetzung des Termsymbols aus Hauptquantenzahl n (n = 1, 2, 3, …), der Nebenquantenzahl l (l = 0 (s), 1 (p), 2 (d), 3 (f)) und Gesamtdrehimpuls j (j = |l ± s|). Adaptiert von Referenz [98].**

Die Intensitätsverhältnisse eines Dubletts ergeben sich aus den Beiträgen von l und s (s = Spindrehimpuls), so dass sich für die p-, d- und f-Orbitale Verhältnisse von 1:2, 2:3 und 3:4 für $p_{1/2}$:$p_{3/2}$, $d_{3/2}$:$d_{5/2}$, und $f_{5/2}$:$f_{7/2}$ ergeben. Im Spektrum können zusätzliche Peaks bei höheren BE vorhanden sein, welche durch Shake-Up-Prozesse verursacht werden (Abb. 17). Dieser Fall tritt ein, wenn ein Valenzelektron in ein leeres Orbital angeregt wird, während ein Rumpfelektron das Material verlässt. Für die Promotion des Elektrons vom Valenzband in einen leeren Zustand wird dem

Photoelektron Energie entzogen, so dass das Elektron die Probe mit einer geringeren KE verlässt. Ein prominentes Beispiel sind Shake-Up Peaks bei CuO, welche bei elementarem Kupfer und $Cu_2O$ nicht auftreten können, so dass Cu(II) sehr gut von Cu(0) und Cu(I) unterschieden werden kann. In $Cu_2O$ ist das d-Orbital voll besetzt ($d^{10}$), während in CuO eine $d^9$-Konfiguration vorliegt. Daher kann ein Elektron von Sauerstoff in das $d^9$-Niveau angeregt werden (L $\rightarrow$ M Shake-Up).

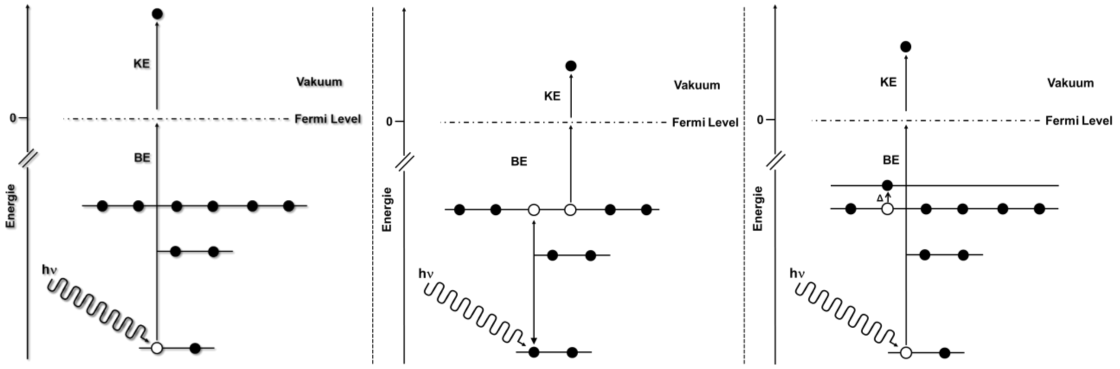

**Abb. 17: Schematische Darstellung der Fotoionisation (links), des Auger Prozess (mitte) und des Shake-Up Prozess(rechts). Adaptiert von Referenz [99].**

In einem XP-Spektrum werden zusätzlich weitere Peaks beobachtet. Das einfach ionisierte Atom kann durch Emission eines weiteren Elektrons (Auger-Elektron) relaxieren, was zu den Auger-Peaks führt (Abb. 17). Bei sauberen Metalloberflächen treten so genannte Plasmonenpeaks auf, welche durch die kollektive Schwingung von Valenzelektronen verursacht werden. Durch inelastische Streuung der Photoelektronen im Feststoff (Abb. 18) tritt in den XP-Spektren auf der Seite niedriger kinetischer Energie ein konturloser Verlustbereich auf (so genannter inelastic scattering tail).

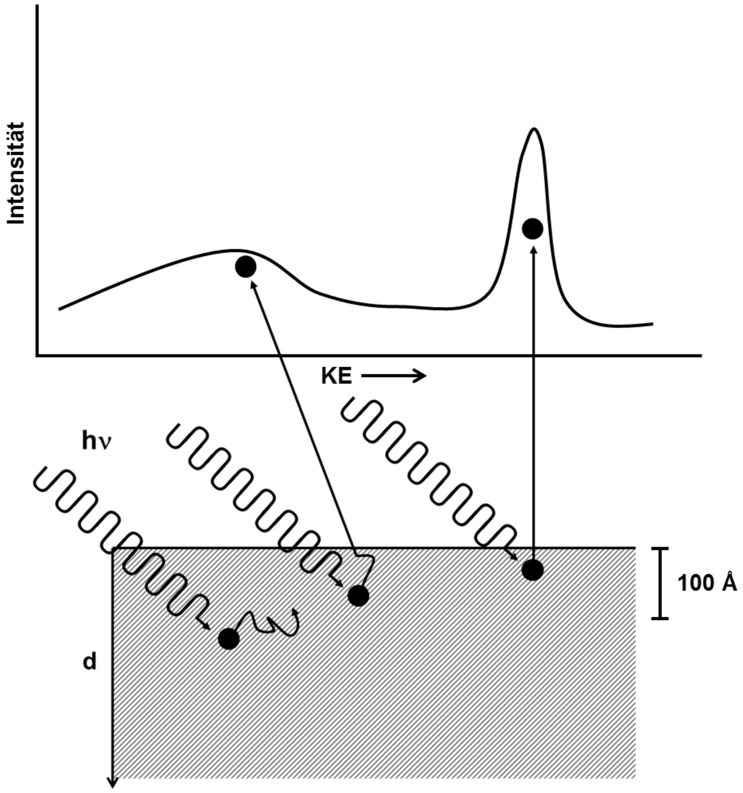

**Abb. 18: Schematische Darstellung von inelastischen Streuprozessen und die resultierenden Auswirkungen auf das XP-Spektrum. Adaptiert von Referenz [99].**

Multiplett-Splitting von Rumpfniveaus tritt auf, wenn z.B. ein Photoelektron aus dem s-Orbital emittiert wird und das verbleibende s-Elektron mit ungepaarten Elektronen z.B. eines d-Orbitals koppelt. Konkretes Beispiel: wenn ein Elektron aus dem 3s-Orbital von $Mn^{2+}$ emittiert ist (Grundzustand: $3s^2$ $3d^5$, $^6S$, S = 5/2, L = 0), führt die Kopplung des $3s^1$-Elektrons mit den d-Elektronen zu den zwei Endzuständen $3s^1$ $3d^5$, $^5S$ (S = 2, L = 0, Spins antiparallel gekoppelt) und $3s^1$ $3d^5$, $^7S$ (S = 3, L = 0, Spins parallel gekoppelt).

Da es sich wie erwähnt um eine Nichtgrundzustandsspektroskopie handelt, tragen intra- und extraatomare Relaxationsphänomene zur gemessenen KE bei. Zusätzlich muss der Madelungterm eines Feststoffes berücksichtigt werden, welcher ebenfalls den Wert der experimentell ermittelten KE beeinflusst.

Die Informationstiefe von XPS beschränkt sich auf bis ca. 100 Å und oft wird für die Abschätzung dieser die universelle Kurve der mittleren freien Weglänge in Abhängigkeit der KE herangezogen (Abb. 19).

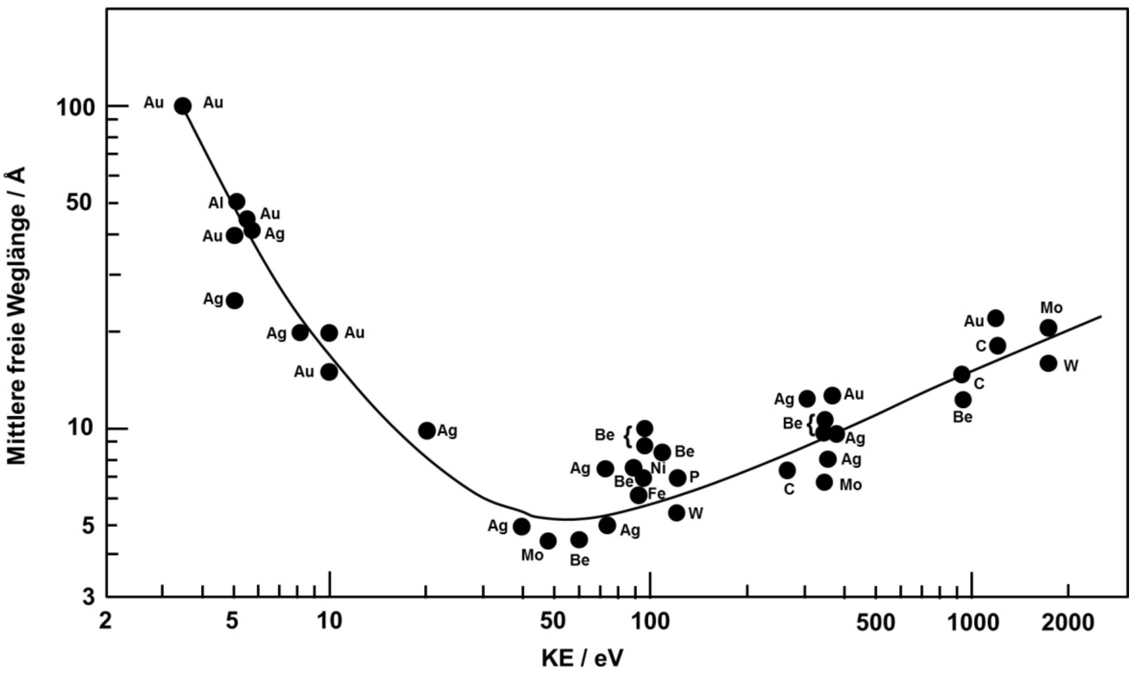

**Abb. 19: Mittlere freie Weglänge als Funktion der KE. Adaptiert von Referenz [99].**

Neben Informationen über den chemischen Zustand eines Elementes eignet sich XPS auch die Bestimmung der quantitativen (Oberflächen)-Zusammensetzung einer Probe. Die Auswertung von relativen Intensitäten eines Atomorbitals für ein Element gibt dabei direkt Auskunft über die Zusammensetzung für die entsprechenden Spezies. Für die Auswertung sind Fotoionisations-Wirkungsquerschnitte/Einfangsquerschnitte ($\sigma$) der jeweiligen Orbitale unter Berücksichtigung von h$\nu$ notwendig, wenn Atomorbitale von verschiedenen Elementen quantitativ über die Intensitäten (I) verglichen werden sollen. Der Fotoionisations-Wirkungsquerschnitt/Einfangsquerschnitt repräsentiert die Wahrscheinlichkeit für die Fotoemission eines Elektrons und wurde von z.B. Scofield tabellarisch zusammengefasst.[100] Die prozentuale Oberflächenzusammensetzung einer Spezies ($C_i$) ergibt sich aus Gl. 11.

$$C_i=(I_i/\sigma_i)/\Sigma_k(I_k/\sigma_k) \qquad (11)$$

Ein XPS-Spektrometer besteht im Allgemeinen aus einer Ultrahochvakuum-Kammer (UHV-Kammer), einer Röntgenquelle (X-ray Quelle), einem Analysator, einem Detektor und einer Steuereinheit (Abb. 21). In den meisten Fällen werden Al- oder Mg-Anoden mit Energien von 1486.6 und 1256.6 eV als X-ray Quelle verwendet. Die auf die Probe einfallenden Photonen erzeugen Fotoelektronen, die über ein Linsensystem in den Halbkreisanalysator gelangen. Diesen können je nach

Einstellung der Gegenspannung (V) nur Elektronen mit bestimmten Energien bis zum Detektor passieren. Die Detektion erfolgt i.d.R. über einen Mehrkanaldetektor, so dass simultan ein Bereich von KE detektiert werden kann und somit die Aufnahme eines Spektrums beschleunigt wird. Detaillierte Hintergrundinformationen zu XPS und Beschreibungen zu Spektrometern sind der Literatur zu entnehmen.[99,101]

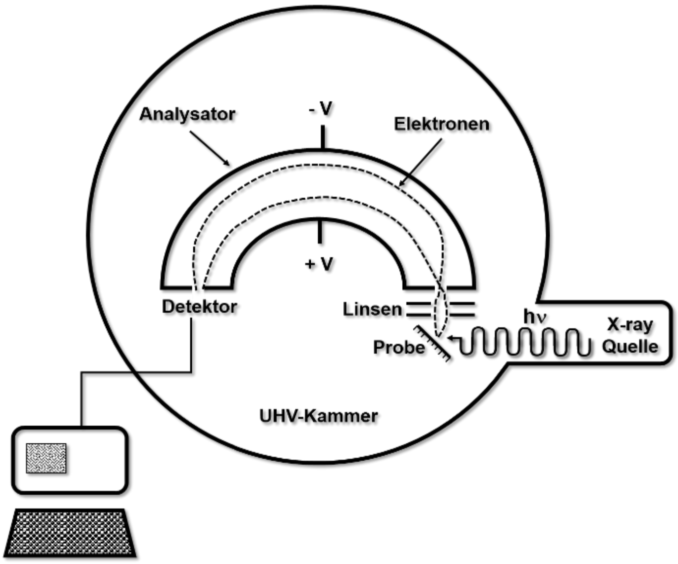

Abb. 20: Schematischer Aufbau eines XPS Spektrometers. Adaptiert von Referenz [99].

## 3.3 Das Gasmesssystem

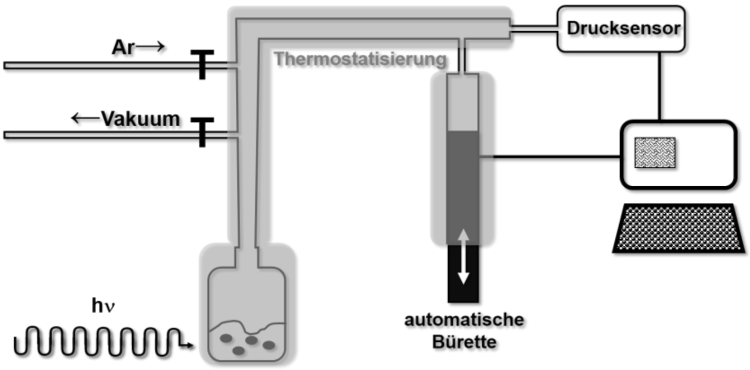

Abb. 21: Schematischer Aufbau des Gasmesssystems.

Das Gasmesssystem erlaubt die kinetische Untersuchung von Reaktionen mit Gasverbräuchen oder –entwicklungen. Entwickelt wurde es 1986 von K. Madeja für

Anwendungen in der asymmetrischen Katalyse. Dabei ging es v.a. um die Verfolgung von Hydrierungsreaktionen, die in Form eines Gasverbrauches aufgezeichnet werden konnten. Im Wesentlichen besteht das Gasmesssystem aus einem Reaktionskolben, einer verbrückenden Glasapparatur, einer automatischen Bürette mit Kolben, einem Drucksensor und einer Steuereinheit (Abb. 21). Des Weiteren wird durch Kühlmäntel an den einzelnen Bauteilen für eine konstante Temperatur während der Messung gesorgt. Dadurch dass die Reaktionen in dieser Arbeit unter inerten Bedingungen (z.B. Ar) stattfanden, verfügt die Glasapparatur über einen Vakuum- und einen Ar-Zugang, damit das System vor jeder Messung sekuriert werden kann. Das Messprinzip beruht auf der konstanten Haltung des Druckes in einem geschlossenen System. Bei einer Reaktion mit Gasmengenänderungen wird eine Druckänderung vom Drucksensor aufgezeichnet, welcher umgehend durch eine Volumenänderung des Systems ausgeglichen wird. Die Volumenänderung erfolgt dabei durch das automatische Verfahren des Kolbens in der Bürette mit Hilfe eines Schrittmotors. Die quantitative Gasmengenänderung wird durch den zurückgelegten Weg des Kolbens bestimmt. Ausführlichere Angaben zum Aufbau der Apparatur sind in der Literatur zu finden.[102]

# 4 Ergebnisse und Diskussionen

## 4.1 Cokatalysatoren auf Basis von $MoS_2$

### 4.1.1 Einfluss des Kohlenstoffgehaltes auf die Struktur und Eigenschaften von $MoS_xC_y$ Fotokatalysatoren für die lichtgetriebene $H_2$-Entwicklung

Zusammenfassung der Veröffentlichung „Influence of Carbon Content on the Structure and Properties of $MoS_xC_y$ Photocatalysts for Light-Driven Hydrogen Generation". Dieser Artikel wurde in der Zeitschrift „Dalton Transaction" (DOI: 10.1039/C2DT31967E) 2013 veröffentlicht.

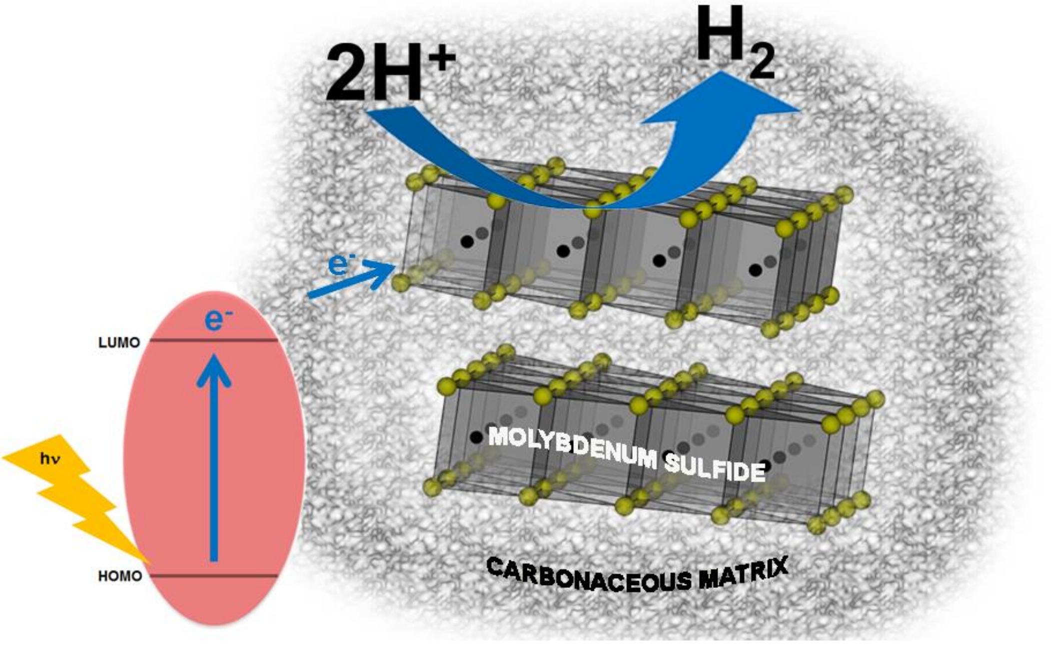

**Abb. 22: Schematische Darstellung der fotokatalytischen $H_2$-Entwicklung an C-haltigen Molybdänsulfiden.**

In der Veröffentlichung werden die Synthese, Charakterisierung und die katalytischen Eigenschaften von C-haltigen Molybdänsulfid-Nanokompositen beschrieben. $MoS_xC_y$ Cokatalysatoren wurden durch den thermischen Abbau von Thiomolybdaten der allgemeinen Formel $(R_4N)_2MoS_4$ mit R = $-H_4$ ($C_0$), $-CH_3$ ($C_1$), $-C_3H_7$ ($C_3$), $-C_6H_{13}$ ($C_6$) erhalten. Mit dieser Syntheseroute wurden nanoskalige Cokatalysatoren hergestellt. Die Bestimmung der chemischen Zusammensetzung erfolgte mit Hilfe der Elementaranalyse und ergab, dass der C-Gehalt in den Molybdänsulfiden durch die

C-Kettenlänge im Edukt gesteuert wird. Folglich nimmt der C-Gehalt von $C_1$ zu $C_6$ zu. Die chemische Natur der C-Spezies in $MoS_xC_y$ ist bisher noch nicht bekannt und wird aktuell in der Literatur diskutiert. Der S-Gehalt folgt keinem eindeutigen Trend, so dass dieser zunächst von $C_0$ nach $C_1$ abnimmt, anschließend wieder bei $C_3$ etwas ansteigt und bei $C_6$ eine unterstöchiometrische Probe erhalten wird. Die Art des Eduktes spiegelt sich zusätzlich in den strukturellen Eigenschaften wider. Die Bildung von $MoS_xC_y$ Nanopartikeln wurde durch XRD- und TEM-Untersuchungen nachgewiesen. Mit zunehmender Kettenlänge im Edukt nehmen Stapelhöhe und Schichtlänge der $MoS_2$-Schichten ab, so dass die größten Partikel bei $C_0$ (3.0 und 4.1 nm) und die kleinsten bei $C_6$ (1.2 und 2.5 nm) beobachtet werden. Dementsprechend steigt die Anzahl der $MoS_2$-Kanten mit dem C-Gehalt in den Edukten an. Neben verbogenen $MoS_2$-Schichten liegen außerdem gegeneinander verschobene und verdrehte Schichten vor. Darüber hinaus deutet der abfallende Untergrund bei kleinen Streuwinkeln in den Pulverdiffraktogrammen auf unkorrelierte $MoS_2$-Monoschichten hin. Allerdings gibt es keinen direkten Zusammenhang zwischen der Art des Eduktes und der spezifischen Oberfläche. Die spezifische Oberfläche nimmt zunächst von $C_0$ (9 $m^2g^{-1}$) nach $C_1$ (67 $m^2g^{-1}$) zu, dann wird über $C_3$ (19 $m^2g^{-1}$) nach $C_6$ (0.4 $m^2g^{-1}$) eine signifikante Abnahme beobachtet. Die Charakterisierungen der Abbauprodukte machen deutlich, dass die Art des Eduktes Einfluss auf strukturelle Eigenschaften und auf die chemische Zusammensetzung der Cokatalysatoren hat. Aus den fotokatalytischen Untersuchungen gehen keine Zusammenhänge zwischen C-Gehalt und generierter $H_2$-Menge hervor. Den größten $H_2$-Umsatz zeigt dabei deutlich $C_3$ (380 µmol/15h) gefolgt von $C_1$ (300 µmol/15h) und $C_0$ (260 µmol/15h). Die Probe mit dem größten C-Anteil ($C_6$) erzeugt mit Abstand die geringste Menge $H_2$ in dieser Versuchsreihe (190 µmol/15h). Alle thermischen Zersetzungsprodukte übertreffen $MoS_2$-Volumenmaterial deutlich in der produzierten Menge an $H_2$ (30 µmol/15h). Dadurch dass sich die Proben neben dem C- und S-Gehalt auch in strukturellen Eigenschaften unterscheiden, ist eine direkte Korrelation zwischen den katalytischen Eigenschaften und C-Gehalt nicht möglich. Möglicherweise sind ein mittlerer C- und S-Gehalt und eine höhere Anzahl von $MoS_2$-Kanten für die katalytische Aktivität von $C_3$ verantwortlich. Zu Vergleichszwecken wurden mechanische Mischungen bestehend aus $C_0$ mit rußartigem Kohlenstoff bzw. Graphen hergestellt und fotokatalytisch untersucht. Dabei wurden Proben mit einem C-Gehalt analog zu $C_1$, $C_3$ und $C_6$ dargestellt. Die mechanischen Mischungen

(~320 µmol/15h) übertreffen $C_0$, $C_1$, $C_6$ und $MoS_2$-Volumenmaterial in der produzierten $H_2$-Menge. Eine Abhängigkeit der C-Menge auf die katalytischen Ergebnisse wird hierbei nicht ersichtlich. Im Allgemeinen stellt sich der Kohlenstoff als förderlicher Zusatz für die fotokatalytische $H_2$-Erzeugung heraus. Die Verbesserung der katalytischen Eigenschaften durch den Kohlenstoff basiert auf der Unterdrückung der Rekombination, Verbesserung des Ladungstransfers und Erhöhung der Anzahl aktiver Zentren.

J. Djamil, S. A. Segler, A. Dabrowski, W. Bensch, A. Lotnyk, U. Schürmann, L. Kienle, S. Hansen, T. Beweries, *Dalton. Trans.* **2013**, *42*, 1287- 1292.- Reproduziert mit der Erlaubnis der Royal Society of Chemistry.

Dalton
Transactions

RSC Publishing

PAPER

View Article Online
View Journal | View Issue

Cite this: *Dalton Trans.*, 2013, **42**, 1287

# The influence of carbon content on the structure and properties of $MoS_xC_y$ photocatalysts for light-driven hydrogen generation†

John Djamil,[a] Stephan A. Segler,[a] Alexandra Dabrowski,[a] Wolfgang Bensch,*[a] Andriy Lotnyk,[b] Ulrich Schürmann,[b] Lorenz Kienle,[b] Sven Hansen[c] and Torsten Beweries[c]

Received 28th August 2012,
Accepted 30th October 2012

DOI: 10.1039/c2dt31967e

**www.rsc.org/dalton**

Carbon containing nano-sized molybdenum sulfide composites ($MoS_xC_y$) obtained by thermal decomposition reactions of $(R_4N)_2MoS_4$ (R = –H ($C_0$), $–CH_3$ ($C_1$), $–C_3H_7$ ($C_3$), and $–C_6H_{13}$ ($C_6$)) show promising performance in visible-light driven photocatalytic hydrogen generation.

## Introduction

In search of renewable and sustainable energy resources, the formation of hydrogen as a clean energy carrier has attracted much attention in science and technology. Especially visible-light driven hydrogen production represents a dynamic and fast growing research field today.[1,2] A large number of photocatalysts has been tested, covering a huge variety of chemical compositions.[3–12] Currently, the photocatalysts in heterogeneous water reduction systems are usually based on transition metal oxides and/or sulfides. In many cases Pt, Pd or other noble metals are added as a cocatalyst. An important challenge is to develop and to identify catalyst systems without precious, expensive and partially environmentally harmful noble metals. Different approaches with $MoS_2$ as a catalyst for light driven hydrogen production have been reported with the aim to replace noble metals.[13–20]

The application of $MoS_2$/CdS nanocomposites and colloidal $MoS_2$ has been demonstrated recently.[13,14] For the colloidal system, the samples were prepared by solvothermal treatment of a $(NH_4)_2MoS_4$ solution in methanol including a polymer as the protecting agent and $N_2H_4{\cdot}H_2O$ as the reductant. The photocatalytic activity was tested in a system using $[Ru(bpy)_3]^{2+}$ (bpy = 2,2′-bipyridine) as the photosensitizer, ascorbic acid as the sacrificial electron donor and an acetonitrile–methanol mixture as the solvent. The best system showed about 850 μmol of hydrogen after 6 h of visible light irradiation. Photocatalytic reactions of $MoS_2$/CdS samples were also carried out in aqueous lactic acid solutions and for comparison cocatalysts such as noble metals were deposited on CdS. However, $MoS_2$ showed the highest activity in this series with a $H_2$ evolution rate of about 530 μmol $h^{-1}$.

CdSe/$MoS_2$ nanocomposites in $Na_2S/Na_2SO_3$ based aqueous systems have also been investigated recently.[15] Depending on the loading of $MoS_2$ on CdSe, the best value for $H_2$ evolution was 45 μmol after 5 h of irradiation with visible light.

The usage of composites like $MoS_2/SiO_2$ with $CdS/SiO_2$ and $TiO_2$ has been examined in earlier studies.[18] Reactions were carried out in a KOH water–methanol solution applying a medium pressure Hg lamp. The best result of 860 μmol $h^{-1}$ was obtained using a mixture of $TiO_2$ with $MoS_2/SiO_2$. Photodeposited $MoS_2$ on titania was explored in an aqueous formic acid solution under UV light.[19] A maximum yield of 11 μmol $H_2$ after 5 h of irradiation was determined.

Very recently a composite material consisting of nanosized $TiO_2$ and $MoS_2$/graphene was investigated for visible-light driven $H_2$ generation. Photocatalytic activity was tested in a water–ethanol mixture by irradiation with a 350 W Xe arc lamp. The best sample composed of 99.5% $TiO_2$ and 0.5% of a $MoS_2$/graphene hybrid (95% $MoS_2$ and 5% graphene) showed photocatalytic $H_2$ activity of about 165 μmol $h^{-1}$.[20] The authors ascribed the enhanced performance compared to the single components to a synergetic effect between $MoS_2$ and graphene layers by suppressed charge recombination, improved charge transfer, more active adsorption sites and photocatalytic reaction centers.

$MoS_2$ and $MoS_2$/Co or $MoS_2$/Ni composites are the most widely used catalysts in the hydrodesulfurization (HDS) reaction of refinery streams. The presence of defective sites in the

---

[a] *Institute of Inorganic Chemistry, Max-Eyth-Str. 2, D-24118 Kiel, Germany. E-mail: wbensch@ac.uni-kiel.de; Fax: +49 431 880 1520; Tel: +49 431 880 2091*
[b] *Institute for Material Science, Kaiserstr. 2, D-24143 Kiel, Germany. E-mail: lk@tf.uni-kiel.de; Fax: +49 431 880 6178; Tel: +49 431 880 6176*
[c] *Leibniz-Institute for Catalysis, Albert-Einstein-Str. 29a, D-18059 Rostock, Germany. E-mail: torsten.beweries@catalysis.de; Fax: +49 381 1281 51104; Tel: +49 381 1281 104*

† Electronic supplementary information (ESI) available: Analytical methods, Preparation of $(NH_4)_2MoS_4$ and of $(NR_4)_2MoS_4$; nitrogen and krypton adsorption measurements; Photocatalytic hydrogen generation with $[Ir(pyb)_2(bpy)](PF_6)$ as sensitizer. See DOI: 10.1039/c2dt31967e

$MoS_2$ structure is one of the most important prerequisites for high catalytic activity. Sulfur vacancies are required and consequently the S coverage of the Mo edges must be less than 50%.[21] Further insight into the function of different sites of $MoS_2$ was provided by several studies on model systems.[22–29]

The suitability of hydrogen adsorption on the (10–10) edge of crystalline $MoS_2$ was shown by DFT studies, indicating that the free energy of adsorbed H is very similar to that of a hydrogenase model and Pt. It was also demonstrated that a certain carbon content increases the HDS activity of the catalysts.[30]

Besides the application of $MoS_2$ based catalysts in the HDS reaction, $MoS_2$ was investigated in photo-oxidation reactions of organic molecules.[31] Moreover in a thorough study of $MoS_2$ nanoclusters in the quantum confinement regime it was concluded that such clusters display several features suitable for solar photocatalysis.[31–33] Recently it has been demonstrated that in electrocatalysis the edge structure of $MoS_2$ nanoparticles is crucial for the hydrogen evolution reaction (HER).[30,34] The HER was also studied on carbon supported $MoS_2$ nanoparticles. It was shown that the activity of the carbon supported $MoS_2$ is comparable to that of $MoS_2$ on Au(111).[35]

According to these results one can expect that materials based on nanosized $MoS_2$ are good photocatalysts for hydrogen evolution. In previous work we demonstrated that simple thermal decomposition of tetraalkylammonium thiomolybdates $(R_4N)_2MoS_4$ generates highly active HDS catalysts[36–39] containing nanoparticulate $MoS_2$. Moreover, the number of stacked $MoS_2$ slabs and C content in the products vary with the size of R and the decomposition conditions. One should note that there is no clear evidence about the nature of the carbonaceous species in the $MoS_2$ based materials. There is still a debate on whether Mo carbides, amorphous carbon, graphitic or aliphatic residues are present in the materials and also carbosulfide phases were considered.[28,39–42]

The effect of different carbon species on the photocatalytic visible light driven hydrogen production was recently studied with different systems. An enhanced light absorption and charge separation due to chemical bonding between multi-walled carbon nanotubes and $Cd_{0.8}Zn_{0.2}S$ leads to improved photocatalytic $H_2$ production.[43] Studies on carbon-incorporated $TiO_2$ microspheres demonstrated an increase in activity ascribed to the sensitization effect of carbon and its enhanced light absorption as well.[44]

## Results and discussion

In the present work, a comparative study of $MoS_xC_y$ catalysts was carried out with the aim to explore the influence of carbon content in the $MoS_2$ photocatalysts on the chemical properties and the photocatalytic activity for hydrogen evolution. $MoS_xC_y$ with different carbon contents were prepared by thermal decomposition of carbon containing precursors $(R_4N)_2MoS_4$ (R = –H ($C_0$), $-CH_3$ ($C_1$), $-C_3H_7$ ($C_3$), $-C_6H_{13}$ ($C_6$)). These compounds are easily available *via* exchanging the ammonium ion in $(NH_4)_2MoS_4$ by $(R_4N)^+$, *cf.* ESI.† $(NH_4)_2MoS_4$ and $(R_4N)_2MoS_4$ were prepared according to a modified literature procedure.[45,46] $MoS_xC_y$ catalysts were obtained by decomposition of the precursors in a rotary tube furnace under nitrogen flow at 350 °C for 1 h. To monitor the influence of the carbon on the catalytic activity, mechanical mixtures of the carbon free $C_0$ precursor, – carbon black and graphene – resp. were prepared by milling the mixtures in a ball mill for 15 min under an inert atmosphere. The carbon content was adjusted, thus producing samples with C amounts of $C_1$, $C_3$ and $C_6$, *cf.* (ESI Table S1†). For comparison, commercially available bulk $MoS_2$ was also tested in the catalytic reaction. The products were characterized using X-ray powder diffraction (XRD), high resolution transmission electron microscopy (HRTEM), nitrogen and krypton adsorption measurements and elemental analysis. Photocatalytic reactions were carried out in a system using $[Ru(bpy)_3](PF_6)_2$ as the photosensitizer and triethylamine as the sacrificial electron donor in an acetonitrile–water mixture as the solvent. The evolved gas was quantified by an automatic burette and qualified by gas chromatography.[47]

The carbon contents of the products $MoS_xC_y$ as a function of the number of C atoms in the precursors vary from $y = 0$ to about 1.5. There is nearly a linear relation between the amounts of carbon in $MoS_xC_y$ and $(R_4N)_2MoS_4$ precursor materials, respectively (Fig. 1a). For $C_1$ and $C_3$ a S content close to $x = 2$ was found while the S concentration in $C_6$ is clearly lower which has already been reported (Fig. 1b).[46] A significant excess of sulfur with $x = 2.45$ was found for the sample $C_0$.

Fig. 2 (top) displays the XRD patterns of the decomposition products and of bulk $MoS_2$. All patterns are characterized by broad reflections with low intensities compared to that of crystalline $MoS_2$ (reference sample). These observations are clear hints for structural disorder, pronounced short-range order, poor crystallinity and sizes of coherent scattering domains within the nanoregime. Furthermore the intensity of the (002) reflection at $2\Theta \approx 14°$ significantly decreases and finally disappears for the sample $C_6$. This observation can be explained by a decreasing number of stacked $MoS_2$ slabs in the products. The particle sizes of $MoS_2$ along the *c*-direction can be estimated from the sizes of coherent scattering domains applying the *Scherrer equation*. A decrease along the *c*-direction from about 4 nm to 2.5 nm for $C_0$ to $C_3$ is obtained. Obviously, such estimation is not possible for the products of the $C_6$ precursor. Nevertheless, the absence of the (002) reflection suggests a size in the *c*-direction of lower than 2.5 nm. Moreover, the position of the (002) reflection of the decomposition products is shifted to lower angles, which may be caused by bending of the $MoS_2$ slabs, strain effects, and defects involving folding of the layers. However, one cannot exclude the possibility that residual C is located in the van der Waals gaps of $MoS_2$, also leading to a shift to larger *d*-values. The peak profiles and the absence of certain reflections indicate turbostratic type disorder, *i.e.*, individual $MoS_2$ layers are twisted and shifted against each other. The mechanical mixtures only show an additional reflection for graphene composites of the (002) reflection of graphene (ESI Fig. S1 and S2†).

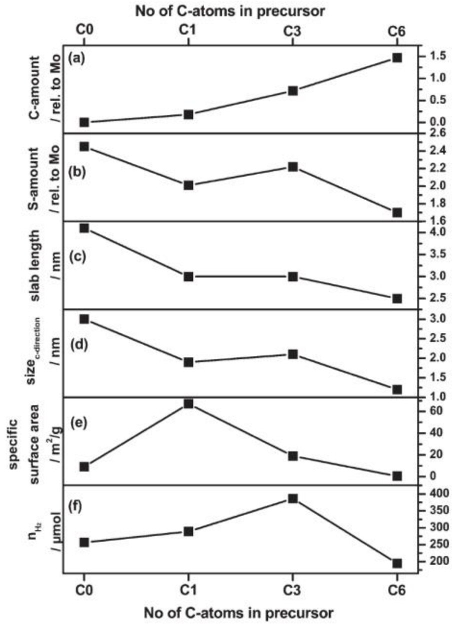

**Fig. 1** Chemical analysis (a) and (b), statistical analysis of TEM images (c–d), BET surface area (e) and photocatalytic hydrogen evolution after 15 h of irradiation (f).

Fig. 2 (bottom) shows HRTEM micrographs of the decomposition products. The $MoS_2$ slabs are bent and show only short-range order in all cases. The statistical analysis of the images reveals average particle sizes of 3.0 nm, 1.9 nm, 2.1 nm and 1.2 nm for $C_0$, $C_1$, $C_3$ and $C_6$ respectively (Fig. 1d) along the *c*-direction. This trend is in accordance with the results obtained from XRD patterns. As the carbon content increases in the alkyl groups, the disorder increases as well. Furthermore, the average slab length varies from about 4.1 nm for $C_0$ to *ca.* 3.0 nm for $C_1$ and $C_3$ and 2.5 nm for $C_6$ (Fig. 1c).

In Fig. 1e the specific surface areas are displayed. These are determined by applying the BET model (adsorption–desorption isotherms in ESI Fig. S3†). While samples $C_0$ to $C_3$ ($9\ m^2\ g^{-1}$, $67\ m^2\ g^{-1}$ and $19\ m^2\ g^{-1}$) exhibit reasonable values, $C_6$ only shows a marginal specific surface area of about $0.4\ m^2\ g^{-1}$. It seems that a higher C content leads to a 'compaction' of the materials.

The results of the structural characterizations on different length scales reveal that the different carbon containing precursors have mainly two effects on the catalysts. The size of R in $(R_4N)_2MoS_4$ strongly affects the microstructural properties: increasing R leads to products with a decreasing number of stacked $MoS_2$ slabs and to a significant change of the slab lengths. The statistical analysis of the slab lengths demonstrates that the $C_0$ sample contains the longest slabs followed by $C_1$, $C_3$ and $C_6$ containing the shortest slabs (Fig. 1c).

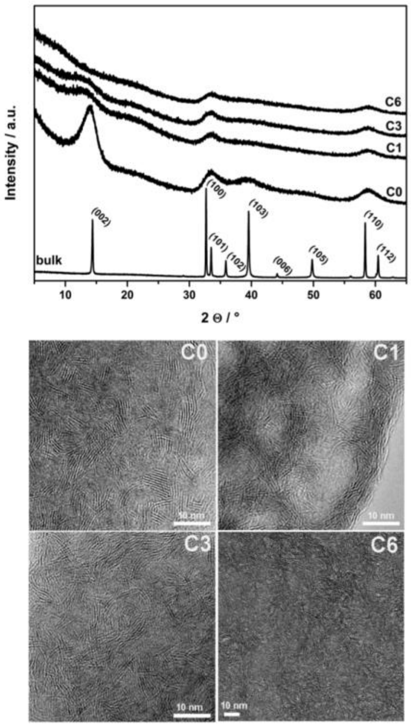

**Fig. 2** Top: XRD patterns of the decomposition products and of bulk $MoS_2$. Bottom: HRTEM micrographs of decomposition products.

All materials show activity for photocatalytic hydrogen generation (Fig. 1f and 3). In the following the amounts of evolved hydrogen are compared after 15 h of irradiation. The bulk material shows the poorest activity with about 30 µmol, while the $C_3$ sample exhibits the highest $H_2$ evolution producing up to 380 µmol. The activity of $C_3$ is followed by $C_1$, $C_0$ and $C_6$. At first glance, no obvious relation exists between particle sizes, specific surface areas and carbon contents on the photocatalytic activity. However, structural data and chemical composition suggest that sample $C_3$ presents the optimal compromise between C and S contents, average slab length and stacking degree. All these properties seem to generate the largest number of catalytically active sites. An influence of the carbon amount on the activity may be derived considering catalysts $C_1$ and $C_3$. Both samples present similar structural properties and particle sizes but a significantly different carbon content. We note that there is no obvious relation between the specific surface areas and the observed photocatalytic activity.

The kinetic studies reveal different reaction rates for all samples (Fig. 3). Sample $C_0$ exhibits higher rates than $C_3$ in the first hour, however, the rate decreases over time. Catalysts

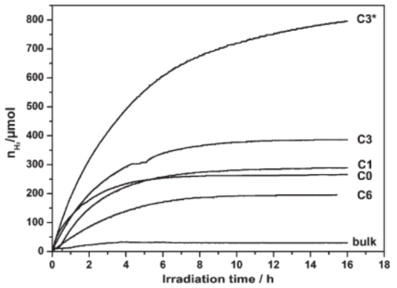

**Fig. 3** Kinetic studies of the photocatalytic hydrogen evolution reaction from a mixture containing triethylamine (8 mL), water (3 mL) and $[Ru(bpy)_3](PF_6)_2$ (1 mM) in acetonitrile (10 mL). Additionally the $C_3$* sample was tested under the same conditions by applying $[Ir(pyb)_2(bpy)](PF_6)$ as the sensitizer.

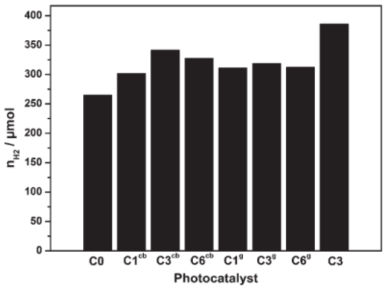

**Fig. 4** Photocatalytic hydrogen evolution reaction from a mixture containing triethylamine (8 mL), water (3 mL) and $[Ru(bpy)_3](PF_6)_2$ (1 mM) in acetonitrile (10 mL) after 15 h of irradiation for molybdenum sulfide photocatalysts composed of carbon black (cb), graphene (g), $C_0$ and $C_3$.

$C_1$ and $C_3$ are more active at longer irradiation times. The catalyst $C_6$ shows the poorest activity and the slowest reaction rate of all decomposition products, but this catalyst is still more active than bulk $MoS_2$ leading to the assumption that nanosized particles in general show better photocatalytic performances. This assumption is confirmed by related studies.[31–33]

Additionally, some $MoS_2$ catalysts were studied in a system applying $[Ir(pyb)_2(bpy)](PF_6)$ (pyb = 2-(pyridin-2-yl)benzen-1-ide) as the sensitizer, *cf.* ESI.† This was recently shown to enhance the hydrogen production yields drastically.[48] The catalytic performance was indeed enhanced tremendously for all tested samples. For the $C_3$ sample the amount of evolved $H_2$ after 15 h of irradiation is significantly larger than for the Ru-based system. These investigations underline the good performance of $MoS_xC_y$ compounds. In the Ir-based systems the catalyst performance decreases much later compared to the Ru systems; even after 16 h where saturation is observed for Ru/$C_3$ (Fig. 3 and ESI Fig. S4†) photocatalytic hydrogen production is still observable.

The carbon containing mechanical mixtures of $C_0$ were tested in the Ru-based system for hydrogen generation as well (Fig. 4, ESI Fig. S5 and S6†). In all photocatalytic reactions an enhancement in hydrogen evolution is observed compared to $C_0$, and all mixtures show more or less the same activity with a $H_2$ evolution of about 320 (±20) µmol after 15 h of irradiation independent of the carbon content. These results are in agreement with previous studies on carbon–$MoS_2$ composites and are attributed to suppressed charge recombination, improved charge transfer and increased adsorption active sites and photocatalytic reaction centers.[20] It is obvious that all mechanical mixtures exhibit higher activities in hydrogen generation than $C_6$ and bulk $MoS_2$ since $C_0$ itself shows better performance. Furthermore, the addition of carbon black and graphene to $C_0$ causes an even higher activity than sample $C_1$. In any case, $C_3$ remains the best material in this work for visible-light driven hydrogen evolution. Pure carbon black and graphene show no activity in the Ru-based system.

Despite the general problem of comparing photocatalytic activities,[49–51] the results of the present study as well as those reported in the literature using $MoS_2$ as a catalyst are compiled in Table 1 ($H_2$ evolution data refer to reactions after one hour). One should keep in mind that only one catalyst consists of pure $MoS_2$ (colloidal $MoS_2$) while all other catalysts are either supported on oxides or are mixtures of $MoS_2$ with a semiconductor. The $MoS_xC_y$ catalysts investigated here contain no additives, are free of toxic materials like CdS or CdSe and are obtained in a very simple synthetic approach. Especially sample $C_3$ shows excellent catalytic activity which significantly increases with irradiation time. A comparison of the activity of the catalysts after a few minutes or hours only partially reflects the real activity. When referring the amount of hydrogen to the weighted samples only colloidal $MoS_2$ shows better catalytic performance. In the present work hydrogen is photocatalytically evolved by heterogeneous catalysts, while colloidal $MoS_2$ may be viewed as a homogeneous photocatalyst. The stable colloidal $MoS_2$ nanoparticles may offer higher contact surface area between $MoS_2$ and $[Ru(bpy)_3]^{2+}$ and therefore more efficient electron transfer. In addition, the colloidal $MoS_2$ particles are stabilized by a polymer on the surface which may have a positive effect on the light-driven hydrogen evolution.

## Conclusions

In conclusion, a series of carbon containing $MoS_2$ composites was investigated in light-driven water reduction. All photocatalysts exhibit different chemical compositions as well as differing microstructures. Despite the rigorous characterization of the compounds no straightforward relations are found between C and S contents, structural properties, specific surface areas and the photocatalytic activity. It seems that a moderate C content and a slight S excess together with a high degree of edge planes lead to the best activity. Further investigations to improve the catalytic activity of $MoS_xC_y$ based materials are ongoing.

**Table 1** Photocatalysts based on $MoS_2$ for light-driven hydrogen generation

| Photocatalyst | Light source | Reaction solution | Amount of photocatalyst/mg | Activity/ µmol $h^{-1}$ | µmol/ mg $h^{-1}$ |
|---|---|---|---|---|---|
| Colloidal $MoS_2$ [13] | 300 W Xe lamp, optical cutoff filter ($\lambda > 420$ nm) | Ascorbic acid, $[Ru(bpy)_3](PF_6)_2$ in acetonitrile–methanol | 2 | 420 | 210 |
| $MoS_2/CdS$[14] | 300 W Xe lamp, optical cutoff filter ($\lambda > 420$ nm) | Lactic acid in water | 100 | 530 | 5.3 |
| $CdSe–MoS_2$[15] | 300 W Xe lamp, optical cutoff filter ($\lambda > 420$ nm) | $Na_2S/Na_2SO_3$ in water | 10 | 8 | 0.8 |
| $MoS_2/SiO_2$[18] | Medium pressure Hg lamp | KOH, $TiO_2$ in water–methanol | 1000 | 860 | 0.86 |
| $MoS_2/TiO_2$[19] | 300 W Xe lamp | Formic acid in water | 30 | 1 | 0.03 |
| $TiO_2/MoS_2$/ graphene[20] | 350 W Xe lamp | Ethanol/water | 80 | 165 | 2.1 |
| $MoS_xC_y$ ($C_3$) | 300 W Xe lamp, optical cutoff filter ($\lambda > 420$ nm) | Triethylamine, water, $[Ru(bpy)_3](PF_6)_2$ in acetonitrile | 10 | 120 | 12 |
| $MoS_xC_y$ ($C_3$) | 300 W Xe lamp, optical cutoff filter ($\lambda > 420$ nm) | Triethylamine, water, $[Ir(pyb)_2(bpy)]$ $(PF_6)$ in acetonitrile | 10 | 190 | 19 |

## Acknowledgements

The authors thank A. Puls for the krypton adsorption measurements, N. Reimer, A. Modrow and C. Stoltenberg for the nitrogen adsorption measurements and U. Cornelissen and S. Pehlke for the elemental analysis measurements. We thank Prof. Uwe Rosenthal (LIKAT) for the continuous support and finally the State of Schleswig-Holstein for the financial support.

## Notes and references

1 N. S. Lewis, *Nature*, 2001, **414**, 589–590.
2 J. Nowotny, C. C. Sorrell, T. Bak and L. R. Sheppard, *Sol. Energy*, 2005, **78**, 593–602.
3 A. Kudo and Y. Miseki, *Chem. Soc. Rev.*, 2009, **38**, 253–278.
4 F. E. Osterloh, *Chem. Mater.*, 2008, **20**, 35–54.
5 X. B. Chen, S. H. Shen, L. J. Guo and S. S. Mao, *Chem. Rev.*, 2010, **110**, 6503–6570.
6 K. Maeda and K. Domen, *J. Phys. Chem. C*, 2007, **111**, 7851–7861.
7 A. Mills and S. LeHunte, *J. Photochem. Photobiol., A*, 1997, **108**, 1–35.
8 A. L. Stroyuk, A. I. Kryukov, S. Y. Kuchmii and V. D. Pokhodenko, *Theor. Exp. Chem.*, 2009, **45**, 209–233.
9 K. Kalyanasundaram, J. Kiwi and M. Grätzel, *Helv. Chim. Acta*, 1978, **61**, 2720–2730.
10 K. Hashimoto, T. Kawai and T. Sakata, *Chem. Lett.*, 1983, **12**, 709–712.
11 K. Hashimoto, T. Kawai and T. Sakata, *New J. Chem.*, 1983, **7**, 247–253.
12 H. Kaga, K. Saito and A. Kudo, *Chem. Commun.*, 2010, 3779–3781.
13 X. Zong, Y. Na, F. Y. Wen, G. J. Ma, J. H. Yang, D. G. Wang, Y. Ma, M. Wang, L. Sun and C. Li, *Chem. Commun.*, 2009, 4536–4538.
14 X. Zong, G. P. Wu, H. J. Yan, G. J. Ma, J. Y. Shi, F. Y. Wen, L. Wang and C. Li, *J. Phys. Chem. C*, 2010, **114**, 1963–1968.
15 F. A. Frame and F. E. Osterloh, *J. Phys. Chem. C*, 2010, **114**, 10628–10633.
16 D. Merki, S. Fierro, H. Vrubel and X. Hu, *Chem. Sci.*, 2011, **2**, 1262–1267.
17 D. Merki and X. Hu, *Energy Environ. Sci.*, 2011, **4**, 3878–3888.
18 A. Sobczynski, *J. Catal.*, 1991, **131**, 156–166.
19 S. Kanda, T. Akita, M. Fujishima and H. Tada, *J. Colloid Interface Sci.*, 2011, **354**, 607–610.
20 Q. J. Xiang, J. G. Yu and M. Jaroniec, *J. Am. Chem. Soc.*, 2012, **134**, 6575–6578.
21 S. Helveg, J. V. Lauritsen, E. Laegsgaard, I. Stensgaard, J. K. Norskov, B. S. Clausen, H. Topsoe and F. Besenbacher, *Phys. Rev. Lett.*, 2000, **84**, 951–954.
22 M. Brorson, A. Carlsson and H. Topsoe, *Catal. Today*, 2007, **123**, 31–36.
23 J. V. Lauritsen, M. V. Bollinger, E. Laesgaard, K. W. Jacobsen, J. K. Norskov, B. S. Clausen, H. Topsoe and F. Besenbacher, *J. Catal.*, 2004, **221**, 510–522.
24 J. V. Lauritsen, J. Kibsgaard, G. H. Olesen, P. G. Moses, B. Hinnemann, S. Helveg, J. K. Norskov, B. S. Clausen, H. Topsoe, E. Laesgaard and F. Besenbacher, *J. Catal.*, 2007, **249**, 220–233.
25 J. V. Lauritsen, J. Kibsgaard, S. Helveg, H. Topsoe, B. S. Clausen, E. Laegsgaard and F. Besenbacher, *Nat. Nanotechnol.*, 2007, **2**, 53–58.
26 J. V. Lauritsen and F. Besenbacher, *Adv. Catal.*, 2006, **50**, 97–147.
27 F. L. Deepak, R. Esparza, B. Borges, X. Lopez-Lozano and M. Jose-Yacaman, *ACS Catal.*, 2011, **1**, 537–543.
28 F. Besenbacher, J. V. Lauritsen and S. Wendt, *Nano Today*, 2007, **2**, 30–39.
29 F. Besenbacher, M. Brorson, B. S. Clausen, S. Helveg, B. Hinnemann, J. Kibsgaard, J. V. Lauritsen, P. G. Moses, J. K. Norskov and H. Topsoe, *Catal. Today*, 2008, **130**, 86–96.

30 B. Hinnemann, P. G. Moses, J. Bonde, K. P. Jorgensen, J. H. Nielsen, S. Horch, I. Chorkendorff and J. K. Norskov, *J. Am. Chem. Soc.*, 2005, **127**, 5308–5309.

31 K. H. Hu, X. Hu, Y. Xu and X. Pan, *React. Kinet. Catal. Lett.*, 2010, **100**, 153–163.

32 B. L. Abrams and J. P. Wilcoxon, *Crit. Rev. Solid State Mater. Sci*, 2005, **30**, 153–182.

33 J. P. Wilcoxon, P. P. Newcomer and G. A. Samara, *J. Appl. Phys.*, 1997, **81**, 7934–7944.

34 T. F. Jaramillo, K. P. Jorgensen, J. Bonde, J. H. Nielsen, S. Horch and I. Chorkendorff, *Science*, 2007, **317**, 100–102.

35 J. Bonde, P. G. Moses, T. F. Jaramillo, J. K. Norskov and I. Chorkendorff, *Faraday Discuss.*, 2008, **140**, 219–231.

36 M. Polyakov, M. Poisot, M. W. E. van den Berg, T. Drescher, A. Lotnyk, L. Kienle, W. Bensch, M. Muhler and W. Grünert, *Catal. Commun.*, 2010, **12**, 231–237.

37 W. Bensch, Z. D. Huang, L. Kienle, S. Fuentes, G. Alonso and C. Ornelas, *Catal. Lett.*, 2009, **127**, 132–142.

38 W. Bensch, Z. D. Huang, L. Kienle, S. Fuentes, G. Alonso and C. Ornelas, *Catal. Lett.*, 2008, **124**, 24–33.

39 M. Poisot, W. Bensch, S. Fuentes, C. Ornelas and G. Alonso, *Catal. Lett.*, 2007, **117**, 43–52.

40 R. R. Chianelli and G. Berhault, *Catal. Today*, 1999, **53**, 357–366.

41 S. P. Kelty, G. Berhault and R. R. Chianelli, *Appl. Catal., A*, 2007, **322**, 9–15.

42 R. R. Chianelli, G. Berhault and B. Torres, *Catal. Today*, 2009, **147**, 275–286.

43 X. Liu, P. Zeng, T. Peng, X. Zhang and K. Deng, *Int. J. Hydrogen Energy*, 2012, **37**, 1375–1384.

44 X. Zhang, Y. Sun, X. Cui and Z. Jiang, *Int. J. Hydrogen Energy*, 2012, **37**, 1356–1365.

45 J. W. McDonald, G. D. Friesen, L. D. Rosenhein and W. E. Newton, *Inorg. Chim. Acta*, 1983, **72**, 205–210.

46 M. Poisot, W. Bensch, S. Fuentes and G. Alonso, *Thermochim. Acta*, 2006, **444**, 35–45.

47 S. Hansen, M. Klahn, T. Beweries and U. Rosenthal, *ChemSusChem*, 2012, **5**, 656–660.

48 S. Hansen, M.-M. Pohl, M. Klahn, A. Spannenberg and T. Beweries, *ChemSusChem*, 2012, DOI: 10.1002/cssc.201200617.

49 T. Maschmeyer and M. Che, *Angew. Chem., Int. Ed.*, 2010, **49**, 1536–1539.

50 T. Maschmeyer and M. Che, *Angew. Chem., Int. Ed.*, 2010, **122**, 9784–9785.

51 H. Kisch, *Angew. Chem., Int. Ed.*, 2010, **122**, 9782–9783.

Electronic Supplementary Material (ESI) for Dalton Transactions
This journal is © The Royal Society of Chemistry 2012

# Supporting Information

## Influence of Carbon Content in Molybdenum Sulfides $MoS_xC_y$ Obtained by Thermal Decomposition On Photocatalytical Hydrogen Generation

John Djamil,[a] Stephan A. Segler,[a] Alexandra Dabrowski,[a] Wolfgang Bensch,[a,*] Andriy Lotnyk,[b] Ulrich Schürmann,[b] Lorenz Kienle,[b] Sven Hansen,[c] Torsten Beweries,[c] Uwe Rosenthal[c]

[a] *Institute of Inorganic Chemistry, Max-Eyth-Str. 2, D-24118 Kiel, Germany. Fax: +49 431 880 1520; Tel: +49 431 880 2091; E-mail: wbensch@ac.uni-kiel.de*
[b] *Institute for Material Science, Kaiserstr. 2, D-24143 Kiel, Germany. Fax: +49 431 880 6178; Tel: +49 431 880 6176; E-mail: lk@tf.uni-kiel.de*
[c] *Leibniz-Institute for Catalysis, Albert-Einstein-Str. 29a, D-18059 Rostock, Germany. Fax:+49 381 1281 51176, Tel:+49 381 1281 176; E-mail: Uwe.Rosenthal@catalysis.de*

### METHODS

X-ray powder diffraction patterns were measured with a STOE-P diffractometer with CuKα radiation in transmission geometry. HRTEM images were recorded with Tecnai $G^2$-ST F30. The chemical composition was investigated with a EuroEA 3000. The samples were heated up to 1010 °C under an oxygen atmosphere. Specific surface areas were determined with nitrogen and krypton sorption measurements at 77 K applying the BET model. Photocatalytic reactions were carried out in a double-walled thermostatically controlled glass vessel that was loaded with 10 mg of $MoS_xC_y$, evacuated and back-filled with argon four times in order to remove other gases. Triethylamine (8 mL), distilled and degassed water (3 mL) and $[Ru(bpy)_3](PF_6)_2$ (1 mM) in acetonitrile (10 mL) were transferred *via* syringe. The mixture was stirred, set at 25 °C and the system was left to equilibrate for 15 min. The reaction was started by switching on the light source (275 W Xe-arc lamp with an optical cut-off filter $\lambda > 420$ nm). An Agilent Technologies 7890A gas chromatograph with a 60/80 Carboxen 1000 (Supelco) column and a TCD was used to qualify the gas. The amount of hydrogen was quantified with an automatic burette.

### Preparation of $(NH_4)_2MoS_4$ and of $(NR_4)_2MoS_4$

$(NH_4)_2MoS_4$ was synthesized by dissolving $(NH_4)_6Mo_7O_{24}*4H_2O$ (0.024 mol) in 200 mL ammonia solution (25 %wt). $H_2S$ was introduced to this solution. The product, red-green shimmery crystals were washed with cold distilled water, ethanol, and diethyl ether. The yield was 65 %. $((CH_3)_4N)_2MoS_4$ was synthesized by dissolving $(NH_4)_2MoS_4$ (0.012 mol) in 60 mL distilled water. $(CH_3)_4NBr$ (0.024 mol) was dissolved in 25 mL aqueous NaOH solution (1.0 M). The first solution was added to the second and a red solid immediately precipitated. The product was washed with distilled water. The yield was 86 %. $((C_3H_7)_4N)_2MoS_4$ was synthesized by dissolving $(NH_4)_2MoS_4$ (0.012 mol) in 60 mL distilled water. $(C_3H_7)_4NBr$ (0.024 mol) was dissolved in 18 mL aqueous NaOH solution (2.0 M). The first solution was added to the second and a red solid immediately precipitated. The product was washed with distilled water. The yield was 11 %.

## Preparation of $MoS_xC_y$

$MoS_xC_y$ photocatalysts were prepared by thermal decomposition of $(R_4N)_2MoS_4$ (R = $-H_4$ (C0), $-CH_3$ (C1), $-C_3H_7$ (C3), $-C_6H_{13}$ (C6)) (0.4 to 1.0 g) at 350 °C for one hour with a heating rate of 100 °C / h in a rotary furnace under $N_2$ flow (200 $cm^3$ / min).

## Preparation of mechanical mixtures

$C_0$ was mechanically mixed with carbon black (cb) and graphene (g) in a ball mill for 15 min. The compositions are given in Table 1.

**S.I. Table 1: Compositions of mechanical mixtures.**

| | **$m_{C0}$/mg** | **$m_{cb}$/mg** |
|---|---|---|
| **cb1** | 197 | 2.7 |
| **cb3** | 190 | 10.0 |
| **cb6** | 179 | 22.8 |
| | **$m_{C0}$/mg** | **$m_g$/mg** |
| **g1** | 197 | 2.5 |
| **g3** | 190 | 9.6 |
| **g6** | 179 | 21.1 |

## XRD patterns of mechanical mixtures

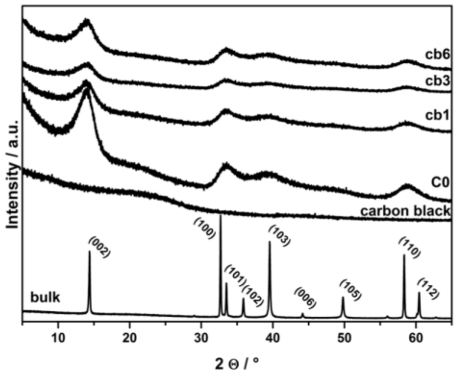

**S.I. Figure 1: XRD patterns for mechanical mixtures of $C_0$ with carbon black (cb).**

Electronic Supplementary Material (ESI) for Dalton Transactions
This journal is © The Royal Society of Chemistry 2012

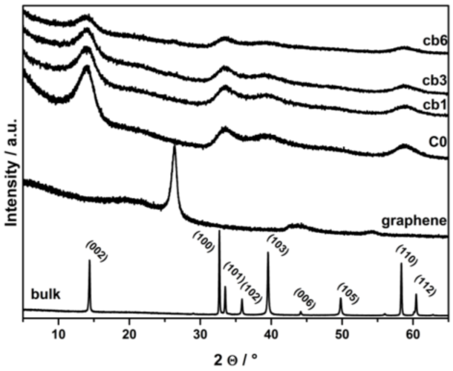

S.I. Figure 2: XRD patterns for mechanical mixtures of $C_0$ with graphene (g).

## Nitrogen and krypton adsorption measurements

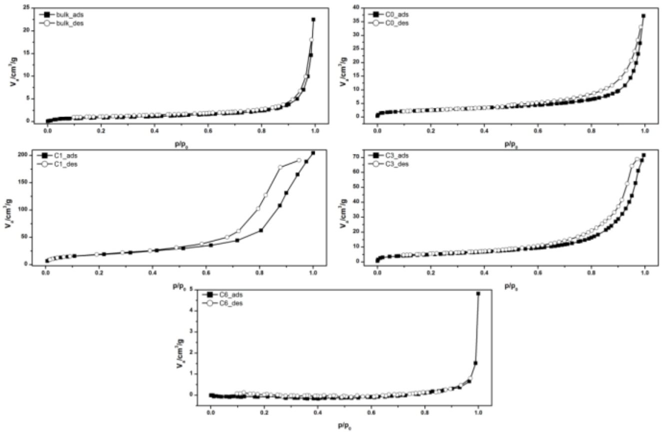

S.I. Figure 3: Nitrogen and krypton adsorption (ads) –desorption (des) isotherms of thermal decomposition products and of bulk $MoS_2$.

## Photocatalytic hydrogen reaction

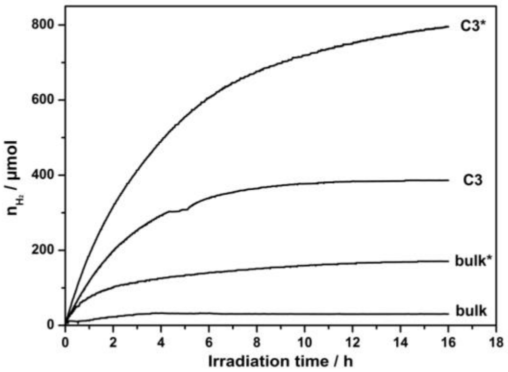

**S. I. Figure 4: Kinetic studies of the photocatalytic hydrogen evolution reaction from a mixture containing triethylamine (8 mL), water (3 mL) and [Ru(bpy)3](PF6)2 (1 mM) in acetonitrile (10 mL). Additionally the C3* and bulk* samples were tested in an equal system applying [Ir(pyb)$_2$(bpy)](PF$_6$) as sensitizer.**

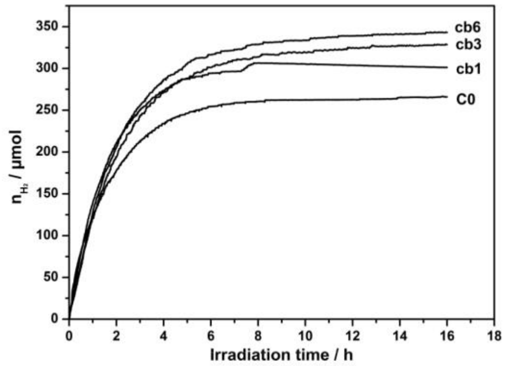

**S. I. Figure 5: Kinetic studies of the photocatalytic hydrogen evolution reaction from a mixture containing triethylamine (8 mL), water (3 mL) and [Ru(bpy)3](PF6)2 (1 mM) in acetonitrile (10 mL) for C0 and its mechanical mixtures composed of carbon black (cb).**

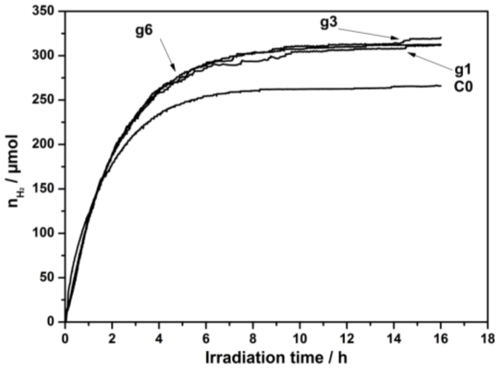

**S. I. Figure 6: Kinetic studies of the photocatalytic hydrogen evolution reaction from a mixture containing triethylamine (8 mL), water (3 mL) and [Ru(bpy)3](PF6)2 (1 mM) in acetonitrile (10 mL) for C0 and its mechanical mixtures composed of graphene (g).**

### 4.1.2 *In situ* Bildung eines $MoS_2$ basierten anorganisch-organischen Nanokomposits durch direkte thermische Zersetzung

Zusammenfassung der Veröffentlichung „*In situ* Formation of a $MoS_2$-based Inorganic-Organic Nanocomposite by Directed Thermal Decomposition“. Dieser Artikel wurde in “Chemistry – A European Journal” (DOI: 10.1002/chem.201406541) 2015 veröffentlicht.

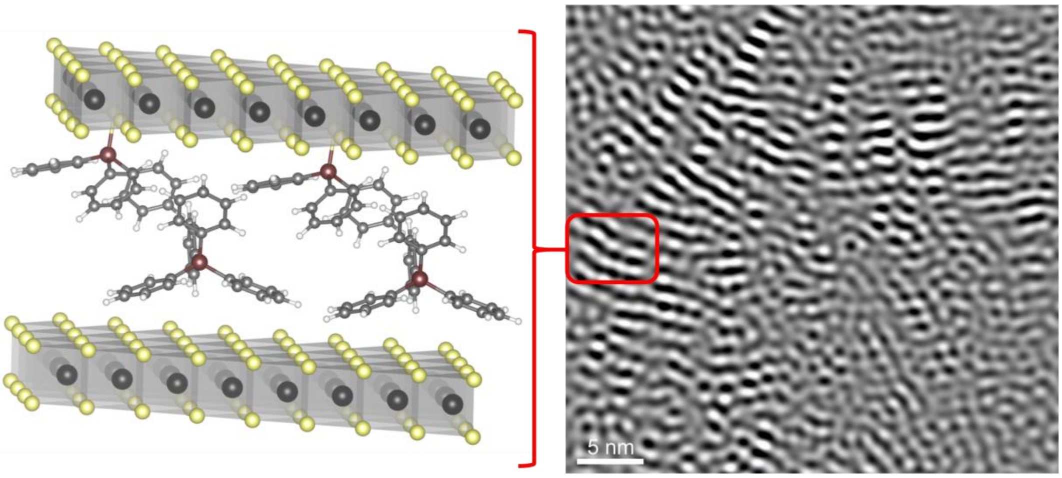

**Abb. 23: Strukturmodell aus Kraftfeldrechnungen (links) und TEM-Abbildung (rechts) von $MoS_xC_yP_z$ (250 °C).**

Diese Veröffentlichung beinhaltet die Synthese und Charakterisierung von nanoskaligen C- und P-haltigen Molybdänsulfiden und deren katalytischen Eigenschaften. Die Cokatalysatoren resultierten aus dem thermischen Abbau von $(Ph_4P)_2MoS_4$ bei 250 °C ($MoS_xC_yP_z$ (250 °C)) und 350 °C ($MoS_xC_yP_z$ (350 °C)). Die Zersetzungstemperatur hat dabei Einfluss sowohl auf die chemische Zusammensetzung der Komposite als auch auf deren strukturelle Eigenschaften. Die Ergebnisse der Elementaranalyse ergeben, dass der C-Gehalt durch eine höhere Zersetzungstemperatur um fast 50 % von 250 °C (C: 32 wt%) auf 350 °C (C: 17 wt%) abnimmt. Im Gegensatz dazu steigt der S-Gehalt mit zunehmender Temperatur von 26 % auf 33 % an. In der DTA-Kurve wird ein exothermes Signal bei $T_{onset} = 233$ °C und ein endothermes Signal bei $T_{onset} = 327$ °C beobachtet, was auf Phasenumwandlungen, Schmelz- oder Verdampfungsvorgänge und/oder Zersetzungsreaktionen deutet. Die Resultate der MIR-Spektroskopie der Zersetzungsprodukte belegen die Anwesenheit von $Ph_4P^+$-Resten (aromatische Schwingungen: $\nu = 523, 688, 720, 755, 995, 1479$ $cm^{-1}$ und P-Ph-Schwingungen: $\nu = 462, 447$ $cm^{-1}$), während die Abwesenheit der Absorptionsbande bei $\nu = 462$ $cm^{-1}$

nachweist, dass keine $MoS_4^{2-}$-Einheiten vorhanden sind. Die Bildung einer $MoS_2$-ähnlichen Schichtverbindung lässt sich sowohl aus den FIR- ($E_{1u}$: 384 $cm^{-1}$) als auch den Raman-Spektren ($E^1_{2g}$: 385 $cm^{-1}$ und $A_{1g}$: 410 $cm^{-1}$) ableiten. In Übereinstimmung zu den MIR-Ergebnissen konnte mit $^{31}P$ NMR-Spektren von $MoS_xC_yP_z$ (250 °C) und $MoS_xC_yP_z$ (350 °C) die Gegenwart von $Ph_4P^+$-Resten ($\delta = 22$ ppm) nachgewiesen werden. Darüber hinaus tritt in $MoS_xC_yP_z$ (250 °C) ein weiteres Signal auf ($\delta = 41.6$ ppm), welches die Bildung von $Ph_3PS$ andeutet. Ergebnisse der temperaturabhängigen $^{31}P$ NMR-Messungen von $MoS_xC_yP_z$ (250 °C) ließen Rückschlüsse auf den dynamischen Zustand von $Ph_4P^+$ und $Ph_3PS$ zu. Dabei nimmt die Breite des Signals der $Ph_4P^+$-Spezies aufgrund von Rotationsbewegungen mit zunehmender Temperatur ab, während keine Änderung in der Signalbreite von $Ph_3PS$ zu beobachten ist. D.h., eine freie Rotationsbewegung von $Ph_3PS$ ist nicht vorhanden, was auf eine kovalente Bindung an $MoS_2$-Schichten hindeutet. Die Partikelgrößen der Zersetzungsprodukte liegen im nm-Bereich, was durch XRD- und TEM-Messungen bewiesen wurde. Zudem bestätigen XRD- und TEM-Ergebnisse die Bildung eines Intermediats bei etwa 250 °C, worauf bereits der DTA-Kurvenverlauf hingewiesen hat. Die Probe $MoS_xC_yP_z$ (250 °C) weist einen intensiven Beugungsreflex bei kleinem Streuwinkel ($2\Theta = 5.9$ °) auf, der einer Schichtaufweitung von 1.5 nm entspricht. In Übereinstimmung dazu sind in den TEM-Aufnahmen $MoS_2$-Schichtabstände von etwa 1.3 nm zu beobachten. Diese Schichtaufweitung kann durch die Einlagerung von $Ph_4P^+$- und $Ph_3PS$-Molekülen in den Interschichtbereichen erklärt werden. Im Gegensatz dazu tauchen bei $MoS_xC_yP_z$ (350 °C) weder in XRD- noch in den TEM-Messungen Hinweise auf eine Schichtaufweitung in einem vergleichbaren Bereich auf. Darüber hinaus deutet der abfallende Untergrund bei kleinen Streuwinkeln im Pulverdiffraktogramm auf unkorrelierte $MoS_2$-Monoschichten hin. In beiden Zersetzungsprodukten sind die $MoS_2$-Schichten gegeneinander verschoben und verdreht, was die Abwesenheit von einigen Beugungsreflexen erklärt. Kraftfeldrechnungen unter Berücksichtigung der analytischen Ergebnisse wurden für die Erstellung eines Strukturmodells von $MoS_xC_yP_z$ (250 °C) durchgeführt. Die fotokatalytischen Messungen belegen, dass beide Zersetzungsprodukte deutlich aktivere Cokatalysatoren für die $H_2$-Entwicklung darstellen als $MoS_2$-Volumenmaterial ($\approx$ 30 µmol/10 h). Gründe dafür können beispielsweise die Nanostrukturierung der Proben und das Einbringen von Kohlenstoff und Phosphor in die Cokatalysatoren sein, so dass einerseits die Anzahl der aktiven Zentren erhöht wird (möglicherweise an den $MoS_2$-Kanten) und andererseits durch Zusätze wie Kohlenstoff und Phosphor der Ladungstransfer verbessert wird und zusätzliche aktive Zentren angeboten werden. Darüber hinaus übersteigt die Aktivität von $MoS_xC_yP_z$ (350 °C) (≈ 320 µmol/10 h) signifikant die von $MoS_xC_yP_z$ (250 °C) (≈ 230 µmol/10 h). Dafür können diverse Faktoren basierend auf der chemischen Zusammensetzung und den strukturellen Eigenschaften verantwortlich sein. Aus diesem Grund lassen sich keine direkten Zusammenhänge zwischen chemischer Zusammensetzung, strukturellen Eigenschaften und der fotokatalytischen $H_2$-Entwicklung herstellen.

J. Djamil, S. A. Segler, W. Bensch, M. Deng, U. Schürmann, L. Kienle, S. Hansen, T. Beweries, L. von Wüllen, S. Rosenfeldt, S. Förster, H. Reinsch, *Chem. Eur. J.* **2015**, *24*, 8918- 8925.- Reproduziert mit der Erlaubnis vom Wiley Verlag.

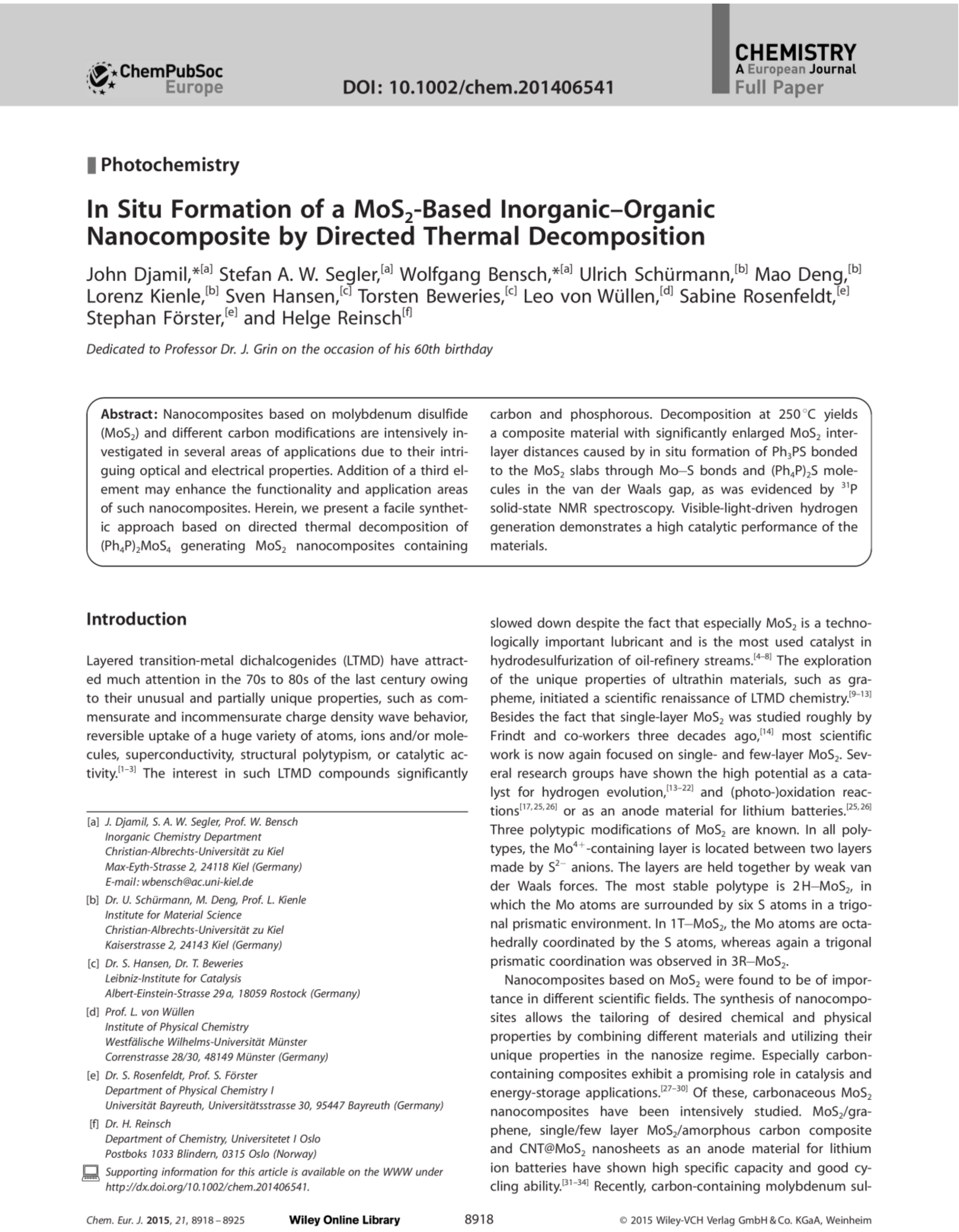

ChemPubSoc Europe

DOI: 10.1002/chem.201406541

CHEMISTRY
A European Journal
Full Paper

**Photochemistry**

# In Situ Formation of a $MoS_2$-Based Inorganic–Organic Nanocomposite by Directed Thermal Decomposition

John Djamil,*[a] Stefan A. W. Segler,[a] Wolfgang Bensch,*[a] Ulrich Schürmann,[b] Mao Deng,[b] Lorenz Kienle,[b] Sven Hansen,[c] Torsten Beweries,[c] Leo von Wüllen,[d] Sabine Rosenfeldt,[e] Stephan Förster,[e] and Helge Reinsch[f]

*Dedicated to Professor Dr. J. Grin on the occasion of his 60th birthday*

**Abstract:** Nanocomposites based on molybdenum disulfide ($MoS_2$) and different carbon modifications are intensively investigated in several areas of applications due to their intriguing optical and electrical properties. Addition of a third element may enhance the functionality and application areas of such nanocomposites. Herein, we present a facile synthetic approach based on directed thermal decomposition of $(Ph_4P)_2MoS_4$ generating $MoS_2$ nanocomposites containing carbon and phosphorous. Decomposition at 250 °C yields a composite material with significantly enlarged $MoS_2$ interlayer distances caused by in situ formation of $Ph_3PS$ bonded to the $MoS_2$ slabs through Mo–S bonds and $(Ph_4P)_2S$ molecules in the van der Waals gap, as was evidenced by $^{31}P$ solid-state NMR spectroscopy. Visible-light-driven hydrogen generation demonstrates a high catalytic performance of the materials.

## Introduction

Layered transition-metal dichalcogenides (LTMD) have attracted much attention in the 70s to 80s of the last century owing to their unusual and partially unique properties, such as commensurate and incommensurate charge density wave behavior, reversible uptake of a huge variety of atoms, ions and/or molecules, superconductivity, structural polytypism, or catalytic activity.[1–3] The interest in such LTMD compounds significantly slowed down despite the fact that especially $MoS_2$ is a technologically important lubricant and is the most used catalyst in hydrodesulfurization of oil-refinery streams.[4–8] The exploration of the unique properties of ultrathin materials, such as graphene, initiated a scientific renaissance of LTMD chemistry.[9–13] Besides the fact that single-layer $MoS_2$ was studied roughly by Frindt and co-workers three decades ago,[14] most scientific work is now again focused on single- and few-layer $MoS_2$. Several research groups have shown the high potential as a catalyst for hydrogen evolution,[13–22] and (photo-)oxidation reactions[17,25,26] or as an anode material for lithium batteries.[25,26] Three polytypic modifications of $MoS_2$ are known. In all polytypes, the $Mo^{4+}$-containing layer is located between two layers made by $S^{2-}$ anions. The layers are held together by weak van der Waals forces. The most stable polytype is 2H–$MoS_2$, in which the Mo atoms are surrounded by six S atoms in a trigonal prismatic environment. In 1T–$MoS_2$, the Mo atoms are octahedrally coordinated by the S atoms, whereas again a trigonal prismatic coordination was observed in 3R–$MoS_2$.

Nanocomposites based on $MoS_2$ were found to be of importance in different scientific fields. The synthesis of nanocomposites allows the tailoring of desired chemical and physical properties by combining different materials and utilizing their unique properties in the nanosize regime. Especially carbon-containing composites exhibit a promising role in catalysis and energy-storage applications.[27–30] Of these, carbonaceous $MoS_2$ nanocomposites have been intensively studied. $MoS_2$/graphene, single/few layer $MoS_2$/amorphous carbon composite and CNT@$MoS_2$ nanosheets as an anode material for lithium ion batteries have shown high specific capacity and good cycling ability.[31–34] Recently, carbon-containing molybdenum sul-

---

[a] *J. Djamil, S. A. W. Segler, Prof. W. Bensch*
*Inorganic Chemistry Department*
*Christian-Albrechts-Universität zu Kiel*
*Max-Eyth-Strasse 2, 24118 Kiel (Germany)*
*E-mail: wbensch@ac.uni-kiel.de*

[b] *Dr. U. Schürmann, M. Deng, Prof. L. Kienle*
*Institute for Material Science*
*Christian-Albrechts-Universität zu Kiel*
*Kaiserstrasse 2, 24143 Kiel (Germany)*

[c] *Dr. S. Hansen, Dr. T. Beweries*
*Leibniz-Institute for Catalysis*
*Albert-Einstein-Strasse 29a, 18059 Rostock (Germany)*

[d] *Prof. L. von Wüllen*
*Institute of Physical Chemistry*
*Westfälische Wilhelms-Universität Münster*
*Corrensstrasse 28/30, 48149 Münster (Germany)*

[e] *Dr. S. Rosenfeldt, Prof. S. Förster*
*Department of Physical Chemistry I*
*Universität Bayreuth, Universitätsstrasse 30, 95447 Bayreuth (Germany)*

[f] *Dr. H. Reinsch*
*Department of Chemistry, Universitetet I Oslo*
*Postboks 1033 Blindern, 0315 Oslo (Norway)*

*Supporting information for this article is available on the WWW under http://dx.doi.org/10.1002/chem.201406541.*

fides have also been successfully used for the electrocatalytic hydrogen-evolution reaction.[35–37] The usage of $MoS_2$/graphene/$TiO_2$ nanoparticles and $MoS_2$ on reduced graphene oxide and $MoS_2$/graphene/ZnS composites has been reported as an efficient photocatalyst for light-driven hydrogen generation.[17,38–40] Recently, the good performance as photocatalyst for hydrogen evolution was also demonstrated for $MoS_2$ deposited on nitrogenated graphene oxide.[39]

Although in most synthetic approaches $MoS_2$ is mixed with a carbon source, we reported an alternative approach for the generation of $MoS_2$-containing carbonaceous species. The samples were prepared by thermal decomposition of $(R_4N)_2MoS_4$ (with $R = CH_3$, $C_3H_7$, $C_6H_{13}$) allowing to control the carbon content in the decomposition products by the size of R. The samples exhibited promising photocatalytic activity for light-driven hydrogen evolution.[22] In our ongoing work, we used $(Ph_4P)_2MoS_4$ as precursor for the preparation of $MoS_xC_yP_z$ which was obtained by thermal decomposition. Herein, we report the synthesis, characterization, and photocatalytic properties for light-driven hydrogen evolution of new composites.

## Results and Discussion

$MoS_xC_yP_z$ nanoparticles were synthesized by thermal decomposition of $(Ph_4P)_2MoS_4$ under $N_2$ gas flow at two temperatures $T = 250\,^{\circ}C$ ($MoS_xC_yP_z$ (250 °C)) and $T = 350\,^{\circ}C$ ($MoS_xC_yP_z$ (350 °C)). More details on the synthesis procedure are given in the (Experimental Section). Thermal decomposition of $(Ph_4P)_2MoS_4$ at 250 °C leads to a material enriched in carbon/hydrogen (C: 32 wt %, H: 2 wt %) compared with the one obtained by decomposition at 350 °C (C: 17 wt %, H: 1 wt %) according to the results of the elemental analysis. On the other hand, the S content increases ($S_{MoSxCyPz\ (250\,^{\circ}C)}$: 26 wt %; $S_{MoSxCyPz\ (350\,^{\circ}C)}$: 33 wt %) compared with C and H, giving products closer to $MoS_2$ stoichiometry with increasing decomposition temperature. The thermal decomposition of $(Ph_4P)_2MoS_4$ occurred in at least two steps (Figure 1). The first step is accompanied by an exothermic event at $T_{onset} = 233\,^{\circ}C$, indicating crystallization of a new compound. The second decomposition step starts at $T_{onset} = 327\,^{\circ}C$, including an accompanying endothermic signal in the differential thermal analysis (DTA) curve. Clearly, large amounts of the organic molecules are released during this event leading to formation of a less carbon/hydrogen-rich material. The total weight loss during the thermal decomposition is lower than expected for the formation of pure $MoS_2$ ($\Delta m = 82\%$), and according to chemical analysis, the residue still contains appreciable amounts of C, H, and P, explaining the difference between experimental and expected weight-loss values.

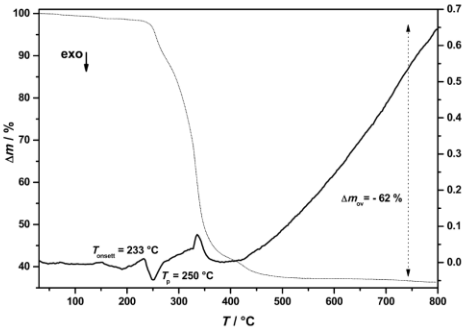

**Figure 1.** DTA and TG curves of $(Ph_4P)_2MoS_4$ decomposition.

The mid-infrared (MIR) spectrum of the precursor presents characteristic bands of the $Ph_4P^+$ cation (aromatic vibrations: $\tilde{\nu} = 523$, 688, 720, 755, 995, 1479 $cm^{-1}$ and P–Ph vibrations: $\tilde{\nu} = 1104$, 1433 $cm^{-1}$)[41] and the typically Mo–S stretching band for $MoS_4^{2-}$, which is split into two bands at around $\nu = 462$ and 447 $cm^{-1}$ (Figure 2). The appearance of these two vibrational signals is attributed to the asymmetric stretching vibration ($\nu_3$) and to the normally MIR-inactive symmetric stretching vibration ($\nu_1$) respectively. The latter becomes MIR active due to a slight distortion of the $MoS_4$ tetrahedron reducing the $T_d$ symmetry. Such a distortion could be explained on the basis of the number and strength of S–H interactions.[42] Both decomposition products show the presence of $Ph_4P^+$ residues and the intensity of the vibrational bands of $MoS_xC_yP_z$ (350 °C) slightly dropped compared to $MoS_xC_yP_z$ (250 °C). The weak band around $\tilde{\nu} = 639\ cm^{-1}$ may be attributed to a P–S stretching vibration in $MoS_xC_yP_z$ (250 °C) and thus indicates the presence of a P–S bond.[43–45] The absence of the strong absorption at $\tilde{\nu} = 462\ cm^{-1}$ in the decomposition products evidences the absence of tetrahedral $MoS_4^{2-}$ units. The far-infrared (FIR) spectra reveal the formation of $MoS_2$ for the decomposition products with a typical vibration ($E_{1u}$) located at $\tilde{\nu} = 384\ cm^{-1}$ (Figure 2).[46]

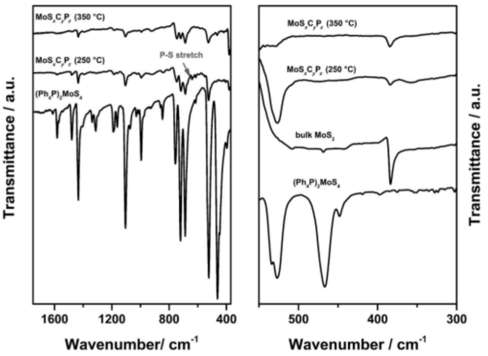

**Figure 2.** MIR (left) and FIR (right) spectra of $(Ph_4P)_2MoS_4$ and $MoS_xC_yP_z$ decomposed at $T = 250$ and 350 °C. For the purpose of comparison, FIR spectrum of bulk $MoS_2$ was recorded as well.

Two Raman-active modes can be clearly identified at $\tilde{\nu} = 385$ and 410 $cm^{-1}$ in both decomposition products (Figure 3). These two peaks resemble those observed for pure $MoS_2$, which are assigned to the in-plane $E^1_{2g}$ and out of-plane $A_{1g}$ modes.[47] The occurrence of these two modes indicates that

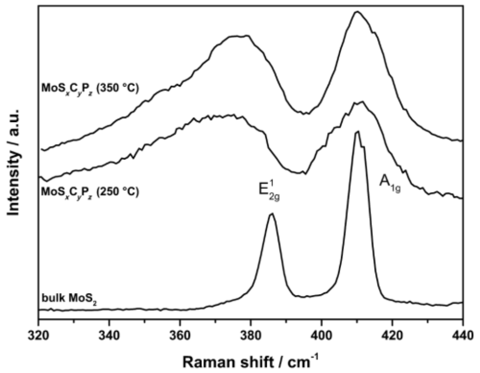

**Figure 3.** Raman spectra of $MoS_xC_yP_z$ decomposed at $T = 250$ and 350 °C and of bulk $MoS_2$.

the materials exhibit a $MoS_2$-like layered character. The broadness of the resonances suggest that the Mo centers are in different environments and/or the presence of defects and disorder in the samples.[48] Solid-state $^{31}P$ NMR measurements confirmed the presence of $Ph_4P^+$ residues in the decomposition products ($\delta = 22$ ppm),[49] but also reveal the appearance of a second phosphorus species in $MoS_xC_yP_z$ (250 °C; Figure 4). The chemical shift of $\delta = 41.6$ ppm may indicate the presence of $Ph_3PS$.[50] A molar ratio of approximately 1:5 between $Ph_3PS$ and $Ph_4P^+$ was estimated based on the $^{31}P$ NMR data. The signal for $Ph_3PS$ disappeared for $MoS_xC_yP_z$ (350 °C). Assuming that the residual heteronuclear dipolar $^{31}P$–$^1H$ coupling is the main source of line broadening for the $^{31}P$ MAS NMR signals, temperature-dependent $^{31}P$ MAS NMR measurements allow a first assessment of the dynamic state of the $Ph_4P^+$ cation and $Ph_3PS$. The corresponding spectra for $MoS_xC_yP_z$ (250 °C) are collected in the inset of Figure 4. Although the signal corresponding to $Ph_4P^+$ at $\delta = 22$ ppm narrows with increasing temperature, no such narrowing was observed for the signal attributed to $Ph_3PS$ at $\delta = 41.6$ ppm. The observed narrowing is compatible with the assumption of an averaging of the residual $^{31}P$–$^1H$ dipolar coupling by a rotational motion of the $Ph_4P^+$ cation. According to our results for the $Ph_3PS$ species, no extended dynamic is possible, which may point towards a bonding to the $MoS_2$ layers (see below).

The X-ray diffraction (XRD) pattern of $MoS_xC_yP_z$ (250 °C) exhibits two relatively sharp features at low scattering angles ($d = 1.5$ nm ($2\theta = 5.9°$) and 0.76 nm ($2\theta = 11.7°$), respectively) together with broad modulations at higher $2\theta$ values (Figure 5). Assuming that the low-angle reflection correlates with the (001) plane of the newly formed material, a widening of the interlayer distance with $d(001) = 1.5$ nm compared with the interlayer distance in bulk $MoS_2$ ($d(002) = 0.62$ nm) is indicated. Calculating the $c$ axis value from the (001) reflection the relatively sharp peak at $d = 0.76$ nm fits with the (002) reflection of the new material, and the hump of the background around $2\theta = 17.2$ may correlate with the very broad (003). The difference between theoretical and experimental $d$ values of

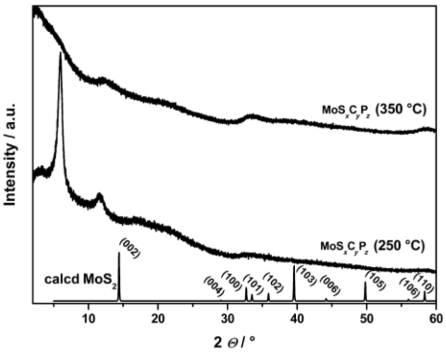

**Figure 5.** XRD patterns of thermal decomposition products. For the purpose of comparison, XRD pattern of calculated $MoS_2$ was integrated.

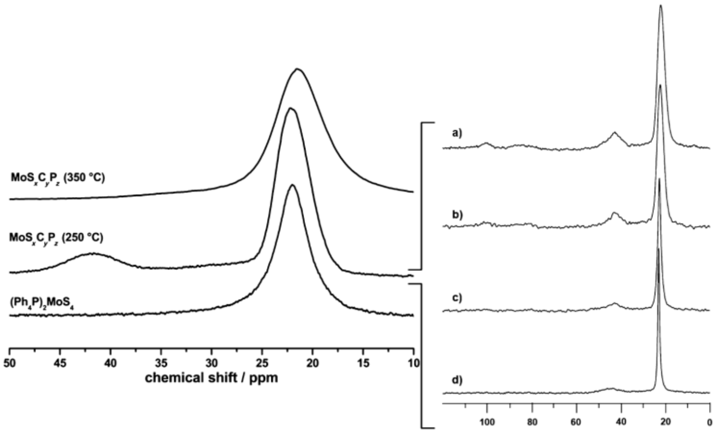

**Figure 4.** $^{31}P$ MAS NMR spectra (MAS@7000 Hz) of $(Ph_4P)_2MoS_4$ and $MoS_xC_yP_z$ samples (left) and $^{31}P$ MAS NMR spectra (MAS @ 7000 Hz) of $MoS_xC_yP_z$ (250 °C) as a function of temperature at a) 25 °C; b) 100 °C; c) 180 °C; and d) 200 °C (right).

0.27 and 0.15 nm, respectively, for the first two reflections points toward a significant interstratification. This assumption is further supported by the pronounced difference in the full width at half-maximum of the first two reflections. Turbostratic disorder in the form of twisted and shifted layers against each other is also present leading to the absence of reflections like (102), (103), and (105), and only modulations of the background can be identified. The occurrence of the two relatively sharp reflections indicates the presence of an at least two-dimensionally long-range ordered structure with a *d* spacing of about 1.5 nm. Due to the fact that $Ph_4P^+$ and $Ph_3PS$ molecules are present in $MoS_xC_yP_z$ (cf. $^{31}P$ NMR), such interlayer expansion suggests an incorporation of guest molecules in interlayer galleries in $MoS_2$ with an at least partially well-defined orientation giving rise to Bragg scattering. The encapsulation of organic molecules between the $MoS_2$ slabs has been reported in earlier studies leading to an intense reflection at low angles with *d* values up to 1.5 nm.[51–57]

The pattern of $MoS_xC_yP_z$ (350 °C) is significantly different to that of the material decomposed at lower temperature. The two prominent features observed for $MoS_xC_yP_z$ (250 °C) disappeared and only modulations at around $2\theta = 12.3$ can be observed. Because residual $Ph_4P^+$ is still present in the sample (cf. IR, $^{31}P$ NMR), the first hump may be explained by the presence of highly defective, but still expanded $MoS_2$ layers. The modulations of the background around the scattering angles of the (100), (101), (102), and (112) reflections are more pronounced than for $MoS_xC_yP_z$ (250 °C), but again turbostratic disorder leads to broad signals. The evolution of the background at low angles indicates the presence of uncorrelated single layers, which are randomly folded and connected with further sheets.[14,58] Thus, in $MoS_xC_yP_z$ (350 °C), a larger volume fraction of basal planes as compared to $MoS_xC_yP_z$ (250 °C) is present. The overall dimensions of the $MoS_xC_yP_z$ particles is in the micrometer range (>100 μm), as was determined by scanning electron microscopy (SEM; cf. Figure S1 in the Supporting Information). In a simple approach, the $MoS_xC_yP_z$ systems appear as huge particles, consisting of a carbonaceous matrix having small sharp inhomogeneities in the electron-density distribution due to molybdenum sulfide slabs. In Figure 6, small angled X-ray scattering (SAXS) intensities of the investigated systems are shown. Additional data can be found in the Supporting Information. Due to the micrometer size of the overall particle, the scattering intensity is dominated by the specific internal surface and obeys a $q^{-4}$ power law for $q < 0.03$ Å$^{-1}$. In accordance to the wide-angle diffraction (XRD) the SAXS measurements of $MoS_xC_yP_z$ (250 °C) powder show Debye–Scherrer rings at high scattering vectors *q* with *d* values of about 1.6 nm. The ratio of the reflections 1:2:3 is typical for a lamellar crystal lattice factor, pointing to a parallel alignment of $MoS_2$ sheets inside the mesoscaled particle. These correlations are missing for $MoS_xC_yP_z$ (350 °C), as was expected for randomly oriented $MoS_2$ slabs.

Transmission electron microscopy (TEM) investigation was performed on $MoS_xC_yP_z$ (250 °C) and $MoS_xC_yP_z$ (350 °C) to study the morphology and microstructure (Figure 7). In both cases, the $MoS_2$ slabs are slightly bent with only short range order. An average slab length of approximately 2.4 and 4.2 nm was determined by statistical analysis of the micrographs for $MoS_xC_yP_z$ (250 °C) and $MoS_xC_yP_z$ (350 °C), respectively. This result demonstrates that the number of slab edges can be varied by the decomposition temperature. Figure 7a and b show typical high-resolution TEM micrographs of the $MoS_xC_yP_z$ (250 °C). An additional reflection with a *d* spacing of 1.357 nm (in Figure 7a) and 1.295 nm (in Figure 7c) is clearly revealed from the FFT pattern in the inset. The reflections of (002) and (101) planes of $MoS_2$ (space group: $P6_3/mmc$) are also shown in the FFT. The inverse FFTs were obtained by applying a mask on the additional rings at small scattering angles. The inverse FFTs (Figure 7b and d) of the marked regions in a and (c) show slabs with expanded *d* spacings ranging from 1.239 to 1.369 nm. In contrast, the large *d* spacing (ca. 1.3 nm) is not seen in $MoS_xC_yP_z$ (350 °C) neither from the HRTEM micrograph (cf. Figure 8a) nor from the FFT (Fig-

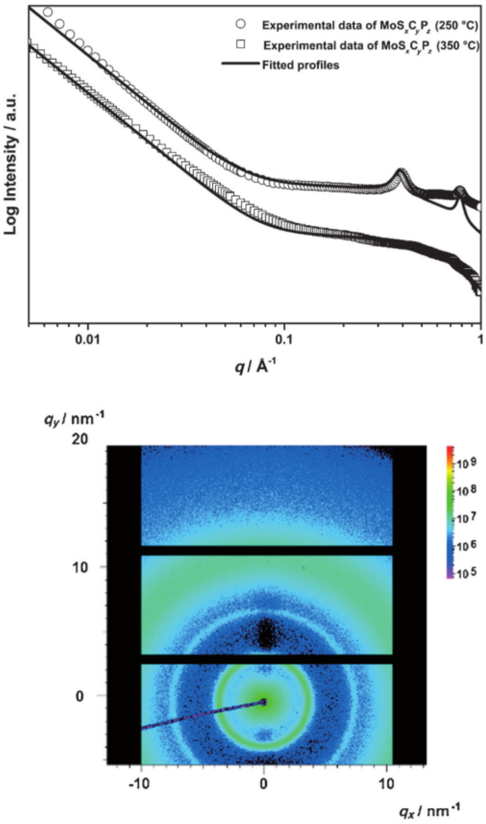

**Figure 6.** SAXS patterns of $MoS_xC_yP_z$ samples. Top: scattering intensities of the powders (○: $MoS_xC_yP_z$ (250 °C), □: $MoS_xC_yP_z$ (350 °C)), and theoretical description (——). Bottom: 2D pattern of $MoS_xC_yP_z$ (250 °C) dispersion.

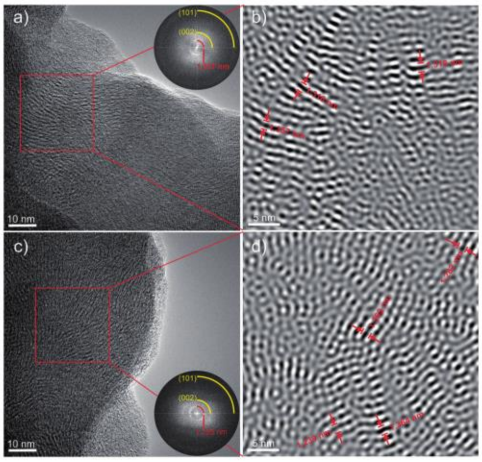

**Figure 7.** a), c) HRTEM micrographs from two different areas of the 250 °C sample. Insets are the corresponding fast Fourier transform (FFT) patterns. b), d) Enlarged inverse FFTs of the areas marked with a red box in the HRTEM micrographs. The additional *d* spacing values of the expanded slabs were observed throughout the sample.

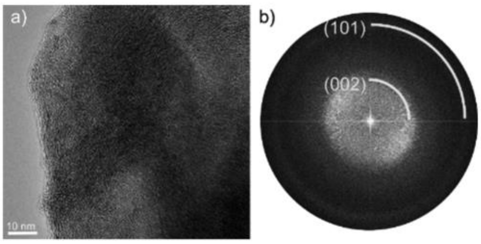

**Figure 8.** a) HRTEM micrograph and b) the corresponding FFT from the 350 °C sample. In the FFT, a diffuse ring, which corresponds to (002) plane of $MoS_2$ and the reflection of (011) plane are shown. No additional *d* spacing was identified from this sample.

ure 8 b), and these observations are in good agreement with the XRD results. The slight deviation of the *d* spacings observed in TEM and XRD might be due to the electron-beam-induced modification of the sample, for example, by partial damage of intercalated molecules in TEM. Consequently, the *d* spacings observed by TEM are smaller than those measured by XRD. The diffuse (002) ring from the FFT pattern indicates a disordered and expanded orientation of the slabs in the sample, which can also be observed from the HRTEM micrograph.

All results of the complementary characterization techniques suggest that an intermediate composite has been formed at 250 °C containing $(Ph_4P)^+$ and most probably $Ph_3PS$. Hence, a structural model consisting of salt-like $(Ph_4P)_2S$ molecules and $Ph_3PS$ molecules being connected to the $MoS_2$ layers by P-S-Mo bonds can be envisaged. Force-field calculations have been carried out by using different models to explain the *d* spacings in the XRD pattern observed for $MoS_xC_yP_z$ (250 °C). The models mainly differ in the connectivity of $Ph_3PS$ in the interlayer space of $MoS_2$, whereas the $Ph_4P^+$ molecules remain free in rotation. The most probable model (M1) contains $Ph_4P^+$ and $Ph_3PS$, in which $Ph_3PS$ is directly bonded by the S atom to a Mo atom of $MoS_2$ (Figure 9). Two other models would also explain the position of the reflections in the X-ray diffractogram but they were discarded on the basis of the analytical results (see Figures S3 and S4 in the Supporting Information).

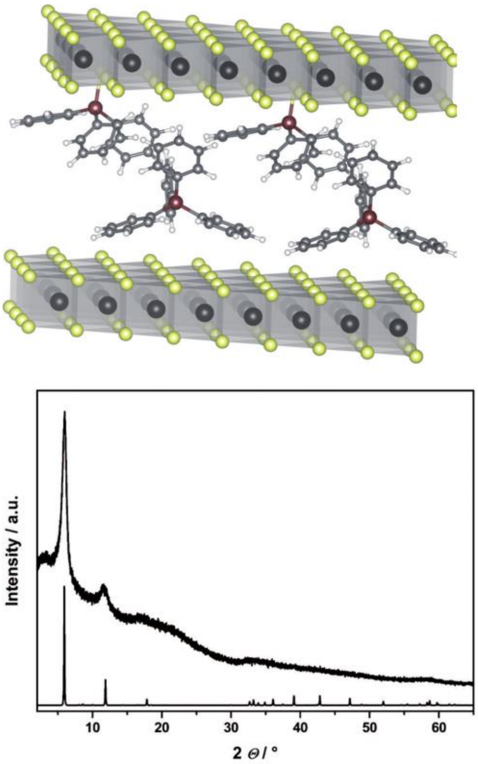

**Figure 9.** Model M1 derived from force-field calculation of $MoS_xC_yP_z$ (250 °C) composite (top) and the corresponding calculated XRD pattern (bottom).

For the investigation of light-driven hydrogen production from water, $MoS_xC_yP_z$ materials were used as a water-reduction catalyst in combination with the sacrificial electron donor triethylamine and the photosensitizer component $[Ru(bpy)_3](PF_6)_2$ (bpy = 2,2′-bipyridine) in an acetonitrile/water mixture. The photosensitizer absorbs light and is promoted to an excited state from which electron transfer to the water reduction catalyst takes place. Re-reduction of the photosensitizer is realized by reaction with the sacrificial electron donor.[59] Light-driven hydrogen-evolution experiments impressively demonstrated that both decomposition products are much more active than bulk $MoS_2$ ($\approx 12\ \mu mol\,h^{-1}$), and $MoS_xC_yP_z$ (350 °C; $\approx 116\ \mu mol\,h^{-1}$) showed a better catalytic performance than $MoS_xC_yP_z$ (250 °C; $\approx 77\ \mu mol\,h^{-1}$; Figure 10). These observations may be attributed to the different chemical compositions and structural properties of the samples. The material $MoS_xC_yP_z$ (250 °C) contains intact organic molecules and $MoS_2$ slabs with a higher stacking degree, whereas the catalyst $MoS_xC_yP_z$ (350 °C) is less C, H, and P rich. $MoS_xC_yP_z$ (350 °C) contains ill-defined carbon species, thus, potentially suppressing charge recombination, improving charge transfer and enhancing light-adsorption properties, as well as the amount of photocatalytic reaction centers.[17,60] Furthermore, the bonding of $Ph_3PS$ to Mo atoms of the molybdenum sulfide might block active sites for hydrogen generation. In addition, the X-ray powder pattern of $MoS_xC_yP_z$ (350 °C) gives evidence for the presence of a low stacking degree of disordered/defective $MoS_2$ slabs, but according to TEM results, the slabs are in average longer than for the sample $MoS_xC_yP_z$ (250 °C). From these observations, one may conclude that the number of edge sites in the $MoS_2$ sheets is not the most important factor determining the photocatalytic activity. The presence of phosphorus species may also play a distinct role for the catalytic activity.[61] It should be noted that hydrogen was found to be the only gaseous reaction product (GC analysis). Despite the widely discussed problems in comparing photocatalytic activities,[62–64] the activity of the photocatalyst $MoS_xC_yP_z$ (350 °C) is listed with those of $MoS_2$-based catalysts reported in literature (Table 1). The data reveal that the photocatalytic activity of $MoS_xC_yP_z$ (350 °C) is comparable with that of $MoS_xC_y$ (C3), which has been reported previously.[22] Only a few $MoS_2$-containing photocatalytic system gave better performances than the $MoS_xC_y$ and $MoS_xC_yP_z$ samples. One of these systems is colloidal $MoS_2$[65] additionally containing a polymer, another system is a composite of nitrogen-doped reduced graphene oxide and $MoS_2$, and recently it was shown that the 1T-$MoS_2$ polytype is a good photocatalyst.[39] The usage of colloidal $MoS_2$ probably gives high performance due to a higher degree of junctions between the light-absorbing agent and $MoS_2$. The stabilizing polymer also may affect the activity by improving the electron transfer. The polytype 1T-$MoS_2$ shows a high photocatalytic performance mainly based on its metallic character and thus a superior transfer of electrons. In any case, the present photocatalysts are free of supporting additives and toxic materials, and they are easily synthesized by a thermal-decomposition procedure. One should also note that comparison of activities after few hours does not always reflect the total activity of a photocatalyst.

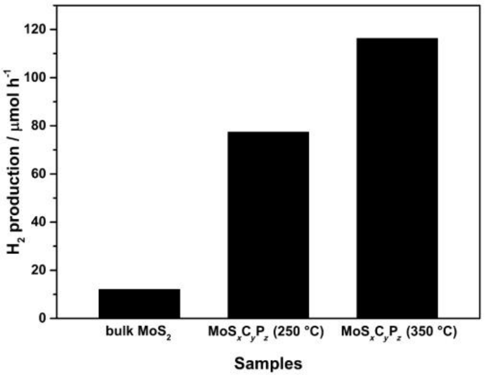

**Figure 10.** Photocatalytic hydrogen-evolution reaction from a mixture containing triethylamine (8 mL), water (3 mL), and $[Ru(bpy)_3](PF_6)_2$ in acetonitrile (10 mL).

**Table 1.** Photocatalysts based on $MoS_2$ for light-driven hydrogen generation.

| Photocatalyst | Reaction conditions | Activity [$\mu mol\,h^{-1}$] | Activity [$\mu mol\,mg^{-1}\,h^{-1}$] |
|---|---|---|---|
| $MoS_xC_yP_z$ (350 °C) | triethylamine, water, $[Ru(bpy)_3](PF_6)_2$ in acetonitrile, 300 W Xe lamp, optical cutoff filter ($\lambda > 420$ nm) | 116 | 11.6 |
| $MoS_2/TiO_2$[15] | $Na_2S/Na_2SO_3$ in water, 300 W Xe lamp | 2.6 | 1.6 |
| $MoS_2/ZnIn_2S_4$[19] | $Na_2S/Na_2SO_3$ in water, 300 W Xe lamp, optical cutoff filter ($\lambda > 420$ nm) | 153 | 3.1 |
| $MoS_xC_y$ (C3)[22] | triethylamine, water, $[Ru(bpy)_3](PF_6)_2$ in acetonitrile, 300 W Xe lamp, optical cutoff filter ($\lambda > 420$ nm) | 120 | 12 |
| $TiO_2/MoS_2$/graphene[17] | ethanol/water, 350 W Xe lamp | 165 | 2.1 |
| ZnS/graphene/$MoS_2$[40] | $Na_2S/Na_2SO_3$ in water, 300 W Xe lamp | 230 | 2.3 |
| 1T–$MoS_2$[39] | eosin Y in water/triethanolamine, 100 W Xe lamp | 52 | 26 |
| NRGO–$MoS_2$[39] | eosin Y in water/triethanolamine, 400 W Xe lamp | 84 | 42 |
| colloidal $MoS_2$[65] | ascorbic acid, $[Ru(bpy)_3](PF_6)_2$ in acetonitrile/methanol, 300 W Xe lamp, optical cutoff filter ($\lambda > 420$ nm) | 420 | 210 |
| $CdSe/MoS_2$[66] | $Na_2S/Na_2SO_3$ in water, 300 W Xe lamp, optical cutoff filter ($\lambda > 420$ nm) | 8 | 0.8 |
| Pt/$MoS_2$/g-$C_3N_4$[67] | methanol/water, 300 W Xe lamp | 23 | 0.23 |

## Conclusion

$MoS_2$-based nanocomposites containing C and P were obtained by applying a simple synthetic approach allowing control of chemical composition and structural textures. A composite material with large interlayer separation of $MoS_2$ slabs was formed at $T = 250$ °C by in situ formation of $Ph_3PS$ and $(PPh_4)_2S$ incorporated in between $MoS_2$-type slabs. Formation of nanosized $MoS_2$ slabs was evidenced by Raman spectroscopy, TEM micrographs, XRD and SAXS studies. The crystallization of $MoS_2$ from the $[MoS_4]^{4-}$ anion in the precursor is seen as an exothermic event in the DTA curve. The presence of two different phosphorous species exhibiting different chemical behavior was demonstrated by $^{31}P$ NMR studies and MIR spectra. The nanocomposite $MoS_xC_yP_z$ (350 °C) contains only one P ($^{31}P$ NMR) and a collapsed interlayer distance between the $MoS_2$ slabs (XRD, SAXS, TEM). Both nanocomposites were structurally characterized by turbostratic disorder of the $MoS_2$ nanoslabs with low stacking degrees, as was evidenced by XRD and TEM data. The large expansion of the interlayer space in the composite $MoS_xC_yP_z$ (250 °C) could be successfully modeled with force-field calculations assuming $Ph_3PS$ bonded to a Mo atom and $(PPh_4)_2S$ in the van der Waals gap. Both decomposition products feature a much higher catalytic activity for light-driven hydrogen generation compared to bulk $MoS_2$. Differences in performance between the two nanocomposites are due to different microstructures and chemical compositions.

## Experimental Section

### Synthesis of $MoS_xC_yP_z$

$(Ph_4P)_2MoS_4$ was synthesized by dissolving $Ph_4PCl$ (18 mmol) in distilled water (45 mL). A solution of $(NH_4)_2MoS_4$ (9 mmol) in distilled water (70 mL) was added, and an orange solid precipitated. The solid was washed with distilled water, ethanol, and ether. The yield was 86 %. $MoS_2$-based compounds were obtained by thermal decomposition of $(Ph_4P)_2MoS_4$ in a rotary furnace (300 $U\,min^{-1}$) with a heating rate of 100 $^{\circ}C\,h^{-1}$ and under $N_2$ flow (200 $cm^3\,min^{-1}$). The precursor was decomposed at two different temperatures $T = 250$ and 350 °C for 1 h.

### Characterization

The chemical composition was determined with an Eurovector elemental analyser by combusting the samples at $T = 1000\,^{\circ}C$ under an oxygen atmosphere. The evolved gases were detected by gas chromatography. MIR spectra were recorded by using a Bruker Alpha P, and FIR spectra were derived from Bruker ISF66 FIR. Raman spectra were obtained with a Raman Dilor XY spectrometer. X-ray powder diffraction patterns were measured with a STOE-P diffractometer with $Cu_{K\alpha}$ radiation in transmission geometry. The scattering samples were measured as received at standard conditions, for example, as powder and as dispersion (7 % wt). The measurements were done in 1 mm glass capillaries (Hilgenberg, code 4007610, Germany). All small-angle X-ray scattering (SAXS) data reported herein were obtained by using the small-angle X-ray system “Double Ganesha AIR” (SAXSLAB, Denmark).[68] The X-ray source of this laboratory-based system is a rotating anode (copper, MicoMax 007HF, Rigaku Corporation, Japan) providing a microfocused beam. The data were obtained by a position-sensitive detector (PILATUS 300 K, Dectris). To cover the range of scattering vectors $q$ between 0.003–2.0 $Å^{-1}$ different detector positions were used ($q = (4\pi/\lambda)\sin(\Theta/2)$, in which $\lambda$ is wavelength, and $\Theta$ is scattering angle). All 2D patterns appeared isotropic. The circularly averaged data were normalized to incident beam, sample thickness, and measurement time before subtraction of the solvent. HRTEM micrographs were taken with a Tecnai $G^2$-STwin F30 (300 kV, field emission gun (FEG) cathode, spherical aberration coefficient $C_s = 1.2$ mm). $^{31}P$ NMR investigations were performed on a Bruker Advance III spectrometer operating at 7 T by using a Bruker 4 mm WVT MAS probe and a 4 mm $ZrO_2$ spinner. The spectra were recorded with a spinning speed of 7 kHz and a pulse length of 2.4 µs. DTA/TG measurements were performed in nitrogen atmosphere (75 $mL\,min^{-1}$) by using a STA-409CD Netzsch thermobalance.

### Photocatalytic hydrogen evolution

Photocatalytic measurements were carried out by applying photocatalyst (10 mg) in a system using $[Ru(bpy)_3](PF_6)_2$ (1 mM) in acetonitrile (10 mL), triethylamine (8 mL), and water (3 mL). The mixture was irradiated in thermostatically controlled, double-walled reaction vessels by using a 300 W Xe-arc lamp with an optical cut-off filter $\lambda > 420$ nm,[69] and the gas evolution was quantified by an automatic buret[70,71] and qualified by gas chromatography (60/80 Carboxen 1000 column (Supelco) for analysis of light gases; TCD).

## *Acknowledgements*

The authors thank U. Cornelissen, S. Pehlke, and J. Pick for spectroscopic (Raman and IR) and elemental analyses measurements, I. Jeß for DTA/TG measurements, and finally the State of Schleswig-Holstein for the financial support.

**Keywords:** hydrogen evolution · layered structures · molybdenum · nanoparticles · photocatalysis

[1] F. Levy, *Physics and Chemistry of Materials with Layered Structures*, D. Reidel Publishing, Dordrecht Holland/Boston, **1976**.
[2] F. Levy, *Physics and Chemistry of Materials with Layered Structures*, D. Reidel Publishing, Dordrecht Holland/Boston, **1979**.
[3] W. Müller-Warmuth, R. Schöllhorn, *Progress in Intercalation Research*, Kluwer Academic Publishers, Dordrecht/Boston/London, **1994**.
[4] E. Furimsky, *Catal. Rev.* **1980**, *22*, 371 – 400.
[5] R. R. Chianelli, M. H. Siadati, M. P. De La Rosa, G. Berhault, J. P. Wilcoxon, R. Bearden, B. L. Abrams, *Catal. Rev.* **2006**, *48*, 1 – 41.
[6] Z. D. Huang, W. Bensch, L. Kienle, S. Fuentes, G. Alonso, C. Ornelas, *Catal. Lett.* **2009**, *127*, 132 – 142.
[7] R. Prins, V. H. J. de Beer, G. A. Somorjai, *Catal. Rev. Sci. Eng.* **1989**, *31*, 1 – 41.
[8] H. Topsoe, B. S. Clausen, *Catal. Rev. Sci. Eng.* **1984**, *26*, 395 – 420.
[9] M. Xu, T. Liang, M. Shi, H. Chen, *Chem. Rev.* **2013**, *113*, 3766 – 3798.
[10] S. Z. Butler, S. M. Hollen, L. Cao, Y. Cui, J. A. Gupta, H. R. Gutiérrez, T. F. Heinz, S. S. Hong, J. Huang, A. F. Ismach, E. Johnston-Halperin, M. Kuno, V. V. Plashnitsa, R. D. Robinson, R. S. Ruoff, S. Salahuddin, J. Shan, L. Shi, M. G. Spencer, M. Terrones, W. Windl, J. E. Goldberger, *ACS Nano* **2013**, *7*, 2898 – 2926.
[11] C. N. R. Rao, A. Nag, *Eur. J. Inorg. Chem.* **2010**, 4244 – 4250.
[12] Q. H. Wang, K. Kalantar-Zadeh, A. Kis, J. N. Coleman, M. S. Strano, *Nat. Nanotechnol.* **2012**, *7*, 699 – 712.
[13] C. N. R. Rao, U. Maitra, U. V. Waghmare, *Chem. Phys. Lett.* **2014**, *609*, 172 – 183.
[14] P. Joensen, R. F. Frindt, S. R. Morrison, *Mater. Res. Bull.* **1986**, *21*, 457 – 461.
[15] W. Zhou, Z. Yin, Y. Du, X. Huang, Z. Zeng, Z. Fan, H. Liu, J. Wang, H. Zhang, *Small* **2013**, *9*, 140 – 147.
[16] Z. Wu, B. Fang, Z. Wang, C. Wang, Z. Liu, F. Liu, W. Wang, A. Alfantazi, D. Wang, D. P. Wilkinson, *ACS Catal.* **2013**, *3*, 2101 – 2107.
[17] Q. J. Xiang, J. G. Yu, M. Jaroniec, *J. Am. Chem. Soc.* **2012**, *134*, 6575 – 6578.
[18] X. Zong, H. J. Yan, G. P. Wu, G. J. Ma, F. Y. Wen, L. Wang, C. Li, *J. Am. Chem. Soc.* **2008**, *130*, 7176 – 7177.
[19] L. Wei, Y. Chen, Y. Lin, H. Wu, R. Yuan, Z. Li, *Appl. Catal. B* **2014**, *144*, 521 – 527.

[20] Y. Yu, S.-Y. Huang, Y. Li, S. N. Steinmann, W. Yang, L. Cao, *Nano Lett.* **2014**, *14*, 553 – 558.
[21] Y. F. Zhao, Y. X. Zhang, Z. Y. Yang, Y. M. Yan, K. N. Sun, *Sci. Technol. Adv. Mater.* **2013**, *14*, 043501.
[22] J. Djamil, S. A. Segler, A. Dabrowski, W. Bensch, A. Lotnyk, U. Schurmann, L. Kienle, S. Hansen, T. Beweries, *Dalton Trans.* **2013**, *42*, 1287 – 1292.
[23] J. P. Wilcoxon, P. P. Newcomer, G. A. Samara, *J. Appl. Phys.* **1997**, *81*, 7934 – 7944.
[24] K. Hu, X. Hu, Y. Xu, J. Sun, *J. Mater. Sci.* **2010**, *45*, 2640 – 2648.
[25] C. Feng, J. Ma, H. Li, R. Zeng, Z. Guo, H. Liu, *Mater. Res. Bull.* **2009**, *44*, 1811 – 1815.
[26] H. Li, W. Li, L. Ma, W. Chen, J. Wang, *J. Alloys Compd.* **2009**, *471*, 442 – 447.
[27] H. Zhang, X. J. Lv, Y. M. Li, Y. Wang, J. H. Li, *ACS Nano* **2010**, *4*, 380 – 386.
[28] X. Q. An, J. M. C. Yu, Y. Wang, Y. M. Hu, X. L. Yu, G. J. Zhang, *J. Mater. Chem.* **2012**, *22*, 8525 – 8531.
[29] Z. Gao, J. Wang, Z. S. Li, W. L. Yang, B. Wang, M. J. Hou, Y. He, Q. Liu, T. Mann, P. P. Yang, M. Zhang, L. Liu, *Chem. Mater.* **2011**, *23*, 3509 – 3516.
[30] H. B. Yang, G. H. Guai, C. X. Guo, Q. L. Song, S. P. Jiang, Y. L. Wang, W. Zhang, C. M. Li, *J. Phys. Chem. C* **2011**, *115*, 12209 – 12215.
[31] K. Chang, W. X. Chen, *Chem. Commun.* **2011**, *47*, 4252 – 4254.
[32] K. Chang, W. X. Chen, L. Ma, H. Li, H. Li, F. H. Huang, Z. D. Xu, Q. B. Zhang, J. Y. Lee, *J. Mater. Chem.* **2011**, *21*, 6251 – 6257.
[33] S. Ding, J. S. Chen, X. W. Lou, *Chem. Eur. J. J.* **2011**, *17*, 13142 – 13145.
[34] C. Lu, W. Liu, H. Li, B. K. Tay, *Chem. Commun.* **2014**, *50*, 3338 – 3340.
[35] A. B. Laursen, P. C. K. Vesborg, I. Chorkendorff, *Chem. Commun.* **2013**, *49*, 4965 – 4967.
[36] Y. Li, H. Wang, L. Xie, Y. Liang, G. Hong, H. Dai, *J. Am. Chem. Soc.* **2011**, *133*, 7296 – 7299.
[37] T. Jia, A. Kolpin, C. Ma, R. C.-T. Chan, W.-M. Kwok, S. C. E. Tsang, *Chem. Commun.* **2014**, *50*, 1185 – 1188.
[38] S. Min, G. Lu, *J. Phys. Chem. C* **2012**, *116*, 25415 – 25424.
[39] U. Maitra, U. Gupta, M. De, R. Datta, A. Govindaraj, C. N. R. Rao, *Angew. Chem. Int. Ed.* **2013**, *52*, 13057 – 13061; *Angew. Chem.* **2013**, *125*, 13295 – 13299.
[40] B. Zhu, B. Lin, Y. Zhou, P. Sun, Q. Yao, Y. Chen, B. Gao, *J. Mater. Chem. A* **2014**, *2*, 3819 – 3827.
[41] G. Socrates, *Infrared and Raman Characteristic Group Frequencies*, Wiley, Chichester, **2001**.
[42] B. R. Srinivasan, S. N. Dhuri, A. R. Naik, C. Nather, W. Bensch, *Polyhedron* **2008**, *27*, 25 – 34.
[43] K. A. Jensen, P. H. Nielsen, *Acta Chem. Scand.* **1963**, *17*, 1875 – 1885.
[44] J. A. W. Dalziel, A. F. le C. Holding, B. E. Watts, *J. Chem. Soc. A* **1967**, 358 – 361.
[45] M. G. King, G. P. McQuillan, *J. Chem. Soc. A* **1967**, 898 – 901.
[46] T. J. Wieting, J. L. Verble, *Phys. Rev. B* **1971**, *3*, 4286 – 4292.
[47] O. P. Agnihotri, H. K. Sehgal, A. K. Garg, *Solid State Commun.* **1973**, *12*, 135 – 138.
[48] G. L. Frey, R. Tenne, M. J. Matthews, M. S. Dresselhaus, G. Dresselhaus, *Phys. Rev. B* **1999**, *60*, 2883 – 2892.
[49] R. Nast, P. Schneller, A. Hengefeld, *J. Organomet. Chem.* **1981**, *214*, 273 – 276.
[50] R. A. Komoroski, A. J. Magistro, P. P. Nicholas, *Inorg. Chem.* **1986**, *25*, 3917 – 3925.
[51] S. Nakagaki, A. S. Mangrich, F. Wypych, *Inorg. Chim. Acta* **1997**, *254*, 213 – 217.
[52] A. V. Powell, L. Kosidowski, A. McDowall, *J. Mater. Chem.* **2001**, *11*, 1086 – 1091.
[53] L. Wang, J. Schindler, J. A. Thomas, C. R. Kannewurf, M. G. Kanatzidis, *Chem. Mater.* **1995**, *7*, 1753 – 1755.
[54] P. J. Ollivier, T. E. Mallouk, P. J. Ollivier, N. I. Kovtyukhova, S. W. Keller, *Chem. Commun.* **1998**, 1563 – 1564.
[55] J. P. Lemmon, M. M. Lerner, *Chem. Mater.* **1994**, *6*, 207 – 210.
[56] W. M. R. Divigalpitiya, R. F. Frindt, S. R. Morrison, *Science* **1989**, *246*, 369 – 371.
[57] W. M. R. Divigalpitiya, R. F. Frindt, S. r. Morrison, *J. Mater. Res.* **1991**, *6*, 1103 – 1107.
[58] R. R. Chianelli, E. B. Prestridge, T. A. Pecoraro, J. P. Deneufville, *Science* **1979**, *203*, 1105 – 1107.
[59] B. Wardle, *Principles and Applications of Photochemistry*, Wiley, Chichester, **2009**.
[60] X. Zhang, Y. Sun, X. Cui, Z. Jiang, *Int. J. Hydrogen Energy* **2012**, *37*, 1356 – 1365.
[61] Y.-P. Yuan, S.-W. Cao, Y.-S. Liao, L.-S. Yin, C. Xue, *Appl. Catal. B* **2013**, *140 – 141*, 164 – 168.
[62] T. Maschmeyer, M. Che, *Angew. Chem. Int. Ed.* **2010**, *49*, 1536 – 1539; *Angew. Chem.* **2010**, *122*, 1578 – 1582.
[63] T. Maschmeyer, M. Che, *Angew. Chem. Int. Ed.* **2010**, *49*, 9590 – 9591; *Angew. Chem.* **2010**, *122*, 9784 – 9785.
[64] H. Kisch, *Angew. Chem. Int. Ed.* **2010**, *49*, 9588 – 9589; *Angew. Chem.* **2010**, *122*, 9782 – 9783.
[65] X. Zong, Y. Na, F. Y. Wen, G. J. Ma, J. H. Yang, D. G. Wang, Y. Ma, M. Wang, L. Sun, C. Li, *Chem. Commun.* **2009**, 4536 – 4538.
[66] F. A. Frame, F. E. Osterloh, *J. Phys. Chem. C* **2010**, *114*, 10628 – 10633.
[67] L. Ge, C. Han, X. Xiao, L. Guo, *Int. J. Hydrogen Energy* **2013**, *38*, 6960 – 6969.
[68] For specifications of the small-angle X-ray system, see: http://www.jjxray.dk
[69] For specifications of the light source (LOT-Oriel-300-W-Xe-Lamp, LSB530) and Cut-off Filter (ITOS, GG420), see: http://www.lot-Oriel.com.
[70] H.-J. Drexler, A. Preetz, H. Schmidt, *The Handbook of Homogenous Hydrogenation*, Wiley-VCH, Weinheim, **2007**.
[71] T. Beweries, J. Thomas, M. Klahn, A. Schulz, D. Heller, U. Rosenthal, *ChemCatChem* **2011**, *3*, 1865 – 1868.

Received: December 18, 2014

CHEMISTRY
A European Journal

Supporting Information

# In Situ Formation of a $MoS_2$-Based Inorganic–Organic Nanocomposite by Directed Thermal Decomposition

John Djamil,*[a] Stefan A. W. Segler,[a] Wolfgang Bensch,*[a] Ulrich Schürmann,[b] Mao Deng,[b] Lorenz Kienle,[b] Sven Hansen,[c] Torsten Beweries,[c] Leo von Wüllen,[d] Sabine Rosenfeldt,[e] Stephan Förster,[e] and Helge Reinsch[f]

chem_201406541_sm_miscellaneous_information.pdf

## Supporting information

SEM

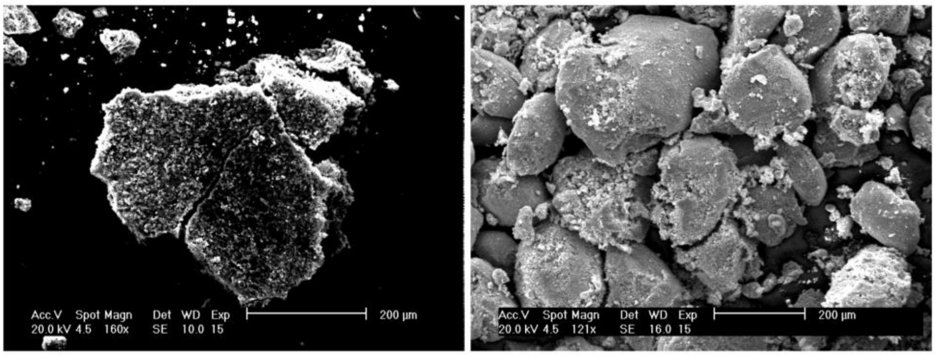

Figure S1. SEM images of $MoS_xC_yP_z$ (250 °C) (left) and $MoS_xC_yP_z$ (350 °C) (right).

SAXS

In a simple approximation the $MoS_xC_yP_z$ sample consists of a matrix having sharp interfaces in the electron density distribution due to the $MoS_2$ inhomogeneity. The scattering intensity I(q) is modeled by adding up two contributions: A scattering contribution due to the specific surface area of the matrix contribution (Porod limit), which is proportional to $q^{-4}$ and an additional contribution due to the smaller static inhomogeneity caused by the $MoS_2$ sheets. It's assumed that the slabs causes that additional scattering contribution, which is Gaussian and scales proportional to $\exp(-Rg^2q^2)$, where Rg denotes the radius of gyration of the static inhomogeneity. In case of sheets the thickness $t$ can be estimated by $t = Rg \cdot \sqrt{12}$. From the fitting of the powder data the thickness was approximated to 6.2 Å, which in the expected range of $MoS_2$ slabs. For the $MoS_xC_yP_z$ (250 °C) a further contribution, a lamellar lattice factor to include possible $MoS_2$-layer-layer correlations in the small homogeneities are added. The agreement between that simple model and the experimental data is good. Slight derivations appear, especially for the dispersions, what may be explained by small variations in the internal structures.

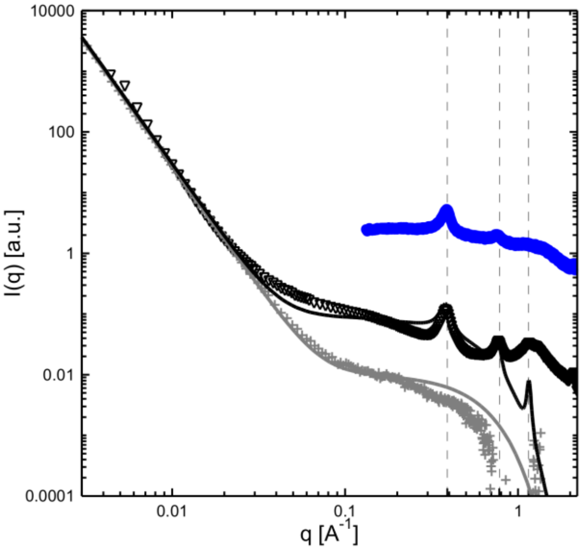

Figure. S2: XRD and SAXS patterns. The blue symbols corresponds to the XRD data of $MoS_xC_yP_z$ (250 °C) powder Black triangles denotes the SAXS data of a $MoS_xC_yP_z$ (250 °C)-dispersion (7 wt%) and gray crosses to a $MoS_xC_yP_z$ (350 °C)-dispersion (7 wt%). The theoretical intensities (lines) corresponds to the modelling of the data using a simple approach of a homogeneous macrosystem having internal fluctuations with a radius of gyration of 1.8 Å. In case of the $MoS_xC_yP_z$ (250 °C) dispersion an additional contribution due to lamellar correlation distance of $MoS_2$ sheets of 16 Å had been added. This distance is slightly increased compared to the result of a stacking distance of 16.5 Å obtained for the powder of that sample.

Force Field Calculations

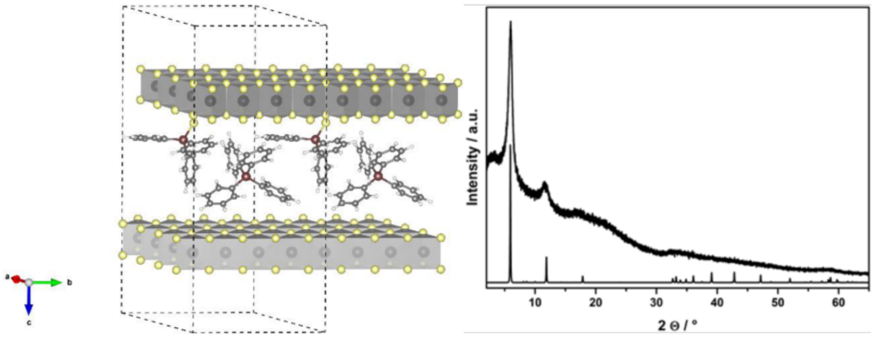

Figure S3. Model M2 derived from force field calculation of $MoS_xC_yP_z$ (250 °C) composite.

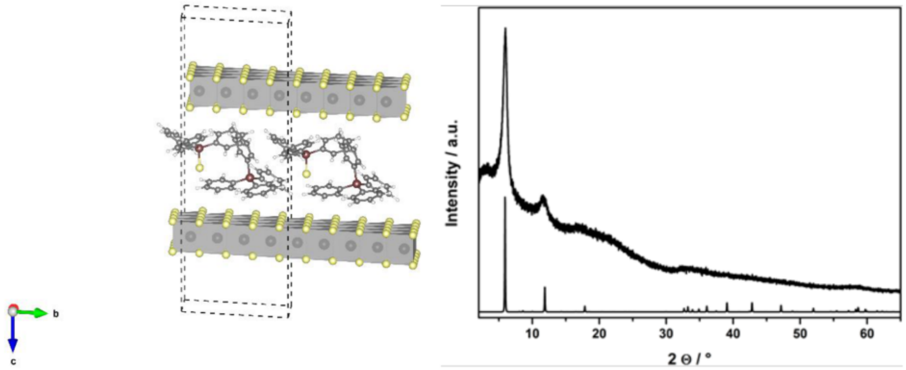

Figure S4. Model M3 derived from force field calculation of $MoS_xC_yP_z$ (250 °C).

### 4.1.2.1 XPS-Untersuchungen an $MoS_xC_yP_z$

Anknüpfend an die Veröffentlichung „*In situ* Formation of a $MoS_2$-based Inorganic-Organic Nanocomposite by Directed Thermal Decomposition“ wurden $MoS_xC_yP_z$ (250 °C) und (350 °C) zusätzlich mit XPS charakterisiert und auf der Basis der anderen analytischen Methoden interpretiert (Abb. 24). Eine tabellarische Zusammenfassung der BE und Intensitäten sowie die sich daraus ergebenden Differenzen und Verhältnisse ist in Tabelle 2 enthalten. Die Auswertungen des Mo- (Mo $3d_{5/2}$: 228.4 eV) und S-Spektrums (S-Hauptsignal bei S $2p_{3/2}$: 161.5 eV) von $MoS_xC_yP_z$ (250 °C) geben Hinweis auf $MoS_2$ ($\Delta_{BE}$ = 66.9 eV), allerdings in einer anderen chemischen Umgebung verglichen zu reinem $MoS_2$ (Mo $3d_{5/2}$: 229.5 eV; S $2p_{3/2}$: 162.4 eV; $\Delta_{BE}$ = 67.1 eV). Die zweite S-Spezies bei geringeren BE (S $2p_{3/2}$: 160.7 eV) kann $S^{2-}$ im $(PPh_4)_2S$ zugeordnet werden. Der thermische Abbau von $(PPh_4)_2MoS_4$ bei 350 °C resultiert in speziesreicheren XPS-Spektren. Ähnlich zu dem Zersetzungsprodukt bei 250 °C deuten das Mo-Hauptsignal (Mo $3d_{5/2}$: 228.7 eV) und das S-Hauptsignal (S $2p_{3/2}$: 161.6 eV) in $MoS_xC_yP_z$ (350 °C) auf $MoS_2$ ($\Delta_{BE}$ = 67.1 eV) in einer anderen chemischen Umgebung verglichen zu reinem $MoS_2$ hin. Die S-Spezies bei geringeren BE kann erneut $(PPh_4)_2S$ zugeordnet werden. Zusätzlich tritt eine weitere Mo-Spezies (Mo $3d_{5/2}$ = 229.5 eV) auf, die zusammen mit der verbleibenden S-Spezies (S $2p_{3/2}$: 162.5 eV) auf das Vorliegen von $MoS_2$ ($\Delta_{BE}$ = 67.0 eV) schließen lässt. Die Zuordnung der Mo-Spezies bei geringen BE (Mo $3d_{5/2}$: 228.1 eV) ist bisher nicht eindeutig.

Die Verschiebungen der BE der Mo- und S-Hauptsignale deuten auf ein elektronenreicheres $MoS_2$ hin, was möglicherweise durch die Einlagerung von $(PPh_4)_2S$ in $MoS_2$ verursacht wird. Eventuell übertragen die $\pi$-Elektronen der Phenylgruppen Elektronendichte an $MoS_2$, so dass die BE zu niedrigeren Werten verschoben werden. Der C-Gehalt ist bei $MoS_xC_yP_z$ (350 °C) halb so groß wie bei $MoS_xC_yP_z$ (250 °C). Daher ist anzunehmen, dass die Menge an $PPh_4^+$-Ionen reduziert ist, was auch in den IR-Spektren deutlich wird (Intensitätsverlust). Folglich wird die Zahl von $PPh_4^+$-$MoS_2$-Wechselwirkungen reduziert und die für $MoS_2$ typischen BE werden beobachtet. Der Einfluss von eingelagerten Molekülen/Ionen auf die elektronischen Eigenschaften von $MoS_2$ bedarf weiterer Untersuchungen, damit die Verschiebung der Mo- und S-BE widerspruchsfrei erklärt werden kann.

Darüber hinaus sind durch solche Einlagerungen möglicherweise elektronische Veränderungen von $MoS_2$ in einfacher Weise zugänglich.

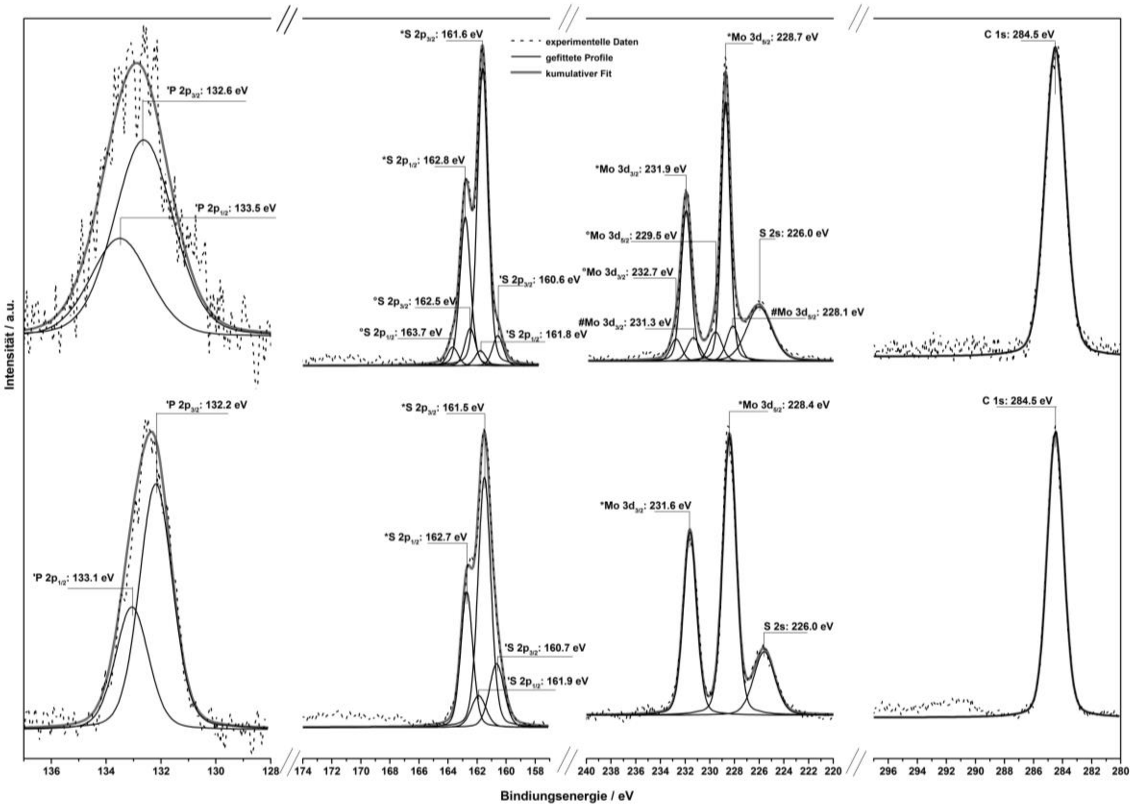

**Abb. 24: XPS-Spektren der P 2p- (links), S 2p- (mitte-links), Mo 3d- (mitte-rechts) und C 1s- (rechts) Region von $MoS_xC_yP_z$ (250 °C) (unten) und $MoS_xC_yP_z$ (350 °C) (oben).**

**Tabelle 2: XPS-Parameter von $MoS_xC_yP_z$ (250 °C) (oben) und $MoS_xC_yP_z$ (350 °C) (unten).**

| $MoS_xC_yP_z$ (250 °C) | | | | | | |
|---|---|---|---|---|---|---|
| BE/eV | $\Delta_{BE}$/eV | FWHM/eV | $\Delta_{FMWH}$/eV | Fläche | Flächenverhältnis | Spezies |
| 132.2 | 0.9 | 1.4 | 0 | 68 | 2.0 | P $2p_{3/2}$ |
| 133.1 | | 1.4 | | 34 | | P $2p_{1/2}$ |
| 160.7 | 1.2 | 1.2 | 0 | 115 | 2.0 | S $2p_{3/2}$ |
| 161.9 | | 1.2 | | 58 | | S $2p_{1/2}$ |
| 161.5 | 1.2 | 1 | 0 | 393 | 2.0 | S $2p_{3/2}$ |
| 162.7 | | 1 | | 197 | | S $2p_{1/2}$ |
| 225.6 | | 2 | - | 366 | | S 2s |
| 228.4 | 3.2 | 1.3 | 0 | 1001 | 1.5 | Mo $3d_{5/2}$ |
| 231.6 | | 1.3 | | 663 | | Mo $3d_{3/2}$ |
| 284.5 | - | 1.3 | - | 1697 | - | C 1s |
| 531 | - | 2.8 | - | 206 | | O 1s |

| $MoS_xC_yP_z$ (350 °C) | | | | | | |
|---|---|---|---|---|---|---|
| BE/eV | $\Delta_{BE}$/eV | FWHM/eV | $\Delta_{FMWH}$/eV | Fläche | Flächenverhältnis | Spezies |
| 132.6 | 0.9 | 2.5 | 0.0 | 41 | 2.0 | P $2p_{3/2}$ |
| 133.5 | | 2.5 | | 21 | | P $2p_{1/2}$ |
| 160.6 | 1.2 | 0.9 | 0.0 | 66 | 2.0 | S $2p_{3/2}$ |
| 161.8 | | 0.9 | | 33 | | S $2p_{1/2}$ |
| 161.6 | 1.2 | 0.9 | 0.0 | 649 | 2.0 | S $2p_{3/2}$ |
| 162.8 | | 0.9 | | 325 | | S $2p_{1/2}$ |
| 162.5 | 1.2 | 0.9 | 0.0 | 82 | 2.0 | S $2p_{3/2}$ |
| 163.7 | | 0.9 | | 41 | | S $2p_{1/2}$ |
| 226.0 | - | 2.4 | - | 791 | - | S 2s |
| 228.1 | 3.2 | 1.2 | 0.0 | 255 | 1.5 | Mo $3d_{5/2}$ |
| 231.3 | | 1.2 | | 170 | | Mo $3d_{3/2}$ |
| 228.7 | 3.2 | 0.9 | 0.1 | 1333 | 1.5 | Mo $3d_{5/2}$ |
| 231.9 | | 1.0 | | 889 | | Mo $3d_{3/2}$ |
| 229.5 | 3.2 | 1.2 | 0.1 | 212 | 1.5 | Mo $3d_{5/2}$ |
| 232.7 | | 1.1 | | 141 | | Mo $3d_{3/2}$ |
| 284.5 | - | 1.6 | - | 1137 | - | C 1s |
| 531.7 | - | 3.1 | - | 353 | - | O 1s |

### 4.1.3 Der Einfluss der Partikelgröße und des Aspektverhältnisses von $MoS_2$ auf die fotokatalytische $H_2$-Entwicklung

Zusammenfassung der Veröffentlichung „The Effect of Particle Size and Aspect Ratio of Molybdenum Sulfide on the Visible-Light Driven Hydrogen Generation“. Dieser Artikel wurde zur Veröffentlichung eingereicht.

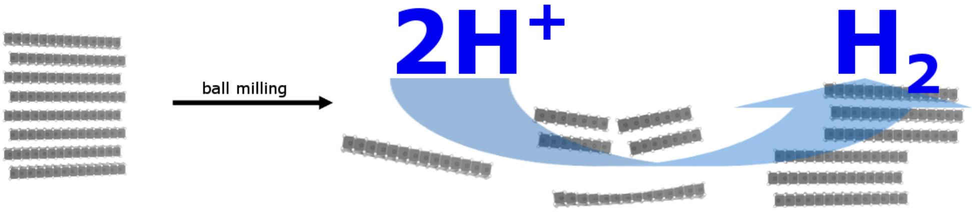

**Abb. 25: Schematische $H_2$-Entwicklung an kugelgemahlenem $MoS_2$.**

In dieser Veröffentlichung wird über die Herstellung, Charakterisierung und fotokatalytische Untersuchungen für die lichtgetriebene $H_2$-Entwicklung mit $MoS_2$-Nanopartikeln berichtet. Die Herstellung dieser Nanopartikel erfolgte durch unterschiedliche Behandlungsdauern von $MoS_2$ Volumenmaterial in einer Hochenergiekugelmühle (Abkürzung der Proben: bmX, X = 1, 2, 4, 8 h) und anschließender thermischen Behandlung bei 150 °C unter $N_2$. Die spezifische Oberfläche der nanopartikulären $MoS_2$-Proben wurde mit der Stickstoffgas-Sorption ermittelt. Die kugelgemahlenen Proben weisen eine höhere spezifische Oberfläche (bm1, bm2, bm4 $\approx$ 16 $m^2/g$) als das Ausgangsmaterial (4 $m^2/g$) auf. Die Abnahme der spezifischen Oberfläche von bm4 auf bm8 (11 $m^2/g$) deutet möglicherweise auf Verdichtung der Aggregate hin. In den TEM-Aufnahmen wird der Einfluss der mechanischen Behandlung auf die $MoS_2$-Partikel deutlich. Das Ausgangsmaterial besteht aus Partikeln mit geraden und langen $MoS_2$-Schichten, welche eine sehr große Stapelung der $MoS_2$-Schichten aufweisen. Sowohl die Schichtlänge als auch die Stapelung nehmen durch die mechanische Behandlung der $MoS_2$-Partikel ab. Zusätzlich führt der Prozess in der Kugelmühle zu Stapelfehlern und Verbiegungen der Schichten. Mit Hilfe von XRD-Analysen der mechanisch behandelten Proben wurden Schichtlängen und Stapelhöhe und daraus das resultierende Aspektverhältnis (Schichtlänge/Stapelhöhe) ermittelt. Die Stapelhöhe nimmt dabei signifikanter mit der Behandlungszeit ab (von 46 auf 6 nm) als die Schichtlänge (von 65 auf 19 nm), so dass das Aspektverhältnis zunimmt. Während bm1 und bm2 Aspektverhältnisse von ungefähr eins aufweisen, liegen bei bm4 (2.5) und bm8 (3.2) deutlich größere Aspektverhältnisse vor, so dass flachere Partikel vorliegen. Sowohl die Abnahme der Schichtlänge als auch der Stapelhöhe führt zu einer größeren Anzahl an $MoS_2$-Kanten. Zusätzlich deutet die Anwesenheit von verbreiterten Beugungsreflexen auf Verzerrungen, Stapelfehler und Verbiegung der Schichten hin. Die Anwesenheit und Zunahme von unkorrelierten $MoS_2$-Einzelschichten in den mechanisch behandelten Proben mit zunehmender Mahlzeit kann durch das Auftreten und zunehmenden diffusen Untergrund bei kleinen Beugungswinkeln $2\Theta$ erkannt werden. Aus den fotokatalytischen Untersuchungen kann eine moderate Korrelation zwischen Behandlungsdauer in der Kugelmühle und der Aktivität abgeleitet werden. In allen Fällen übertreffen die kugelgemahlenen Proben die Aktivität von $MoS_2$ Volumenmaterial (≈ 12 µmol/g) aufgrund der größeren Zahl an $MoS_2$-Kanten. Für bm1 und bm2 wird trotz unterschiedlicher Schichtlängen und Stapelhöhen aber ähnlichem Aspektverhältnis eine vergleichbare katalytische Aktivität beobachtet (23 µmol/g an $H_2$). Die produzierte Menge $H_2$ ist bei bm4 (37 µmol/g) am größten und nimmt zu bm8 (34 µmol/g) geringfügig ab. Beide Proben weisen eine größere Dichte an $MoS_2$-Kanten und ein höheres Aspektverhältnis auf gegenüber bm1 und bm2. Die Abnahme der katalytisch erzeugten $H_2$-Menge von bm8 gegenüber bm4 ist wahrscheinlich in der Verringerung der spezifischen Oberfläche begründet.

# The Effect of Particle Size and Aspect Ratio of Molybdenum Sulfide on the Catalytic Activity in Visible Light Driven Hydrogen Generation

John Djamil,[a] Anna-Lena Hansen,[a] Stefan Permien,[a] Wolfgang Bensch,*[a] Ulrich Schürmann,[b] Lorenz Kienle,[b] Andre Düvel,[c] Paul Heitjans,[c] Laura Dura,[d] Torsten Beweries,[d] Udo Bauer,[e] Inga Niedermaier,[e] Christian Papp,[e] Hans-Peter Steinrück[e]

Dedication ((optional))

**Abstract:** Mechanical activation of $MoS_2$ was applied to transform macroscopic catalytically inactive material into an active co-catalyst for visible light driven hydrogen generation. Pristine $MoS_2$ was treated in a high-energy ball mill for different time periods to reduce particle sizes and to increase the aspect ratio. The resulting structural changes were studied with X-ray diffraction, HR-TEM and $N_2$ physisorption. During the milling process the stacking heights and slab lengths of the crystallites decrease. Because the stacking height is more reduced than the basal plane area an increasing aspect ratio is observed. Structure related changes like bending and distortion of the $MoS_2$ slabs are observed for ball-milled samples. The nanosized co-catalysts exhibit high photocatalytic activities with respect to macroscopic $MoS_2$ due to high densities of exposed actives sites, i.e. $MoS_2$ edge sites developed during the treatment. The specific surface area also affects the catalytic activity.

## Introduction

Growing energy demands as a result of expanded industrialization, modernization, population growth and urbanization as well as the current lifestyle standards like mobility and comfort in general result in steadily increasing energy consumption. Therefore the development and enhancement of renewable energy technologies plays an important role as possible replacement for fossil fuels. Different approaches like the usage of solar energy, wind power, hydropower, biomass energy and geothermal power have been investigated in terms of addressing energy and environmental issues.[1,2] Corresponding to that, light driven hydrogen generation has attracted much attention since the production from fossil fuels represents more critical environmental route. Therefore, numerous compounds mostly based on semiconductors have been investigated for photocatalytic, photoelectrochemical and electrochemical hydrogen evolution.[3–8] Among these, transition metal chalcogenides like cadmium sulfide, zinc sulfide and molybdenum sulfide have shown promising performances for light-driven hydrogen generation.[3,6,7,9] However, many of the transition metal sulfides suffer photocorrosion during light driven catalytic processes.[3,6,10,11] In contrast to that, $MoS_2$ is resistant to photocorrosion,[12,13] making this compound a promising and effective catalyst for photocatalytic hydrogen evolution.[14–17] Especially the investigation of $MoS_2$ particles on the nanoscale with different shapes and exposed surface sites for photocatalysis has been a subject of intense research. Exploration of active sites in $MoS_2$ samples originates from hydrodesulfurization (HDS) reactions as a well-established catalyst and the rim-edge model for unsupported $MoS_2$ was developed to explain the selectivity differences in the HDS.[18] In a number of experimental and theoretical studies the $MoS_2$ edge sites have been identified as the active sites for the HDS reaction, whereas the basal plane is supposed to be catalytically inactive. Nowadays, it is widely accepted that two different edge sites, the so called Mo- and S-edges, exhibit different reactivity.[19–22] Identification of active sites for catalytic hydrogen generation on $MoS_2$ is of particular interest for improving performances by tailoring the $MoS_2$ morphology. In accordance with the experimental and theoretical studies it was possible to establish a correlation between the hydrogen evolution reaction (HER) activity and the number of edge sites.[23] In further experiments the Mo-edge site was identified as active site for HER, while the S-edge was considered to be catalytically inactive.[24,25] Hence, control of the morphology of $MoS_2$ particles may increase the HER activity.[26] Hitherto, exploration of $MoS_2$ actives sites is concerned mostly with preliminary electrochemical studies or electrochemical hydrogen generation. In contrast to that, studies of active sites for photocatalytical hydrogen generation on $MoS_2$ are scarce.

The effect of mechanically treated $MoS_2$ on diverse potential catalytic applications (HDS, photocatalytic $H_2$ evolution, electrochemical $H_2$ evolution, hydrogenation and isomerization of alkenes) was studied before.[27–33] It was demonstrated that ball milling enhances the catalytic activity by introducing various defects like stacking faults, rotational disorder, distortion, vacancies,

---

[a] J. Djamil, A.-L-. Hansen, S. Permien, Prof. W. Bensch
Institute of Inorganic Chemistry
Christian-Albrechts-Universität zu Kiel
Max-Eyth-Str. 2, 24118 Kiel
E-mail: wbensch@ac.uni-kiel.de
[b] Dr. U. Schürmann, Prof. L. Kienle
Institute for Material Science
Christian-Albrechts-Universität zu Kiel
Kaiserstr. 2, 24143 Kiel
[c] Dr. A. Düvel, Prof. P. Heitjans
Institute of Physical Chemistry and Electrochemistry
Leibniz Universität Hannover
Callinstr. 3-3a, 30167 Hannover
[d] L. Dura, Dr. T. Beweries
Leibniz-Institute for Catalysis
Albert-Einstein-Str. 29a, 18059 Rostock
[e] U. Bauer, I. Niedermaier, C. Papp, H.-P. Steinrück
Physikalische Chemie II
Friedrich-Alexander-Universität Erlangen-Nürnberg
Egerlandstraße 3, 91058 Erlangen

Supporting information for this article is given via a link at the end of the document.

dislocations, grain boundaries and strain. Hence, mechanical high-energy ball milling of bulk material can be used to obtain materials deviating from the equilibrium situation. For introductory accounts of comminution by high-energy ball milling and mechanochemical activation and synthesis see, e.g. [34,35].

In the present work, catalytic properties of $MoS_2$ samples in light driven proton reduction are studied based on their altered structural features achieved by mechanical treatment of bulk $MoS_2$ in a high-energy ball mill. The change of stacking height and slab length as a function of ball-milling time is of particular interest. Thus, further insights towards the identification of active sites in $MoS_2$ for light-driven hydrogen generation are supposed to be uncovered.

## Results and Discussion

In a top down approach bulk $MoS_2$ was mechanically agitated in a high-energy ball mill for 1 (bm1), 2 (bm2), 4 (bm4) and 8 h (bm8). $MoS_2$ is a layered material with only weak van der Waals interactions between the $MoS_2$ slabs (Figure 1). X-ray powder diffraction patterns (XRPD) of ball milled $MoS_2$ samples exhibit the reflections expected for crystalline 2H-$MoS_2$ (Figure 2). In general, the reflections become broader and exhibit less intensity with increasing ball-milling time compared to pristine material. Several reflections show significant alterations of the profile shape indicating structural changes in form of decreased crystallite sizes and the appearance of defects such as turbostratic disorder and stacking faults. The XRD data were analyzed with the Pawley method to extract the evolution of the microstructural properties (Figure S1). While the broadening of the (002) reflection at $2\Theta \approx 14°$ is caused by a decrease of the stacking height (number of stacked $MoS_2$ slabs), alterations of the (100) reflection at $2\Theta \approx 33°$ suggest changes of the slab length (Figure 1). The stacking height decreases more rapidly (for each sample by about 50 %) than the slab length (< 40 %) yielding crystallites with an increasing aspect ratio as identified by the intensity ratio (*h*00)/(00*l*) (Figure 2, Figure S2), which has been reported similarly for mechanically treated $MoS_2$ and graphite samples.[27,36,37] A related example has been Li intercalated $TiS_2$.[38,39]

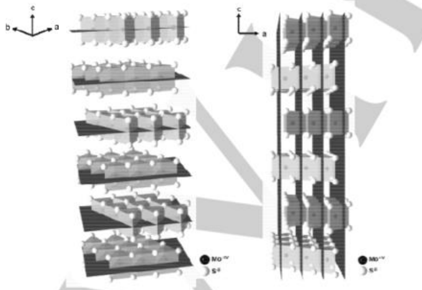

**Figure 1.** (002) and (100) planes in $MoS_2$.

While bm1 and bm2 exhibit comparable aspect ratios close to one, further milling results in gradually thinner particles for bm4 and bm8. Hence, not only the crystallite sizes in general are reduced by mechanical treatment, the shape of $MoS_2$ crystallites is affected as well. The stacking height decreases from 46 (≈ 74 stacked slabs) to 6 nm (≈ 10 stacked slabs) and from 65 to 19 nm for the slab length. Due to the large bond strength difference between the strong covalent in-plane $MoS_2$ bonds and the weaker cross-slab van der Waals interactions, the stacking height is clearly more reduced than the slab length. The increased aspect ratio caused an asymmetric broadening of the reflections. Compared to the crystallite size decrease, turbostratic disorder, bending of the slabs and stacking faults remained minor effects since the density of these defects was too low to significantly affect the reflection profiles. The powder pattern could be well fitted just by refining the asymmetric crystallite shape. Additionally, non-Bragg scattering at low angles appears with increasing milling time (starting at bm2) and is an indication for the presence of uncorrelated $MoS_2$ single layers.[40,41]

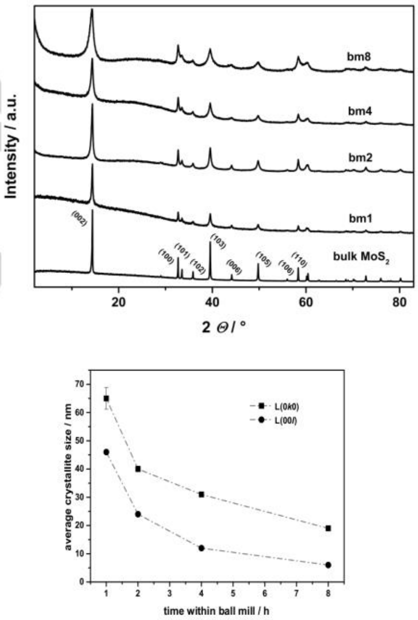

**Figure 2.** XRD powder patterns (top) and crystallite sizes (bottom) of ball milled $MoS_2$.

The specific surface areas were determined by applying the Brunauer-Emmett-Teller (BET) model. The adsorption-desorption isotherms indicate textural porosity for ball milled $MoS_2$ samples (Figure S3). According to IUPAC nomenclature all mechanically treated samples exhibit a type IV isotherm evidencing the presence of a mesoporous system. On the contrary, the isotherm of bulk $MoS_2$ shows hardly any hysteresis implying a non-porous character. The shape of the hysteresis loop of the ball-milled series gives information about the pore structure. The nearly horizontal and parallel evolution of the adsorption and desorption branch (type H3 according to IUPAC nomenclature) is typical for plate-like particles forming aggregates with slit-shaped pores.[42] The treatment in the high-energy ball mill clearly affects the surface area yielding larger specific surface areas compared to the starting material (Figure 3). Thus the values increase from 4 $m^2/g$ for bulk $MoS_2$ to ~ 16 $m^2/g$ for bm1, bm2 and bm4. Interestingly, the specific surface area of bm8 drops to 11 $m^2/g$ which may be attributed to agglomeration of the nanoparticles, i.e. formation of large cluster-like aggregates.[34,43,44]

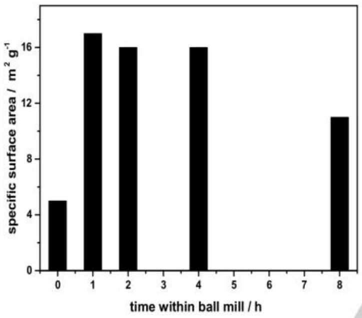

**Figure 3.** Specific surface area of ball milled $MoS_2$ samples.

All samples are characterized by the typical well-stacked lamellar structure of bulk $MoS_2$ with straight and long slabs evidenced by transmission electron microscopy (TEM). The micrographs also show $MoS_2$ layers with high densities of structural defects like bending and splitting of $MoS_2$ slabs which increase with prolonged mechanical treatment (Figure 4). Bending of $MoS_2$ sheets result in the formation of nanoarches with angles up to ~ 130°. These curved slabs possibly provide additional active sites at the top of the arches. Truncation of $MoS_2$ slabs leads to access of more edge sites due to formation of vacancies and sharp edges at tips of $MoS_2$ sheets (cf. Figure S4). In addition to changes of lateral features of $MoS_2$ slabs, properties like the stacking height and stacking sequence are influenced also by mechanical agitation. As already indicated by XRD analysis, $MoS_2$ slabs are cleaved horizontally due to milling. Thus, the presence of few and single layer $MoS_2$ becomes more representative with increasing milling time. Moreover, TEM micrographs of ball milled samples are increasingly characterized by a random layer structure with interleaved sheets and rotational disorder, evidenced by diffuse intensity on concentric circles in selected area electron diffraction (SAED) patterns as well (Figure 4, Figure S5).

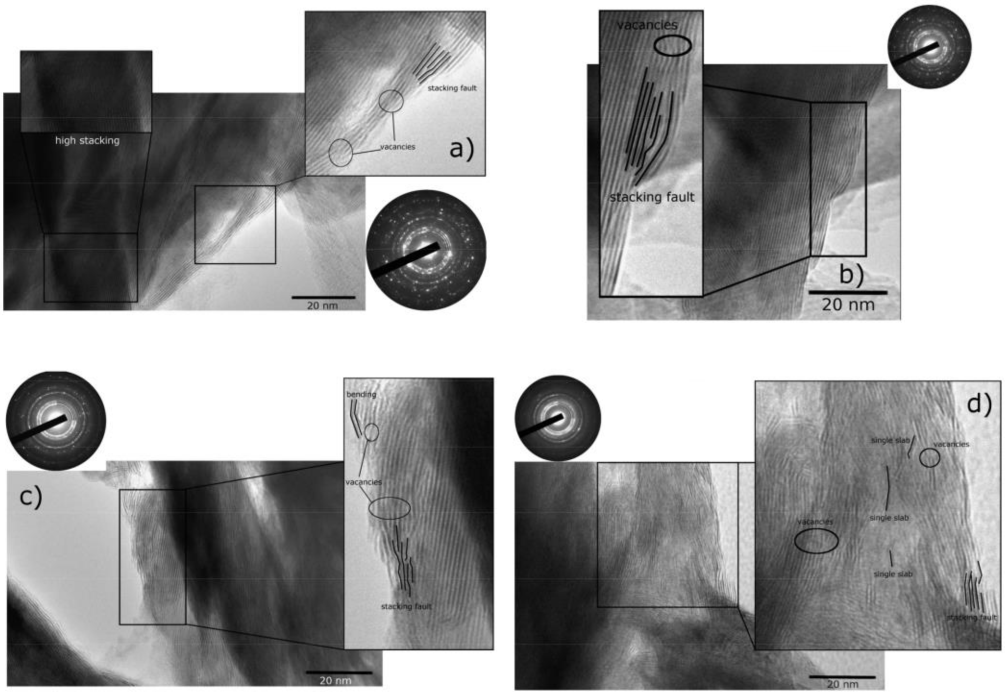

**Figure 4.** TEM micrographs and SAED patterns of a) bm1, b) bm2, c) bm4 and d) bm8.

To exclude surface contaminations during ball milling, exemplary X-ray photoelectron spectra are shown for bm4 in Figure S6. The focus of these studies was on the S 2p and Mo 3d regions to prove the absence of $SO_x$- ($S\ 2p_{3/2} > 164$ eV)[30,45] and $MoO_x$-species (Mo 3d5/2 > 232 eV).[46–48] Indeed, the X-ray photoelectron spectroscopy (XPS) results for S 2p and Mo 3d regions only evidence the presence of Mo and S[46,48,49] with negligible amounts of $SO_x$ and no traces of $MoO_x$.

All samples treated in the ball mill exhibit better photocatalytic performances than the bulk material (Figure 5). The amount of generated hydrogen increases from 12 µmol/g for bulk $MoS_2$ to ~23 µmol/g for bm1 and bm2, respectively. A further increase of the catalytic activity is observed for sample bm4 with a hydrogen generation of 37 µmol/g. Interestingly, the catalytic activity of sample bm8 is slightly lower with 34 µmol/g evolved hydrogen. In general the enhancement of hydrogen production of ball milled samples compared to bulk material can be ascribed to changes in structural properties. During the milling process, the slab length decreases with agitation time leading to an increased number of edge sites and thus an enhancement of active sites. The reduction of the slab length of $MoS_2$ sheets is accompanied by a significant decrease of the stacking height yielding high densities of basal planes. Even newly formed basal planes might enhance hydrogen generation due to fractures of $MoS_2$ sheets, where additional edge-sites are created (Figure 6).[36,50–52]

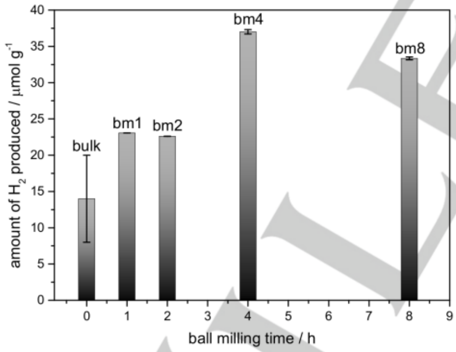

**Figure 5.** Maximum amount of $H_2$ produced during $H_2$ generation experiments with ball milled $MoS_2$ samples relative to the mass of WRC in dependence of ball milling time. For calculation of the amounts of $H_2$ the maximum volume change was determined using the upper limit of the Hill function and a vapour pressure correction of 0.3 mL.[53] Conversion into mol followed Van der Waals with Van der Waals coefficients as reported earlier.[54]

Comparable performances between bm1 and bm2 can be explained by nearly equal specific surface areas and aspect ratios and thus a similar particle shape. The role of the aspect ratio and the morphology of the catalysts has already been investigated in depth and has been found to be a fundamental property for various catalytic applications.[55–61] The pronounced increase of hydrogen evolution observed for bm4 and bm8 may be explained by cracks in the sheets and the shorter $MoS_2$ slabs resulting in more edge sites in both cases. Since the stacking height decreases more rapidly than the slab length, more $MoS_2$ basal planes are present, which most probably are damaged during the ball milling process and hence provide additional edge sites. In addition, the aspect ratio of bm4 and bm8 increased remarkably giving flatter particles compared to bm1 and bm2, which might affect the photocatalytic performance as well. The slight drop of photogenerated hydrogen for bm8 draws the attention to the impact of the specific surface area on HER. The value for bm8 decreases to 11 $m^2$/g which might be the reason for the slight decrease of hydrogen amount. After an initial period of high activity, the hydrogen evolution of all multicomponent catalyst systems ceased within 9-22 h irradiation time. This could be assigned to degradation of the photosensitizer, which was corroborated by a distinct shift of the $[Ru(bpy)_3]^{2+}$ main absorption in the UV-Vis spectra. Furthermore, reactivation of inactive multicomponent catalyst systems could only be achieved by addition of a solution of fresh photosensitizer (Figure S7).

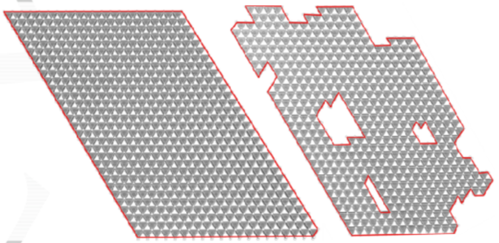

**Figure 6.** Schematic top view of untreated (left) and fractured (right) $MoS_2$ basal planes. The red border marks $MoS_2$ edge sites.

## Conclusions

In summary, nanosized $MoS_2$ was synthesized in a facile approach using a high-energy ball mill. Thereby changes of structural features were monitored. Both stacking height and slab length decreased with comminution time. In doing so, the stacking height is reduced more rapidly than the slab length, resulting in increasing aspect ratios and hence in flatter particles. These structural alterations are accompanied by increasing number of edge sites either due to shortened slabs, cleavage of $MoS_2$ stacks and cracked basal planes. In addition, the specific surface area of $MoS_2$ samples grows from bulk $MoS_2$ to bm4 as a function of milling time, but drops significantly for bm8 due to agglomeration effects. These mentioned properties caused by mechanical treatment of bulk $MoS_2$ are reflected in the photocatalytic performance. All ball milled samples exceed pristine $MoS_2$ in the amount of generated hydrogen. This behaviour is most probably caused by reduction of the particle size in general which is accompanied with high densities of exposed edge sites combined with increasing specific surface areas. Thereby comparable results were achieved with bm1 and bm2 since similar aspect ratios and specific surface areas were obtained for these two samples. Further enhancement of photocatalytic properties were observed for bm4 and bm8 due to high densities of edge sites. Moreover the aspect ratio increased with comminution time giving flatter particles which is probably favourable for hydrogen evolution. The slight decrease of produced hydrogen for bm8 compared to bm4 might be explained by the significant drop of specific surface area for bm8. Hence, the importance of structural features namely particle size, aspect ratio, exposed edge sites and specific surface area in $MoS_2$ catalyst was illustrated in this work.

## Experimental Section

Bulk $MoS_2$ (1 g / batch) from Sigma Aldrich (> 99 %) was treated in a high-energy ball shaker mill (Spex 8000M)[62], using a corundum vial and a single ball(3.6 g) under argon atmosphere. The comminution procedure yielded samples with different crystallite sizes controlled by the milling times: 1, 2, 4, 8 h.

Activation treatments of $MoS_2$ catalysts at elevated temperatures under different conditions have been established for enhanced catalytic activity.[29,30,63] Therefore, all mechanically treated samples (0.5 g / batch) were tempered for one hour at 150 ℃ in $N_2$ flow. The relatively moderate temperature was chosen in order to retain the essential structural properties obtained by the mechanical treatment. Therefore, the photocatalytic properties of $MoS_2$ samples are only related to variations in structural features.

Light driven $H_2$ evolution experiments: All reactions were carried out in a double-walled thermostatically controlled reaction vessel using an automatically operating burette (MesSen Nord GmbH, Stäbelow, Germany) which was described previously.[64] Triethylamine and acetonitrile were dried over $CaH_2$ and distilled under argon. Furthermore all liquids were degassed by ultrasound treatment for at least 15 min prior to use. $[Ru(bpy)_3](PF_6)_2$ was synthesised as describe previously.[65] In a standard procedure 10 mL of a $10^{-3}$M solution of $[Ru(bpy)_3](PF_6)_2$ in acetonitrile, 8 mL trimethylamine and 3 mL distilled water were transferred via syringe into the air- and moisture-free glass reaction vessel which contained 10 mg of a ball milled $MoS_2$ sample. After equilibration, the freshly assembled multicomponent catalyst system was irradiated with visible light at isothermic conditions for both liquid and gaseous phase at 298.15 K. As light source a 300 W Xe lamp along with a 420 nm cut-off filter was used. At the end of the reaction a gas sample was taken and analysed by GC. X-ray powder diffraction data for $MoS_2$ were collected on a STOE Stadi X-ray diffractometer (monochromatic Cu $K\alpha$ radiation, $\lambda_1$ = 1.54056 Å, MYTHEN detector). Data was collected in transmission geometry using 0.1 mm glass capillaries from 5 to 85ϒ2$\Theta$ in steps of 3° with an effective scan time of 120 s pe r step. Structural elaboration were carried out by Pawley refinement using the program TOPAS Academic.[66] A Thomson-Cox-Hastings profile function was determined using the $LaB_6$ NIST (660a) Standard, which was measured using the same setup as described previously. The NIST standard has a neglectable size and strain contribution to the diffraction profile and therefore was used to substract the instrumental profile. This approach allows extraction of crystallite sizes and strain. The crystallite size is given as the volume weighted mean column height based on integral breadth (DV) and the strain parameter *e*, both according to Balzar, 2004.[67] We used an approach by A. Coelho (*anisotropic hkl*) to correct the peak broadening caused by highly anisotropic crystallite shape.[68]. This macro allowed the determination of crystallite size perpendicular to certain (*hkl*) and consequently the calculation of the aspect ratio.

Specific surface areas were determined with nitrogen sorption measurements (BEL Sorp max) at 77 K applying the BET model. HRTEM micrographs were recorded with a JEM-2100 (JEOL, 200 kV, $LaB_6$, Cs = 1.0 mm). XPS spectra were measured with monochromatized Al $K_\alpha$ radiation (1486.6 eV) using an Omicron instrument (Argus electron analyser with a MCD (128 channels) and a XM 1000 X-ray tube). The spectra were collected with an energy resolution of 0.40 eV (35 eV pass energy) at normal emission. Base pressure was $1 \cdot 10^{-10}$ mbar during measurements, which were performed at RT. To compensate for sample charging an electron flood gun (Omicron CN 10) was used with 2 µA emission, 4 eV beam energy and 10 V extractor voltage. The powder samples were prepared on double-sided taping and conducting polycarbonate/graphite slices (Plano G3347).

## Acknowledgements

The authors thank J. Timm for the nitrogen adsorption measurements and the State of Schleswig-Holstein for the financial support.

**Keywords:** Heterogeneous Catalysis • Layered Compounds • Nanoparticles • High-Energy Ball Milling • Photocatalysis

[1] F. R. Pazheri, M. F. Othman, N. H. Malik, *Renew. Sustain. Energy Rev.* **2014**, *31*, 835–845.
[2] X. Ling, W. Fang, Y.-H. Lee, P. T. Araujo, X. Zhang, J. F. Rodriguez-Nieva, Y. Lin, J. Zhang, J. Kong, M. S. Dresselhaus, *Nano Lett.* **2014**, *14*, 3033–3040.
[3] X. B. Chen, S. H. Shen, L. J. Guo, S. S. Mao, *Chem. Rev.* **2010**, *110*, 6503–6570.
[4] K. Maeda, K. Domen, *J. Phys. Chem. C* **2007**, *111*, 7851–7861.
[5] F. E. Osterloh, *Chem. Mater.* **2008**, *20*, 35–54.
[6] A. Kudo, Y. Miseki, *Chem. Soc. Rev.* **2009**, *38*, 253–278.
[7] F. Fresno, R. Portela, S. Suarez, J. M. Coronado, *J. Mater. Chem. A* **2014**, *2*, 2863–2884.
[8] T. Hisatomi, J. Kubota, K. Domen, *Chem Soc Rev* **2014**, *43*, 7520–7535.
[9] K. Zhang, L. Guo, *Catal. Sci. Technol.* **2013**, *3*, 1672–1690.
[10] Y. Min, G. He, Q. Xu, Y. Chen, *J. Mater. Chem. A* **2014**, *2*, 2578–2584.
[11] Y. Y. Gurevich, Y. V. Pleskov, *Semicond. Semimet.* **1983**, *19*, 255–328.
[12] R. Coehoorn, C. Haas, R. A. Degroot, *Phys. Rev. B* **1987**, *35*, 6203–6206.
[13] W. Ho, J. C. Yu, J. Lin, J. Yu, P. Li, *Langmuir* **2004**, *20*, 5865–5869.
[14] D. Merki, X. Hu, *Energy Environ. Sci.* **2011**.
[15] Y. F. Zhao, Y. X. Zhang, Z. Y. Yang, Y. M. Yan, K. N. Sun, *Sci. Technol. Adv. Mater.* **2013**, *14*, DOI 10.1088/1468-6996/14/4/043501.
[16] C. N. R. Rao, K. Gopalakrishnan, U. Maitra, *ACS Appl. Mater. Interfaces* **2015**, *7*, 7809–7832.
[17] J. Djamil, S. A. Segler, A. Dabrowski, W. Bensch, A. Lotnyk, U. Schurmann, L. Kienle, S. Hansen, T. Beweries, *Dalton Trans.* **2013**, *42*, 1287–1292.
[18] M. Daage, R. R. Chianelli, *J. Catal.* **1994**, *149*, 414–427.
[19] P. Raybaud, J. Hafner, G. Kresse, H. Toulhoat, *Surf. Sci.* **1998**, *407*, 237–250.
[20] P. Raybaud, J. Hafner, G. Kresse, S. Kasztelan, H. Toulhoat, *J. Catal.* **2000**, *189*, 129–146.

[21] M. V. Bollinger, K. W. Jacobsen, J. K. Nørskov, *Phys. Rev. B* **2003**, *67*, 085410.

[22] C. Tsai, F. Abild-Pedersen, J. K. Nørskov, *Nano Lett.* **2014**, *14*, 1381–1387.

[23] T. F. Jaramillo, K. P. Jorgensen, J. Bonde, J. H. Nielsen, S. Horch, I. Chorkendorff, *Science* **2007**, *317*, 100–102.

[24] H. G. S. Casalongue, J. D. Benck, C. Tsai, R. K. B. Karlsson, S. Kaya, M. L. Ng, L. G. M. Pettersson, F. Abild-Pedersen, J. K. Nørskov, H. Ogasawara, et al., *J. Phys. Chem. C* **2014**, *118*, 29252–29259.

[25] H. Wang, C. Tsai, D. Kong, K. Chan, F. Abild-Pedersen, J. K. Nørskov, Y. Cui, *Nano Res.* **2015**, *8*, 566–575.

[26] D. Y. Chung, S.-K. Park, Y.-H. Chung, S.-H. Yu, D.-H. Lim, N. Jung, H. C. Ham, H.-Y. Park, Y. Piao, S. J. Yoo, et al., *Nanoscale* **2014**, *6*, 2131–2136.

[27] Y. Kuriki, K. Uchida, E. Sekreta, S. Ohshima, M. Yumura, F. Ikazaki, *Fuel Process. Technol.* **1999**, *59*, 189–200.

[28] M. Kouzu, K. Uchida, Y. Kuriki, F. Ikazaki, *Appl. Catal. Gen.* **2004**, *276*, 241–249.

[29] M. Polyakov, S. Indris, S. Schwamborn, A. Mazheika, M. Poisot, L. Kienle, W. Bensch, M. Muhler, W. Grünert, *J. Catal.* **2008**, *260*, 236–244.

[30] M. Polyakov, M. W. E. van den Berg, T. Hanft, M. Poisot, W. Bensch, M. Muhler, W. Grünert, *J. Catal.* **2008**, *256*, 126–136.

[31] D. Wang, Z. Wang, C. Wang, P. Zhou, Z. Wu, Z. Liu, *Electrochem. Commun.* **2013**, *34*, 219–222.

[32] Y. Zhu, Q. Ling, Y. Liu, H. Wang, Y. Zhu, *Phys. Chem. Chem. Phys.* **2014**, *17*, 933–940.

[33] A. Ambrosi, X. Chia, Z. Sofer, M. Pumera, *Electrochem. Commun.* **2015**, *54*, 36–40.

[34] P. Heitjans, S. Indris, *J. Phys. Condens. Matter* **2003**, *15*, R1257.

[35] V. Šepelák, A. Düvel, M. Wilkening, K.-D. Becker, P. Heitjans, *Chem. Soc. Rev.* **2013**, *42*, 7507–7520.

[36] A. Milev, M. Wilson, G. S. K. Kannangara, N. Tran, *Mater. Chem. Phys.* **2008**, *111*, 346–350.

[37] M. Antisari, A. Montone, N. Jovic, E. Piscopiello, C. Alvani, L. Pilloni, *Scr. Mater.* **2006**, *55*, 1047–1050.

[38] R. Winter, P. Heitjans, *J. Phys. Chem. B* **2001**, *105*, 6108–6115.

[39] R. Winter, P. Heitjans, *J. Non-Cryst. Solids* **2001**, *293–295*, 19–24.

[40] P. Joensen, R. F. Frindt, S. R. Morrison, *Mater. Res. Bull.* **1986**, *21*, 457–461.

[41] R. R. Chianelli, E. B. Prestridge, T. A. Pecoraro, J. P. Deneufville, *Science* **1979**, *203*, 1105–1107.

[42] K. S. W. Sing, D. H. Everett, R. A. W. Haul, L. Moscou, R. A. Pierotti, J. Rouquerol, T. Siemieniewska, *Pure Appl. Chem.* **1985**, *57*, 603–619.

[43] T. Xing, L. H. Li, L. Hou, X. Hu, S. Zhou, R. Peter, M. Petravic, Y. Chen, *Carbon* **2013**, *57*, 515–519.

[44] M. Francke, H. Hermann, R. Wenzel, G. Seifert, K. Wetzig, *Carbon* **2005**, *43*, 1204–1212.

[45] C. Papp, H.-P. Steinrück, *Surf. Sci. Rep.* **2013**, *68*, 446–487.

[46] D. Ganta, S. Sinha, R. T. Haasch, *Surf. Sci. Spectra* **2014**, *21*, 19–27.

[47] T. Weber, J. C. Muijsers, H. J. M. C. vanWolput, C. P. J. Verhagen, J. W. Niemantsverdriet, *J. Phys. Chem.* **1996**, *100*, 14144–14150.

[48] H. W. Wang, P. Skeldon, G. E. Thompson, *Surf. Coat. Technol.* **1997**, *91*, 200–207.

[49] S. Mattila, J. A. Leiro, M. Heinonen, T. Laiho, *Surf. Sci.* **2006**, *600*, 5168–5175.

[50] J. Xie, H. Zhang, S. Li, R. Wang, X. Sun, M. Zhou, J. Zhou, X. W. (David) Lou, Y. Xie, *Adv. Mater.* **2013**, *25*, 5807–5813.

[51] S. M. Tan, A. Ambrosi, Z. Sofer, Š. Huber, D. Sedmidubský, M. Pumera, *Chem. – Eur. J.* **2015**, *21*, 7170–7178.

[52] X. Yue, H. Wang, S. Wang, F. Zhang, R. Zhang, *J. Alloys Compd.* **2010**, *505*, 286–290.

[53] The correction value was obtained via reference measurements without PS and WRC.

[54] F. Gärtner, A. Boddien, E. Barsch, K. Fumino, S. Losse, H. Junge, D. Hollmann, A. Brückner, R. Ludwig, M. Beller, *Chem. – Eur. J.* **2011**, *17*, 6425–6436.

[55] K. Hu, X. Hu, Y. Xu, X. Pan, *React. Kinet. Mech. Catal.* **2010**, *100*, 153–163.

[56] A. R. Tao, S. Habas, P. Yang, *Small* **2008**, *4*, 310–325.

[57] J. Chen, B. Lim, E. P. Lee, Y. Xia, *Nano Today* **2009**, *4*, 81–95.

[58] S. Cheong, J. D. Watt, R. D. Tilley, *Nanoscale* **2010**, *2*, 2045–2053.

[59] T. R. Gordon, M. Cargnello, T. Paik, F. Mangolini, R. T. Weber, P. Fornasiero, C. B. Murray, *J. Am. Chem. Soc.* **2012**, *134*, 6751–6761.

[60] Z. R. Tian, J. A. Voigt, J. Liu, B. Mckenzie, M. J. Mcdermott, M. A. Rodriguez, H. Konishi, H. Xu, *Nat. Mater.* **2003**, *2*, 821–826.

[61] Y. Li, T. Bian, J. Du, Y. Xiong, F. Zhan, H. Zhang, D. Yang, *CrystEngComm* **2014**, *16*, 8340–8343.

[62]http://www.spexsampleprep.com/knowledgebase/resources/applications_notes/SP003.pdf

[63] Z. D. Huang, W. Bensch, L. Kienle, S. Fuentes, G. Alonso, C. Ornelas, *Catal. Lett.* **2008**, *122*, 57–67.

[64] T. Beweries, J. Thomas, M. Klahn, A. Schulz, D. Heller, U. Rosenthal, *ChemCatChem* **2011**, *3*, 1865–1868.

[65] J. A. Broomhead, C. G. Young, P. Hood, in *Inorg. Synth.* (Ed.: R.J. Angelici), John Wiley & Sons, Inc., **1990**, pp. 338–340.

[66] A. A. Coelho, *TOPAS-Academic*, Coelho Software, Brisbane, **n.d.**

[67] D. Balzar, N. Audebrand, M. R. Daymond, A. Fitch, A. Hewat, J. I. Langford, A. Le Bail, D. Louër, O. Masson, C. N. McCowan, et al., *J. Appl. Crystallogr.* **2004**, *37*, 911–924.

[68] J. S. O. Evans, *Mater. Sci. Forum* **2010**, *651*, 1–9.

## The effect of particle size and aspect ratio of molybdenum sulfide on visible light-driven hydrogen generation

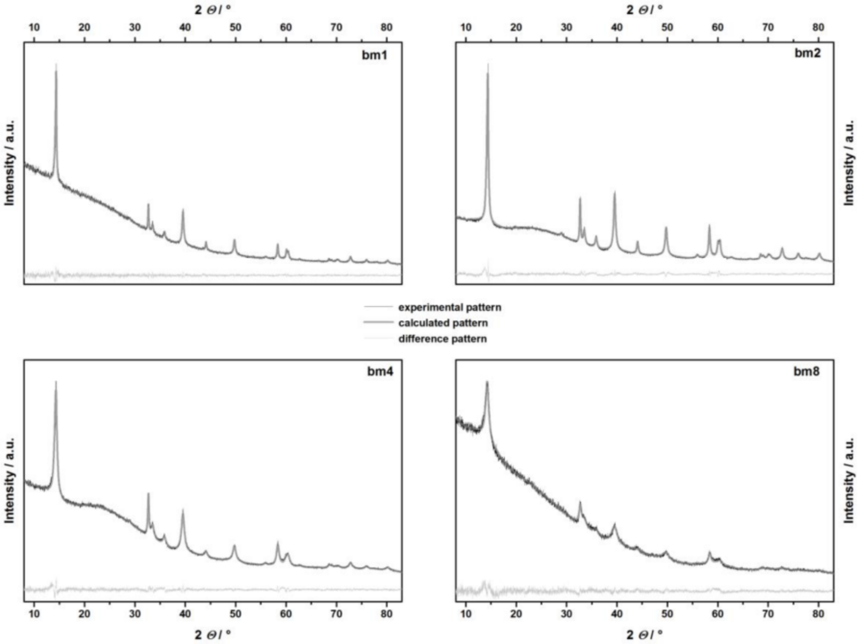

**Figure S1.** XRD powder patterns of ball milled $MoS_2$ samples including Pawley fits.

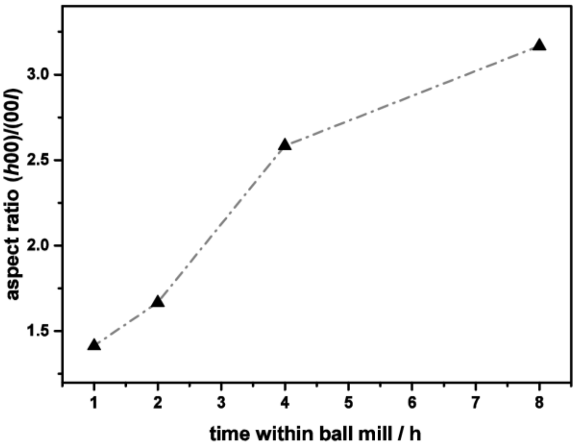

**Figure S2.** Aspect ratio of ball milled $MoS_2$ samples.

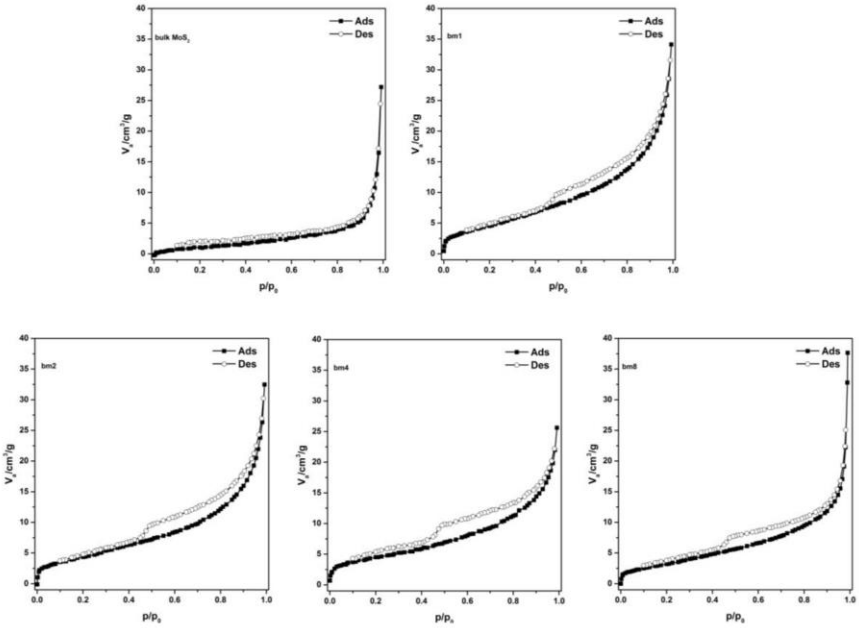

**Figure S3.** Adsorption-desorption isotherms of ball milled $MoS_2$ samples and of bulk $MoS_2$.

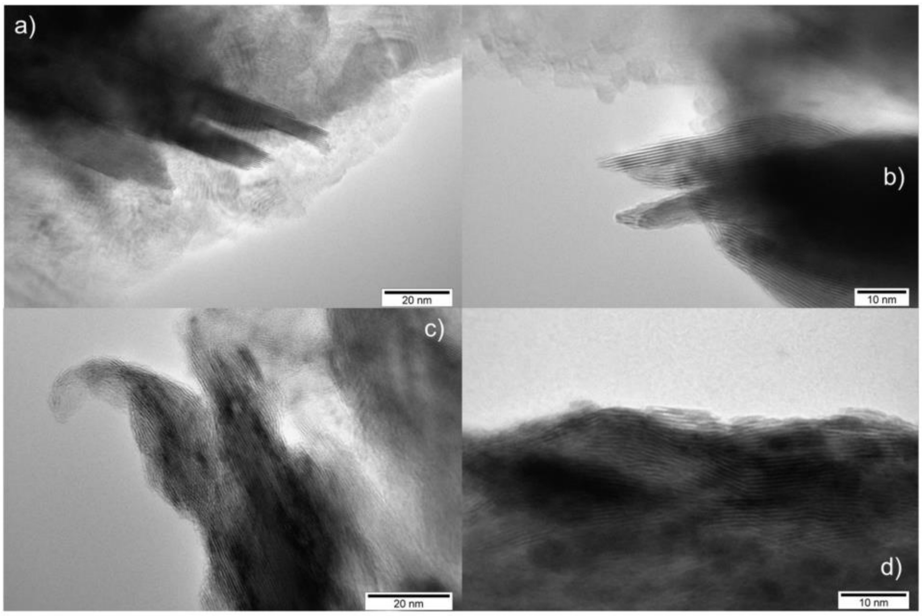

**Figure S 4.** TEM micrographs of a) bm1, b) bm2, c) bm4 and d) bm8.

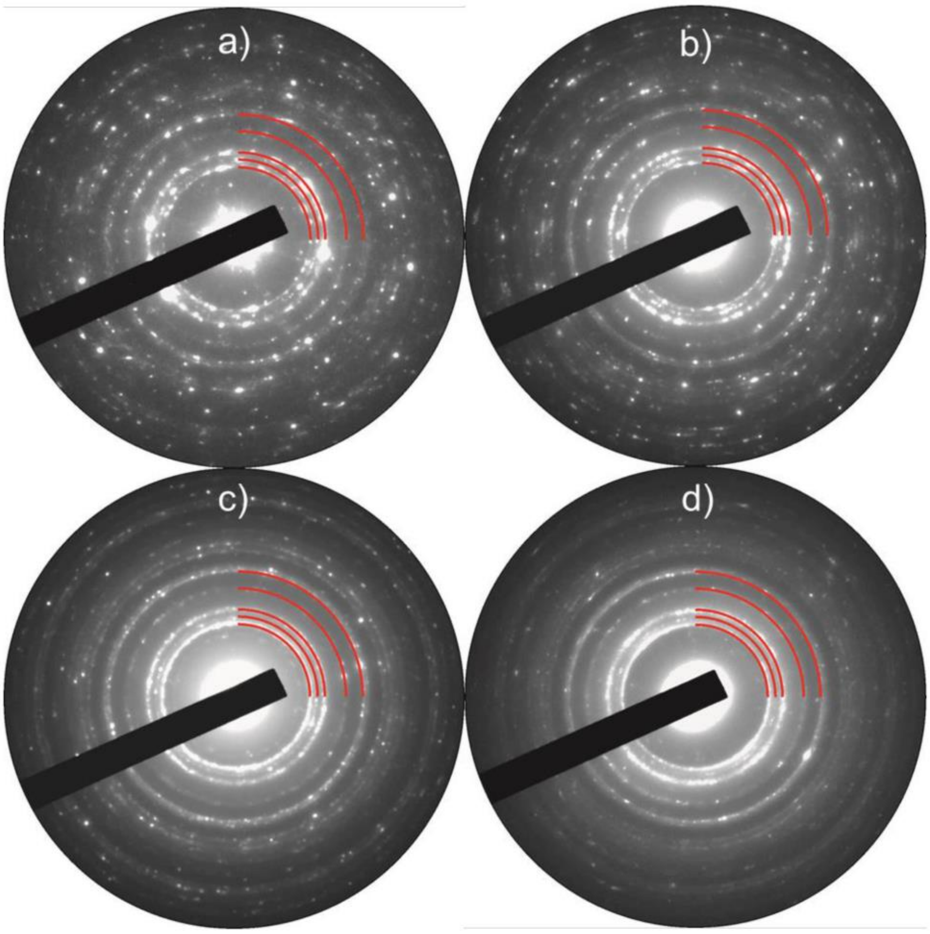

**Figure S 5.** SAED patterns of a) bm1, b) bm2, c) bm4 and d) bm8. The red quarter-circles represents the lattice planes (100), (102), (103) and (105) from inside to outside.

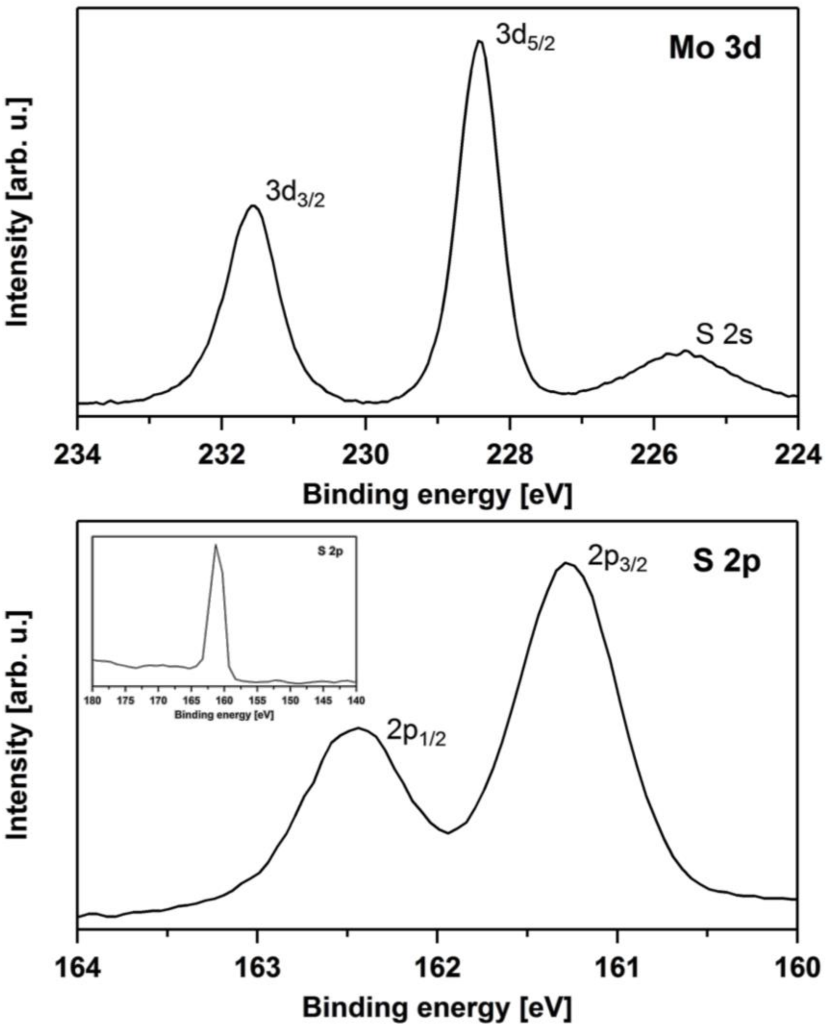

**Figure S 6.** High resolution XP spectra, measured with monochromatized Al-K$\alpha$ radiation of the ball-milled sample bm4. The Mo 3d spectra show the spin-orbit split $3d_{5/2}$ and $3d_{3/2}$ components of $MoS_2$ at 228.4 and 231.6 eV, respectively, at an intensity ratio of 3:2, with no sign of $MoO_x$ species (Mo $3d_{5/2}$ > 232 eV). The S 2p spectra show the spin-orbit split $2p_{3/2}$ and $2p_{1/2}$ components of $MoS_2$ at 161.3 and 162.5 eV, respectively, at an intensity ratio of 2:1, with no significant contribution (<2%) from $SO_x$ species (S $2p_{3/2}$ > 164 eV; see also spectrum with lower resolution as inset).

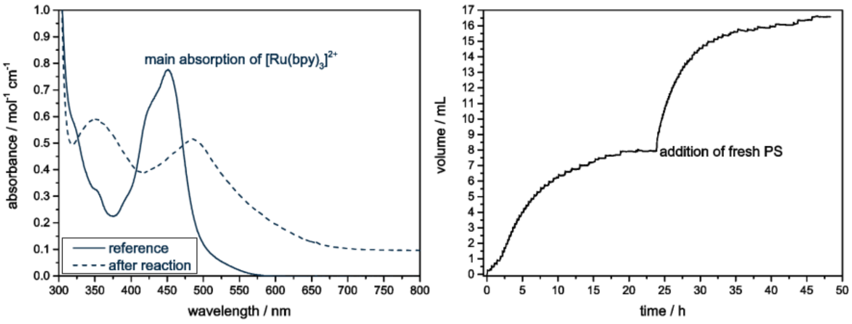

**Figure S 7.** Left: UV-Vis spectra of $[Ru(bpy)_3]^{2+}$ after the photocatalytic reaction (dashed line) and for the purpose of comparison reference spectrum (continuous). Right: Volumetric trace of the photocatalytic hydrogen evolution reaction from a mixture containing triethylamine (8 mL), water (3 mL) and $[Ru(bpy)_3](PF_6)_2$ (1 mM) in acetonitrile (10 mL). Reactivation of inactive multicomponent catalysts system was achieved by addition of fresh photosensitizer.

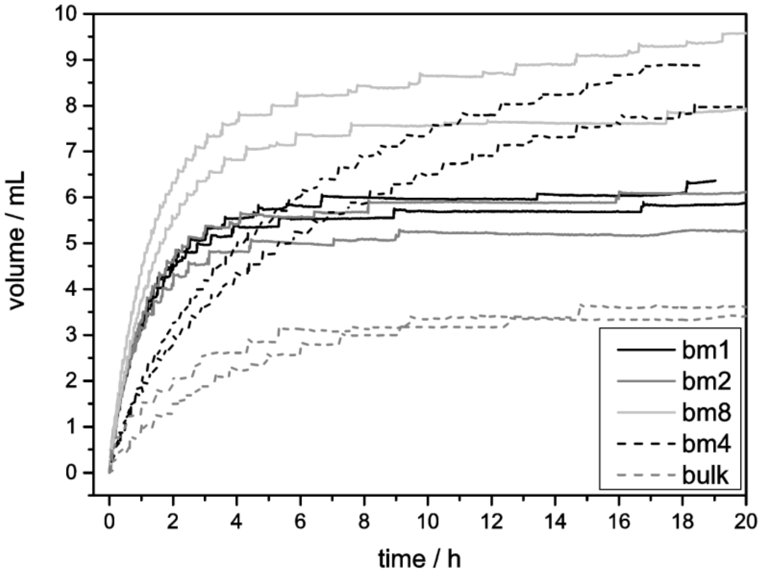

**Figure S 8.** Original volumetric curves from the hydrogen evolution experiments. Two batches were measured per ball milled $MoS_2$ sample showing a reproducibility of ±1 mL.

### 4.1.4 Die thermische Zersetzung von $(NH_4)_2MoS_4$ zu $MoS_y$

Der Einfluss der Zersetzungsatmosphäre und der -temperatur auf die Produkte des thermischen Abbaus von $(NH_4)_2MoS_4$ wurde untersucht. Dieses Manuskript befindet sich noch in der Vorbereitung, so dass im Folgenden nur die wesentlichen Ergebnisse vorgestellt werden.

Die thermische Zersetzung von $(NH_4)_2MoS_4$ erfolgte bei unterschiedlichen Temperaturen (T = 200, 250, 350, 550, 700, 850 °C) in einem $H_2/N_2$- bzw. $N_2$-Gasstrom. Während die thermische Behandlung von $(NH_4)_2MoS_4$ in $H_2/N_2$ unabhängig von der Zersetzungstemperatur ein Mo:S-Verhältnis von etwa 1:2 ergibt, führt der Abbau in $N_2$ bis T = 350 °C zu einem Mo:S-Verhältnis von etwa 1:3 und erst ab T = 550 °C wird ein Mo:S-Verhältnis von etwa 1:2 erhalten (Abb. 26). Die Resonanz-Ramanspektren der beiden Probenserien belegen den Einfluss der Zersetzungstemperatur und –atmosphäre auf die Produktbildung (Abb. 26). Die Anwesenheit der $E^1_{2g}$-und $A_{1g}$-Bande ab T = 250 °C in der $H_2/N_2$-Probenserie deuten auf die Bildung von $MoS_2$ hin und die schmalen Signale mit hoher Intensität sind typisch für kristallines Material. Mit zunehmender Temperatur nehmen die Halbwertsbreite ab und die Peakintensität zu. Bei der $N_2$-Serie setzt die $MoS_2$-Bildung ab T = 350 °C ein. Auch in dieser Probenreihe nehmen in den Ramanspektren die Halbwertsbreiten der Signale ab und die Peakintensitäten mit steigender Temperatur zu. Die Pulverdiffraktogramme der Zersetzungsprodukte sind von breiten Beugungsreflexen mit geringer Intensität gekennzeichnet, was auf $MoS_2$-Nanopartikel schließen lässt (Abb. 26). Zusätzlich weisen die Profilform und die Abwesenheit einiger Reflexe auf Stapelfehler bzw. Verdrehung der Schichten gegeneinander hin. Eine Erhöhung der Zersetzungstemperatur bewirkt in beiden Probenserien eine Intensitätszunahme der Reflexe und Abnahme der Reflexbreite. D.h., die Kristallinität von $MoS_2$ nimmt mit steigender Temperatur zu. Trotzdem liegen auch bei den bei höheren Temperaturen zersetzten $MoS_y$-Proben Fehlordnungen (turbostratische Fehlordnung, keine gleichmäßige Schichtabfolge) vor. Der Einfluss der Zersetzungsatmosphäre auf die Eigenschaften der Produkte wird bei der Analyse der Pulverdiffraktogramme sichtbar. Zum einen weisen die Proben der $H_2/N_2$-Reihe bei vergleichbaren Temperaturen eine höhere Kristallinität als die Proben der $N_2$-Reihe auf. Zum anderen treten in der $H_2/N_2$-Probenreihe bei T = 850 °C neben den $MoS_2$-Reflexen auch zusätzliche Reflexe auf, die auf elementares Molybdän schließen lassen. Die Charakterisierung der Proben mit XPS und mit

Zielmoleküladsorption/-desorption soll Aufschluss über den Einfluss der Zersetzungstemperatur und der -atmosphäre auf die Mo- und S-Spezies sowie der Oberflächenbeschaffenheit geben. Die fotokatalytischen Experimente für die lichtgetriebene $H_2$-Entwicklung stehen noch aus.

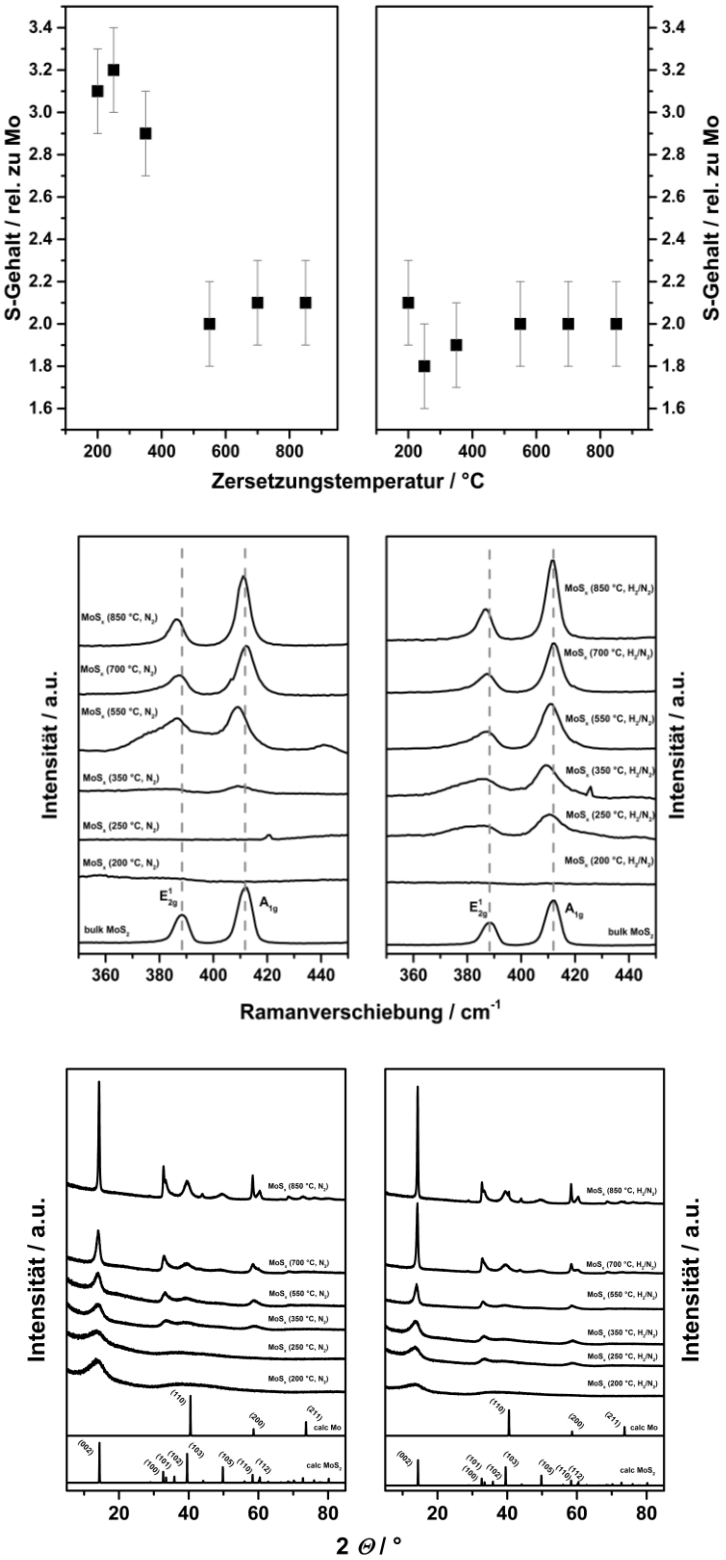

**Abb. 26: S-Gehalt (oben), Resonanz-Ramanspektren (mitte) und XRD-Pulverdiffraktogramme (unten) der thermischen Abbauprodukte $MoS_y$ in $N_2$ (links) und $H_2/N_2$ (rechts).**

### 4.1.5 Raumtemperatursynthese eines amorphen Komposites basierend auf $MoS_2$, welches über N-Donor Liganden stabilisert wird und seine Eigenschaften für die fotokatalytische $H_2$-Entwicklung

Zusammenfassung der Veröffentlichung „Room temperature synthesis of an amorphous $MoS_2$ based composite stabilzed by N-donor ligands and its photocatalytic hydrogen production“. Dieser Artikel wurde in „RSC Advances“ (DOI: 10.1039/c5ra14438h) 2015 publiziert.

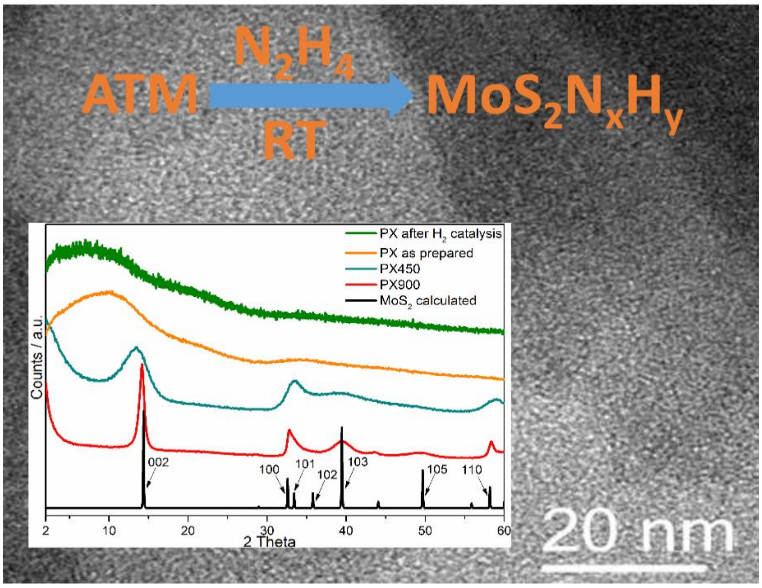

**Abb. 27: Analytische Ergebnisse (XRD und TEM) und Reaktionsschema von PX.**

Gegenstand dieser Veröffentlichung ist die neue und einfache Synthese eines amorphen Molybdänsulfids (PX) bei Raumtemperatur. Die Herstellung von PX erfolgte über die Reaktion von $(NH_4)_2MoS_4$ in Anwesenheit von gasförmigem Hydrazin in einem Exsikkator. Die Abwesenheit von Beugungsreflexen im XRD, von $MoS_2$-Schichten in TEM-Bildern und der prominenten Ramanbanden $E^1_{2g}$ und $A_{1g}$ belegen eindeutig den amorphen Charakter des Molybdänsulfids. Die Bildung von amorphen $MoS_3$ konnte über die Elementaranalyse (Mo:S–Verhältnis von etwa 1:2) und darüber hinaus mit Hilfe von XPS-Untersuchungen (charakteristische Form der S 2p Peaks in $MoS_3$) ausgeschlossen werden. Die Ergebnisse der Elementaranalyse belegen die Anwesenheit von Stickstoff, so dass die Mo–Atome sowohl von S- als auch von N-Atomen (end-on verbrückend und side-on koordiniertes Hydrazin und $NH_3$) umgeben sind. Diese Vermutung wurde mit XPS-, NMR-, und IR-Messungen bestätigt. Während in der S 2p Region lediglich eine S-Spezies vorliegt, besteht das

Mo 3d Signal aus drei Mo-Spezies in unterschiedlicher chemischer Umgebung. Die Bindungsenergiedifferenz zwischen der intensivsten Mo $3d_{5/2}$ Komponente und dem S $2p_{3/2}$ Signal beträgt 67 eV und kann als Indiz für die Bildung von $MoS_2$ betrachtet werden. In Ergänzung zu den verbleidenden zwei Mo-Spezies wurden in der N 1s Region zwei N-Spezies (verbrückendes Hydrazin und side-on koordiniertes Hydrazin oder $NH_3$) gefunden. Daraus kann geschlossen werden, dass 3 verschiedene Mo-Atome in PX vorliegen: nur von Schwefel koordiniert, zusätzlich von verbrückendem Hydrazin oder side-on von Hydrazin und $NH_3$ koordiniert. Die Anwesenheit von Hydrazin und $NH_3$ wurde mit Hilfe der NMR-Spektroskopie ($^1H$ und $^{15}N$ NMR) bestätigt. In weiteren Experimenten wurde der Kristallisationsprozess von PX untersucht. Die Kristallisation wurde sowohl thermisch als auch *in situ* durch Bestrahlung mit dem Elektronenstrahl im TEM initiiert. Sowohl aus den XRD- (charakteristische $MoS_2$-Beugungsreflexe) als auch aus den TEM-Untersuchungen ($MoS_2$-Schichten) ist die Bildung von $MoS_2$ erkennbar. Erstaunlich ist die thermische Stabilität von PX, da erst ab ca. 350 °C die Bildung von $MoS_2$-Kristalliten einsetzt. Die Kristallinität nimmt erwartungsgemäß mit zunehmender Temperatur bzw. zunehmender Verweilzeit im Elektronenstrahl zu. Alle Proben wurden hinsichtlich der fotokatalytischen $H_2$-Entwicklung untersucht und alle weisen eine höhere Aktivität als $MoS_2$-Volumenmaterial auf. Die Aktivität nimmt dabei mit zunehmender Kristallinität ab und ist bei PX am höchsten (etwa das Dreifache). Diese Beobachtung legt den Schluss nahe, dass sich der amorphe Charakter von PX mit Mo-Atomen in S- und N-Umgebung positiv auf die lichtgetriebene $H_2$-Generierung auswirkt.

F. Niefind, J. Djamil, W. Bensch, B. R. Srinivasan, I. Sinev, W. Grünert, M. Deng, L. Kienle, A. Lotnyk, M. B. Mesch, J. Senker, L. Dura, T. Beweries, *RSC Advances*, **2015**, *5*, 67742-67751. - Reproduziert mit der Erlaubnis der Royal Society of Chemistry.

RSC Advances

PAPER

View Article Online
View Journal | View Issue

Cite this: *RSC Adv.*, 2015, **5**, 67742

# Room temperature synthesis of an amorphous $MoS_2$ based composite stabilized by N-donor ligands and its light-driven photocatalytic hydrogen production†

Felix Niefind,[a] John Djamil,[a] Wolfgang Bensch,*[a] Bikshandarkoil R. Srinivasan,[b] Ilya Sinev,[c] Wolfgang Grünert,[c] Mao Deng,[d] Lorenz Kienle,[d] Andriy Lotnyk,[e] Maria B. Mesch,[f] Jürgen Senker,[f] Laura Dura[g] and Torsten Beweries[g]

Herein an entirely new and simple room temperature synthesis of an amorphous molybdenum sulfide stabilized by complexing ammonia and hydrazine is reported. The resulting material exhibits an outstanding activity for the photocatalytic hydrogen evolution driven by visible light. It is chemically stable during the reaction conditions of the photocatalysis and shows unusual thermal stability up to 350 °C without crystallization. The new material is obtained by a reaction of solid ammonium tetrathiomolybdate and gaseous hydrazine. In the as-prepared state Mo atoms are surrounded by $\mu_2$-briding $S^{2-}$, $NH_3$ and hydrazine, the latter being coordinated to Mo(IV) in a bridging or side-on mode. Heating at 450 °C or irradiation with an electron beam generates nanosized crystalline $MoS_2$ slabs. The two modes for crystallization are characterized by distinct mechanisms for crystal growth. The stacking of the slabs is low and the material exhibits a pronounced turbostratic disorder. Heat treatment at 900 °C yields more ordered $MoS_2$ but structural disorder is still present. The visible-light driven hydrogen evolution experiments evidence an outstanding performance of the as-prepared sample. The materials were thoroughly characterized by optical spectroscopy, chemical analysis, *in situ* HRTEM, XRD, $^1H$ and $^{15}N$ solid-state NMR, XPS, and thermal analysis.

Received 14th July 2015
Accepted 27th July 2015

DOI: 10.1039/c5ra14438h

www.rsc.org/advances

## 1. Introduction

Since the world's population keeps on growing, forecasted to reach the 9.5 billion mark around the middle of the century, the most pressing challenge of our time is the sufficient supply of clean energy. The use of fossil fuels is reaching its limit due to the harmful effect of combustion products upon the environment, which is shifting the focus of research towards renewable energy sources like solar or wind energy.[1,2] Hydrogen generated by sunlight is widely discussed as a clean energy source which generates only water as exhaust. Since solar light is accessible in most regions on the planet the photocatalytic hydrogen production[3–5] or the photoelectrochemical hydrogen evolution[6–10] reaction are considered to be promising approaches. The best electrocatalysts for the hydrogen evolution reaction (HER) are platinum group metals which unfortunately are rare and expensive. Hence, these metals are not suitable for large scale applications and therefore intense research is going on worldwide to identify materials, which can replace these precious metals.

Molybdenum sulfide ($MoS_2$) has been intensely studied as possible catalysts for HER since the 1970s, most notably as nanocrystalline $MoS_2$.[11–14] Besides application of nanocrystalline $MoS_2$ as electrocatalyst or for photoelectrochemical application in HER,[15–17] particular interest has been devoted to the visible-light driven hydrogen production.[18–21] In the last few years amorphous $MoS_{2+x}$ was identified as efficient photocatalyst for HER,[22,23] which are highly active catalyst materials, often even more active than their crystalline counterpart,[24–26] and they can be synthesized using electrodeposition or wet chemical reactions with no need for a thermal sulfidization treatment.[27–30] Amorphous $MoS_{2+x}$ materials exhibit Mo(IV) centers with a local environment of $S^{2-}$ and $S_2^{\,2-}$ anions.[31–34]

---

[a] *Christian-Albrechts-Universität zu Kiel, Institute of Inorganic Chemistry, 24118 Kiel, Germany. E-mail: wbensch@ac.uni-kiel.de*
[b] *Goa University, Department of Chemistry, Goa 403206, India*
[c] *Ruhr-Universität Bochum, Laboratory of Industrial Chemistry, 44801 Bochum, Germany*
[d] *Christian-Albrechts-Universität zu Kiel, Institute for Materials Science, 24143 Kiel, Germany*
[e] *Leibniz Institute of Surface Modification IOM, 04318 Leipzig, Germany*
[f] *Inorganic Chemistry III, University of Bayreuth, 95440 Bayreuth, Germany*
[g] *Universität Rostock, Leibniz-Institut für Katalyse e.V. (LIKAT), 18059 Rostock, Germany*

† Electronic supplementary information (ESI) available. See DOI: 10.1039/c5ra14438h

Upon applying a cathodic potential to amorphous $MoS_{2+x}$ materials in the HER the surface composition changes to $MoS_2$, as was revealed by chemical and physical characterizations.[35–37] The results of these studies suggest that amorphous $MoS_2$ is at least an important component of the catalytically active material. In the past it was shown that solution based syntheses applying $(NH_4)_2MoS_4$ (ATM) as source and using *e.g.* hydrazine as reducing agent yield amorphous sulfur rich products $MoS_{2+x}$ and only if the reaction slurry was refluxed at $T \approx 90$ °C poorly crystalline $MoS_2$ with some S excess was obtained.[38–45] The large excess of hydrazine always generates $S_2^{2-}$ species which are bound to the Mo center yielding $MoS_{2+x}$.

These observations led to the main idea of the present work: is it possible to develop a new kinetically controlled synthetic route for the direct preparation of amorphous $MoS_2$ avoiding formation of $MoS_3$ or $MoS_{2+x}$ as intermediates, which must then be transformed to $MoS_2$ by applying elevated temperature yielding inevitable nanocrystalline $MoS_2$?

## 2. Results and discussion

### 2.1. Analysis of as prepared PX

Amorphous PX was synthesized by decomposition of ammonium tetrathiomolybdate (ATM) in a desiccator under hydrazine atmosphere (see Experimental section). The gaseous $N_2H_4$ molecules are proposed to be decomposed on the surface of ATM crystallites according to the reaction $N_2H_4 \rightarrow N_2 + 4H^+ + 4e^-$. The protons attack the sulfide anions forming $H_2S$ of the $[MoS_4]^{2-}$ ion and the electrons simultaneously reduce Mo(VI) to Mo(IV). The chemical analyses of numerous syntheses yield as average composition $MoS_{2.0(2)}N_{0.8(2)}H_{3.3(2)}$ for the reaction products. Obviously the amorphous products contain $NH_3$ and may be also some residual hydrazine (see below). The presence of $NH_3$ was verified by reacting PX with Nessler's reagent in water.

X-Ray powder patterns of as prepared PX, of samples heated to 450 °C and 900 °C (PX450 and PX900) and a simulated pattern of bulk $MoS_2$ are displayed in Fig. 1. The pattern of PX is dominated by a very broad hump between 4° and 15° 2$\theta$ and a less intense modulation at around 32–33° 2$\theta$ reminiscent of a glass-like state. The evolution of the background at low scattering angles gives also hints that no single or double-layered material was formed.[46]

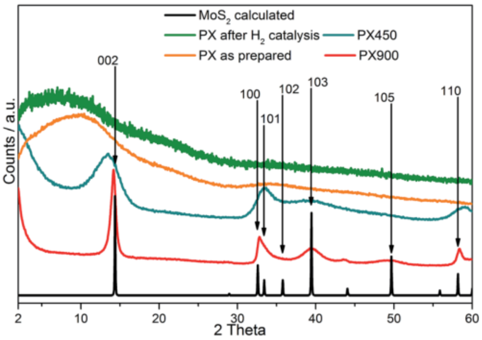

Fig. 1 XRD pattern of PX (orange trace), PX after $H_2$-production (green trace), of PX heated to 450 and 900 °C (blue and red trace), and for comparison a calculated pattern of $MoS_2$ (black trace).

Transmission electron microscopy (TEM) analysis of PX revealed several remarkable results. Specifically crystallization phenomena occurred during analysis, which are documented in Fig. 2.

For the pristine state, a combined approach of high resolution (HR)TEM/FFT (Fast Fourier Transformation) confirmed a completely amorphous structure of the sample, as depicted by the HRTEM micrograph and the corresponding FFT in Fig. 2a and (d).

For further characterization Raman spectroscopy was applied to probe the layer character of PX. The Raman active modes $E^1_{2g}$ and $A_{1g}$ of $MoS_2$ representing the in-plane and out-of-plane vibrations, are typically located at about 386 and 411 $cm^{-1}$, respectively (Fig. S1†).[47,48] These signals differ in intensity and energy separation depending on the number of stacked $MoS_2$ layers. The more layers are stacked the higher is the intensity of the peaks and the smaller is the energy difference between these signals. No resonances occur in the Raman spectrum of PX supporting the findings of the TEM and XRD measurements (see below).

Comparison of the FIR spectra of PX as obtained, PX450, PX900 and commercial $MoS_2$ demonstrates that the amorphous material PX does not have a $MoS_2$ like structure because the typical vibrations of crystalline $MoS_2$ are absent (see Fig. S2†). The spectrum shows a band at 478 $cm^{-1}$, which can be assigned to a Mo–N vibration and an absorption at 334 $cm^{-1}$ which fits to the deformation vibration of a Mo–S–Mo group (see Fig. S3†). This $\mu_2$-$S^{2-}$ bridging ligand between two Mo atoms can be observed by FIR in $MoS_2$ because of imperfections in the arrangement of the $MoS_2$ sheets having defects in their basal sulfur atom arrangement.[49]

To get more information about the nitrogen species in the sample $^{15}N$ CP MAS and $^1H$ spin echo NMR spectra of PX as prepared were recorded (Fig. 3). The $^{15}N$ NMR spectrum shows a single broad peak centered at −380 ppm with a FWHM of roughly 50 ppm, which is a result of the weak proton decoupling (see Experimental details) and distributions of the chemical shift. The observed chemical shift region between −300 and −450 ppm is consistent with expected shifts of hydrazine (−320 to −390 ppm), ammonia (around −382 ppm) and ammonium (−340 to −360 ppm).[50] For hydrazine three different coordination types have to be distinguished. While for the bridging and side-on coordination in several metal–organic compounds only one signal is observed between −370 and −390 ppm, the end-on coordination reveals two peaks at around −370 ppm for the metal coordinated $NH_2$ unit and around −320 ppm for the non-coordinated $NH_2$ group.[51] Although all three target molecules are in agreement with the $^{15}N$ MAS spectral data the end-on coordination of hydrazine is unlikely since the spectral intensity around −320 ppm is low compared to the other regions.

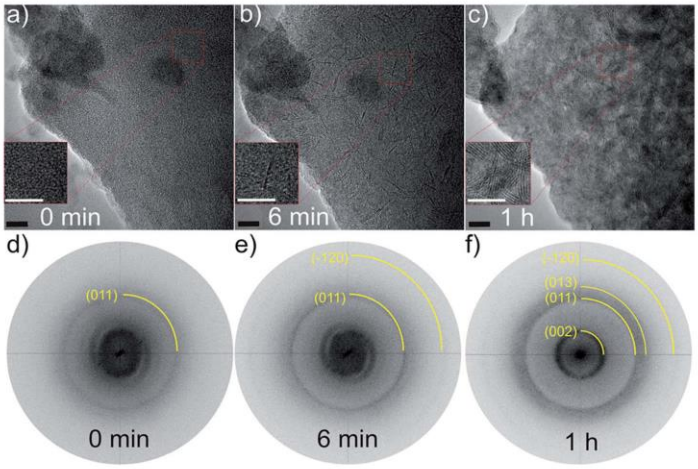

Fig. 2 Time resolved series of HRTEM micrographs of a region of the PX showing the evolution of (002) slabs under irradiation with an electron beam voltage of 300 kV for (a) 0 min, (b) 6 min, (c) 1 h, and the corresponding Fast Fourier Transformation (FFT) patterns (d)–(f). Insets show enlarged views of the development of $MoS_2$ slabs in the same position of the bulk material. Scale bar is 10 nm. The measured *d*-values of the (002): 0.637 nm, (011); 0.264 nm, (013): 0.222 nm, (−120): 0.156 nm, as compared to the theoretical values: 0.615 nm, 0.267 nm, 0.228 nm, 0.158 nm, the (002) *d*-spacing is larger than the theoretical one indicating a more bended and disordered arrangement of the $MoS_2$ basal planes produced *via in situ* electron irradiation.

Further insight is provided by the high-resolution $^1H$ NMR spectrum (Fig. 3, right). Here, one resonance around 4.34 ppm with a broad and intense shoulder at about 2.8 ppm is observed. While the former signal favors $NH_3$ (4–7 ppm),[52] or $N_2H_4$ in a side-on coordination (5–6 ppm) the latter one might be assigned to bridging (2–5 ppm) hydrazine molecules.[50,53–55] Since the resonance for the non-coordinated unit of $N_2H_4$ in an end-on coordination is usually high-field shifted by about one ppm only a small amount of end-on bonded hydrazine is expected. This is in accordance with the $^{15}N$ NMR results. Additionally, the low intensity in the downfield region above 7 ppm indicates a rather low concentration of ammonium (7–9 ppm).[56] Combined with the elemental analysis, the NMR data favor a scenario where both $NH_3$ and $N_2H_4$ are present in PX, with $NH_3$ being the majority component. For $N_2H_4$ either a bridging or a side-on coordination is possible.

Since from NMR spectroscopy only the nitrogen-containing molecules could be identified XPS measurements were performed to gain more information of the chemical states of the constituents. In the survey spectra (see Fig. S5†) peaks of Mo, S, and N are clearly visible, but also those of C 1s and a very small O 1s signal caused by a slight surface contamination. Note that no Mo, S or N oxidic species can be detected in the Mo 3d, S 2p or N 1s regions (see discussion below). The surface composition of the sample derived from the XPS spectrum using the Mo 3d, S 2p and N 1s core level lines and applying the Scofield cross-section values is $MoS_{2.1}N_{0.8}$ which is very close to the data obtained by chemical analysis. For an overview of the XPS data the binding energies of the Mo 3d and S 2p fits are provided in Table 1.

Generally, the electron density of an atom, which is often related to the oxidation state, depends on several factors like

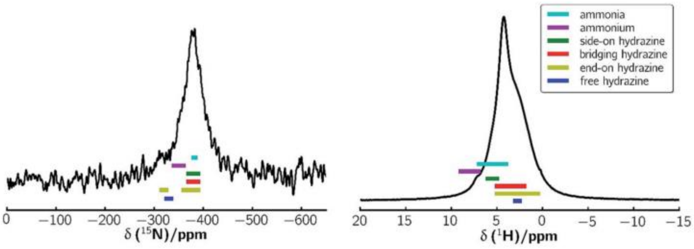

Fig. 3 $^{15}N$ CP MAS (left) and $^1H$ spin echo (right) NMR spectrum of PX collected at a spinning speed of 10 and 60 kHz, respectively.

**Table 1** Overview over the binding energies of the Mo 3d and S 2p peaks of PX and $MoS_3$ and $MoS_2$ for comparison

| Compound | Mo $3d_{5/2}$ | Assignment | S $2p_{3/2}$ | Assignment |
|---|---|---|---|---|
| PX[a] | 228.4<br>(0.9) | $Mo^{4+}$, most N-donors | 161.4<br>(1.36) | $S^{2-}$ |
| | 228.9<br>(0.9) | $Mo^{4+}$, less N-donors | | |
| | 229.9<br>(1.2) | $Mo^{4+}$, lowest amount of N-donors | | |
| $MoS_3$ | 229.1 | $Mo^{IV}$ | 161.6 | $S_2^{2-}$ terminal and/or $S^{2-}$ |
| | | | 162.9 | $S_2^{2-}$ bridging |
| $MoS_2$ | 229.2 | $Mo^{IV}$ | 161.8 | Basal plane $S^{2-}$ |

[a] PX as prepared.

number and type of ligands (covalency), difference of electronegativity as well as on the interatomic bond lengths. Thus, the $E_b$ values reported for a distinct element in literature often scatter in a wide range depending on the actual chemical composition. Moreover, the measured $E_b$ is affected by intra- and extraatomic relaxation and the Madelung contribution. Since PX is amorphous and contains N and H besides S, a comparison with data of crystalline bulk materials for the assignment of the species should be done with some caution.

In Fig. 4c the XPS spectrum of the N 1s and Mo $3p_{3/2}$ region is depicted. It is dominated by the Mo $3p_{3/2}$ peak at 394.5 eV, which extends into the region of the N 1s peak at 399.3 eV. In accordance with the analysis of the Mo 3d signal (see below), the Mo $3p_{3/2}$ peak was fitted with three overlapping peaks at 394.3 eV, 394.8 eV and 395.7 eV, which reproduced the signal shape perfectly. Depending on the N containing chemical compound, N 1s binding energies are located between about 407 eV (nitrate) and *ca.* 397 eV (nitride).[57,58] Two N 1s lines at 399.3 eV and 401.3 eV (ratio: ≈8 : 1) can be identified which can be assigned to $NH_3$ and $N_2H_4$ coordinating the Mo center in the bridging or side-on mode, in accordance with the NMR data.

Fig. 4a depicts the XPS spectrum of the S 2p region. The S 2p peak of PX can be fitted with contributions from S $2p_{3/2}$ and $2p_{1/2}$ levels with $E_b$ = 161.4 and 162.6 eV respectively with a spin–orbit splitting of 1.2 eV. The presence of amorphous $MoS_3$ can be safely excluded, because the S 2p region of $MoS_3$ consists of two doublets with $E_b$ = 162.0 and 163.3 eV for the two S $2p_{3/2}$ signals due to the presence of bridging $S_2^{2-}$, apical $S^{2-}$ ligands (higher energy doublet) and terminal $S_2^{2-}$ and/or $S^{2-}$ (lower energy doublet).[46–48,59–62] Typical binding energies of the S $2p_{3/2}$ level in $MoS_2$ extracted from the NIST database range between 161.5 and 163 eV,[63] with most data at around 162.2 eV. The lower value for the S 2p signal in PX indicates different bond strength and/or a differing binding mode of the S atoms. Most likely PX contains $\mu_s$-$S^{2-}$ species as observed in $K_5[Mo_3S_4(CN)_9]\cdot 3KCN\cdot 4H_2O$, for which an $E_b$ = 161.6 eV was reported.[53]

Fig. 4b shows the Mo 3d and S 2s region of PX. The deconvolution of the Mo 3d region yields three distinct Mo species, *i.e.* three Mo species in different chemical environments. The main contribution comes from the doublet located at 228.4 and 231.5 eV ($3d_{5/2}$ and $3d_{3/2}$) while two further doublets are located

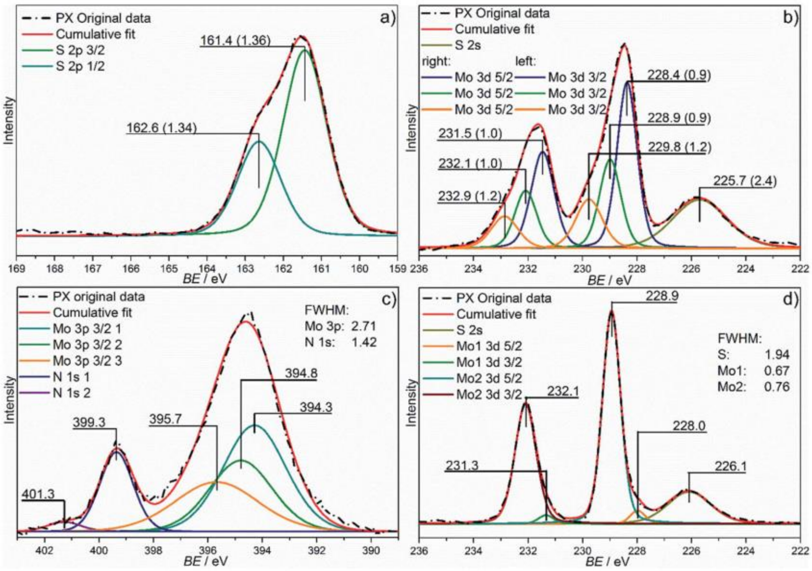

Fig. 4 XPS measurements of the S 2p (a), Mo 3d (as obtained: (b) and heated to 450 °C: (d)), and the N 1s (c) region of PX. The dash-dotted lines represent the original data and the red lines the cumulative fits.

at 228.9/232.1 and 229.7/233.0 eV for the 5/2 and 3/2 levels (ratios are 3 : 2).

For crystalline $MoS_2$ the Mo $3d_{5/2}$ signal occurs at 229.4 eV, which is near the signal observed at 228.9 eV. Hence, this Mo species is most likely surrounded by only sulfur. The shift of the $E_b$ relative to values reported for crystalline $MoS_2$ is caused by a different bonding situation. The most intense Mo $3d_{5/2}$ peak represents a Mo center with higher electron density compared to the middle $Mo^{IV}$ peak being assigned to Mo in a predominantly $S^{2-}$ environment. Both $NH_3$ and $N_2H_4$ are electron donors reducing the positive charge on the Mo center leading to a shift to lower $E_b$. Such shift to lower $E_b$ is also observed for 1 T-$MoS_2$ with an $E_b$ of the $3d_{5/2}$ shifted by ≈1 eV to a lower binding energy. The third peak at 229.8 eV represents a Mo species with less electron density compared to the other two species although the small energy shift does not allow assigning a significant higher oxidation state and one can safely assume that this Mo center has a different environment.

All the results indicate that Mo in PX is surrounded predominantly by four S atoms in a glass-like manner, with the three different Mo species being surrounded by different numbers of $NH_3/N_2H_4$ neighbors. The Mo center with the lowest $E_b$ for Mo $3d_{5/2}$ has the largest number of $NH_3/N_2H_4$ in the coordination environment while that with the highest $E_b$ is surrounded only by few donor molecules.

### 2.2. Heating of PX – crystallization

The thermal stability of as-prepared PX was investigated by heating the sample either in a furnace or by irradiation with the electronic beam of the TEM *in situ*. The XRD patterns of two samples heated in the furnace are shown in Fig. 1 for comparison. Apparently, the heating process initiated nucleation and crystallization of a layered material after heating at 450 °C. The absence of the (103) and (105) reflections clearly evidences a pronounced turbostratic disorder. Assigning the reflection at 14° $\theta$ to the (002) plane leads to an interlayer distance of 6.6 Å which is about 0.4 Å larger than in crystalline $MoS_2$ and smaller than the interlayer distance of (002) planes determined *via* TEM (6.37 Å). Using the Scherrer formula a size of coherently scattering domains of 2.7 nm is obtained from the (002) reflection, giving a number of 4 stacked layers, which is consistent with the histogram obtained from *in situ* TEM heating (*cf.* Fig. S7†). The pronounced shift of the (002) reflection to a lower scattering angle compared to crystalline $MoS_2$ is typical for layered materials with low stacking and/or the presence of residues between the layers (see also below). The background at low scattering angles indicates the presence of slabs with a lower stacking degree than 4. Heating at 900 °C yields a more crystalline sample with a size of coherently scattering domains of about 10.8 nm, *i.e.* about 17 $MoS_2$ layers are stacked. Despite the high temperature of 900 °C the material still exhibits a pronounced disorder (stacking faults, turbostratic disorder) as can be seen from the shapes of the reflections. It is gratifying to note that the XRD results of the heating experiments are consistent with the results from the TEM analysis.

Irradiating the sample with a 300 kV electron beam, the characteristic (002) single slabs of crystalline $MoS_2$ (space group: $P6_3/mmc$) were formed, as demonstrated in the HRTEM micrographs in Fig. 5b and e. The length and stacking numbers of these slabs increased with extended exposure times, *cf.* result of long-term irradiation experiments of Fig. 2c and f. By closer inspection of the FFTs of Fig. 2e and f the formation of (011), (013), and (−120) lattice planes were also observable under irradiation.

Furthermore, applying a heating stage for *in situ* observation and a lower dose of electrons also revealed an increase of crystallinity of the as prepared pristine $MoS_2$. TEM overview bright field images (Fig. 5) from the same position of the sample are shown from 300 °C up to 500 °C. The corresponding inverse FFT images (Fig. 5c, f, i and l) exhibit more clearly the development of the (002) slabs of $MoS_2$. At 300 °C the sample is

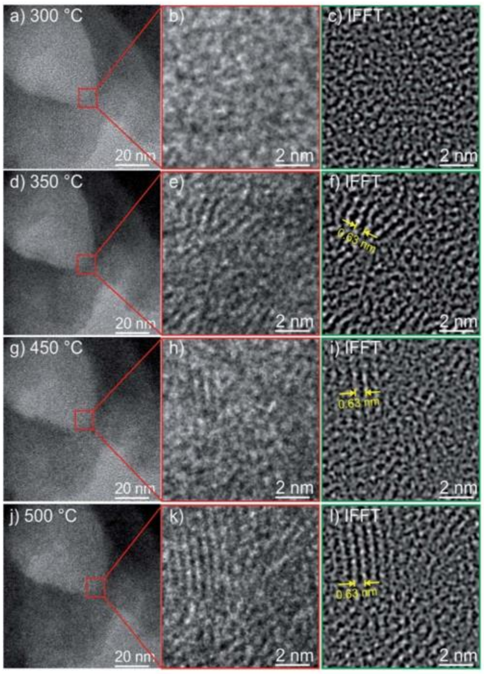

**Fig. 5** (a), (d), (g), and (j): Temperature resolved series of TEM bright-field images of the as prepared $MoS_2$ during the *in situ* heating experiment. (b), (e), (h), and (k): The enlarged region from the same position (marked with a red box) of the sample showing the development of the (002) slabs as temperature increased. (c), (f), (i) and (l) are the corresponding inverse FFT (IFFT) showing more clearly the contrast from the (002) slabs. The measured (002) *d*-spacing is indicated. The IFFT is generated by applying a band pass mask to the FFT pattern of HRTEM micrograph with a frequency range from 2.35 nm$^{-1}$ to 7.50 nm$^{-1}$, and filters out all the noises outside this range. It means that, in real space, the filtered IFFT images exhibit only those $MoS_2$ lattice planes with *d*-spacings from 0.267 nm to 0.85 nm.

mainly amorphous (*cf.* Fig. 2c), and at $T = 350$ °C the first indication of formation of the (002) slabs is detectable (Fig. 2f). The measured dimension (0.63 nm) of the individual slab is comparable to the theoretical value (0.615 nm) of the (002) plane of $MoS_2$. At 450 °C and 500 °C, the length of the slabs is increasing and they are becoming more ordered as depicted in Fig. 5i and l, which is a sign of an increase of crystallinity of the sample upon heating.

Surprisingly, in contrast to the irradiation experiment, the stacking height of the (002) slabs, and even the length of the slabs formed during heating are more uniform between the regions examined in the sample, indicating an evolution of mostly the same sizes of the $MoS_2$ grains when the as prepared material is heated (*cf.* Fig. 5c and j) and the size distribution histograms in Fig. S8.† The histogram for the *in situ* heating to 500 °C shows a stacking number of 4 layers for the (002) plane, and a basal plane length of 2 nm. These values are in good agreement with those of the sample heated to 450 °C and examined by XRD (see below). On the other hand, the size distribution obtained by *in situ* irradiation for 1 h is more broadened, with a stacking number of 5 and a longer basal plane length of 4–5 nm. The two contrary observations might be due to different crystallization mechanisms under electron irradiation and under heat treatment for nanosized materials.[64] Electron irradiation generates highly localized heating in the sample particles, especially when the thermal conductivity of the specimen is relatively low, for example, monolayer $MoS_2$ or amorphous $MoS_2$, which is also presenting itself in the PX sample here. While in the thermal heating process, the good thermal conductivity of the carbon lacy network created a more uniform heat distribution over the whole sample grid, thus a more uniform size of $MoS_2$ particles was produced.

The crystallization of $MoS_2$ slabs can be monitored by Raman spectroscopy. The two typical modes $E^1_{2g}$ and $A_{1g}$ start to develop after heating PX at $T = 450$ °C and the intensity increased for the sample treated at $T = 900$ °C (see Fig. S1†). The highest intensity is observed for commercial $MoS_2$ which is characterized by the largest number of stacked $MoS_2$ slabs. The energy difference between the two Raman modes of $MoS_2$ may be used to estimate the number of stacked layers. Four stacked layers showed a difference of the Raman modes of about 24.3 $cm^{-1}$, which fits perfectly for the sample heated at 450 °C and is in full agreement with the result of the XRD investigation, where also four slabs were estimated. The larger energy separation obtained for PX900 and bulk $MoS_2$ is in line with the larger number of stacked $MoS_2$ slabs.[46]

Upon heating to 450 °C the compound crystallizes at least partially to form $MoS_2$ slabs and on the first sight the XPS spectrum of the Mo 3d region (Fig. 4d) is very similar to that of $MoS_2$. The spectrum of the N 1s region only shows the Mo 3p peaks while the N 1s peaks have vanished. In the Mo 3d spectrum, there seems to be a small asymmetry of the peaks towards lower binding energies, which has been fitted as a second Mo species at 228.1 and 231.2 eV. However, due to uncertainties inherent in Shirley background subtraction this signal should be treated with caution. The predominant Mo species appears at 228.9 eV and 232.1 eV (Mo $3d_{5/2}$ and $3d_{3/2}$). In contrast to the as prepared PX material only two Mo species can be identified, one of which is hardly significant. This observation is in good agreement with formation of crystalline $MoS_2$ slabs (minor component) embedded in a matrix of glassy like amorphous molybdenum sulfide (dominating component), a scenario which would not necessarily require two different Mo 3d peaks as both species are close to be $Mo^{IV}$. The higher binding energy species observed in the spectrum of as prepared PX disappeared, which is accompanied by the disappearance of the N 1s signal (Fig. S7†). Furthermore the main Mo peak of the heated sample has the same binding energy as the second species in PX as prepared. These observations substantiate that the other Mo species detected in the as prepared material were associated with the presence of nitrogen containing ligands in the sample.

### 2.3. Visible light driven hydrogen evolution

Many publications in literature deal with the application of $MoS_2/MoS_3$ based materials as catalysts for the light driven photocatalytic hydrogen production.[60,65–71] Commonly used multicomponent catalyst systems for this purpose contain a photosensitizer (PS) for light harvesting, a sacrificial agent (SA) as electron donor and a proton source, usually water, besides a water reduction catalyst (WRC). For solubility or performance reasons organic solvents are added. The results presented herein were obtained from multicomponent catalyst systems with $[Ru(bpy)_3](PF_6)_2$ as PS, water as proton source and triethylamine as SA in acetonitrile. All materials (PX, PX450, PX900) as well as two additional reference samples (commercial $MoS_2$ and a sample of $MoS_2$ prepared from ATM at 350 °C) were tested as WRCs in this system and proved active in light driven proton reduction (Fig. 6). Although activity of all catalyst systems ceased after ~20 h of irradiation with visible light, this is most certainly due to degradation of the PS $[Ru(bpy)_3](PF_6)_2$ as reported

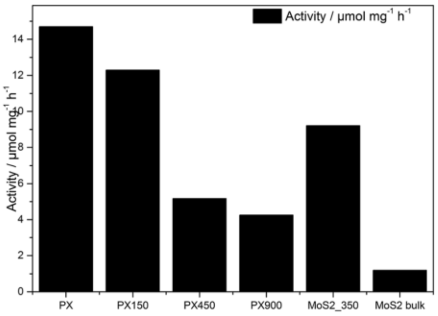

Fig. 6 Comparison of activities ($t = 1$ h) of different catalysts based on $MoS_2$ in photocatalytic hydrogen evolution from mixtures containing triethylamine (8 mL), water (3 mL) and $[Ru(bpy)_3](PF_6)_2$ (1 mM) in acetonitrile (10 mL). PX as obtained and heated samples are displayed. For comparison results with $MoS_2$ prepared from ATM by decomposition at 350 °C and commercial bulk $MoS_2$ are displayed.

previously.[72] This was additionally demonstrated by reapplication of PS after the reaction had stopped completely. After equilibration the reaction was reinitialized and showed the same hydrogen evolution trend as before, indicating that the PS is degraded during the experiment while the catalyst PX is stable under the reaction conditions (Fig. S11†). Furthermore, the chemical analysis show no major difference in composition to the pristine material and the XRD pattern of the post-catalytic material (Fig. 1, green trace) evidence no significant change. Because the catalyst was washed three times with isopropyl alcohol the carbon and hydrogen contents are increased, but the ratios of Mo : S and Mo : N did not change. A follow-up catalytic test with the recovered material exhibited significant catalytic activity even though a solid comparison is not possible due to a high loss of material during the recovery process, since only 10 mg were used for the respective initial catalytic tests.

Of all materials tested, PX showed the best results with a hydrogen production of 14.7 μmol $mg^{-1}$ catalyst in 1 h (Fig. 6). This remarkable activity decreased only slightly after heating a sample of PX to 150 °C to exclude the contribution of gaseous species (Fig. 6). Heating of the catalyst material to temperatures above the crystallization point however caused a considerable decrease in activity compared to PX with values of 5.17 μmol $mg^{-1}$ catalyst and 4.25 μmol $mg^{-1}$ catalyst in 1 h for heat treatment at 450 °C and 900 °C, respectively.

This is still a clear enhancement of activity compared to a sample of commercial bulk $MoS_2$, which produced 1.2 μmol $mg^{-1}$ catalyst in 1 h in an identical multi-component catalyst system. In accordance with previous results this suggests enhanced activity in catalytic proton reduction with decreasing particle size for $MoS_2$ materials.[73] Further enhancement of photocatalytic activity for amorphous samples compared to their crystalline counterparts has not been reported yet. Further support that the amorphous state improves the properties of $MoS_2$ materials as WRCs in light driven proton reduction arises from a comparison to a conventional nanocrystalline sample of $MoS_2$. This was obtained by thermal decomposition of ATM at 350 °C and shows similar properties to PX450 with respect to composition as well as structure and stacking behavior.[72,74] Even activity in light driven proton reduction in an identical multi-component catalyst system is similar to PX450, thus suggesting the electronic properties and local environment of PX as reason for the remarkable activity of the material. The present results support reports[21–23] that amorphous Mo sulfide based materials are partially more active than crystalline $MoS_2$. With the $MoS_2$ materials presented here, a direct comparison of amorphous to crystalline catalysts is available, which results in the conclusion that amorphous $MoS_2$ can be basis for highly active WRCs, too. Concerning the catalytically active sites in PX a direct comparison with models widely accepted for crystalline $MoS_2$ cannot be done. It was demonstrated that in crystalline $MoS_2$ the so-called Mo-edge is catalytically active for hydrogen evolution while the S-edge seems to be catalytically inactive.[74,75] Because PX is X-ray amorphous no such edges exist and only for the crystalline samples investigated here the model can be invoked to explain the catalytic properties.

## 3. Conclusion

In conclusion a new preparation method utilizing kinetic control was developed to synthesize an amorphous molybdenum sulfide based material and the product has been thoroughly characterized with various methods to elucidate the chemical nature of the constituents. The product is completely amorphous as evidenced by XRD, TEM and Raman spectroscopy. According to chemical analysis the Mo : S ratio is near 1 : 2 like in crystalline 2H–$MoS_2$ excluding the formation of amorphous $MoS_3$. Appreciable amounts of N are present and taking into account the XPS, NMR and spectroscopic data different locally varying environments of the Mo centers must be postulated. The material shows an unusual thermal stability and only if the samples is heated at $T \geq$ 350 °C crystallization takes place being accompanied by a mass loss, which is primarily attributed to the emission of hydrazine leading to formation of 2H–$MoS_2$. The crystallization process can be controlled by applying different temperatures or dwelling times or even using different methods like the electron beam of a TEM. The photocatalytic activity is highest for the amorphous material indicating that most likely Mo centers with N and S as neighbors are the catalytic active species.

## 4. Experimental section

### 4.1. Sample preparation

The starting materials (ammonium heptamolybdate and ammonia) were obtained in high-purity from Sigma-Aldrich. Adding ammonium heptamolybdate ($(NH_4)_6Mo_7O_{24}\cdot 4H_2O$, 30 g) to a 25 wt% solution of ammonia (200 mL) and bubbling $H_2S$ for half an hour through the solution leads to crystallization of the precursor ammonium tetrathiomolybdate ($(NH_4)_2MoS_4$, ATM) which was obtained in high yield.

The amorphous molybdenum sulfide based material (PX) has been synthesized by storing freshly prepared ATM in a desiccator over hydrazine monohydrate (99%) (**Caution!** Highly toxic material!). Typically hydrazine (20 mL) was deposited in a Petri dish located in the lower chamber of a desiccator and after ball milling ATM (1 h, 2 g) was finely dispersed on another Petri dish and stored above. The reaction at room temperature is observed by change in color of ATM to anthracite and is completed in about twenty to thirty days as evidenced by the formation of insoluble products. The complete conversion of ATM was further confirmed as the product (PX) did not give any red color on reaction with water. However, products isolated before a period of 20–30 d always contained still some ATM as evidenced by a red coloration on treatment with water. The gas–solid reaction can be significantly accelerated increasing the temperature. At about 32 °C the reaction is completed after 7 d. After completion of the reaction the Petri dish was taken out and kept in another desiccator containing silica granules as desiccant for yet another day for thorough drying after which the reaction product was weighed.

### 4.2. Characterization

X-Ray powder patterns were recorded with a STOE STADI-P instrument (monochromatized $CuK_{\alpha 1}$ radiation, $\lambda = 1.54056$ Å) in transmission mode with a position sensitive detector (Mythen).

### 4.3. Raman

Raman measurements were carried out on a Dilor RamanXY instrument equipped with an Ar/Kr mixed gas ion laser (type: RM2018 by Spectra-Physics) with various possible excitation wavelengths (488–648.2 nm) and a $N_2$-cooled CCD detector for imaging. The sample was rotated during the measurement and cooled to 20 K.

### 4.4. Thermal analysis

DTA-TG was performed in a nitrogen atmosphere (purity: 5.0; heating rate 4 K $min^{-1}$; flow rate: 75 mL $min^{-1}$; $Al_2O_3$ crucibles) using a Netzsch STA-409CD instrument.

### 4.5. Spectroscopy

IR/NIR/FIR spectra were recorded at room temperature using an Alpha P FT-IR spectrometer from Bruker. The IR spectra were measured from 200 to 4000 $cm^{-1}$.

### 4.6. Transmission electron microscopy

TEM investigations were performed with a Tecnai 30 STwin microscope (300 kV, FEG cathode, $C_s = 1.2$ mm). The samples for TEM investigations were prepared as follows. A small amount of precursor powder was suspended in methanol and ultrasonically grinded for 15 min. Afterwards, a transfer of the suspended powder on a TEM support (a lacey carbon film on 200 mesh cooper grid) was carried out by dipping the TEM support into the solution. The prepared TEM samples were dried at room temperature for several minutes. All images were recorded with a Gatan Multiscan CCD camera (2k × 2k) and evaluated (including Fourier analyses) with the program Digital Micrograph (Gatan). EDS analyses were performed in the TEM mode with a Si/Li detector (EDAX System).

### 4.7. X-ray photoelectron spectroscopy

XPS measurements were carried out in an ultra-high vacuum (UHV) chamber equipped with a monochromatic Al Kα X-ray source ($h\nu = 1486.6$ eV), operated at 14.5 kV and 35 mA, and a high resolution Gammadata-Scienta SES 2002 analyzer. The base pressure in the measurement chamber was maintained at about $5 \times 10^{-10}$ mbar. The measurements were done in the fixed transmission mode with pass energy of 200 eV resulting in an overall energy resolution of 0.25 eV. A flood gun was applied to compensate charging effects. High-resolution spectra for C 1s, O 1s, N 1s, S 2p and Mo 3d photoelectron lines were recorded. The C 1s signal (284.5 eV) was used as an internal standard for calibration of the spectra. The Casa XPS software with Gaussian–Lorentzian product function and Shirley background subtraction was used for peak deconvolution, whereas the ratio of the Lorentzian to the Gaussian portion of the function was set to 30%/70% (profile shape factor $\mu = 0.3$). The energy scale calibration of the machine was carried out using Au $4f_{7/2} = 84.0$ eV, Ag $3d_{3/2} = 368.3$ eV and Cu $2p_{3/2} = 932.7$ eV.

### 4.8. $^1H$ MAS NMR

NMR spectra were recorded at ambient temperature on an Avance III HD 600 solid-state NMR spectrometer (Bruker) with an external magnetic field 14.1 T, operating at a frequency of 600.1 MHz using a spin echo pulse sequence. The sample was contained in a 1.3 mm $ZrO_2$ rotor which was mounted in a standard double resonance MAS probe (Bruker) and spun at 60 kHz. The spectrum was referenced relative to TMS.

### 4.9. $^1H^{15}N$ cross-polarization (CP) MAS NMR

NMR spectra were recorded at ambient temperature on an Avance III HD 400 solid-state NMR spectrometer (Bruker) with an external magnetic field of 9.4 T, operating at frequencies of 400.1 MHz and 40.6 MHz for $^1H$ and $^{15}N$, respectively. The sample was contained in a 4 mm $ZrO_2$ rotor which was mounted in a standard triple resonance MAS probe (Bruker) and spun at 10 kHz. During a contact time of 1 ms a ramped-amplitude (RAMP) CP pulse, the RF field was linearly varied about 30% on $^1H$, was used. Due to the metal-like properties of the sample severe heating and detuning of the probe took place upon RF irradiation. Therefore low power continuous wave (CW) decoupling (roughly 10 kHz RF field) was applied during the acquisition of the $^{15}N$ signal. The recycle delay was set to 1s. The $^{15}N$ chemical shifts were referenced relative to nitromethane.

### 4.10. Photocatalytic reactions

All reactions were carried out in a double-walled thermostatically controlled reaction vessel using an automatically operating burette (MesSen Nord GmbH, Stäbelow, Germany) described previously.[76] All liquids were degassed by ultrasound treatment for at least 15 min prior to use. Triethylamine and acetonitrile were dried on $CaH_2$ and distilled under argon. A 300 W Xe lamp was used as light source along with a 420 nm cut-off filter, which leaves a light power at the flask of about 900 mW. In a standard procedure 10 mL of a $10^{-3}$ M solution of $[Ru(bpy)_3](PF_6)_2$ in acetonitrile, 8 mL trimethylamine and 3 mL distilled water were transferred *via* syringe into an air- and moisture-free glass reaction vessel which contained 10 mg of the WRC. After equilibration the freshly assembled multicomponent catalyst system was irradiated with visible light at isothermal conditions for both liquid and gaseous phase at 298.15 K. At the end of the reaction a gas sample was taken and analyzed by GC.

## Acknowledgements

L. Dura and T. Beweries thank Dr Sven Hansen (LIKAT) for assistance and Prof. Uwe Rosenthal (LIKAT) for support and fruitful discussions.

## References

1 J. D. Benck, T. R. Hellstern, J. Kibsgaard, P. Chakthranont and T. F. Jaramillo, *ACS Catal.*, 2014, **4**, 3957–3971.
2 C. G. Morales-Guio and X. Hu, *Acc. Chem. Res.*, 2014, **47**, 2671–2681.

3 X. Zong, G. P. Wu, H. Yan, G. Ma, J. Shi, F. Wen, L. Wang and C. Li, *J. Phys. Chem. C*, 2010, **114**(4), 1963–1968.
4 W. K. Ho, J. C. Yu, J. Lin, J. Yu and P. Li, *Langmuir*, 2004, **20**(14), 5865.
5 D. Merki and X. Hu, *Energy Environ. Sci.*, 2011, **4**(10), 3878.
6 H. Tributsch, *Z. Naturforsch. A*, 1977, **32**(9), 972.
7 H. J. Tributsch and C. Bennett, *J. Electroanal. Chem.*, 1977, **81**, 97.
8 H. Vrubel and X. Hu, *ACS Catal.*, 2013, **3**, 2002.
9 X. Ge, L. Chen, L. Zhang, Y. Wen, A. Hirata and M. Chen, *Adv. Mater.*, 2014, **26**, 3100.
10 D. Wang, Z. Pan, Z. Wu, Z. Wang and Z. Liu, *J. Power Sources*, 2014, **264**, 229.
11 B. Hinnemann, P. G. Moses, J. Bonde, K. P. Jørgensen, J. H. Nielsen, S. Horch, I. Chorkendorff and J. K. Nørskov, *J. Am. Chem. Soc.*, 2005, **127**, 5308–5309.
12 T. F. Jaramillo, K. P. Jørgensen, J. Bonde, J. J. Nielsen, S. Horch and I. Chorkendorff, *Science*, 2007, **317**, 100–102.
13 H. Y. Li, L. Wang, Y. Xie, G. Liang, H. Hong and H. Dai, *J. Am. Chem. Soc.*, 2011, **133**, 7296–7299.
14 H. Wang, Z. Lu, S. Xu, D. Kong, J. J. Cha, G. Zheng, P.-C. Hsu, K. Yan, D. Bradshaw, F. B. Prinz and Y. Cui, *Proc. Natl. Acad. Sci. U. S. A.*, 2013, **110**, 19701–19706.
15 C. G. Morales-Guio, L.-A. Stern and X. Hu, *Chem. Soc. Rev.*, 2014, **43**, 6555.
16 A. B. Laursen, S. Kegnaes, S. Dahl and I. Chorkendorff, *Energy Environ. Sci.*, 2012, **5**, 5577–5591.
17 D. Merki and X. Hu, *Energy Environ. Sci.*, 2011, **4**, 3878–3888.
18 A. Kudo and Y. Miseki, *Chem. Soc. Rev.*, 2009, **38**, 253.
19 X. Chen, S. Shen, L. Guo and S. S. Mao, *Chem. Rev.*, 2010, **110**, 6503.
20 F. E. Osterloh, *Chem. Mater.*, 2008, **20**, 35.
21 D. Y. C. Leung, X. Fu, C. Wang, M. Ni, M. K. H. Leung, X. Wang and X. Fu, *ChemSusChem*, 2010, **3**, 681.
22 C. G. Morales-Guio and X. Hu, *Acc. Chem. Res.*, 2014, **47**, 2671–2681.
23 D. Merki, S. Fierro, H. Vrubel and X. Hu, *Chem. Sci.*, 2011, **2**, 1262–1267.
24 H. Vrubel, D. Merki and X. Hu, *Energy Environ. Sci.*, 2012, **5**, 6136–6144.
25 T.-W. Lin, C.-J. Liu and J.-Y. Lin, *Appl. Catal., B*, 2013, **134–135**, 75–82.
26 Y. Li, Y. Yu, Y. Huang, R. A. Nielsen, W. A. Goddard, Y. Li and L. Cao, *ACS Catal.*, 2015, **5**, 448–455.
27 J. D. Benck, Z. Chen, L. Y. Kuritzky, A. J. Forman and T. F. Jaramillo, *ACS Catal.*, 2012, **2**, 1916–1923.
28 C.-L. Hsu, Y.-H. Chang, T.-Y. Chen, C.-C. Tseng, K.-H. Wei and L.-J. Li, *Int. J. Hydrogen Energy*, 2014, **39**, 4788–4793.
29 Y.-H. Chang, C.-T. Lin, T.-Y. Chen, C.-L. Hsu, Y.-H. Lee, W. Zhang, K.-H. Wei and L.-J. Li, *Adv. Mater.*, 2013, **25**, 756–760.
30 Y.-H. Chang, F.-Y. Wu, T.-Y. Chen, C.-L. Hsu, C.-H. Chen, F. Wiryo, K.-H. Wei, C.-Y. Chiang and L.-J. Li, *Small*, 2014, **10**, 895–900.
31 S. J. Hibble and G. B. Wood, *J. Am. Chem. Soc.*, 2004, **126**, 959–965.
32 S. J. Hibble, R. I. Walton, D. M. Pickup and A. C. Hannon, *J. Non-Cryst. Solids*, 1998, **232–234**, 434–439.
33 T. Weber, J. C. Muijsers and J. W. Niemantsverdriet, *J. Phys. Chem.*, 1995, **99**, 9194–9200.
34 S. J. Hibble, D. A. Rice, D. M. Pickup and M. P. Beer, *Inorg. Chem.*, 1995, **34**, 5109–5113.
35 J. D. Benck, Z. B. Chen, L. Y. Kuritzky, A. J. Forman and T. F. Jaramillo, *ACS Catal.*, 2012, **2**, 1916–1923.
36 D. Merki, S. Fierro, H. Vrubel and X. L. Hu, *Chem. Sci.*, 2011, **2**, 1262–1267.
37 D. Merki, H. Vrubel, L. Rovelli, S. Fierro and X. Hu, *Chem. Sci.*, 2012, **3**, 2515–2525.
38 P. Afanasiev, G.-F. Xia, G. Berhault, B. Jouguet and M. Lacroix, *Chem. Mater.*, 1999, **11**, 3216–3219.
39 A. Müller, V. Fedin, K. Hegetschweiler and W. Amrein, *Chem. Commun.*, 1992, **24**, 1795–1796.
40 A. Müller, E. Diemann, E. Krickmeyer, H.-J. Walberg, H. Bögge and A. Armatage, *Eur. J. Solid State Inorg. Chem.*, 1993, **30**, 565.
41 H. Jiao, Y. Li, B. Delmon and J. Halet, *J. Am. Chem. Soc.*, 2001, **123**, 7334.
42 S. J. Hibble and G. B. Wood, *J. Am. Chem. Soc.*, 2004, **126**, 959–965.
43 I. Bezverkhy, P. Afanasiev and M. Lacroix, *Inorg. Chem.*, 2000, **39**, 5416–5417.
44 P. Afanasiev, G.-F. Xia, G. Berhault, B. Jouguet and M. Lacroix, *Chem. Mater.*, 1999, **11**, 3216–3219.
45 I. Bezverkhyy, P. l. Afanasiev and M. l Lacroix, *J. Catal.*, 2005, **230**, 133–139.
46 P. Joensen, E. D. Crozier, N. Alberding and R. F. Frindt, *J. Phys. C: Solid State Phys.*, 1987, **20**, 4043.
47 C. Lee, H. Yan, L. E. Brus, T. F. Heinz, J. Hone and S. Ryu, *ACS Nano*, 2010, **4**, 2695.
48 A. Molina-Sánchez and L. Wirtz, *Phys. Rev. B: Condens. Matter Mater. Phys.*, 2011, **84**, 155413.
49 T. Weber, J. C. Muijsers, J. H. M. C. van Wolput, C. P. J. Verhagen and J. W. Niemantsverdriet, *J. Phys. Chem.*, 1996, **100**, 14144.
50 M. Witanowski, L. Stefaniak and G. A. Webb, *Annu. Rep. NMR Spectrosc.*, 1987, **18**, 1.
51 L. D. Field, H. L. Li and S. J. Dalgarno, *Inorg. Chem.*, 2010, **49**, 6214.
52 F. Haase and J. Sauer, *J. Phys. Chem.*, 1994, **98**, 3083.
53 G. V. Lagodzinskaya, N. G. Yunda and G. B. Manelis, *Russ. Chem. Bull., Int. Ed.*, 2003, **55**, 577.
54 G. Albertin, S. Antoniutti and C. Girardi, *Polyhedron*, 2012, **38**, 162.
55 G. Albertin, S. Antoniutti, A. Bacchi, M. Bergamo, E. Bordignon and G. Pelizzi, *Inorg. Chem.*, 1998, **37**, 479.
56 K. J. D. Mackenzie and M. E. Smith, *Multinuclear Solid-state NMR of Inorganic Materials, Pergamon Materials Series Volume 6*, Elsevier Science Ltd, Oxford, 2002.
57 D. N. Hendrickson, J. M. Hollander and W. L. Jolly, *Inorg. Chem.*, 1969, **8**, 2642.
58 K. Artyushkova, B. Kiefer, B. Halevi, A. Knop-Gericke, R. Schlögl and P. Atanassov, *Chem. Commun.*, 2013, **49**, 2539.

59 T. Weber, J. C. Muijsers and J. W. Niemantsverdriet, *J. Phys. Chem.*, 1995, **99**, 9194.

60 T. A. Patterson, J. C. Carber, D. E. Leyden and D. M. Hercules, *J. Phys. Chem.*, 1976, **80**(15), 1700.

61 D. Merki, S. Fierro, H. Vrubel and X. Hu, *Chem. Sci.*, 2011, **2**, 1262.

62 H. Vrubel, D. Merki and X. Hu, *Energy Environ. Sci.*, 2012, **5**, 6136.

63 *NIST X-ray Photoelectron Spectroscopy Database, Version 4.1*, National Institute of Standards and Technology, Gaithersburg, MD 20899-8370, 2015, http://srdata.nist.gov/xps/, accessed: January.

64 M. Deng, V. Hrkac, L. Kienle *et al.*, to be submitted.

65 J. Djamil, S. A. Segler, A. Dabrowski, W. Bensch, A. Lotnyk, U. Schürmann, L. Kienle, S. Hansen and T. Beweries, *Dalton Trans.*, 2013, **42**, 1287.

66 X. Zong, Y. Na, F. Y. Wen, G. J. Ma, J. H. Yang, D. G. Wang, Y. Ma, W. Wang, L. Sun and C. Li, *Chem. Commun.*, 2009, **30**, 4536.

67 X. Zong, G. P. Wu, H. J. Yan, G. J. Ma, J. Y. Shi, F. Y. Wen, L. Wang and C. Li, *J. Phys. Chem. C*, 2010, **114**, 1963.

68 F. A. Frame and F. E. Osterloh, *J. Phys. Chem. C*, 2010, **114**, 10628.

69 A. Sobczynski, *J. Catal.*, 1991, **131**, 156.

70 S. Kanda, T. Akita, M. Fujishima and H. Tada, *J. Colloid Interface Sci.*, 2011, **354**, 607.

71 Q. J. Xiang, J. G. Yu and M. Jaroniec, *J. Am. Chem. Soc.*, 2012, **134**, 6575.

72 A. Vaidyalingam and P. K. Dutta, *Anal. Chem.*, 2000, **72**, 5219.

73 T. F. Jaramillo, K. P. Jörgensen, J. Bonde, J. H. Nielsen, S. Horch and I. Chorkendorff, *Science*, 2007, **319**, 100–102.

74 H. G. Sanchez Casalongue, J. D. Benck, C. Tsai, R. K. B. Karlsson, S. Kaya, M. L. Ng, L. G. M. Pettersson, F. Abild-Pedersen, J. K. Nørskov, H. Ogasawara, T. F. Jaramillo and A. Nilsson, *J. Phys. Chem. C*, 2014, **118**(50), 29252.

75 H. Wang, C. Tsai, D. Kong, K. Chan, F. Abild-Pedersen, J. K. Nørskov and Y. Cui, *Nano Res.*, 2015, **8**, 566–575.

76 T. Beweries, J. Thomas, M. Klahn, A. Schulz, D. Heller and U. Rosenthal, *ChemCatChem*, 2011, **3**, 1865–1868.

Electronic Supplementary Material (ESI) for RSC Advances.

*Supporting Information*

# Room Temperature Synthesis of an Amorphous Molybdenum Sulfide Based Composite: Characterization and Photocatalytic Hydrogen Evolution.

*Felix Niefind, John Djamil, Wolfgang Bensch,* Bikshandarkoil R. Srinivasan, Ilya Sinev, Wolfgang Grünert, Mao Deng, Andriy Lotnyk, Lorenz Kienle, Laura Dura, Sven Hansen, Torsten Beweries*

## 1. Raman measurements

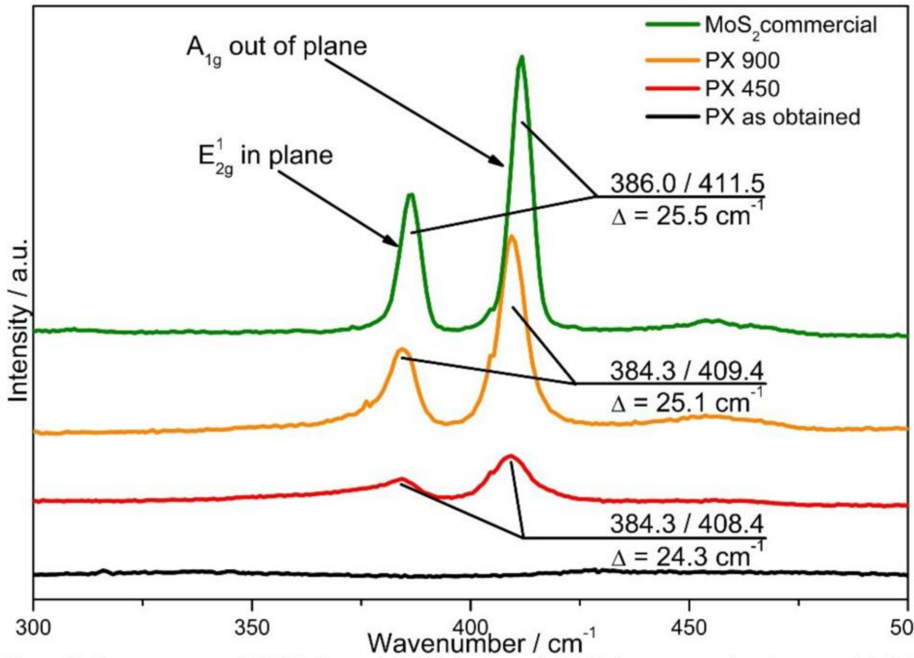

**Figure S1.** Raman spectra of PX (black trace), PX450 (red trace), PX900 (orange trace) and commercial $MoS_2$ (green trace).

## 2. Infrared measurements

**Figure S2** shows the MIR spectra of PX, ATM, hydrazine and ammonia for comparison. If residues of the starting material ATM are still in the sample vibrations of $NH_4^+$ in the MIR and $MoS_4^{2-}$ in the MIR and FIR regions should be observable. Comparison of the MIR spectra of ATM and PX demonstrates that the intense absorption of the $MoS_4^{2-}$ ion is absent in PX. But some other broad bands can be observed although not very intense and quite broad which renders the assignment rather difficult: the band at 1580 $cm^{-1}$ can be assigned as the deformation vibration of a N-$NH_2$ group, 1400 $cm^{-1}$ fits with the deformation vibration of H-N-H, and the weak band at 986 $cm^{-1}$ may be assigned to the N-N vibration of a Mo-$NH_2NH_2$ group.[1] Note that the intensities of the absorptions in Figure 8 are normalized (against the peak with the highest intensity) and without this normalization the bands of PX were not visible due to a very low intensity indicating a low concentration of N species in PX.

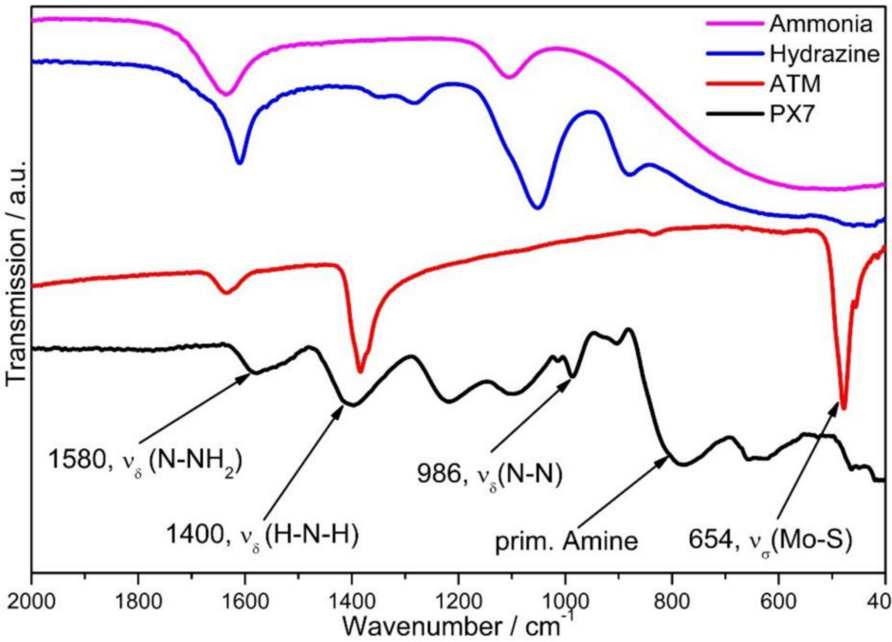

**Figure S2**. Comparison of the MIR spectra of PX (black trace), ATM (red trace), hydrazine (blue trace), and ammonia (purple trace).

A distinct assignment of the remaining absorptions is not straightforward due to the broadness of the bands. In any case, the vibrational spectroscopy data give clear evidences that no $MoS_4^{2-}$ units are present in PX.

### 3. Far Infrared Measurements (FIR)

The FIR spectra (**Figure S3**) of PX heated to 450/900 °C and of commercial $MoS_2$ display the signals of the $A_{2u}$ (out-of-plane) and the $E_{1u}$ (in-plane) vibrations of the planes of $MoS_2$ at 468 and 383 $cm^{-1}$. The $A_{2u}$ vibration exhibits a pronounced variation of the intensity. While commercial $MoS_2$ only shows a weak $A_{2u}$ band, those of the materials heated to 450 and 900 are more intense. The other band can be assigned to the in plane vibration of $MoS_2$ which is present in all three samples - commercial $MoS_2$, PX450 and PX900 – with more or less the same intensities which does not depend on the number of stacked $MoS_2$ layers. For the as prepared sample none of these absorptions can be seen in the spectrum, but two broad signals at about 480 and 340 $cm^{-1}$.

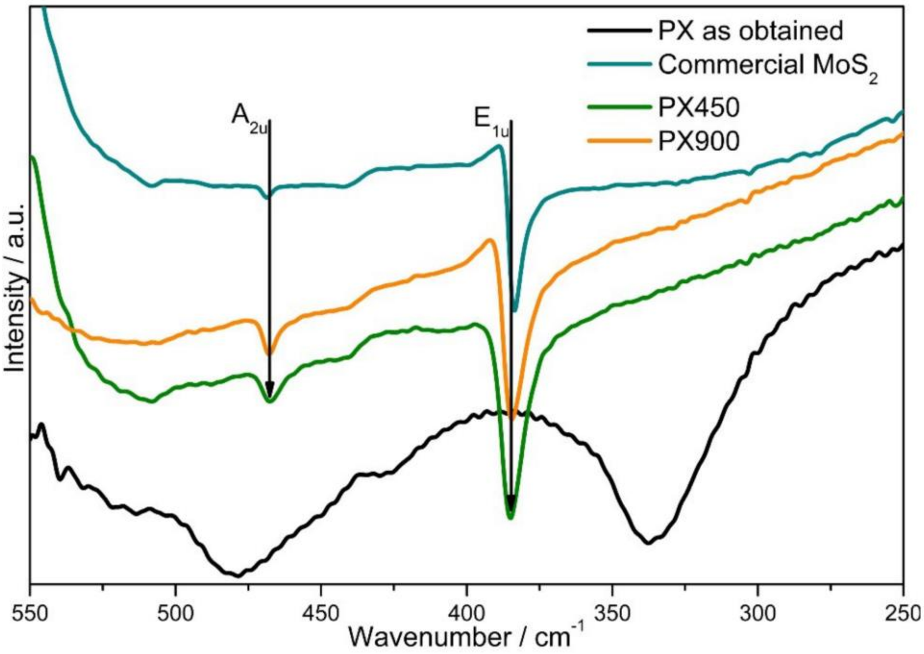

**Figure S3.** FIR of PX (black trace) in comparison with PX450 (green trace), PX900 (orange trace) and commercial $MoS_2$ (light blue trace).

**Figure S4** again depicts the FIR of PX in comparison with ATM and commercial $MoS_2$. The absorption at 480 $cm^{-1}$ may be caused by a Mo-$H_2O$ vibration (477 $cm^{-1}$) due to contamination with water from the air, but in this case two more bands at about 511 $cm^{-1}$ and 551 $cm^{-1}$ should be seen which are not present. The XPS measurements (see SI Figure S2) in the O 1s region give no hints for the presence of $H_2O$. According to literature the signal can be assigned to the Mo-N vibration of a Mo-$NH_2$-$NH_2$ coordination.[1,2] The second band at 334 $cm^{-1}$ can be assigned to a bridging ⍰$_2$-$S^{2-}$ ligand between two Mo atoms. This band was assigned to imperfections in the arrangement of $MoS_2$ sheets which have defects in their basal sulphur atom arrangement or in other words interconnections of two layers by Mo-S-Mo bridges.[3]

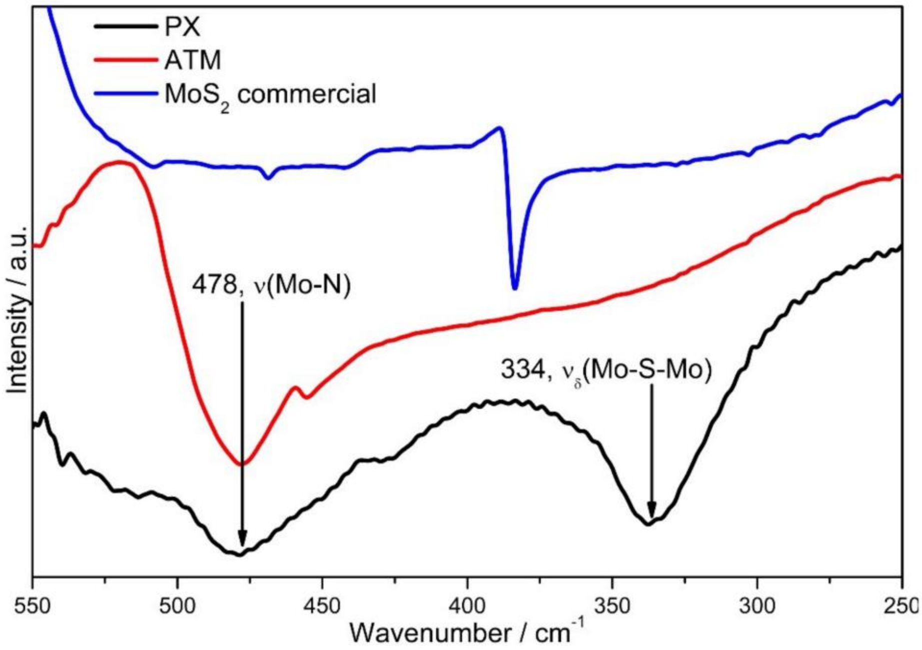

**Figure S4.** FIR of PX (black trace) in comparison with ATM (red trace) and commercial bulk MoS2 (blue trace).

**4. X-ray photoemission spectroscopy (XPS)**

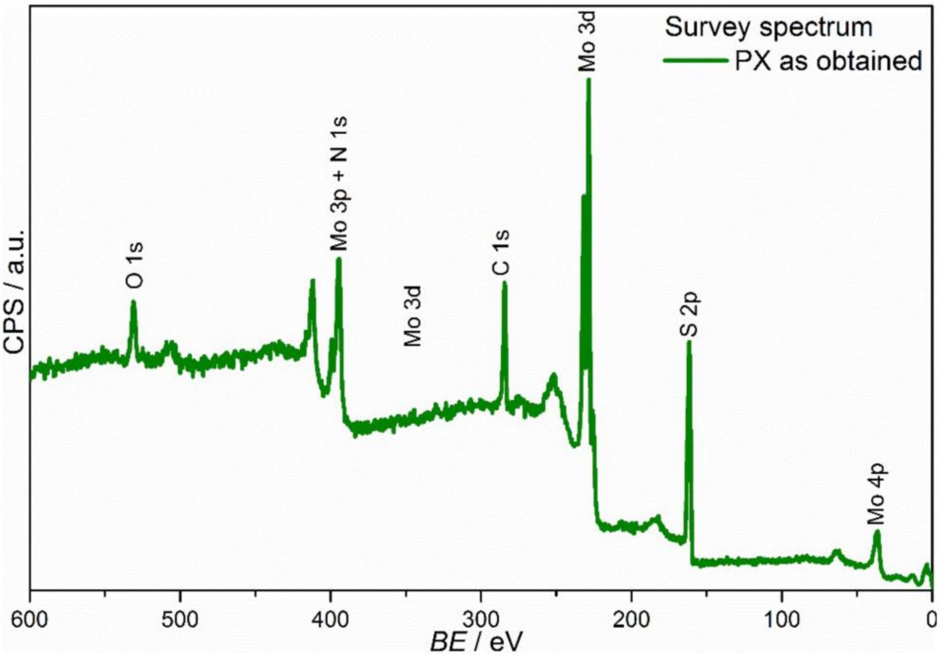

**Figure S5.** XPS survey spectrum of PX.

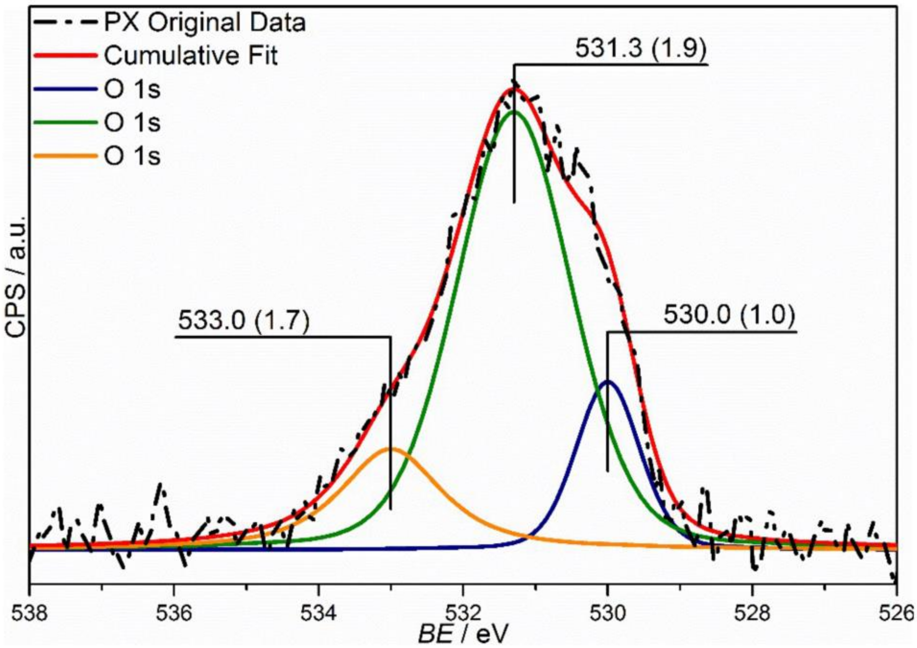

**Figure S6.** XPS measurement of the O 1s region of PX as obtained with the original data (black dash dotted trace), the cumulative fit (red trace) and the O 1s fitted curves (various colors).

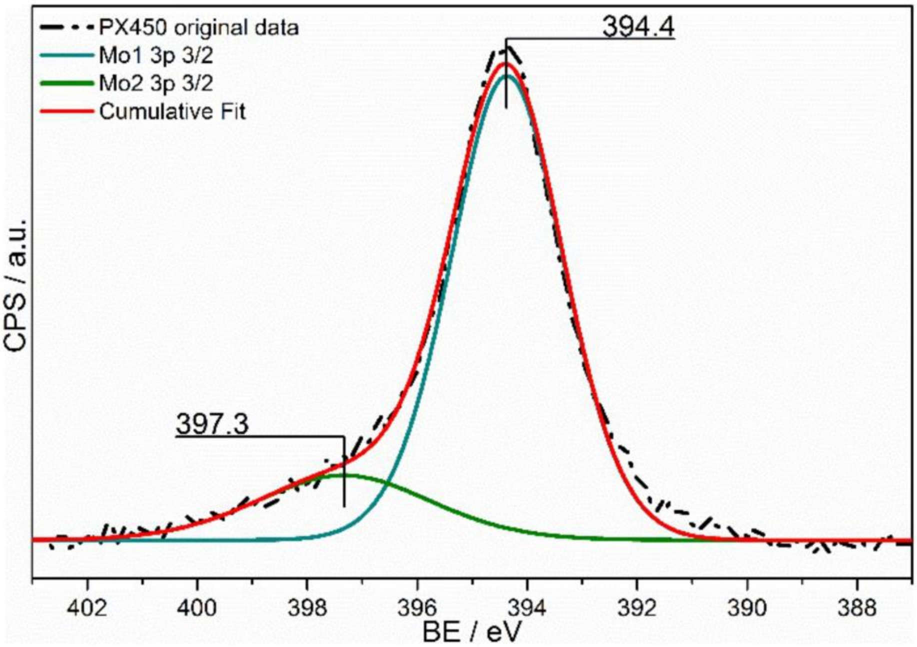

**Figure S7.** XPS measurement of the N 1s region of PX after heating to 450 °C (PX450) with the original data (black dash dotted trace), the cumulative fit (red trace) and the Mo $2p_{3/2}$ fitted curves (green and blue trace).

## 6. TEM analysis

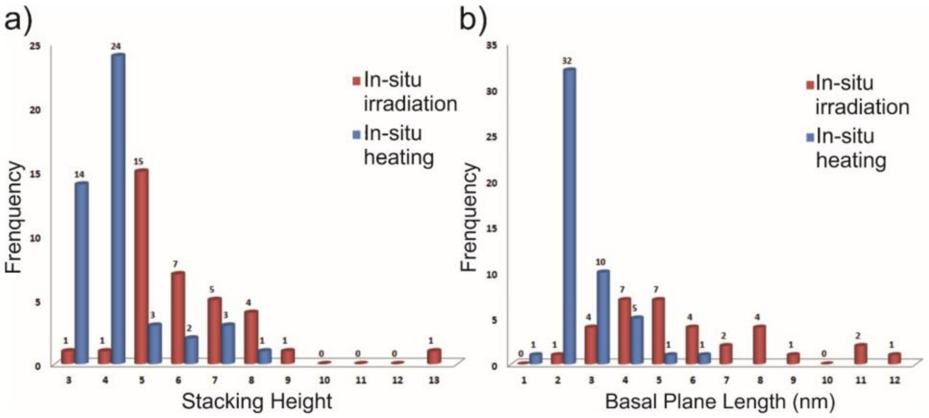

**Figure S8**. (a) Stacking height distribution counted from the HRTEM micrograph where PX was under in-situ irradiation after 1 hour (red column), and from the micrographe where the sample was in-situ heated to 500 °C (blue column). (b) Basal plane length distribution of the in-situ irraditated (red column) and in-situ heated (blue column) PX sample.

### 7. Thermal analyses (DTA/TG)

The thermal decomposition reaction of PX was studied with DTA-TG up to 900 °C in inert atmosphere (heating rate: 4 K/min; **Figure S9**). The weight loss starts at relatively low temperatures and a not well resolved step occurs at about 350 °C. During this decomposition reaction several N containing species such as $NH_3$ and $N_2H_4$ are emitted from the sample (MS spectra not shown here). Above about 350 °C another mass loss of about 3.3 % is accompanied by an exothermic event in the DTA curve indicative for the onset of crystallization of $MoS_2$. For the thermal decomposition of ATM it is proposed that $MoS_3$ forms as an intermediate material[4,5] followed by decomposition of $MoS_3$ and crystallization of $MoS_2$ which is also accompanied by an exothermic event. The XRD pattern of the compound heated to 450 °C (Fig. 2) shows the presence of highly disordered $MoS_2$ slabs supporting the assumption that the exothermic event is caused by the crystallization process. In the temperature range from 400 to 900 °C only a small weight loss of about 2 % occurs which may be due to the emission of material incorporated between the expanded van der Waals gaps (see discussion above). The formation of $MoS_2$ slabs also matches the XPS measurements of PX heated to 450 °C, where a new Mo species occurred with a binding energy matching with Mo in the oxidation state +IV while the two other species vanished.

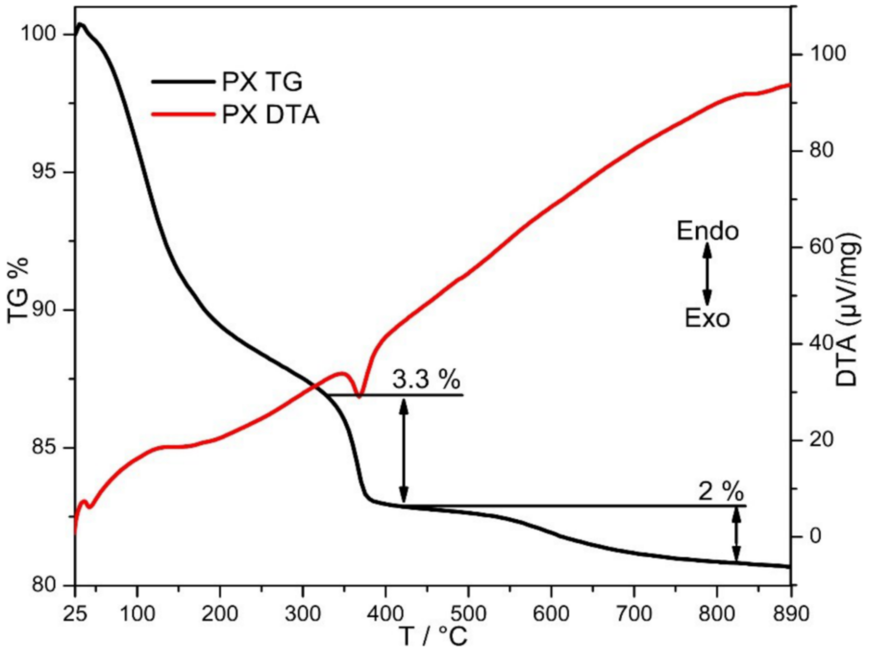

**Figure S9.** Thermal analysis (DTA/TG) of PX up to 900 °C.

Another set of heating experiments has been conducted where the temperature has been raised successively to specific values and the respective samples were directly examined via elemental analyses (Table S1).

**Table S1**. Heating experiments of PX to various temperatures and results of the elemental analyses.

| Sample | Heating temperature / °C | N % | H % | N : H molar ratio |
|---|---|---|---|---|
| PX | --- | various | various | Between 1 : 4 and 1:5 |
| PX100 | 100 | 4.95 | 1.41 | 1 : 4.0 |
| PX200 | 200 | 4.01 | 0.95 | 1 : 3.3 |
| PX300 | 300 | 2.98 | 0.51 | 1 : 2.4 |
| PX340 | 340 | 2.03 | 0.31 | 1 : 2.2 |
| PX350 | 350 | 1.98 | 0.28 | 1 : 2.0 |
| PX360 | 360 | 1.50 | 0.16 | 1 : 1.4 |

The as prepared PX contains ratios of N : H between 1 : 4 and 1 : 5. This depends on the sample as the nitrogen and hydrogen contents are varying. Upon heating the sample loses both N and

H, but H at a larger rate. Thus the molar ratio of N : H reaches 1 : 2.0 exactly at 350 °C, which is the temperature of crystallization. This ratio fits perfectly to hydrazine ($N_2H_4$) and gives another hint that up to that crystallization hydrazine is involved in the material. Another $NH_x$ species seems to be present in the as prepared compound as well but is emitted upon heating prior to hydrazine.

## 8. Visible-light driven hydrogen evolution

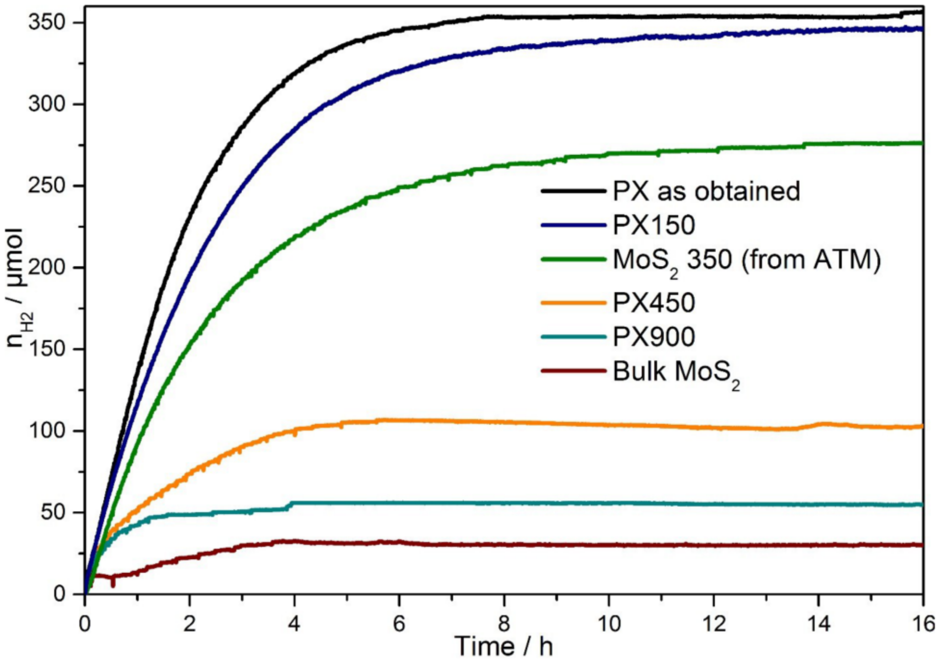

**Figure S10.** Development of the $H_2$ production during 16 hours of irradiation of PX as obtained (black trace), three heated samples (150 °C dark blue trace, 450 °C orange trace, 900 °C light blue trace), commercial bulk $MoS_2$ (dark red trace), and nanocrystalline $MoS_2$ prepared via a thermal decomposition of ATM at 350 °C for comparison (green trace).

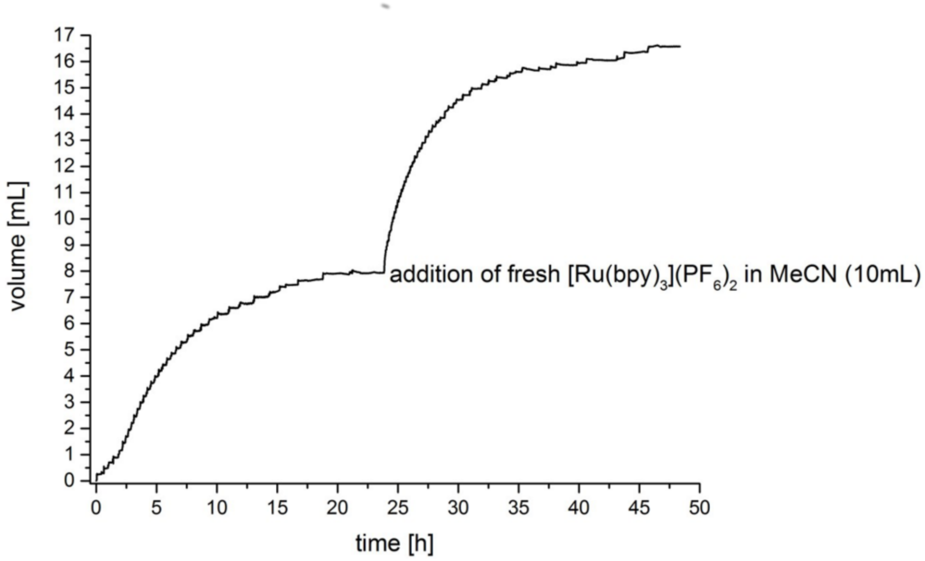

**Figure S11.** Depiction of a measurement of PX and the deactivation of the photosensitizer and addition of fresh PS to reinitialize the reaction.

The deactivation of the Ru dye leads to a retardation of the whole reaction. To proof that the photosensitizer is the weak component it was reapplied after the reaction had completely stopped after 25 h of reaction. After the PS was added, the system had time to equilibrate and then the reaction was reinitialized with light, which started the reaction immediately. This proofed that the catalyst is stable under the reaction conditions.

---

[1] S. Baskaran, C. Sivasankar, *J. Mol. Catal. A Chem.* **2013**, 370, 140-144.

[2] H. Vrubel, V. H. C. Verzenhassi, S. Nakagaki, F. S. Nunes, *Inorg. Chem. Commun.* **2008**, 11, 1040-1043.

[3] T. Weber, J. C. Muijsers, J. H. M. C. van Wolput, C. P. J. Verhagen, J. W. Niemantsverdriet, *J. Phys. Chem.* **1996**, 100, 14144-14150.

[4] A. Müller, T. P. Prasad, R. Menge, *Z. Anorg. Allg. Chem.* **1972**, 391, 107-112.

[5] T. P. Prasad, E. Diemann, A. Müller, *J. Inorg. Nucl. Chem.* **1973**, 35, 1895-1904.

## 4.2 Cokatalysatoren auf Basis von weiteren Übergangsmetallsulfiden und –oxiden

### 4.2.1 Synthese von neuen [Ni(aepa)$_2$]-Verbindungen und deren fotokatalytischen Eigenschaften für die $H_2$-Entwicklung

Zusammenfassung der Veröffentlichung „From Zero- to Three-Dimensional Thioantimonates: [Ni(aepa)$_2$]$_3$Sb$_6$S$_{12}$ (aepa = $C_5H_{15}N_3$ = N-(aminoethyl)-1,3-propandiamine), Containing the Unique [Sb$_6$S$_{12}$]$^{6-}$ Cyclic Anion, [Ni(aepa)$_2$]$_6$(Sb$_3$S$_6$)$_2$(SO$_4$)$_3$*2H$_2$O, with Isolated [Sb$_3$S$_6$]$^{3-}$ anions and [Ni(aepa)$_2$]Sb$_4$S$_7$, Characterized by a Three-Dimensional Network Structure”. Dieser Artikel wurde in der Zeitschrift “Crystal Growth & Design” (DOI: 10.1021/cg201122e) 2011 veröffentlicht.

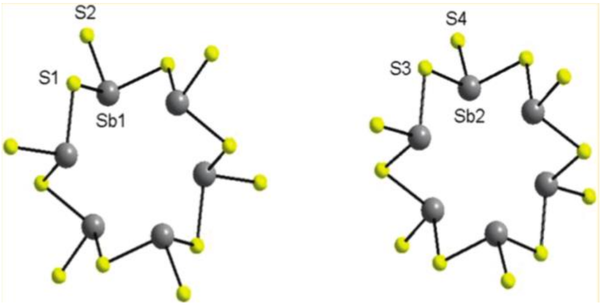

**Abb. 28: Zwei unterschiedliche [Sb$_6$S$_{12}$]$^{6-}$-Anionen in [Ni(aepa)$_2$]$_3$Sb$_6$S$_{12}$.**

Vier neue Verbindungen auf Basis von [Ni(aepa)$_2$]$^{2+}$ wurden in dieser Arbeit unter solvothermalen Bedingungen hergestellt und mit Einkristallstrukturanalyse charakterisiert. Fotokatalytische Untersuchungen wurden mit [Ni(aepa)$_2$]$_3$Sb$_6$S$_{12}$ und [Ni(aepa)$_2$]Sb$_4$S$_7$ durchgeführt. Der erstgenannte Komplex kristallisiert in der Raumgruppe $R\bar{3}$ mit sechs Formeleinheiten pro Elementarzelle. Dabei bilden zwei kristallographisch unabhängige und neuartige [Sb$_6$S$_{12}$]$^{6-}$ - heterocyclische Anionen und ein verzerrt oktaedrischer [Ni(aepa)$_2$]$^{2+}$ - Komplex in der *mer-fac* Konformation die Baueinheiten der Kristallstruktur. Die Verknüpfung der [Sb$_6$S$_{12}$]$^{6-}$ - Anionen erfolgt über die Ecken der SbS$_3$–Pyramiden mit unterschiedlichen geometrischen Parametern für die zwei unabhängigen Heterocyclen. In [Ni(aepa)$_2$]Sb$_4$S$_7$ sind vier Formeleinheiten pro Elementarzelle vorhanden und die Verbindung kristallisiert in der Raumgruppe C2/*c*. Sb$_4$S$_8$$^{4-}$-Ketten sind entlang (110) und ($\bar{1}$10) vorhanden, welche aus über Sb$_2$S$_2$ verknüpfte [Sb$_4$S$_8$]$^{8-}$-Baugruppen bestehen. Durch Verknüpfung der

Ketten über S-Atome entsteht ein 3-dimensionales Netzwerk mit der Formel $[Sb_4S_7]^{2-}$. Ober- und unterhalb von $Sb_{14}S_{14}$-Ringen sind die $[Ni(aepa)_2]^{2+}$ - Komplexe angeordnet. Die fotokatalytischen Ergebnisse fallen sehr unterschiedlich aus. Die Aktivität von $[Ni(aepa)_2]Sb_4S_7$ (565 µmol $h^{-1}$ $g^{-1}$) ist um fast sechs Größenordnungen größer als von $[Ni(aepa)_2]_3Sb_6S_{12}$ (97 µmol $h^{-1}$ $g^{-1}$).

B. Seidlhofer, J. Djamil, C. Näther, W. Bensch, *Cryst. Growth. Des.* **2011**, *11*, 5554-5560. - Reproduziert mit der Erlaubnis der American Chemical Society.

CRYSTAL GROWTH & DESIGN
ARTICLE
pubs.acs.org/crystal

# From Zero- to Three-Dimensional Thioantimonates: [Ni(aepa)$_2$]$_3$Sb$_6$S$_{12}$ (aepa = C$_5$H$_{15}$N$_3$ = *N*-(aminoethyl)-1, 3-propandiamine), Containing the Unique [Sb$_6$S$_{12}$]$^{6-}$ Cyclic Anion, [Ni(aepa)$_2$]$_6$(Sb$_3$S$_6$)$_2$(SO$_4$)$_3\cdot$2H$_2$O, with Isolated [Sb$_3$S$_6$]$^{3-}$ anions and [Ni(aepa)$_2$]Sb$_4$S$_7$, Characterized by a Three-Dimensional Network Structure

Beatrix Seidlhofer, John Djamil, Christian Näther, and Wolfgang Bensch*

Institut für Anorganische Chemie, Christian-Albrechts-Universität Kiel, Max-Eyth-Strasse 2, D-24118 Kiel, Germany

*Supporting Information*

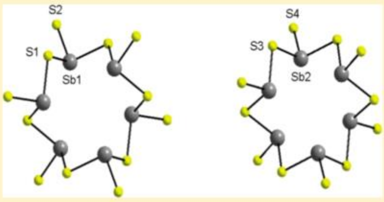

**ABSTRACT:** The new thioantimonates [Ni(aepa)$_2$]$_3$Sb$_6$S$_{12}$ (**1**), [Ni(aepa)$_2$]$_6$(Sb$_3$S$_6$)$_2$(SO$_4$)$_3\cdot$2H$_2$O (**2**), and [Ni(aepa)$_2$]Sb$_4$S$_7$ (**3**) (aepa = C$_5$H$_{15}$N$_3$ = *N*-(aminoethyl)-1,3-propandiamine) were obtained under solvothermal conditions by slightly varying the reaction conditions. In all compounds the [Ni(aepa)$_2$]$^{2+}$ complexes were formed in situ during the chemical reactions. Compound **1** features the new unique [Sb$_6$S$_{12}$]$^{6-}$ cyclic anion composed by vertex-linked SbS$_3$ trigonal pyramids. This [Sb$_6$S$_{12}$]$^{6-}$ cyclic anion represents the largest isolated thioantimonate(III) anion. In the structure of [Ni(aepa)$_2$]$_6$(Sb$_3$S$_6$)$_2$(SO$_4$)$_3\cdot$2H$_2$O, three SbS$_3$ units are corner-linked to form a Sb$_3$S$_3$ hetero ring adopting a twist conformation. Additionally, the new nickel complex [Ni(aepa)$_2$]$_2$Cl$_2$ was isolated from the same reaction slurry and was structurally characterized. Compound **3** represents a rare example of a three-dimensional thioantimonate(III) network. The [Sb$_4$S$_7$]$^{2-}$ anion contains large Sb$_{14}$S$_{14}$ rings with dimension of 6.1 × 16.1 Å$^2$. The structure directing effect of the in situ formed cations is obvious because [Ni(aepa)$_2$]$^{2+}$ molecules are located in pairs above and below the large rings. The first photocatalytic hydrogen evolution tests exhibit promising results for compound **3**.

## INTRODUCTION

Thioantimonate chemistry is characterized by a fascinating structural and chemical diversity.[1] One intriguing structural feature is that for a given Sb/S ratio the dimensionality of the thioantimonate anion may range from zero-dimensional (0D) isolated anions to three-dimensional (3D) networks. Analyzing the thioantimonate(III) structures containing charge compensating cations of different sizes and charges, only a moderate influence on the dimensionality could be identified. For instance, 0D Ni$^{2+}$ containing thioantimonates(III) were obtained with diethylenetriamine (dien) as solvent; one-dimensional (1D) chains with ethylenediamine (en), dien, and tris(2-aminoethyl)amine (tren); two-dimensional (2D) layers with 1,2-diaminopropane (1,2-dap), dien, and tren; and 3D networks with en, dien, and 1,4,8,11-tetraazacyclotetradecane (cyclam). This clearly demonstrates that the choice of the size/charge of the solvent/structure director has no effect on the dimensionality of the inorganic part of the compounds. There are no general rules allowing prediction of the chemical composition and/or crystal structure of thioantimonates formed under solvothermal conditions. Thiometallate compound formation was investigated by us applying in situ X-ray scattering and X-ray absorption techniques demonstrating the complexity of the reactions occurring under solvothermal conditions.[2−5]

Concerning the structural chemistry of thioantimonates containing Ni-amine complexes as structure directing and charge balancing agents, two compounds are 0D, namely, [Ni(dien)$_2$]Sb$_4$S$_8$[6] and [Ni(dien)$_2$]$_3$(Sb$_3$S$_6$)$_2$.[7] In the former compound, four SbS$_3$ moieties share common corners to form the [Sb$_4$S$_8$]$^{4-}$ heterocycle.[6] The [Sb$_3$S$_6$]$^{3-}$ anion[7] is constructed by three vertex-linked SbS$_3$ pyramids. Several isolated thioantimonate(V) anions could also be isolated like [Ni(en)$_3$]$_3$(SbS$_4$)(NO$_3$),[8] [Ni(dien)$_2$]$_3$(SbS$_4$)$_2$,[9] (paH)[Ni(tren)SbS$_4$],[10] [Ni(chxn)$_3$]$_3$(SbS$_4$)$_2\cdot$4H$_2$O[11] and [Ni(en)$_3$(enH)]SbS$_4$.[12] Only in (paH)[Ni(tren)SbS$_4$][10] the Ni$^{2+}$ ion is octahedrally surrounded by four N atoms of the amine and by two S atoms of the [SbS$_4$]$^{3-}$ anion. 1D chain anions are found in [Ni(tren)]Sb$_2$S$_4$,[13] [Ni(dien)$_2$]Sb$_4$S$_9$,[14] [Ni(tren)Sb$_4$S$_7$],[15] [Ni(en)$_3$]Sb$_2$S$_4$, and [Ni(en)$_3$]Sb$_4$S$_7$.[16] The compound [Ni(tren)]Sb$_2$S$_4$[13] is a rare example where the Ni$^{2+}$ ion is incorporated in the thioantimonate network via Ni−S bonds.

**Received:** August 26, 2011
**Revised:** September 21, 2011
**Published:** October 10, 2011

dx.doi.org/10.1021/cg201122e | *Cryst. Growth Des.* 2011, 11, 5554–5560

**Table 1. Selected Crystal Data and Refinement Results for Compounds 1−3**

| | **1** | **2** | **3** |
|---|---|---|---|
| empirical formula | $C_{30}H_{90}N_{18}$<br>$Ni_3S_{12}Sb_6$ | $C_{60}H_{184}N_{36}$<br>$Ni_6O_{14}S_{15}Sb_6$ | $C_{10}H_{30}N_6$<br>$NiS_7Sb_4$ |
| formula weight | 1994.55 | 3198.09 | 1004.53 |
| $T$ (K) | 293 | 170 | 293 |
| wavelength (Å) | 0.71073 | 0.71073 | 0.71073 |
| crystal system | trigonal | triclinic | monoclinic |
| space group | $R\bar{3}$ | $P\bar{1}$ | $C2/c$ |
| $a$ (Å) | 22.1486(11) | 13.3436(8) | 14.3884(10) |
| $b$ (Å) | | 14.1266(9) | 12.1193(6) |
| $c$ (Å) | 23.6629(13) | 18.3991(12) | 16.1524(11) |
| $\alpha$ (deg) | 90 | 73.635(7) | 90 |
| $\beta$ (deg) | 90 | 85.432(7) | 94.175(8) |
| $\gamma$ (deg) | 120 | 63.200(7) | 90 |
| volume/(Å$^3$) | 10052.9(9) | 2965.7(3) | 2809.1(3) |
| Z | 6 | 1 | 4 |
| $D_{calc}/(g \cdot cm^{-3})$ | 1.977 | 1.791 | 2.375 |
| $\mu/(mm^{-1})$ | 3.615 | 2.599 | 4.987 |
| collected/independent ($R_{int}$) | 32787/5411 (0.038) | 19111/9945 (0.054) | 16300/2733 (0.033) |
| GOF | 1.067 | 0.935 | 0.835 |
| $R_1$ for $F_o > 4\sigma(F_o)$ | 0.0380 | 0.0406 | 0.0284 |
| $wR_2$ for all reflections | 0.1028 | 0.0850 | 0.0942 |
| max/min $\Delta\rho$ [e Å$^{-3}$] | −1.121/1.028 | −0.662/1.018 | −1.040/1.183 |

$[Ni(dien)_2]Sb_4S_9$[14] is a mixed-valent compound with corner-sharing $Sb(III)S_3$ pyramids and $Sb(V)S_4$ tetrahedra. One $SbS_4$ unit and four $SbS_3$ pyramids are corner- and edge-linked to form the $[Sb_4S_7]^{2-}$ chain in $[Ni(tren)Sb_4S_7]$[15] with $Ni^{2+}$ being in a distorted octahedral environment of four N atoms and two S atoms of a $SbS_3$ pyramid. The thioantimonate anion in $[Ni(en)_3]Sb_2S_4$[16] is made by $SbS_3$ pyramids that are connected via common corners. The $[Sb_4S_7]^{2-}$ chains in $[Ni(en)_3]Sb_4S_7$[16] are composed of vertex-linked $SbS_3$ pyramids forming six-membered $[Sb_3S_6]^{3-}$ units which are joined by a $SbS_3$ pyramid.

2D thioantimonate networks are observed in the structures of $[Ni(dien)_2]_9Sb_{22}S_{42} \cdot 0.5H_2O$,[17] $[Ni(dien)_2]Sb_4S_7 \cdot H_2O$,[18] $[Ni(dien)(tren)]Sb_4S_7$,[15] $[Ni(dien)_2]Sb_6S_{10} \cdot 0.5H_2O$,[19] and $[Ni(1,2\text{-}dap)_3]Sb_4S_7$.[20,21] The main structural feature of $[Ni(dien)_2]_9Sb_{22}S_{42} \cdot 0.5H_2O$[17] is a very large $Sb_{30}S_{30}$ hetero ring. Interestingly, the charge compensating $[Ni(dien)_2]^{2+}$ complexes adopt all three different isomeric forms *s*-, *mer*-, and *u-fac*. The 2D sheet anions $[Sb_4S_7]^{2-}$ in $[Ni(dien)_2]Sb_4S_7 \cdot H_2O$[18] and $[Ni(dien)(tren)]Sb_4S_7$[15] are constructed by fusion of $Sb_4S_4$ and $Sb_8S_8$ rings. $[Ni(dien)_2]Sb_6S_{10} \cdot 0.5H_2O$[19] contains a 32-membered $Sb_{16}S_{16}$ ring formed by $SbS_3$ and $SbS_4$ units. A similar $Sb_{16}S_{16}$ heteroring is condensed in the structure of $[Ni(1,2\text{-}dap)_3]Sb_4S_7$[20,21] leading to the layered network. Only three 3D thioantimonates(III) are known: $[Ni(dien)_2]_3Sb_{12}S_{21} \cdot H_2O$,[18] $[Ni(cyclam)]Sb_4S_7$,[22] and $[Ni(en)_3]Sb_{12}S_{19}$.[19] So-called secondary building units like $Sb_2S_6$, $Sb_2S_5$, $Sb_3S_3$, and $Sb_4S_4$ are joined into layers which are interconnected by S atoms yielding the 3D anion in $[Ni(dien)_2]_3Sb_{12}S_{21} \cdot H_2O$.[18] In $[Ni(cyclam)]Sb_4S_7$,[22] the 3D network is realized by interconnection of perpendicular arranged $Sb_4S_8{}^{4-}$ chains. In $[Ni(en)_3]Sb_{12}S_{19}$,[19] $SbS_3$ and $SbS_4$ units share corners and edges and form $Sb_2S_2$, $Sb_3S_7$, and $Sb_6S_{12}$ secondary building units and they are connected to the final 3D framework.

As demonstrated above, thioantimonates with the $[Ni(dien)_2]^{2+}$ complex exhibit a rich structural chemistry. In our work we altered the reaction conditions of these compounds and applied the larger amine *N*-(aminoethyl)-1,3-propandiamin (aepa) containing an additional C atom compared to dien. In-situ formed $[Ni(aepa)_2]^{2+}$ complexes are more bulky than $[Ni(dien)_2]^{2+}$ cations leading to the formation of compounds with different network topologies. Three new thioantimonates(III) could be synthesized displaying different dimensionalities of the inorganic anion: $[Ni(aepa)_2]_3Sb_6S_{12}$ (**1**) (0D), $[Ni(aepa)_2]_6(Sb_3S_6)_2(SO_4)_3 \cdot 2H_2O$ (**2**) (0D), and $[Ni(aepa)_2]Sb_4S_7$ (**3**) (3D). The compound $[Ni(aepa)_2]_3Sb_6S_{12}$ features a novel and hitherto not observed $[Sb_6S_{12}]^{6-}$ cyclic anion. As a byproduct, the complex $[Ni(aepa)_2]_2Cl_2$ (**2.1**, see Supporting Information) could be isolated from the reaction slurry of $[Ni(aepa)_2]_6(Sb_3S_6)_2(SO_4)_3 \cdot 2H_2O$ and was structurally characterized.

## ■ EXPERIMENTAL SECTION

**Materials and General Measurements.** All reagents were purchased from commercial suppliers and were used as received. Thermogravimetric analyses were performed on a Netzsch STA-429 DTA-TG device. All data were corrected for buoyancy and current effects and were done with heating rates of 4 K min$^{-1}$ in $Al_2O_3$ crucibles under dynamic argon atmosphere with a flow rate of 75 mL min$^{-1}$. The Raman spectra were measured from 100 to 3500 cm$^{-1}$ with a Bruker IFS 66 Fourier transform Raman spectrometer with a wavelength of 514.5 nm. X-ray powder diffraction patterns were measured on a STOE STADI-P with Cu−K$\alpha_1$ radiation. The photocatalytic reactions were performed in pyrex cells with 10 mg of **1** respectively **3** suspended in 10 mL of a mixture containing triethylamine (3.8 mL), distilled water (1.4 mL), and $[Ru(bpy)_3](PF_6)_2$ (0.01 M) as sensitizer in acetonitrile (4.8 mL). The suspension was irradiated with a 250 W Fe-doped metal halogen lamp without an optical filter for 2 h. The developed gas was quantified by gas chromatography (molecular sieve pillar: 5 Å, TCD) with Ar as carrier gas. Prior to the catalytic measurements, the samples were ground in a mortar.

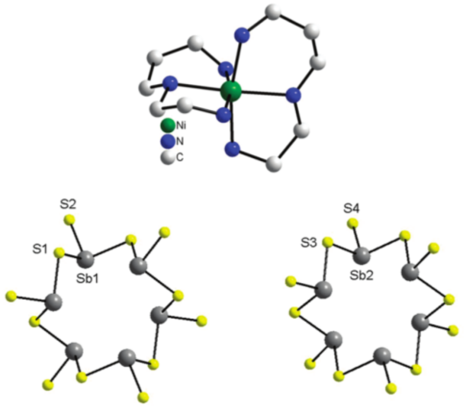

**Figure 1.** The $[Ni(aepa)_2]^{2+}$ complex (top) and the two independent $[Sb_6S_{12}]^{6-}$ cyclic anions (bottom) in the structure of $[Ni(aepa)_2]_3Sb_6S_{12}$.

**Crystal Structure Determination.** The single crystal X-ray intensity data were collected at room temperature (**1**, **2.1**, and **3**) and 170 K (**2**) on an IPDS-1 or IPDS-2 Imaging Plate Diffraction System from STOE & Cie with graphite monochromated Mo$K_\alpha$ radiation (IPDS-1 for **1**, **2** and **3**, IPDS-2 for **2.1**). Selected crystal data and details of the structure determination are summarized in Table 1. The raw intensities were corrected for Lorenz and polarization effects. A numerical absorption correction was performed for **2.1**. The structures were solved with direct methods using SHELXS-97,[23] and the refinement was performed against $F^2$ using SHELXL-97.[24] All non-hydrogen atoms except disordered C and N atoms in **1** and **3** and C, N, S, and O atoms in **2** were refined using anisotropic displacement parameters. The H atoms were positioned with idealized geometry and refined isotropically using a riding model. Crystallographic data have been deposited with the Cambridge Crystallographic Data Centre (CCDC: 844792−844795). Copies of the data may be obtained free of charge on application to CCDC, 12 Union Road, Cambridge CB2 1E2, U.K. (fax int. code +(44)01223/336033 or e-mail deposit@chemcrys.cam.ac.uk).

**Synthesis of $[Ni(aepa)_2]_3Sb_6S_{12}$.** Single crystals of **1** were prepared under solvothermal conditions in Teflon-lined stainless steel autoclaves. A mixture of S (2 mmol, 0.064 g), Sb (0.5 mmol, 0.061 mg), Ni (0.75 mmol, 0.440 mg) and 4 mL of 100% *N*-(aminoethyl)-1,3-propanediamine (aepa) was heated for 7 days at 130 °C. Dark red rhombohedral crystals were obtained (yield: 40% based on Sb). Optical bandgap = 1.9 eV. Elemental analysis calcd for **1** ($C_{30}H_{90}N_{18}Ni_3S_{12}Sb_6$, 1994.55): C, 18.07; H, 4.55; N, 12.64%. Found: C, 18.57; H, 4.67; N, 12.65%. IR ($cm^{-1}$): 3449(m), 3204(m), 3106(m), 2914(m), 2858(m), 1597(m), 1450(w), 1047(m). Raman ($cm^{-1}$): 370(m), 330(s), 239(w), 154(m), 117(m).

**Synthesis of $[Ni(aepa)_2]_6(Sb_3S_6)_2(SO_4)_3 \cdot 2H_2O$.** Compound **2** was prepared under conditions identical to that of **1** with the exception that Ni was replaced by $NiSO_4 \cdot 6\ H_2O$ (0. 75 mmol, 0.197 g). The compound crystallized as yellow needles (yield: 30% based on Sb). A minor phase consisting of violet crystals was observed besides **2**, which was identified as the new complex $[Ni(aepa)_2]Cl_2$. We suppose that the Teflon liner was slightly contaminated with $Cl^-$ ions from the cleaning procedure using nitrohydrochloric acid. The synthesis of the complex was also successful applying $NiCl_2 \cdot 6\ H_2O$ (0.75 mmol, 0.178 g) as source. Both compounds are not stable after removing from the mother liquor.

**Synthesis of $[Ni(aepa)_2]Sb_4S_7$.** Single crystals of **3** were synthesized applying S (3 mmol, 0.096 g), Sb (1 mmol, 0.122 g), Ni (1 mmol, 0.059 mg), and 2 mL of 50% aepa. The reaction slurry was heated for 10 days at 140 °C giving orange rhombohedral crystals (yield: 70% based on Sb). The solid products were filtered and washed with water and acetone. Optical bandgap = 2.4 eV. Elemental analysis calcd for **3** ($C_{10}H_{30}N_6NiS_7Sb_4$, 1004.53): C, 11.83; H, 2.91; N, 8.09%. Found: C, 11.96; H, 3.01; N, 8.37%. IR ($cm^{-1}$): 3450(m), 3232(m), 2913(m), 2864(m), 1635(m), 1585(m), 1465(w), 1040(m). Raman ($cm^{-1}$): 346(s), 316(s), 294(m), 238(m), 166(m), 137(m).

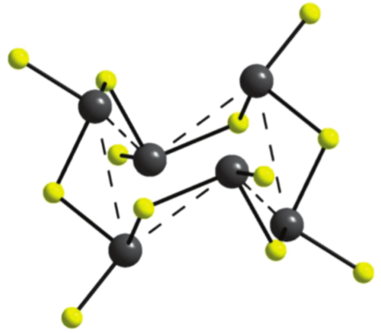

**Figure 2.** The $[Sb_6S_{12}]^{6-}$ unit showing the chair conformation of the arrangement of the Sb atoms (dashed line).

## ■ RESULTS AND DISCUSSION

**Crystal Structures.** The new compound $[Ni(aepa)_2]_3Sb_6S_{12}$ (**1**) crystallizes in the rhombohedral space group $R\bar{3}$ (Table 1). The crystal structure consists of two crystallographically independent hitherto never observed $[Sb_6S_{12}]^{6-}$ anions and one charge balancing $[Ni(aepa)_2]^{2+}$ complex in the *mer*-fac conformation (Figure 1). Six $SbS_3$ pyramids share common corners to form $Sb_6S_6$ hetero rings (Figure 1) with terminal Sb−S atoms in trans-configuration and the Sb atoms being arranged to adopt the chair conformation (Figure 2, dotted line). The Sb−S bonds range from 2.3337(14) to 2.4912(15) Å with $Sb-S_{term}$ being significantly shorter than $Sb-S_{br}$ indicating some double bonding character. Distances and angles (Table 1, Supporting Information) are in the range reported for isolated thioantimonates(III).[6,7] The dimensions of the two cyclic anions are signficantly different with $Sb(1)\cdots Sb(1) = 5.8412(2)$ and $Sb(2)\cdots Sb(2) = 5.6085(2)$ Å. Hence, the geometric parameters of the two $[Sb_6S_{12}]^{6-}$ anions are slightly different (Table 1, Supporting Information). The anions are stacked along the *c* axis with four heterocycles laying on the corners and two in the middle of the unit cell (Figure 3). Along [110], a chain-like arrangement of the anions is observed.

The $Ni^{2+}$ cation is in a distorted octahedral coordination of two amine molecules (Ni−N: 2.129(5)−2.173(8) Å; N−Ni−N: 81.37(18)−175.4(2)°). Bonds and angles are in the range reported for such $Ni^{2+}$ amine complexes.[6−22,25−27]

The $[Sb_6S_{12}]^{6-}$ anions are surrounded by the cations and hydrogen bonding interactions lead to the formation of a 3D network.

The anion in **1** belongs to the class of thioantimonates(III) with the Sb/S ratio of 1:2 and represents the first compound with the $[Sb_6S_{12}]^{6-}$ moiety. Examples for this Sb:S ratio are $(CH_3NH_3)_2Sb_2S_4$[28] with a $[Sb_2S_4]^{2-}$ chain anion or $[Co(tren)]Sb_2S_4$[13] with a layered $[Sb_2S_4]^{2-}$ ion hosting the $[Co(tren)]^{2+}$ complex in a large

$Sb_{10}S_{10}$ ring via Co−S bond formation. One-dimensional thioantimonate anions with composition $[Sb_2S_4]^{2-}$ are observed in $[Ni(tren)]Sb_2S_4$[13] and in the two nonisostructural thioantimonates $[Mn(tren)]Sb_2S_4$.[29] Finally, $[SbS_2]^-$ chains are found in $[TM(en)_3]Sb_2S_4$ (TM = Co, Ni).[16]

$[Ni(aepa)_2]_6(Sb_3S_6)_2(SO_4)_3 \cdot 2H_2O$ (**2**) crystallizes in the triclinic spacegroup $P\bar{1}$ (Table 1). Three crystallographically independent $[Ni(aepa)_2]^{2+}$ cations, one heterocyclic $[Sb_3S_6]^{3-}$ anion, 1.5 $SO_4^{2-}$ anions, and two $H_2O$ molecules are in the crystal structure (Figure 4). The $S(8)O_4^{2-}$ ion is located on a mirror plane, whereas all remaining constituents are on general positions. All three unique $Ni^{2+}$ cations are in a distorted octahedral environment of six N atoms of two aepa ligands adopting the *mer*-fac conformation (Figure 4). The Ni−N distances (2.120(5)−2.179(5) Å) and N−Ni−N angles (80.2(3)−172.8(3)°) (Table 2, Supporting Information) match well with literature data.[6−22,25−27] The geometric parameters of the two $SO_4^{2-}$ anions are normal.

Three pyramidal $SbS_3$ units are vertex-linked forming the $[Sb_3S_6]^{3-}$ anion (Figure 4) with geometric parameters matching those reported for other isolated thioantimonates.[6,7]

The anions and cations are stacked parallel to the *a* axis (Figure 5). Two Ni(1) and two Ni(3) complexes surround the $S(7)O_4^{2-}$ anion, and this cation−anion arrangement is directed along [010] with intervening $S(8)O_4^{2-}$ anions. The heterocyclic $[Sb_3S_6]^{3-}$ units and Ni(2) centered complexes form separate rods along this direction.

The $[Sb_3S_6]^{3-}$ anion was only observed in $[Ni(dien)_2]_3(Sb_3S_6)_2$, and compound **2** represents the second example with this anion.[7] Whereas in **2** the $Sb_3S_3$ ring adopts a twist conformation, the anion in $[Ni(dien)_2]_3(Sb_3S_6)_2$ adopts a boat-like conformation (Figure 6). We note that in extended thioantimonates such $Sb_3S_3$ rings occur mostly in chair- and/or boat-like conformations as secondary building units.[30−43] The twist-like conformation like in the title compound was only observed in the two compounds $[Ni(dien)_2]_3Sb_{12}S_{21} \cdot H_2O$ and $[Ni(dien)_2]_2Sb_4S_9$.[14,18]

A 3D arrangement of the anions and cations is achieved by N−H···S (2.4531(3)−2.9924(2) Å) and N−H···O (1.8076(1)−2.9994(2) Å) intermolecular hydrogen bonding interactions.

The new compound $[Ni(aepa)_2]Sb_4S_7$ (**3**) crystallizes in the monoclinic space group $C2/c$ (Table 1). In contrast to **1** and **2** the structure of **3** contains a $Sb(1)S_4$ unit besides a $Sb(2)S_3$ trigonal pyramid (Figure 7). The Sb−S bond lengths of the $SbS_3$ moiety (2.3982(1)−2.4813(1) Å) are shorter than in the $SbS_4$

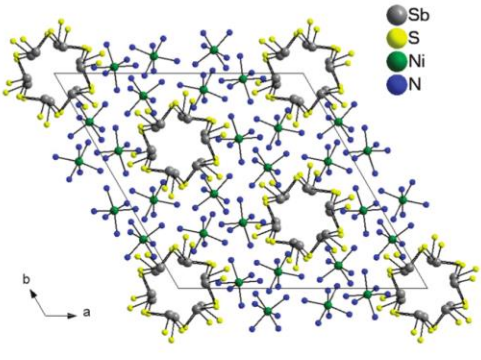

**Figure 3.** Crystal structure of $[Ni(aepa)_2]_3Sb_6S_{12}$ viewed along the *c* axis (hydrogen and carbon atoms are omitted for clarity).

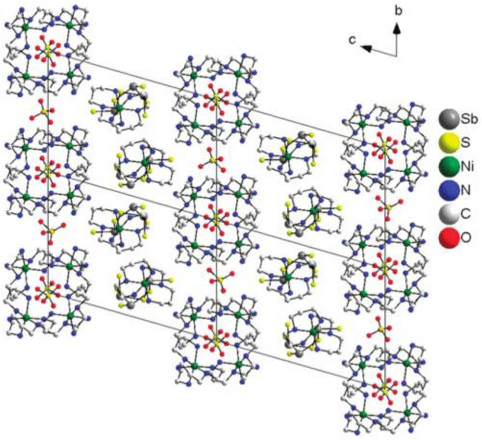

**Figure 5.** Crystal structure of $[Ni(aepa)_2]_6(Sb_3S_6)_2(SO_4)_3 \cdot 2H_2O$ viewed along the *a* axis (hydrogen atoms are omitted for clarity).

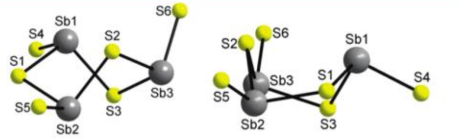

**Figure 6.** The twist- and boat-like conformation of the $[Sb_3S_6]^{3-}$ anion in $[Ni(aepa)_2]_6(Sb_3S_6)_2(SO_4)_3 \cdot 2H_2O$ (left) and $[Ni(dien)_2]_3(Sb_3S_6)_2$[7] (right).

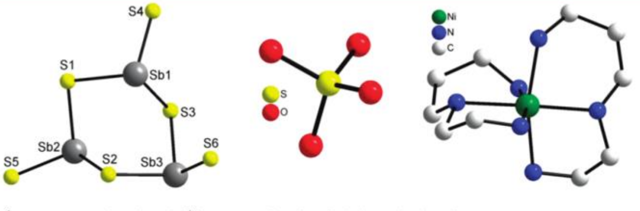

**Figure 4.** $Sb_3S_6^{3-}$ and $SO_4^{2-}$ anions and $[Ni(aepa)_2]^{2+}$ cation in $[Ni(aepa)_2]_6(Sb_3S_6)_2(SO_4)_3 \cdot 2H_2O$.

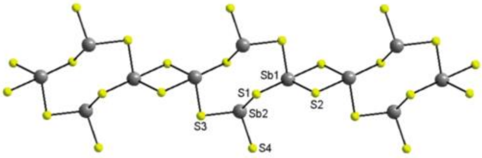

**Figure 7.** The $Sb_4S_8{}^{4-}$ chain constructed by the condensation of the annular $Sb_4S_{10}{}^{8-}$ cluster with the $Sb_2S_2$ ring.

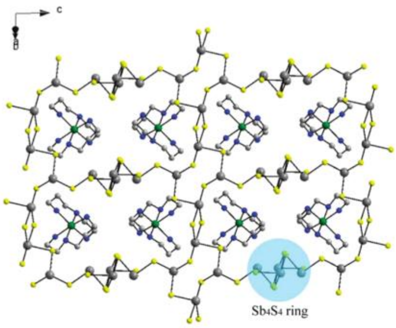

**Figure 8.** $Sb_{14}S_{14}$ ring formed by the condensation of $Sb_2S_2-Sb_4S_4-S(4)-Sb_4S_4-S(4)-Sb_4S_4-Sb_2S_2$ and location of the $[Ni(aepa)_2]^{2+}$ complexes in the channels along $[1\bar{1}0]$ (hydrogen atoms are omitted for clarity).

unit with two long (2.6885(2) and 2.8021(2) Å) and two short (2.3987(1) and 2.4580(2) Å) bonds (Table 3, Supporting Information). This bonding pattern is typical for $SbS_4$ groups and was observed in several other thioantimonates(III).[8,14,15,17,18,20] We note that the Sb−S bonds in the $[Sb^VS_4]^{3-}$ anion are much shorter and scatter around 2.3 Å.[8−12,44−49] Interestingly, no further Sb···S contacts below 3 Å are found in the structure of **3**.

Alternating vertex-linked $SbS_3$ and $SbS_4$ units form a $Sb_4S_{10}{}^{8-}$ cluster. Neighboring clusters are condensed by $Sb(1)_2S(2)_2$ rings yielding $Sb_4S_8{}^{4-}$ chains directed along [110] and $[\bar{1}10]$ (Figure 7). These chains are further joined by the S(4) atom along [001] to form the final 3D $[Sb_4S_7]^{2-}$ network. The connection mode generates $Sb_{14}S_{14}$ rings (Figure 8) with approximate dimensions of 6.1 × 16.1 Å measured from coordinate to coordinate. A system of three mutually perpendicular channels can be identified hosting the complex cations. The complexes are not located within the plane of the $Sb_{14}S_{14}$ but are found above and below the plane (Figure 8).

The charge balancing octahedral $[Ni(aepa)_2]^{2+}$ complex (Ni−N bonds: 2.138(4)−2.153(4) Å; N−Ni−N angles: 89.33(16)−170.96(16)°) adopts the *mer*-fac configuration.[6−22,25−27] Hydrogen bonds (S···H: 2.63 to 2.96 Å, N−H···S angles: 136.16−170.39°) are formed between the amine groups of the complex and the thioantimonate network, and these interactions may stabilize the arangement of the complexes in the structure.

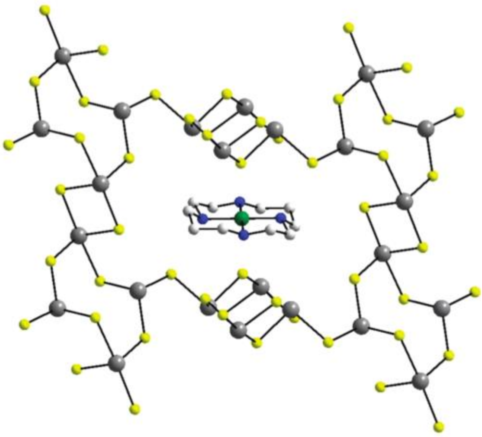

**Figure 9.** Location of the $[Ni(cyclam)]^{2+}$ complex in $[Ni(cyclam)]Sb_4S_7$ (**4**).

The 3D network topology of **3** is similar to that of $[cyclamH_2]Sb_4S_7$, $[Ni(cyclam)]Sb_4S_7$ (**4**), and $[Co(cyclam)]_x$-$[cyclamH_2]_{1-x}Sb_4S_7$.[22] But there are significant differences in the unit cell parameters, Sb−S bond lengths, and S−Sb−S angles of the networks. This may be explained by the different sizes of the structure directing molecules located in the channels. In the title compound, the dimensions of the $[Ni(aepa)_2]^{2+}$ complex measure about 4.2 × 6.4 Å, whereas the extension of the $[Ni(cyclam)]^{2+}$ cation in **4** is 3.9 × 5.9 Å. In addition, the "flat" $[Ni(cyclam)]^{2+}$ complex in **4** is located within the plane of the $Sb_{14}S_{14}$ ring (Figure 9), whereas two cations in **3** reside above and below the ring.

The different arrangements of the complexes in the two compounds lead to significantly different diameters of the $Sb_{14}S_{14}$ rings: 12.6 × 6.1 Å in **4** vs 16.1 × 6.1 Å in **3**. All these differences result in a volume expansion of about 355 Å$^3$ compared to that of **4** (Figure 9). Calculation of the potential solvent area yields 1262 Å$^3$ for **4** and 1633 Å$^3$ for **3**, that is, roughly 51% of the unit cell volume of **4** is occupied by the cation and 58% in **3**.

**Photocatalytic Properties.** In preliminary test reactions for the photocatalytic generation of hydrogen the application of 0.005 mmol of **1** afforded 1.94 $\mu$mol of $H_2$ (0.97 $\mu mol \cdot h^{-1}$ $H_2$ respectively 97 $\mu mol \cdot h^{-1} \cdot g^{-1}$) and 0.01 mmol of **3** produced about 11.3 $\mu$mol of $H_2$ (5.65 $\mu mol \cdot h^{-1}$ $H_2$ respectively 565 $\mu mol \cdot h^{-1} \cdot g^{-1}$). Both values are comparable or even better than those reported for several transition metal sulphides (photocatalytic experiments without a cocatalyst).[50] Unfortunately, both materials undergo photocorrosion which is a well-known phenomenon for metal sulphide catalysts.[50−56] Often photocatalytic reaction of metal sulphides are performed in the presence of sacrificial ions like $S^{2-}$ or $SO_3{}^{2-}$ to suppress the photocorrosion process.[50,53,54] Note that the $[Ru(bpy)_3](PF_6)_2$ acts only as photosensitizer to harvest the radiation emitted by the halogen lamp. A sensitizer is typically used together with an electron relay. In such a system, the excited photosensitizer is quenched by the electron relay through an electron transfer, generating a reactive species which will then reduce protons to diatomic hydrogen gas.

## ■ CONCLUSIONS

The results presented here demonstrate that the size and/or charge of the structure directing molecules have no obvious effect on the dimensionality of the thioantimonate(III) network.

All three compounds were obtained with in situ formed $[\mathrm{Ni(aepa)}]^{2+}$ complexes as counterions and structure directing molecules. The main factors determining the dimensionality are the reaction temperature, reaction time, educt ratio, amine concentration, and volume as well as the sources applied in the reaction slurries. Analyzing the reaction conditions used for the synthesis of compounds **1**−**3** together with those reported in literature, there are no obvious rules at hand allowing prediction of the composition and dimensionality of the reaction products. As there are only a few 3D thioantimonates(III) containing Ni-amine complexes, their formation might be more difficult with such large sized metal-amine complexes than for 0 to 2D thioantimonates(III). The structure of compound **1** features the hitherto never observed $[\mathrm{Sb_6S_{12}}]^{6-}$ cyclic anion which is the largest isolated thioantimonate(III) anion. The $[\mathrm{Sb_3S_6}]^{3-}$ anion in the structure of **2** occurs in a different conformation than in $[\mathrm{Ni(dien)_2}]_3$-$(\mathrm{Sb_3S_6})_2$, which is a nice example of the variability of the interconnection of $\mathrm{SbS_3}$ pyramids. The enormous flexibility of thioantimonate networks is demonstrated by the structure of **3**. Despite the larger size of the $[\mathrm{Ni(aepa)}]^{2+}$ complex compared to $[\mathrm{Ni(cyclam)}]^{2+}$, an identical network topology of the 3D $[\mathrm{Sb_4S_7}]^{2-}$ anion is observed. The thioantimonate anion responds to the space requirements of the $[\mathrm{Ni(aepa)}]^{2+}$ cations by an unit cell expansion realized by changes of the Sb−S bond lengths and S−Sb−S angles. Compound **3** exhibits promising photocatalytic $H_2$ generation, and further studies with cocatalysts and sacrificial compounds are underway to check whether it is a suitable material for such an application.

## ■ ASSOCIATED CONTENT

Ⓢ **Supporting Information.** Tables of selected bond lengths, angles, and hydrogen bonds of **1**, **2**, and **3**. Selected crystallographic data, bond lengths, angles, hydrogen bonds, and figures showing the structure of the complex $[\mathrm{Ni(aepa)_2}]\mathrm{Cl_2}$. Figures showing X-ray powder diffraction patterns, DTA/TG, MS, Raman, and UV/vis data of **1** and **3**. X-ray crystallographic files in CIF format. This information is available free of charge via the Internet at http://pubs.acs.org.

## ■ AUTHOR INFORMATION

### Corresponding Author

*E-mail: wbensch@ac.uni-kiel.de.

## ■ ACKNOWLEDGMENT

Financial support by the State Schleswig-Holstein and the Deutsche Forschungsgemeinschaft is gratefully acknowledged. We also thank N. Herzberg and J. Lichte for their help.

## ■ REFERENCES

(1) Seidlhofer, B.; Pienack, N.; Bensch, W. *Z. Naturforsch.* **2010**, *65b*, 937–975.

(2) Pienack, N.; Näther, C.; Bensch, W. *Eur. J. Inorg. Chem.* **2009**, 937–946.

(3) Engelke, L.; Schaefer, M.; Schur, M.; Bensch, W. *Chem. Mater.* **2001**, *13*, 1383–1390.

(4) Engelke, L.; Schaefer, M.; Porsch, F.; Bensch, W. *Eur. J. Inorg. Chem.* **2003**, 506–513.

(5) Kiebach, R.; Pienack, N.; Ordolff, M.-E.; Studt, F.; Bensch, W. *Chem. Mater.* **2006**, *18*, 1196–1205.

(6) Stähler, R.; Näther, C.; Bensch, W. *Chem. Commun.* **2011**, 477–478.

(7) Kiebach, R.; Studt, F.; Näther, C.; Bensch, W. *Eur. J. Inorg. Chem.* **2004**, 2553–2556.

(8) Schur, M.; Bensch, W. *Acta Crystallogr.* **2000**, *C56*, 1107–1108.

(9) Stähler, R.; Näther, C.; Bensch, W. *Acta Crystallogr.* **2001**, *C57*, 26–27.

(10) Stähler, R.; Bensch, W. *Acta Crystallogr.* **2002**, *C58*, m537–m538.

(11) Engelke, L.; Näther, C.; Leisner, P.; Bensch, W. *Z. Anorg. Allg. Chem.* **2008**, *634*, 2959–2965.

(12) Jia, D.-X.; Zhang, Y.; Dai, J.; Zhu, Q.-Y.; Gu, X.-M. *J. Solid State Chem.* **2004**, *177*, 2477–2483.

(13) Stähler, R.; Bensch, W. *Eur. J. Inorg. Chem.* **2001**, 3073–3078.

(14) Stähler, R.; Mosel, B.-D.; Eckert, H.; Bensch, W. *Angew. Chem.* **2002**, *114*, 4671–4673.

(15) Lühmann, H.; Rejai, Z.; Möller, K.; Leisner, P.; Ordolff, M.-E.; Näther, C.; Bensch, W. *Z. Anorg. Allg. Chem.* **2008**, *634*, 1687–1695.

(16) Stephan, H.-O.; Kanatzidis, M. G. *Inorg. Chem.* **1997**, *36*, 6050–6057.

(17) Stähler, R.; Bensch, W. *Z. Anorg. Allg. Chem.* **2002**, *628*, 1657–1662.

(18) Stähler, R.; Näther, C.; Bensch, W. *J. Solid State Chem.* **2003**, *174*, 264–275.

(19) Lees, R. J. E.; Powell, A. V.; Chippindale, A. M. *J. Phys. Chem. Solids* **2007**, *68*, 1215–1219.

(20) Zhang, M.; Sheng, T. L.; Huang, X. H.; Fu, R. B.; Wang, X.; Hu, S. M.; Xiang, S. C.; Wu, X. T. *Eur. J. Inorg. Chem.* **2007**, 1606–1612.

(21) Zhou, J.; Bian, G.-Q.; Zhang, Y.; Dai, J.; Cheng, N. *Z. Anorg. Allg. Chem.* **2007**, *633*, 2701–2705.

(22) Powell, A. V.; Lees, R. J. E.; Chippindale, A. M. *Inorg. Chem.* **2006**, *45*, 4261–4267.

(23) Sheldrick, G. M. *SHELXS-97: Program for Crystal Structure Determination*; University of Göttingen: Göttingen, Germany, 1997.

(24) Sheldrick, G. M. *SHELXS-97: Program for the Refinement of Crystal Structures*; University of Göttingen: Göttingen, Germany, 1997.

(25) Ellermeier, J.; Stähler, R.; Bensch, W. *Acta Crystallogr.* **2002**, *C58*, m70–m73.

(26) Ellermeier, J.; Bensch, W. *Monatsh. Chem.* **2001**, *132*, 565–573.

(27) Lühmann, H.; Näther, C.; Bensch, W. *Z. Anorg. Allg. Chem.* **2011**, *637*, 1007–1012.

(28) Schur, M.; Gruhl, A.; Näther, C.; Jess, I.; Bensch, W. *Z. Naturforsch.* **1999**, *54b*, 1524–1528.

(29) Schaefer, M.; Kurowski, D.; Pfitzner, A.; Näther, C.; Rejai, Z.; Möller, K.; Ziegler, N.; Bensch, W. *Inorg. Chem.* **2006**, *45*, 3726–3731.

(30) Schur, M.; Bensch, W. *Z. Naturforsch.* **1997**, *52b*, 505–409.

(31) Schaefer, M.; Stähler, R.; Kiebach, W.-R.; Näther, C.; Bensch, W. *Z. Anorg. Allg. Chem.* **2004**, *630*, 1816–1822.

(32) Spetzler, V.; Kiebach, R.; Näther, C.; Bensch, W. *Z. Anorg. Allg. Chem.* **2004**, *630*, 2398–2404.

(33) Kiebach, R.; Näther, C.; Sebastian, C. P.; Mosel, B. D.; Pöttgen, R.; Bensch, W. *J. Solid State Chem.* **2006**, *179*, 3082–3086.

(34) Puls, A.; Näther, C.; Kiebach, R.; Bensch, W. *Solid State Sci.* **2006**, *8*, 1085–1097.

(35) Puls, A.; Näther, C.; Bensch, W. *Acta Crystallogr.* **2006**, *E62*, 1045–1047.

(36) Ko, Y.; Tan, K.; Parise, J. B.; Darovsky, A. *Chem. Mater.* **1996**, *8*, 493–496.

(37) Wang, X. *Eur. J. Solid State* **1995**, *32*, 303–312.

(38) Ko, Y.; Parise, J. B. *Chem. Mater.* **1992**, *4*, 1446–1450.

(39) Tan, K.; Ko, Y.; Parise, J. B.; Park, J.-H.; Darovski, A. *Chem. Mater.* **1996**, *8*, 2510–2515.

(40) Wang, X.; Jacobsen, A. J.; Liebau, F. *J. Solid State Chem.* **1998**, *140*, 397–395.

(41) Powell, A. V.; Boissiere, S.; Chippindale, A. M. *Chem. Mater.* **2000**, *12*, 182–187.

(42) Vaqueiro, P.; Darlow, D. P.; Powell, A. V.; Chippindale, A. M. *Solid State Ionics* **2004**, *172*, 601–605.

(43) Paniagua, R.; Vaqueiro, P.; Chippindale, A. M. *Chem. Mater.* **2002**, *14*, 1220–1224.

(44) Bensch, W.; Dürichen, P. *Z. Kristallogr.* **1997**, *212*, 95–96.

(45) Lichte, J.; Näther, C.; Bensch, W. *Z. Anorg. Allg. Chem.* **2010**, *636*, 108–113.

(46) Schaefer, M.; Engelke, L.; Näther, C.; Bensch, W. *Z. Anorg. Allg. Chem.* **2003**, *629*, 1912–1918.

(47) Poisot, M.; Näther, C.; Bensch, W. *Acta Crystallogr.* **2007**, *E63*, m1751–m1752.

(48) Jia, D.; Zhao, Q.; Zhang, Y.; Dai, J.; Zuo, J. *Inorg. Chem.* **2005**, *44*, 8861–8867.

(49) Jia, D.-X.; Zhu, Q.-Y.; Dai, J.; Lu, W.; Guo, W. J. *Inorg. Chem.* **2005**, *44*, 819–821.

(50) Kudo, A.; Miseki, Y. *Chem. Soc. Rev.* **2009**, *38*, 253–278.

(51) Meissner, D.; Memming, R. *J. Phys. Chem.* **1988**, *92*, 3476–3483.

(52) Gurevich, Y. Y.; Pleskov, Y. V. *Semicond. Semimetals* **1983**, *19*, 255–328.

(53) Kudo, A.; Tsuji, I.; Kato, H. *Chem. Commun.* **2002**, 1958–1959.

(54) Kudo, A. *Int. J. Hydrogen* **2006**, *31*, 197–202.

(55) Yan, H.; Yang, J; Ma, G.; Wu, G.; Zong, X.; Lei, Z.; Shi, J.; Li, C. *J. Catal.* **2009**, *266*, 165–168.

(56) Chen, X.; Shen, S.; Guo, L.; Mao, S. S. *Chem. Rev.* **2010**, *110*, 6503–6570.

### 4.2.2 Synthese eines neuen Polyoxovanadates auf Basis von Ge/$NH_4VO_3$/S/dien und dessen fotokatalytische Eigenschaft für die $H_2$-Entwicklung

Zusammenfassung der Veröffentlichung “(VO(dien)$_2$)$GeS_4$: Solvothermal Synthesis and Crystal Structure with an ortho-Thiogermanate as Tetradentate Ligand“. Dieser Artikel wurde in der Zeitschrift „Zeitschrift für anorganische und allgemeine Chemie“ (DOI: 10.1022/zaac.201200174) 2012 veröffentlicht.

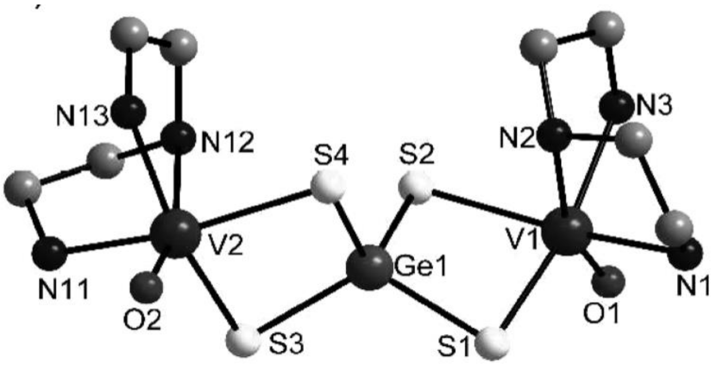

**Abb. 29: Molekulare Struktur von [VO(dien)]$_2$$GeS_4$.**

In der Veröffentlichung wird über die Synthese, Kristallstruktur und Eigenschaft als Cokatalysator für die $H_2$-Entwicklung der Verbindung (VO(dien)$_2$)$GeS_4$ berichtet. Die neuartige Verbindung kristallisiert in der nicht-zentrosymmetrischen orthorhombischen Raumgruppe $Pna2_1$ mit vier Formeleinheiten pro Elementarzelle. In der Struktur wurde erstmals die Anwesenheit von $[GeS_4]^{4-}$ als tetradentater Ligand beobachtet, der mit zwei verzerrten $VOS_2N_3$-Oktaedern durch zwei gegenüberliegende Kanten verbunden ist. Die katalytische Aktivität von (VO(dien)$_2$)$GeS_4$ beträgt 180 µmol $h^{-1}$ $g^{-1}$.

J. Wang, C. Näther, J. Djamil, W. Bensch, *Z. Anorg. Allg. Chem.* **2012**, *638*, 1452-1456. - Reproduziert mit der Erlaubnis vom Wiley Verlag.

DOI: 10.1002/zaac.201200174

# $[VO(dien)]_2GeS_4$: Solvothermal Synthesis and Crystal Structure with an *Ortho*-Thiogermanate as Tetradentate Ligand

**Jing Wang,[a] Christian Näther,[a] John Djamil,[a] and Wolfgang Bensch*[a]**

*In Memory of Professor Welf Bronger*

**Keywords:** Solvothermal synthesis; Crystal structure; Thiogermanates; Germanium; Sulfur

**Abstract.** The compound $[VO(dien)]_2GeS_4$ (**1**, dien = diethylenetriamine) features an *ortho*-thiogermanate anion $[GeS_4]^{4-}$, which acts as tetradentate ligand joining $[VO(dien)]^{2-}$ complexes. The compound was obtained under solvothermal conditions crystallizing in the non-centrosymmetric orthorhombic space group $Pna2_1$ with $a = 19.8310(11)$, $b = 8.0814(5)$, $c = 12.0889(9)$ Å, $V = 1937.4(2)$ Å$^3$ and $Z = 4$. The $V^{4+}$ cations are in a distorted octahedral environment of a tridentate dien molecule, one oxygen atom and two sulfur atoms from the $[GeS_4]^{4-}$ anion. A three-dimensional network is generated by hydrogen bonding interactions.

## Introduction

Since 1989, when *Bedard* et al. isolated thiogermanate and -stannate compounds under hydrothermal conditions,[1] the thiometallate chemistry has attracted a lot of attention. Thiometallates exhibit a diverse and fascinating structural variability, unusual optical, magnetic and electrical properties.[2–6] Up to now several thiogermanate compounds were prepared and characterized.[7] The basic building unit in the structures of these compounds is the $[GeS_4]^{4-}$ tetrahedron. Decreasing the pH-value of the reaction solution leads to condensation of the $[GeS_4]^{4-}$ tetrahedron forming dimeric species like $[Ge_2S_7]^{6-}$ or $[Ge_2S_6]^{4-}$, polymeric species $[GeS_3{}^{2-}]_n$, tetrameric adamantane-like units $[Ge_4S_{10}]^{4-}$ or $[Ge_8S_{19}]^{6-}$ by sharing corners or edges.[7c] The study of the incorporation of transition metals complexes (TMCs) into thiogermanates is in the focus of research because unique topological structures and interesting properties may be generated. Until now cations of the metals Cr, Mn, Ni, Fe, Co, Ag, Cu, Zn, Hg and Cd have been successfully incorporated in such compounds.[8] In the structures the transition metal ions are either coordinated by amine ligands acting as counterions or they are connecting adamantane-like thiogermanate species. Furthermore, in a new zeolite analogous thiogermanate the tetravalent $Ge^{4+}$ was partially replaced by trivalent cations such as $Ga^{3+}$ or $In^{3+}$.[9] In the structure adamantane-like units are interconnected through corner-sharing to form a 3D framework with high surface area.

In 2005, the compound $[Na(H_2O)_4][Cr(en)_3]_2[GeS_3OH]_2$-$[Cr(en)_2(GeS_4)]$ was reported representing the first example containing the $[GeS_4]^{4-}$ tetrahedron acting as a bidentate ligand for a transition metal cation.[8a] In the title compound, the $[GeS_4]^{4-}$ unit acts as a tetradentate ligand, and two $[V(dien)OS_2]^{2-}$ complexes are bridged via $Ge^{4+}$. To the best of our knowledge, $[VO(dien)]_2GeS_4$ (**1**) is the first *ortho*-thiogermanate obtained under solvothermal conditions. In the paper we report the synthesis, crystal structure and selected physical properties of this compound. Furthermore, compound **1** was tested in the photocatalytic hydrogen evolution reaction. In the past it was demonstrated that germanium compounds are promising candidates as photocatalysts.[10]

## Results and Discussion

Compound **1** crystallizes in the non-centrosymmetric orthorhombic space group $Pna2_1$ with four formula units per unit cell. All unique atoms are located on general positions. In the center of the complex (Figure 1a) a slightly distorted $[GeS_4]^{4-}$ tetrahedron represents the central structural motif. The Ge–S bond lengths of 2.1932(11) and 2.2152(12) Å (Table 1) are in the range observed for other thiogermanates.[8d,8f,13–15] The *ortho*-thiogermanate anion can be considered as a ligand for the two independent $V^{4+}$ ions. The $V^{4+}$ ions are coordinated by one oxygen atom, one tridentate *dien* molecule, and two sulfur atoms of the chelating thiogermanate anion. The two $[VOS_2N_3]$ octahedra are linked by the $[GeS_4]^{4-}$ tetrahedron via two opposite common edges (Figure 1b). The $[VOS_2N_3]$ octahedra are distorted with bond lengths V=O 1.608(4)–1.606(4) Å, V–N = 2.135(4)–2.361(4) Å, and V–S = 2.4256(12)–2.4525(13) Å. The trans O–V–N angles ranging from 160.73(18) to 164.14(18)° (Table 2) exhibit a deviation from ideal 180°. The short V–O bond is caused by a significant double bonding character and is often observed in polyoxovanadates with $VO_5$ pyramids and a terminal $V^{IV}$=O bond.[16] The

---

* Prof. Dr. W. Bensch
Fax: +49-431-880-1520
e-Mail: wbensch@ac.uni-kiel.de
[a] Institut für Anorganische Chemie
Christian-Albrechts-Universität zu Kiel
Max-Eyth-Str. 2
24118 Kiel, Germany

V–N distance to the secondary nitrogen atoms (N(2) and N(12)) are 0.18 Å longer than the other V–N bonds to primary nitrogen atoms (N(1), N(3), N(11) and N(13)). This can be attributed to the influence of the oxygen atom in *trans* position. The V–N bonds are close to values reported for $[VO(dien)]^{2+}$ complexes.[17] The oxidation states of vanadium and germanium were calculated with the bond valence sum method (BVS).[18] The resulting values of 3.7 for V(1), 3.8 for V(2) and 4.1 for Ge(1) justify the assignment of the valence states 4+ for vanadium and 4+ for germanium.

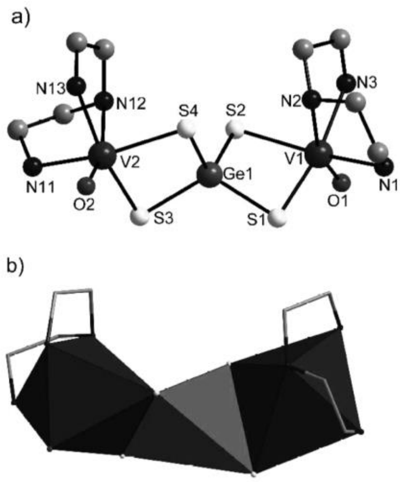

**Figure 1.** The molecular structure of **1**: a) Balls and sticks diagram, and b) polyhedral representation.

**Table 1.** Selected bond lengths /Å for **1**. Estimated standard deviations are given in parentheses.

| | | | |
|---|---|---|---|
| Ge(1)–S(1) | 2.1932(11) | Ge(1)–S(2) | 2.2100(12) |
| Ge(1)–S(3) | 2.2097(11) | Ge(1)–S(4) | 2.2152(12) |
| V(1)–O(1) | 1.608(4) | V(2)–O(2) | 1.606(4) |
| V(1)–N(1) | 2.162(4) | V(2)–N(13) | 2.135(4) |
| V(1)–N(3) | 2.179(4) | V(2)–N(11) | 2.143(4) |
| V(1)–N(2) | 2.337(4) | V(2)–N(12) | 2.143(4) |
| V(1)–S(1) | 2.4256(12) | V(2)–S(4) | 2.4417(13) |
| V(1)–S(2) | 2.4525(13) | V(2)–S(3) | 2.4456(13) |

Two kinds of hydrogen bonds are observed (Table 3, Figure 2). The hydrogen bonds with H···S distances between 2.5094(11) and 2.8940(11) Å (N–H···S angles: 138.14 to 165.19°) as well as H···O distances ranging from 2.173(4)–2.314(4) Å (N–H···O angles: 142.90–143.09°) connect the isolated [VO(dien)]$_2$GeS$_4$ units to form a neutral three-dimensional network. The intramolecular hydrogen bonds may be responsible for the unusual twisted molecular structure, whereas intermolecular hydrogen bonds stabilize the three dimensional network structure.

Figure 3 shows the arrangement of the molecules in the (010) plane. Along the *c*-axis the moieties are arranged in an ···ABAB··· fashion with the *dien*-ligands being oriented in an up-down mode along [100].

The powder X-ray diffraction pattern of compound **1** is in good agreement with the calculated pattern based on the single crystal data (Figure 4).

The thermal stability was investigated using simultaneous differential thermal analysis (DTA) and thermogravimetry experiments (TG). In the range from 25 to 196 °C (Figure 5) no significant weight loss can be observed. The first weight loss ($\Delta m = 29.3\,\%$) occurs between 196 and 460 °C being accompanied by two not well resolved endothermic events with $T_p$ = 306 and 376 °C. Such phenomenon has been reported in literature and is attributed to the existence of the strong bonds between $V^{4+}$ and the dien ligands, as well as the large number of hydrogen bonds in the compound.[17] For the second mass loss of 26.1 % an endothermic event is found at about 670 °C. The CHNS analysis of the thermal decomposition product yields a relative large nitrogen (2.5 %), carbon (13.6 %) and sulfur (28.4 %) content. The results of the EDX measurement shows a ratio V:S of about 1:1. Germanium could not be identified in the product obtained at 800 °C. Maybe germanium is emitted as a volatile species. Hence, an exact assignment of the mass losses is not possible.

In the UV/Vis spectrum presented as a Kubelka–Munk plot a broad absorption occurs with a maximum located at 1.65 eV (Figure 6). This strong absorption is caused by a charge-transfer transition most likely from an occupied sulfur based orbital to an unoccupied orbital located at the vanadium atoms (LMCT).

Compound **1** was tested for photocatalytic hydrogen evolution in a Ru(bpy)$_3$-based system giving 3.6 µmol of hydrogen (180 $\mu mol\cdot h^{-1}\cdot g^{-1}$). Compared to the activity of two thioantimonates recently investigated under identical conditions,[19] the activity of compound **1** exhibits a similar performance. A comparison with data of other compounds is not straightforward because often noble metals like platinum or rhodium are used as co-catalysts, different radiation sources and sacrificial systems like aqueous $Na_2S$–$Na_2SO_3$ solutions are applied. Nevertheless, a few examples are shortly presented to give an impression of the catalytic activity of the title compound. For nickel-doped ZnS (300 W, Xe lamp, $\lambda > 420$ nm) 280 $\mu mol\cdot h^{-1}\cdot g^{-1}$ were reported for $H_2$ evolution in aqueous $Na_2S/K_2SO_3$ solution[20] while doping ZnS with lead produced 15 $\mu mol\cdot h^{-1}\cdot g^{-1}$ in a $SO_3^{2-}$ solution.[21] $(AEP)_6In_{10}S_{18}$ evolved 40 $\mu mol\cdot h^{-1}\cdot g^{-1}$ $H_2$ (AEP = protonated 1-(2-aminoethyl)piperazine) and $Na_{14}In_{17}Cu_3S_{35}$ 18 $\mu mol\cdot h^{-1}\cdot g^{-1}$ $H_2$ in aqueous $Na_2S$ solution using a 300 W Xe lamp with $\lambda > 420$ nm.[22]

## Conclusions

The $[GeS_4]^{4-}$ tetrahedron acts as a tetradentate ligand joining two independent $V^{4+}$-centered complexes in the new *ortho*-thiogermanate complex [VO(dien)]$_2$GeS$_4$. Intermolecular hydrogen bonding interactions generate a three dimensional network.

**Table 2.** Selected angles /° for **1**. Estimated standard deviations are given in parentheses.

| | | | |
|---|---|---|---|
| S(1)–Ge(1)–S(3) | 117.29(4) | S(1)–Ge(1)–S(4) | 115.01(5) |
| S(1)–Ge(1)–S(2) | 98.46(4) | S(3)–Ge(1)–S(4) | 98.83(4) |
| S(3)–Ge(1)–S(2) | 116.69(4) | S(2)–Ge(1)–S(4) | 111.40(5) |
| O(1)–V(1)–N(1) | 93.11(18) | O(2)–V(2)–N(13) | 95.15(19) |
| O(1)–V(1)–N(3) | 92.21(17) | O(2)–V(2)–N(11) | 94.0(2) |
| N(1)–V(1)–N(3) | 92.69(17) | N(13)–V(2)–N(11) | 89.764(18) |
| O(1)–V(1)–N(2) | 160.73(18) | O(2)–V(2)–N(12) | 164.14(18) |
| N(1)–V(1)–N(2) | 74.58(14) | N(13)–V(2)–N(12) | 73.76(15) |
| N(3)–V(1)–N(2) | 73.99(14) | N(11)–V(2)–N(12) | 75.02(15) |
| O(1)–V(1)–S(1) | 104.24(14) | O(2)–V(2)–S(4) | 103.58(16) |
| N(1)–V(1)–S(1) | 87.76(12) | N(13)–V(2)–S(4) | 88.45(14) |
| N(3)–V(1)–S(1) | 163.49(11) | N(11)–V(2)–S(4) | 162.45(12) |
| N(2)–V(1)–S(1) | 90.28(10) | N(12)–V(2)–S(4) | 87.70(10) |
| O(1)–V(1)–S(2) | 104.65(15) | O(2)–V(2)–S(3) | 105.22(16) |
| N(1)–V(1)–S(2) | 162.16(12) | N(13)–V(2)–S(3) | 159.63(13) |
| N(3)–V(1)–S(2) | 88.37(12) | N(11)–V(2)–S(3) | 88.89(13) |
| N(2)–V(1)–S(2) | 88.65(10) | N(12)–V(2)–S(3) | 86.24(11) |
| S(1)–V(1)–S(2) | 86.25(4) | S(4)–V(2)–S(3) | 86.87(4) |
| Ge(1)–S(1)–V(1) | 85.69(4) | Ge(1)–S(3)–V(2) | 85.88(4) |
| Ge(1)–S(2)–V(1) | 84.68(4) | Ge(1)–S(4)–V(2) | 85.85(4) |

**Table 3.** Possible hydrogen bonds: distances /Å and angles /° for **1**. Estimated standard deviations are given in parentheses.

| D–H | *d*(H···A) /Å | ∠DHA /° | *d*(D···A) /Å | A |
|---|---|---|---|---|
| N1–H1 (inter) | 2.807(1) | 142.1(3) | 3.561(4) | S2 |
| N1–H2(inter) | 2.788(1) | 165.2(3) | 3.665(4) | S3 |
| N2–H2(intra) | 2.720(1) | 155.5(2) | 3.568(4) | S4 |
| N3–H5(inter) | 2.722(1) | 147.0(2) | 3.510(4) | S3 |
| N3–H6(inter) | 2.314(4) | 143.0(3) | 3.082(5) | O2 |
| N11–H7(inter) | 2.688(1) | 138.1(3) | 3.411(4) | S4 |
| N11–H8(inter) | 2.509(1) | 153.2(3) | 3.337(4) | S1 |
| N12–H12(intra) | 2.894(1) | 163.0(3) | 3.774(4) | S2 |
| N13–H12(inter) | 2.173(4) | 142.9(3) | 2.941(6) | O1 |

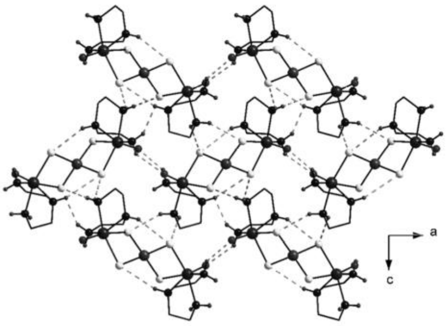

**Figure 2.** View of the hydrogen bonded arrangement viewed along [010] (intermolecular hydrogen bonds indicated by light gray dotted lines and intramolecular hydrogen bonds by dark dotted lines).

**Figure 3.** Crystal packing of the molecules in the structure of **1** viewed along the b axis (polyhedral representation).

## Experimental Section

Crystals of **1** (Figure 7) were obtained under solvothermal conditions, using germanium (219 mg, 3 mmol), $NH_4VO_3$ (232 mg, 2 mmol) and sulfur (192 mg, 6 mmol) in 100 % diethylenetriamine (dien) at 160 °C for 9 d. The color of the crystals was dark green. The yield was about 70 % based on vanadium. The pH of the reaction mixture before the reaction was 12.5. The title compound was sensitive against moisture and slowly decomposed in air. The degradation products were identified as elemental germanium and $VS_4$ using X-ray powder diffraction.

CHNS analysis. Calcd.: N%, 15.5 %; C%, 17.8 %; H%, 4.8 %; S%, 23.7 %. Found: N%, 15.5 %; C%, 18.0 %; H%, 5.0 %; S%, 23.4 %. IR (KBr, $cm^{-1}$): 3276 (m), 3204 (m), 3123 (m), 2892 (w), 1580 (s), 1447 (w), 1423 (w), 1313 (w), 1154 (m), 1091 (s), 938 (s), 797 (w), 662 (m), 425 (s).

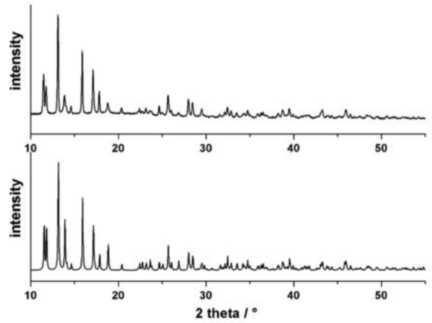

**Figure 4.** Experimental (top) and simulated (bottom) powder X-ray powder diffraction pattern of **1**.

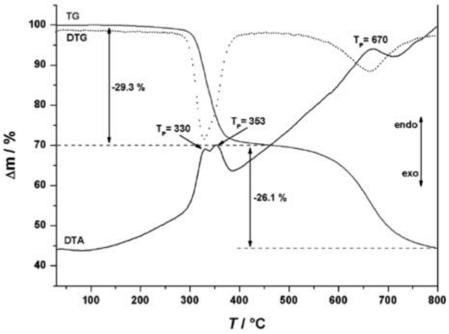

**Figure 5.** DTA-TG curves for compound **1**.

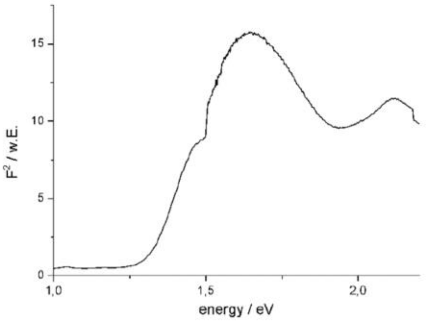

**Figure 6.** Kubelka–Munk plot of the UV/Vis data of compound **1**.

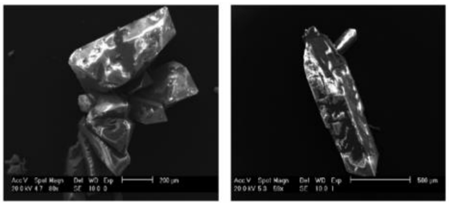

**Figure 7.** SEM micrographs of crystals of **1**.

The X-ray intensity data of a single crystal of **1** was collected at room temperature using a STOE-1 Imaging Plate Diffraction System (IPDS-1) with Mo-$K_\alpha$ radiation ($\lambda = 0.71073$ Å). The intensities were corrected for Lorentz and polarization effects. The structure was solved with SHELXS 97[11] and refined against $F^2$ with SHELXL 97.[12] All non-hydrogen atoms were refined using anisotropic displacement parameters. The C–H and N–H hydrogen atoms were positioned with idealized geometry and refined using a riding model. A numerical absorption correction was performed ($T_{\text{min.}}$: 0.543/$T_{\text{max.}}$: 0.686). The measured crystal is racemically twinned and therefore a twin refinement was performed (BASF = 0.43(1)). After structure refinement relatively large electron density maxima were found in the difference map indicating a disorder. A close examination of the residual electron densities yielded a second orientation of **1** which is occupied to only 5 % but the disorder could not be resolved especially for the atoms of the dien ligands. Therefore, the disorder was not considered in the final refinement. The GeS$_4$V$_2$ unit can successfully be refined isotropic but the carbon, nitrogen and oxygen atoms could not be located. Selected crystal data and details of the structure determination for **1** are summarized in Table 4.

**Table 4.** Details of the data collection and selected refinement results for **1**.

| | **1** |
|---|---|
| empirical formula | $C_8N_6H_{26}GeO_2S_4V_2$ |
| formula weight | 541.06 |
| crystal system | orthorhombic |
| space group | $Pna2_1$ |
| $a$ /Å | 19.8310(11) |
| $b$ /Å | 8.0814(5) |
| $c$ /Å | 12.0889(9) |
| $V$ /Å$^3$ | 1937.4(2) |
| $Z$ | 4 |
| density (calculated) /g·cm$^{-3}$ | 1.855 |
| $F(000)$ | 1096 |
| reflections collected | 14751 |
| independent reflections | 4635 |
| $R$(int) | 0.0368 |
| GooF on $F^2$ | 1.051 |
| $R_1$ [$I > 2\sigma(I)$] | 0.0491 |
| $wR_2$ | 0.1182 |

The crystallographic data for compound **1** has been deposited with the Cambridge Crystallographic Data Center as publication No. CCDC-875105. Copies of the data can be obtained, free of charge, on application to CCDC, 12 Union Road, Cambridge CB2 1 EZ, UK (E-Mail: deposit@ccdc.ca.ac.uk).

CHNS analysis was carried out using an EURO EA Elemental Analyzer (EURO VECTOR Instruments and Software). IR spectroscopy measurement (3600–400 cm$^{-1}$) was performed at room temperature with a Bruker Alpha P FT-IR spectrometer. DTA-TG measurement was realized using a STA-409CD thermobalance from Netzsch. The sample was placed in an Al$_2$O$_3$ crucible and heated from 25 to 800 °C under flowing $N_2$ with a heating rate of 4 $K \cdot min^{-1}$. For photocatalytic measurements, the compound (0.57 mmol) was added to a solution of $[Ru(bpy)_3]Cl_2$ in acetonitrile (10 mL), triethylamine (8 mL) and distilled water (3 mL). The suspension was irradiated with a Fe-doped metal halogen lamp (250 W) for 2 h. The evolved amount of hydrogen was analyzed with gas chromatography (Agilent 6890 plus, with a 5 Å molecular sieve column and a TCD).

## Acknowledgement

Financial support by the State of Schleswig-Holstein is grateful acknowledged. JW is gratefully for the support by *Dr. D. Pitzschke* and *Dr. E. Quiroga-González*.

## References

[1] R. L. Bedard, S. T. Wilson, L. D. Vail, J. M. Bennett, E. M. Flanigen, *Stud. Surf. Sci. Catal.* **1989**, *49*, 375–386.

[2] B. Seidlhofer, N. Pienack, W. Bensch, *Z. Naturforsch.* **2010**, *65b*, 937–975.

[3] a) W. S. Sheldrick, M. Wachhold, *Angew. Chem. Int. Ed. Engl.* **1997**, *36*, 206–224; b) W. S. Sheldrick, M. Wachhold, *Coord. Chem. Rev.* **1998**, *176*, 211–322.

[4] J. Zhou, J. Dai, G.-Q. Bian, C.-Y. Li, *Cood. Chem. Rev.* **2009**, *253*, 1221–1247.

[5] a) C. L. Cahill, Y.-H. Ko, J. C. Hanson, K.-M. Tan, J. B. Parise, *Chem. Mater.* **1998**, *10*, 1453–1458; b) K. K. Rangan, M. G. Kanatzidis, *Inorg. Chim. Acta* **2004**, *357*, 4036–4044; c) F. Bonhomme, M. G. Kanatzidis, *Chem. Mater.* **1998**, *10*, 1153–1159.

[6] a) M. Wachhold, K. K. Rangan, M. Lei, M. F. Thorpe, S. J. L. Billinge, V. Petkov, J. Heising, M. G. Kanatzidis, *J. Solid State Chem.* **2000**, *152*, 21–36; b) K. K. Rangan, P. N. Trikalitis, M. G. Kanatzidis, *J. Am. Chem. Soc.* **2000**, *122*, 10230–10231; c) P. N. Trikalitis, K. K. Rangan, M. G. Kanatzidis, *J. Am. Chem. Soc.* **2002**, *124*, 2604–2613; d) L. Engelke, R. Stähler, M. Schur, C. Näther, W. Bensch, R. Pöttgen, M. H. Möller, *Z. Naturforsch.* **2004**, *59b*, 869–876; e) M. Schaefer, R. Stähler, W.-R. Kiebach, C. Näther, W. Bensch, *Z. Anorg. Allg. Chem.* **2004**, *630*, 1816–1822; f) N. Pienack, A. Puls, C. Näther, W. Bensch, *Inorg. Chem.* **2008**, *47*, 9606–9611; g) Z. Rejai, C. Näther, R. K. Kremer, W. Bensch, *Inorg. Chem.* **2010**, *49*, 1651–1657; h) E. Quiroga-González, C. Näther, W. Bensch, *Solid State Sci.* **2010**, *12*, 1235–1241; i) E. Quiroga-González, L. Kienle, C. Näther, V. S. K. Chakravadhanula, H. Lühmann, W. Bensch, *J. Solid State Chem.* **2010**, *183*, 2805–2812.

[7] a) C. L. Cahill, J. B. Parise, *Chem. Mater.* **1997**, *9*, 807–811; b) J. B. Parise, K.-M. Tan, *Chem. Commun.* **1996**, 1687–1688; c) B. Krebs, *Angew. Chem. Int. Ed. Engl.* **1983**, *22*, 113–134.

[8] a) M. Melullis, M. K. Brandmayer, S. Dehnen, *Z. Anorg. Allg. Chem.* **2006**, *632*, 64–72; b) D.-X. Jia, J. Dai, Q.-Y. Zhu, L.-H. Cao, H.-H. Lin, *J. Solid State Chem.* **2005**, *178*, 874–881; c) O. M. Yaghi, Z. Sun, D. A. Richardson, T. L. Groy, *J. Am. Chem. Soc.* **1994**, *116*, 807–808; d) G.-N. Liu, G.-C. Guo, M.-S. Wang, L.-Z. Cai, J.-S. Huang, *J. Mol. Struct.* **2010**, *983*, 104–111; e) C. L. Bowes, A. J. Lough, A. Malek, G. A. Ozin, S. Petrov, D. Young, *Chem. Ber.* **1996**, *129*, 283–287; f) J.-F. Chen, Q.-Y. Jin, Y.-L. Pan, Y. Zhang, D.-X. Jia, *Z. Anorg. Allg. Chem.* **2010**, *636*, 230–235; g) C. L. Bowes, W. U. Huynh, S. J. Kirkby, A. Malek, G. A. Ozin, S. Petrov, M. Twardowski, D. Young, R. L. Bedard, R. Broach, *Chem. Mater.* **1996**, *8*, 2147–2152; h) N.-F. Zheng, X.-H. Bu, P.-Y. Feng, *Chem. Commun.* **2005**, 2805–2807; i) Y.-C. Zhu, M.-H. Baiyin, X. Liu, C.-Y. Jia, X.-Y. Liu, Y.-L. An, *Huaxue Xuebao(Chin.)(Acta Chim.Sinica)* **2006**, *64*, 371–374; j) O. Achak, J. Y. Pivan, M. Maunaye, M. Louer, D. Louer, *J. Solid State Chem.* **1996**, *121*, 473–478.

[9] a) N.-F. Zheng, X.-H. Bu, B. Wang, P.-Y. Feng, *Science* **2002**, *298*, 2366–2369; b) D. Pitzschke, W. Bensch, *Z. Anorg. Allg. Chem.* **2003**, *629*, 2206–2210.

[10] a) J. Sato, H. Kobayashi, K. Ikarashi, N. Saito, H. Nishiyama, Y. Inoue, *J. Phys. Chem. B* **2004**, *108*, 4369–4375; b) J. Sato, N. Saito, Y. Yamada, K. Maeda, T. Takata, J. N. Kondo, M. Hara, H. Kobayashi, K. Domen, Y. Inoue, *J. Am. Chem. Soc.* **2005**, *127*, 4150–4151.

[11] G.M. Sheldrick, *SHELXS-97*, University of Göttingen, **1997**.

[12] G.M. Sheldrick, *SHELXL-97*, University of Göttingen, **1997**.

[13] a) G.-N. Liu, J.-D. Lin, Z.-N. Xu, Z.-F. Liu, G.-C. Guo, J.-S. Huang, *Cryst. Growth Des.* **2011**, *11*, 3318–3322; b) J.-J. Liang, J. Zhao, W.-W. Tang, Y. Zhang, D.-X. Jia, *Inorg. Chem. Commun.* **2011**, *14*, 1023–1026.

[14] a) D. Pitzschke, J. Wang, D. Hoffmann, R. Pöttgen, W. Bensch, *Angew. Chem.* **2006**, *118*, 1327–1331; *Angew. Chem. Int. Ed.* **2006**, *45*, 1305–1308; b) J. Wang, C. Näther, P. Kögerler, W. Bensch, *Eur. J. Inorg. Chem.* **2012**, 1237–1242.

[15] Y.-D. Wu, C. Näther, W. Bensch, *Acta Crystallogr., Sect. E* **2003**, *59*, i137–i138.

[16] a) E. Antonova, C. Näther, P. Kögerler, W. Bensch, *Angew. Chem.* **2011**, *123*, 790–793; b) J. Wang, C. Näther, P. Kögerler, W. Bensch, *Inorg. Chim. Acta* **2010**, *363*, 4399–4404; c) A. Wutkowski, C. Näther, M. Speldrich, P. Kögerler, W. Bensch, *Z. Anorg. Allg. Chem.* **2009**, *635*, 1094–1099.

[17] M.-L. Fu, G.-C. Guo, A.-Q. Wu, B. Liu, L.-Z. Cai, J.-S. Huang, *Eur. J. Inorg. Chem.* **2005**, 3104–3108.

[18] M. O′Keeffe, N. E. Brese, *J. Am. Chem. Soc.* **1991**, *113*, 3226–3229.

[19] B. Seidlhofer, J. Djamil, C. Näther, W. Bensch, *Cryst. Growth Des.* **2011**, *11*, 5554–5560.

[20] A. Kudo, M. Sekizawa, *Chem. Commun.* **2000**, 1371–1372.

[21] I. Tsuji, A. Kudo, *J. Photochem. Photobiol. A: Chem.* **2003**, *156*, 249–252.

[22] N. Zheng, X. H. Bu, H. Vu, P. Y. Feng, *Angew. Chem. Int. Ed.* **2005**, *44*, 5299–5303.

Received: April 13, 2012

### 4.2.3 Zwei pseudopolymorphe sternenförmige tetranukleare $Co^{3+}$-Verbindungen mit Disulfidanionen, die zwei unterschiedliche Bindungsmodi und viel versprechende fotokatalytische Eigenschaften aufweisen

Zusammenfassung der Veröffentlichung „Two pseudopolymorphic star-shaped tetranuclear $Co^{3+}$ compounds with disulfide anions exhibiting two different connection modes and promising light-driven photocatalytic properties“. Dieser Artikel wurde in der Zeitschrift “ Chemistry – A European Journal” (DOI: 10.1002/chem.201501796) 2015 veröffentlicht.

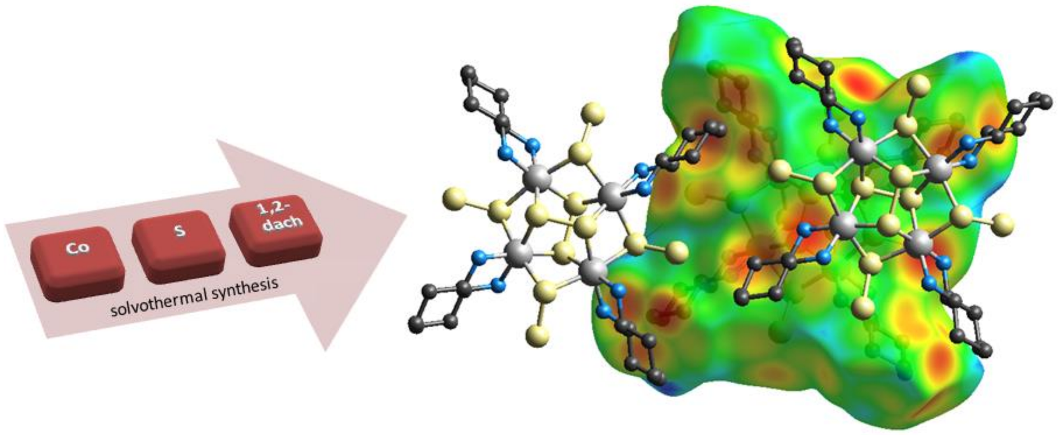

**Abb. 30: Synthese-Schema und Hirshfield Oberfläche von $[Co_4(C_6H_{14}N_2)(\mu_4\text{-}S_2)_2(\mu_2\text{-}S_2)_4]$.**

In dem Artikel wird über die Verbindung $[Co_4(C_6H_{14}N_2)(\mu_4\text{-}S_2)_2(\mu_2\text{-}S_2)_4]$ (I) und das Pseudopolymorph $[Co_4(C_6H_{14}N_2)(\mu_4\text{-}S_2)_2(\mu_2\text{-}S_2)_4]$ 4 $H_2O$ (II) berichtet, welche unter solvothermalen Bedingungen dargestellt wurden. Besonders interessant in den Strukturen sind die bisher noch nicht beobachteten Bindungsmodi der $S_2^{2-}$-Liganden an die $Co^{3+}$-Zentren. Die terminalen $S_2^{2-}$-Einheiten verbrücken zwei $Co^{3+}$-Zentren im $\mu_2$-Modus, während eine $\mu_4$-Verbrückung der zentralen $S_2^{2-}$-Einheiten mit vier $Co^{3+}$-Zentren beobachtet wird. Die unterschiedlichen Verbrückungen der $S_2^{2-}$-Einheiten hat verschiedene Bindungsabstände zur Folge. In den zentralen $S_2^{2-}$-Anionen liegen längere Abstände als in den terminalen Anionen vor. Diese Beobachtungen konnten mit DFT-Berechnungen bestätigt werden. Die thermische Behandlung von II und anschließende Lagerung über $P_2O_5$ führt zur Umwandlung in I und Lagerung von I in Anwesenheit von Luftfeuchtigkeit führt zur Bildung von II. Aus diesem Grund wurden die fotokatalytischen Messungen an II durchgeführt bzw. die daraus resultierenden Ergebnisse auf II bezogen. Neben einer viel versprechenden Menge produziertem $H_2$

(9800 µmol $h^{-1}$ $g^{-1}$) weist II während der Reaktion eine hohe Stabilität auf, so dass mehrere fotokatalytische Zyklen mit analogen Ergebnissen durchgeführt werden konnten.

N. Pienack, H. Lühmann, J. Djamil, S. Permien, C. Näther, S. Haumann, R. Weihrich, W. Bensch, *Chem. Eur. J.* **2015**, *21*.- Reproduziert mit der Erlaubnis vom Wiley Verlag.

# Two pseudopolymorphic star-shaped tetranuclear $Co^{3+}$ compounds with disulfide anions exhibiting two different connection modes and promising light-driven photocatalytic properties

Nicole Pienack,[a] Henning Lühmann,[a] John Djamil,[a] Stefan Permien,[a] Christian Näther,[a] Sebastian Haumann,[b] Richard Weihrich,[b] and Wolfgang Bensch*[a]

Dedicated to Prof. Dr. Manfred Scheer on the occasion of his 60th birthday

**Abstract:** The compound $[Co_4(C_6H_{14}N_2)_4(\mu_4\text{-}S_2)_2(\mu_2\text{-}S_2)_4]$ (**I**) and the pseudo-polymorph $[Co_4(C_6H_{14}N_2)_4(\mu_4\text{-}S_2)_2(\mu_2\text{-}S_2)_4]\cdot 4H_2O$ (**II**) were obtained under solvothermal conditions ($C_6H_{14}N_2$ = *trans*-1,2-diaminocyclohexane). The structures feature $S_2^{2-}$ anions exhibiting two different coordination modes. Terminal $S_2^{2-}$ entities join two $Co^{3+}$ centres in a $\mu_2$-fashion while the central $S_2^{2-}$ groups connect four $Co^{3+}$ cations in the $\mu_4$-coordination mode. Compound **II** can be transformed into **I** by heat and storage over $P_2O_5$ and storing **I** in humid air yields in **II**. The intermolecular interactions investigated *via* Hirshfeld surface analysis reveals that besides S···H bonding close contacts are associated with relatively weak H···H interactions. A detailed DFT analysis of the bonding situation explains the long S-S bonds in the $\mu_4$-bridging $S_2^{2-}$ units and the short bonds for $S_2^{2-}$ in the $\mu_2$-connecting mode. Light-driven photocatalytic hydrogen evolution experiments demonstrate the potential of compound **II** as catalyst.

## Introduction

Polysulfide ligands $S_n^{2-}$ ($n \geq 2$) exhibit a beautiful and versatile structural chemistry either with main group or transition metal cations as reviewed in several papers.[1,2] Various examples can be found in these papers concerning the binding modes, chelating properties and also regarding the synthesis approaches for the preparation of polysulfide containing complexes. The smallest anion $S_2^{2-}$ connects metal cations in eleven different ways which were classified in Ref. [2] and are shown in Scheme 1.

Focusing on group 9 metal cations a search in the CSD demonstrates that some of the modes were never observed for these ions. Especially complexes containing $S_2^{2-}$ anions featuring more than one connection mode are extremely rare and until now no such compound was reported for $Co^{2+}/Co^{3+}$. To highlight the variability of the binding modes to the cations of group 9 metals some examples are shortly presented. Compounds like $Cp_4Co_4(\mu_3\text{-}S)_3(\mu_3\text{-}S_2)$ or $Cp_4Co_4(\mu_3\text{-}S)(\mu_3\text{-}S_2)_3$ featuring the binding mode IIc were obtained by reacting $CpCo(CO)_2$ with $S_8$.[3,4] In the compound $[SCo_3(CO)_7]_2S_2$ the disulfide anion bridges four Co centers in the mode IId.[5] The Ib mode is found in the structure of $[(\eta^5\text{-}C_5Me_5)_2Co_2S_4]$ which was synthesized in toluene using $[C_5Me_5(CO)Co]_2$ and $S_8$.[6] The structures of $[Co(\mu\text{-}S_2)([15]aneN_4)]_2X_2$ ($[15]aneN_4$ = 1,4,8,12-tetraazacyclopentadecane; X = $BPh_2$, $ClO_4$) contain two $S_2^{2-}$ dianions bridging two Co atoms in the IIb mode to form a $Co_2S_4$ heterocycle.[7] A heterometallic $[AsCo_3(S_2)(S)_3]$ core in the compound $[(C_5Me_4Et)_3Co_3AsS_5]I$ exhibits the $S_2^{2-}$ unit acting in the IIc fashion.[8] The thermal reaction of a cobalt dicarbonyl complex $Co(\eta^5\text{-}C_{60}Ar_5)(CO)_2$ ($C_{60}Ar_5$ = pentaaryl[60]fullerene) with sulfur in *p*-xylene at T = 140 °C afforded first crystallization of $CoS_3(\eta^5\text{-}C_{60}Ar_5)$ which could be transformed to the bimetallic compound $Co_2(S_2)_2(\eta^5\text{-}C_{60}Ar_5)_2$.[9] The two Co centers are joined by two $S_2^{2-}$ anions showing the Ib connection mode. A type IIb connection mode was reported for $[\{Co(salphen)\}_2S_2Na(thf)_2]BPh_4$ (salphen = NN'-*o*-phenylenebis(salicylideneiminate) which was synthesized by reacting [Co(salphen)] with sulfur in tetrahydrofuran (thf) in the presence of $NaBPh_4$.[10]

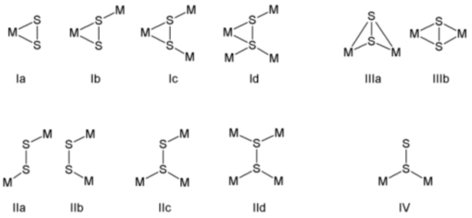

**Scheme 1.** The different binding modes of the $S_2^{2-}$ anion.[2]

The treatment of $[Cp^*Ir(\mu\text{-}S\textit{i}Pr)_2IrCp^*]$ at room temperature in toluene with $S_8$ afforded first the crystallization of $[Cp^*Ir(\mu\text{-}S\textit{i}Pr)_2(\mu\text{-}S_9)IrCp^*]$ which was then converted in solution using $NaBPH_4$ to form $[Cp^*Ir(_{\mu}\text{-}S\textit{i}Pr)_2(\mu S_2)IrCp^*][BPh_4]$ containing the $S_2^{2-}$ dumbbell acting in the IIb mode.[11] Irradiation of a solution of $[(triphos)Rh(S_2CO)]BPh_4$ in $CH_2Cl_2$ with visible light afforded the

---

[a] Dr. N. Pienack, H. Lühmann, J. Djamil, S. Permien, Prof. Dr. C. Näther, Prof. Dr. W. Bensch
Institute of Inorganic Chemistry
Christian-Albrechts-University of Kiel
Max-Eyth-Str. 2, 24118 Kiel, Germany
E-mail: wbensch@ac.uni-kiel.de
[b] S. Haumann, Dr. R. Weihrich
Institute of Inorganic Chemistry
University of Regensburg
Universitätsstr. 31, 93040 Regensburg, Germany

Supporting information for this article is given via a link at the end of the document.((Please delete this text if not appropriate)) formation of [(triphos)Rh(μ-$S_2$)$_2$Rh(triphos)](BPh$_4$)$_2$·1.75 $CH_2Cl_2$ containing two $S_2^{2-}$ anions bridging the two Rh centers in the Ib mode.[12] All these compounds were synthesized in solution mainly applying mild reaction conditions. Hydrothermally synthesized transition metal polysulfide complexes are less common and no such compound was reported until now for the cations of group 9.

In our continuing explorative work to prepare new chalcogenide compounds containing transition metal cations we successfully isolated the star-shaped molecule with composition [$Co_4(C_6H_{14}N_2)_4(\mu_4\text{-}S_2)_2(\mu_2\text{-}S_2)_4$] in two pseudo-polymorphs containing a {$Co_4(S_2)_6$} core where the $S_2^{2-}$ anions exhibit two different bridging modes, the very rare IV and the more common IId modes. In this context it is noted that Co-based compounds have been reported as promising catalysts for light-driven hydrogen evolution [13] and therefore photocatalytic hydrogen generation experiments were performed with compound **II**.

Here we report the solvothermal synthesis, crystal structures, catalytic properties and a DFT based analysis of the bonding situation of the title complex.

## Results and Discussion

*Synthetic Aspects*

Solvothermal syntheses are mainly an explorative approach where complex reaction mechanisms occur which are still not well understood. Once a new compound was obtained the reaction conditions are optimized giving the largest yield by systematic variation of the synthesis parameters. In the present case about 100 syntheses were performed until the best conditions were achieved. But even if all reaction parameters for the preparation of a distinct compound are known, often minute changes of the conditions may affect product formation. The first solvothermal syntheses afforded crystallization of [$Co_4(C_6H_{14}N_2)_4(\mu_4\text{-}S_2)_2(\mu_2\text{-}S_2)_4$] (**I**). After detailed product characterization applying single crystal structure analysis, XRD and CHNS analysis, optical spectroscopy, etc. preliminary photocatalytic hydrogen generation experiments were done which were quite promising. The syntheses using a new charge of the amine applying identical reaction conditions as for **I** yielded compound **II**, [$Co_4(C_6H_{14}N_2)_4(\mu_4\text{-}S_2)_2(\mu_2\text{-}S_2)_4$]·$4H_2O$. The reason is not clear as no differences were observed in the $^1$H-NMR spectra of the two amine charges. Compound **II** can be transformed into **I** by heating **II** at 150 °C (Fig. S1, see supporting information (SI)) or by storing **II** over $P_2O_5$ (Fig. S2, SI). Applying **I** for stability tests before the photocatalytic hydrogen generation experiments showed the at least partial transformation of **I** into **II** (Fig. S3, SI).

*Crystal structure*

The new compound [$Co_4(C_6H_{14}N_2)_4(\mu_4\text{-}S_2)_2(\mu_2\text{-}S_2)_4$] (**I**) crystallizes in the monoclinic space group *C2/c* with 8 formula units in the unit cell with all atoms being located on general positions. The pseudo-polymorphic phase [$Co_4(C_6H_{14}N_2)_4(\mu_4\text{-}S_2)_2(\mu_2\text{-}S_2)_4$]·$4H_2O$ (**II**) crystallizes in the monoclinic space group *P*2$_1$/*n* with Z = 4. Selected details of the data collection and structure refinements are listed in Tab. 1.

**Table 1.** Selected details of the data collection and structure refinement results.

| | [Co($C_6H_{14}N_2$)]$_4$$S_{12}$ (**I**) | [Co($C_6H_{14}N_2$)]$_4$$S_{12}$·$4H_2O$ (**II**) |
|---|---|---|
| crystal system | monoclinic | monoclinic |
| space group | *C2/c* | *P*2$_1$/*n* |
| Molecular weight / g/mol | 1077.21 | 1149,27 |
| a / Å | 38.0508(9) | 19.5879(8) |
| b / Å | 11.84200(10) | 11.8015(3) |
| c / Å | 26.9699(6) | 19.6925(9) |
| β / ° | 133.8430(10) | 90.033(4) |
| V / Å$^3$ | 8764.9(3) | 4552.2(3) |
| Temperature / K | 293 | 200 |
| Z | 8 | 4 |
| $D_{calculated}$ / g/cm$^3$ | 1.633 | 1.677 |
| μ/ mm$^{-1}$ | 2.089 | 2.023 |
| Scan Range | $1.87 \leq \theta \leq 26.00°$ | $1.726 \leq \theta \leq 25.005°$ |
| Reflections collected | 61555 | 30917 |
| Refl. with $F_o > 4\sigma(F_o)$ | 8615 | 7146 |
| Independent reflections | 7765 | 7976 |
| Goodness-of-fit on $F^2$ | 1.199 | 1.034 |
| Final R indices [$I > 2\sigma$] | R1 = 0.0375, wR2 = 0.0754 | R1 = 0.0575, wR2 = 0.1506 |
| R indices (all data) | R1 = 0.0443, wR2 = 0.0779 | R1 = 0.0658, wR2 = 0.1589 |
| Res. Elec. Dens. / e.Å$^{-3}$ | 0.410 and -0.419 | 0.737 and -0.617 |

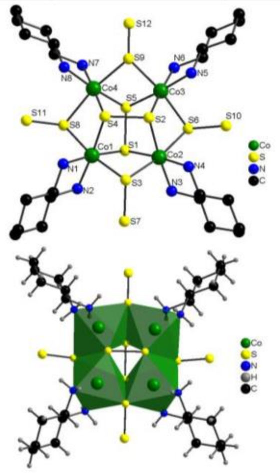

**Figure 1.** Connection of the $Co^{3+}$ centers *via* $S_2^{2-}$ anions in the title compound (top) and polyhedral representation (bottom). Not all atoms are labeled and H atoms are omitted in the top graph.

The relation between the unit cell dimensions are a(**I**) ≈ 2·a(**II**), b(**I**) ≈ b(**II**) and c(**I**) ≈ √2·c(**II**). The X-ray powder patterns of the two pseudo-polymorphs are shown in Fig. S4. The structural motif is identical for both compounds and therefore, the primary and secondary building units will be discussed for compound **I** as a representative. In the remarkable structures four unique $[Co(C_6H_{14}N_2)]^{3+}$ cations are connected via six $S_2^{2-}$ anions to form the star-shaped molecule $[Co_4(C_6H_{14}N_2)_4(\mu_4\text{-}S_2)_2(\mu_2\text{-}S_2)_4]$. Each $Co^{3+}$ ion is surrounded by four S atoms of four different $S_2^{2-}$ dumbbells and two N atoms of the amine ligands yielding a distorted $CoS_4N_2$ octahedral environment as evidenced by the trans-angles around the $Co^{3+}$ centers varying from 168.87(3) to 177.42(7) ° (Tab. S1 / S2 for **II**). Such deviations are not unusual and were also reported in literature.[6,7,14] The $CoS_4N_2$ octahedra each share two edges with neighbored octahedra leading to non-bonding $Co^{3+}$-$Co^{3+}$ separations of 3.249 – 3.291 Å, and the $Co^{3+}$ ions form a rectangular plane (mean deviation: 0.0002 Å). The $Co^{3+}$ $d^6$ centers are in the low spin state as expected.

The six unique $S_2^{2-}$ anions connect the four unique $Co^{3+}$ ions in two different binding modes. Two $S_2^{2-}$ dumbbells act in a $\mu_4$-fashion being located in the center of the molecule (connection mode IId in Scheme 1) while the remaining four dianions are $\mu_2$-bridging (Fig. 1, top). The S-S bonds scatter in a relatively large range from 2.0363(12) to 2.1243(10) Å (Tab. 2). The longest S-S bonds are observed for the $\mu_4$-acting $S_2^{2-}$ anions and the shorter for the remaining dumbbells. The long S-S bonds are not very common and an analysis of data in the CSD shows that the average bond length increases with increasing number of bonds of the S atoms to transition metal cations. For type IIc $S_2^{2-}$ (CSD: 89 hits) the average bond length is 2.080 Å (min.: 1.926 Å, max.: 2.211 Å) and for type IId (32 hits) 2.091 Å (min.: 1.984 Å, max.: 2.168 Å).

**Table 2.** Selected bond lengths (Å) of compound **I**. Estimated standard deviations are given in parentheses.

| | | | |
|---|---|---|---|
| Co1-N2 | 1.982(2) | Co2-N3 | 1.974(2) |
| Co1-N1 | 1.983(3) | Co2-N4 | 1.979(2) |
| Co1-S4 | 2.2276(8) | Co2-S1 | 2.2274(8) |
| Co1-S1 | 2.2277(8) | Co2-S2 | 2.2426(8) |
| Co1-S3 | 2.3175(8) | Co2-S3 | 2.3026(8) |
| Co1-S8 | 2.3201(8) | Co2-S6 | 2.3210(8) |
| Co3-N5 | 1.976(3) | Co4-N7 | 1.978(2) |
| Co3-N6 | 1.980(3) | Co4-N8 | 1.998(3) |
| Co3-S5 | 2.2243(9) | Co4-S5 | 2.2247(8) |
| Co3-S2 | 2.2426(8) | Co4-S4 | 2.2401(8) |
| Co3-S9 | 2.3130(9) | Co4-S9 | 2.3112(9) |
| Co3-S6 | 2.3196(8) | Co4-S8 | 2.3305(9) |
| S1-S5 | 2.1091(10) | S6-S10 | 2.0419(12) |
| S2-S4 | 2.1243(10) | S8-S11 | 2.0398(12) |
| S3-S7 | 2.0479(11) | S9-S12 | 2.0363(12) |

The values for the Co-N bond lengths vary from 1.974(2) to 1.998(3) Å (Tab. 2) being in the typical range and match with values reported for e.g. a $CoN_3S_3$ containing complex[15] or in $[C_{12}H_{26}CoN_2S_4]^{3+}(PF_6)_3{\cdot}3H_2O$.[16] The Co-S bonds ranging from 2.2243(9) to 2.3305(9) Å can be divided into two groups. The shorter Co-S distances are to S atoms in the center of the star-shaped molecule acting in the $\mu_4$-bridging mode and the longer ones to the S atoms of $S_2^{2-}$ anions pointing outwards of the molecule. The Co-S bond lengths distribution is significantly different to those reported for other $S_2^{2-}$ containing Co compounds. E.g., in $Cp_4Co_4(\mu_3\text{-}S)_3(\mu_3\text{-}S_2)$, the Co-S bonds are between 2.2003 and 2.2350 Å[3] while in $[(\eta^5\text{-}C_5Me_5)_2Co_2S_4]$ values in a more narrow range 2.244 – 2.247 Å are observed.[6] In all Co compounds with $S_2^{2-}$ dianions[3–10] no Co-S bond longer than 2.3 Å were reported.

The S atoms of the dianions pointing out of the molecules are involved in intramolecular S···H-N bonding interactions while the atoms S1, S4, S6 and S7 also have intermolecular H-bonding interactions to neighbored S atoms (Table S3 / S4 for **II**). Within the (010) plane the molecules are arranged that the hydrophobic parts of the molecules point to each other (Fig. 2).

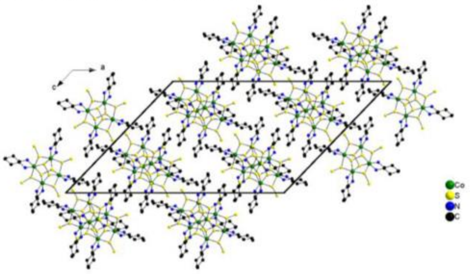

**Figure 2.** Arrangement of the molecules of compound **I** in the (010) plane. The hydrogen atoms are omitted for clarity.

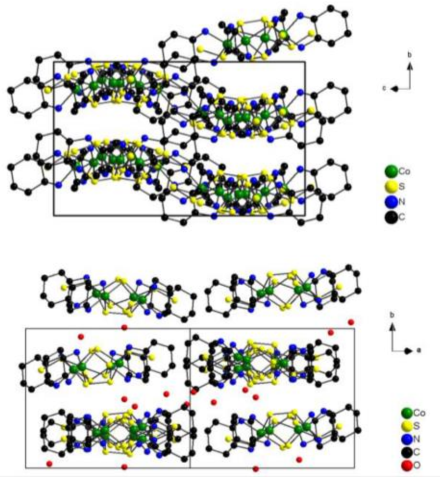

**Figure 3.** Arrangement of the molecules of the title compounds **I** (top) and **II** (bottom) in the (100) plane. The hydrogen atoms are omitted for clarity.

The difference between the crystal structures of compounds **I** and **II** (beside the presence of water molecules) is the arrangement of the star-shaped molecules. In **I** a wave-like assembly along [001] is observed whereas in **II** the arrangement is more linear (Fig. 3). The complexes in **II** form rods running along [001] and along [010] and the water molecules are located between the rods. More specifically, the O atoms of the $H_2O$ molecules are in the neighborhood of terminal S atoms with S···O separations between 3.223 and 3.389 Å.

*Hirshfeld surface analysis*

For further understanding intermolecular interactions stabilizing the arrangement of the molecules the Hirshfeld surface of the title compounds were calculated using CrystalExplorer 3.1[17] which provides a three-dimensional picture of close contacts in a crystal. The quantities $d_e$ and $d_i$ characterize the distance from the Hirshfeld surface to the nearest atoms outside and inside the surface, respectively. The value $d_{norm}$ represents the normalized contact distance based on $d_e$ and $d_i$, and is calculated according to $d_{norm} = (d_i - r_i^{vdW})/r_i^{vdW} + (d_e - r_e^{vdW})/r_e^{vdW})$, with $r_i^{vdW}$ and $r_e^{vdW}$ being the van der Waals radii of the atoms. Fig. 4 shows the $d_{norm}$ surface of molecule of **I** and **II** in one orientation together with two further molecules having contacts to the former.

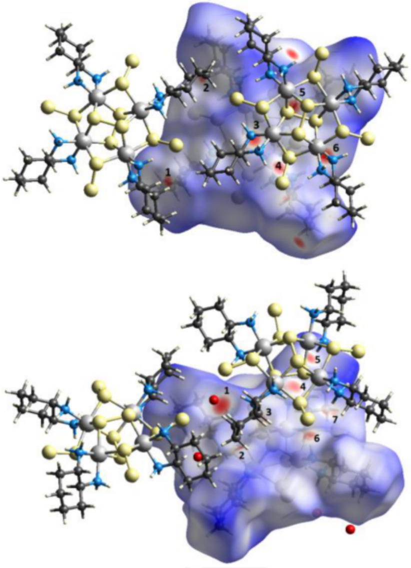

**Figure 4.** View of the Hirshfeld surface of one molecule of the title compound **I** (top, mapped with $d_{norm}$, range -0.24 to 2.29) and compound **II** (bottom, mapped with $d_{norm}$, range -0.46 to 2.05). It demonstrates contact distances relative to the sum of van der Waals radii. The closest contacts are shown as red areas.

Several H···H interactions can be identified (labels 1 and 2 in Fig. 4, top, resp. labels 2 and 5 in Fig. 4, bottom) as well as S···H intermolecular interactions (labels 3-6 in Fig. 4, top, resp. labels 3, 4, 6, 7 in Fig. 4, bottom). The O···H interactions are labeled with 1 in Fig. 4, bottom. A more detailed analysis using the finger print plot of the contacts in the structures reveals that S···H bonding presents 27.1% (**II**: 21.2%), S···S contacts 1.2% (**II**: 1.4%) and H···H interactions 71.7% (**II**: 58.5%). As expected from the presence of water molecules in **II** the intermolecular interaction pattern is slightly different because additionally O···H (13.8%) and S···O contacts (2.7%) are present. From this analysis it is obvious that taking weak intermolecular interactions into account a more detailed picture about the arrangement of the molecules in the structure is obtained than considering only S···H bonding interactions.

*Bonding situation*

The quantum chemical calculations address structure and bonding of the title compound **I** with a focus on the observed peculiarities of Co-S, Co-N, and S-S ($\mu_2$ and $\mu_4$) bonds. First, structure optimizations were performed on the crystal structure of **I** and molecular models. Second, chemical bonding is analyzed from the characteristics of the frontier orbitals.

**Table 3.** Atomic distances (d/Å) from DFT optimizations (B3LYP) on the crystal structure of **I** compared to experimental data (X) (for details see Tab. S5).

| d/Å | Co-N | Co-S ($\mu_4$) | Co-S ($\mu_2$) | S-S ($\mu_4$) | S-S ($\mu_2$) | N-H C-H | S-H | S-H | N-C C-C |
|---|---|---|---|---|---|---|---|---|---|
| X | 1.98-1.99 | 2.23-2.24 | 2.32-2.33 | 2.11-2.12 | 2.04-2.05 | 0.90<br>0.98 | 2.34-2.43 | 2.72-3.00 | 1.49<br>1.51 |
| DFT | 1.99-2.00 | 2.23-2.24 | 2.31-2.33 | 2.12-2.13 | 2.04-2.06 | 0.93<br>1.00 | 2.24-2.38 | 2.67-2.99 | 1.49<br>1.52 |

The significance of the electronic origin of the found Co-S, Co-N, and S-S distances is underlined by good agreement for predicted (B3LYP level of theory) and experimentally observed atomic distances in **I** (Tab. 3, see also Tab. 2 and Tab. S1, S5, SI). The differences in Co-S (2.2 Å vs. 2.3 Å) are reproduced, as well as the deviations for $\mu_4$- (2.11 Å) and $\mu_2$-bridging (2.05 Å) $S_2$ units. Optimizations on the crystal structure result in slight deviations of Co-S and Co-N distances for the different Co sites as experimentally found. To the contrary optimizations of the title compound and simplified models ($NH_3$ as N-coordinating ligands, Ia) converge to $C_{2v}$ symmetry where all Co atoms become equivalent. Again, experimentally found differences for bond lengths of $\mu_4$- and $\mu_2$-bridged $S_2$ units to Co and S neighbors are systematically reproduced. Thus, packing effects must be responsible for the distortion of the molecules in the real crystal, but local bonding for the observed characteristic Co-S and S-S distances.

To shed light on the origin of the different S-S-distances comparisons are drawn to model calculations on charged $[S_2]^{2-}$ units. In isolated molecular units the S-S distances increase with higher charge from $S_2$ ($d_{SS}$ =1.95 Å) to $[S_2]^-$ (2.05 Å) and $[S_2]^{2-}$ (2.20 Å). For real crystal structures, the distances are further known to be influenced by back-bonding to heteroatoms, e.g. for pyrite type $CoS_2$ ($d_{SS}$ = 2.11 Å), $FeS_2$ (2.18 Å).[18] $CoS_2$ also serves as example for long distances Co-S (2.32 Å), whereas they are short (2.19 Å) in $InSnCo_3S_2$ with linear S-Co-S arrangements.[19,20] For the title compound one has to conclude on different charges and bonding characteristics for the $\mu_2$- and $\mu_4$-bridging $S_2$ units with an additional effect of the Co-S bonds.

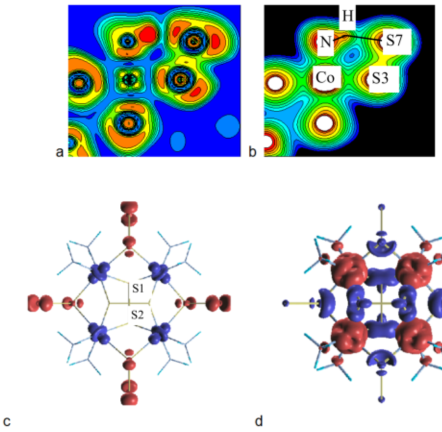

**Figure 5.** a) ELF plot for a cut through $CoS_2N_2$ plane of the $CoN_2S_4$ polyhedron with Co-N-H bonds to $\mu_2$-bridging Co-S3-S7; b) related charge density plot; Visualization of LUMO (c) and HOMO (d) for the molecular model Ia of the title compound with $\mu_4$- and $\mu_2$-bridging atoms.

Indeed, direct space bonding in Ia (Fig. 5, more details in Fig. S5, S6) reveals an asymmetry in the S-S bonds of the $\mu_2$-bridging units. It is shown within the $CoS_2N_2$ plane through the $CoN_2S_4$ polyhedron together with the N-H···S hydrogen bond. Therein, maxima (red) of the electron localization function (ELF, Fig. 5a, Fig. S6) indicate the lone and bonding electron pairs for the S and N atoms (ELF > 0.8). The ELF maximum that corresponds to the S-S bond is shifted to the S atom next to Co. To the contrary, ELF for all bridging $S_2$ units is highly symmetrical (see supplement for further graphical data), bond critical points (BCPs) are in the middle of S-S. In the electronic charge density (Fig. 5b) the polarization of the terminal S-S unit is found numerically by a shift of the respective BCP from the S-S centre to the terminal S atom. According to Bader´s theory of atoms in molecules (AIM) BCPs are saddle points in the 3D charge density. Along a polarized bond the BCP is thus shifted according to charge depletion. BCPs are further detected for the N-H···S hydrogen bond as visualized in Fig. 5b. According to the ELF plot the H bond fixes the free electron pair of S that points to the N-H bond and stabilizes the structural arrangement (the position of H itself is not seen in the ELF as it has no core electrons).

Further insight into the bonding situation is gained from orbital analysis (Fig. 5c-d). Accordingly, the LUMO is mainly localized at the S atoms that bridge Co neighbors. It is symmetrical for the $\mu_4$-bridged, but asymmetrical for the $\mu_2$-bridged $S_2$ units. The HOMO is predicted 1.4 eV above the LUMO and formed from antibonding S-p and Co-d states. This is due to differences in the Co-S and S-S interactions as shown from the atomic orbital projected density of states (PDOS, Fig. 6; IDOS see Fig. S7). For the $\mu_4$-bridged $S_2$ units (S1) the occupied $\sigma(s)$, $\sigma(s)^*$, $\sigma(p)$, $\pi(p)$, $\pi(p)^*$ below the Fermi energy ($E_F$) correspond to a MO scheme for dumbbells with 14 electrons. The $\sigma(p)^*$ like states are unoccupied at +2 eV. In line with the short Co-S bonds (2.23 Å) the DOS maxima of $\sigma(p)$ and $\sigma(p)^*$ indicate bonding to Co orbitals. To the contrary, DOS contributions of the S-3p orbitals of the $\mu_2$-bridging $S_2$ units (S3-S9 in Fig. 6) show significant differences. For the terminal S atom high DOS just below $E_F$ is indicative for its free electron pairs. In line with the longer Co-S distances (2.32 Å) the DOS for the S3 site indicates interactions to Co that are however weaker than for the $\mu_4$-bridged S atoms. As a conclusion the $\mu_2$-bridging $S_2$ units show asymmetry in bonding and a distortion of 3p-3p interactions. The reason might be the H-bonds that fix the free electron pair of the terminal S site. As a consequence the formation and occupation of antibonding $\pi(p)^*$ orbitals is avoided and the S-S distance is shorter. In case of the $\mu_4$-bridging $S_2$ unit the $\pi(p)^*$ orbitals are occupied. This causes longer S-S distances, but stronger back-bonding to Co-$e_g$ states and shorter Co-S bonds. These results are in line with the calculated charges for Co (+0.48), S1 (-0.14), S3 (-0.05), S7 (-0.45).

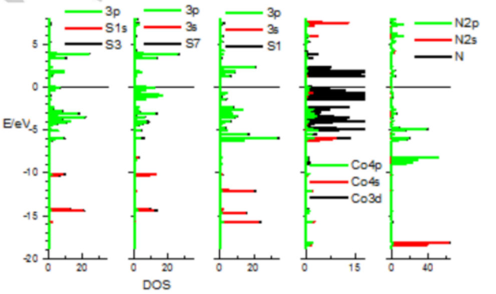

**Figure 6**. Analyses of orbital contributions of the S3, S7 (both in the terminal S2 unit), and S1 (central S2 unit) atoms.

*Photocatalytic tests*

A test of the performance of $[Co_4(C_6H_{14}N_2)_4(\mu_4\text{-}S_2)_2(\mu_2\text{-}S_2)_4]\cdot 4H_2O$ (**II**) as catalyst in the light driven photocatalytic hydrogen evolution using $[Ru(bpy)_3](PF_6)_2$ as sensitizer was done in a triethylamine/water/acetonitrile system (note: compound **I** transforms into **II** in the presence of water). As can be seen in Fig. 7 the photocatalytic hydrogen evolution strongly increases with increasing irradiation time and reaches a value of about 206 µmol after 3 h. At longer reaction times the $H_2$ evolution decreases indicating decomposition of at least one of the components in the system. The stability of the title compound was proved by recovering the catalyst after the first run and applying the material in a second run with new solvents and additives (details see SI, Figs. S8 - S10). The results clearly demonstrate that the compound does not decompose by corrosion because the amount of generated hydrogen of the first and second run is very similar. Additionally, XRD analysis confirms the stability of the sample during the photocatalytic reaction (Fig. S11). The powder patterns of the starting material and of the recovered catalyst are nearly unchanged suggesting that the photocatalytic reaction is of heterogeneous nature.

The amount of hydrogen evolved during light driven photocatalytic reactions is reported in diverse quantities e.g. in µmol, mL, as turnover number or turnover frequency, as quantum efficiency or quantum yield to mention the most often used quantities. Furthermore, the experimental reaction conditions vary widely like the light sources, solvent system, the usage of a co-catalyst, the amount the catalyst applied, the photosensitizer used, the set-up of the instrument etc. The lack of standard conditions, how data are reported, and widely differing measurement setups makes a comparison of the performance of catalysts more or less impossible. These problems were addressed in a number of papers and suggestions were made to overcome such difficulties.[21].

**Table 4.** Cobalt based photocatalysts for light-driven hydrogen generation.

| Photocatalyst | Light source | Reaction solution | Activity / µmol/h | Activity / µmol/mg*h |
|---|---|---|---|---|
| Title compound | 300 W Xe lamp | Triethylamine, water, $[Ru(bpy)_3](PF_6)_2$ in acetonitrile | 98 | 9.8 |
| $[Co(dmgBF_2)_2(H_2O)_2]$[22] | 500 W Xe lamp ($\lambda > 400$ nm) | water, acetonitrile, TEA, Rose Bengal | 460 | 2300 |
| $[Co(DPA\text{-}bpy)OH_2]^{3+}$ [23] | 150 W Xe lamp ($420 < \lambda < 520$ nm) | water, sodium ascorbat, acetic acid buffer, $[Ru(bpy)_3]^{2+}$ | 15 | 1070 |
| $CoS_x$/graphene[24] | 300 W Xe lamp ($\lambda > 455$ nm) | water, TEOA, Eosin Y | 300 | 125 |
| $CoS_x/TiO_2$[25] | 300 W Xe lamp | water, ethanol | 838 | 16.8 |
| CoS/mpg-CN[26] | 300 W Xe lamp | water, triethanolamine | 37 | 0.7 |

Nevertheless, for the purpose of a rough estimation the catalytic performances of different Co-based compounds expressed as µmol/h as well as µmol/h mg are compiled and compared to the performance of the present catalyst (Tab. 4). Obviously, homogeneous catalysts like $[Co(dmgBF_2)_2(H_2O)_2]$ or $[Co(DPA\text{-}bpy)OH_2]^{3+}$ are more active than the present material, [22–26] while the activity is comparable with cobalt sulfides applied as heterogeneous catalysts (Tab. 4).

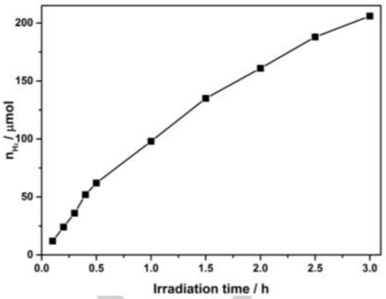

**Figure 7.** Light driven photocatalytic hydrogen evolution applying compound **II**.

## Conclusions

A hitherto not observed combination of binding modes of $S_2^{2-}$ moieties in $Co^{3+}$ based compounds generates a star-shaped molecule obtained under solvothermal conditions. The two compounds can be regarded as pseudo-polymorphs and the water free sample can be transformed into the tetrahydrate by treatment in humid atmosphere/water. The quantum chemical calculations reveal significant differences for the bonding states of the bridging and the terminal $S_2^{2-}$ units in compound **I**. The different distances are well reproduced with B3LYP calculations. According to the orbital analysis the longer distances of the bridging $S_2^{2-}$ dianions are due to occupied $\pi(p)^*$ states that are imposed by geometry. Respective s(p)* bonds form the HOMO. The terminal $S_2$ unit can avoid this situation by the formation of a polarized S-S bond with major contributions of S-3p orbitals to the LUMO. It is stabilized asymmetrically by intramolecular H-bonds to neighboring N-H units. The Hirshfeld surface analysis yields a detailed picture about all interactions within and between the molecules. $[Co_4(C_6H_{14}N_2)_4(\mu_4\text{-}S_2)_2(\mu_2\text{-}S_2)_4]\cdot 4H_2O$ as catalyst for light-driven hydrogen generation exhibits promising results, which are worthwhile for further studies.

## Experimental Section

*Synthesis*

General: All chemicals were purchased and used without further purifications. All syntheses were conducted under solvothermal conditions in Teflon-lined steel autoclaves (inner volume 30 mL) using cobalt, sulfur and amine. The crystalline products were filtered off after the reactions, washed with water and ethanol or acetone and dried in vacuum. The reaction products were separated manually and the homogeneity of the crystalline part was checked by X-ray powder diffraction.

### *Synthesis of* $[Co_4(C_6H_{14}N_2)_4(\mu_4\text{-}S_2)_2(\mu_2\text{-}S_2)_4]$ *(**I**):*

64.25 mg (2.01 mmol) S and 28.85 mg (0.49 mmol) Co with 5 mL aqueous *trans*-1,2-diaminocyclohexane ($C_6H_{14}N_2$, 63 %) were heated for 96 h at 130 °C. In the reaction products, black needles of the compound were obtained in a yield of about 25 % (based on Co) besides Co sulfides. Elemental analysis, results in %: found: C 25.0, H 5.5, N 9.9; calculated: C 26.8, H 5.2, N 10.4.

### *Synthesis of* $[Co_4(C_6H_{14}N_2)_4(\mu_4\text{-}S_2)_2(\mu_2\text{-}S_2)_4]\cdot 4H_2O$ *(**II**):*

64.17 mg (2.00 mmol) S and 29.85 mg (0.51 mmol) Co with 5 mL aqueous *trans*-1,2-diaminocyclohexane ($C_6H_{14}N_2$, 63 %) were heated for 98 h at 130 °C. In the reaction products, black needles of the title compound were obtained in a yield of about 25 % (based on Co) besides Co sulfides. Elemental analysis, results in %: found: C 24.2, H 5.1, N 8.6; calculated: C 25.1, H 5.61, N 9.8.

Different parameters have been varied as e.g. the amine concentration, the reaction time, ratio of educts or stirring conditions (ca. 100 syntheses), but the best conditions are 0.5 mmol Co and 2.0 mmol S in 63% *trans*-1,2-diaminocyclohexane.

The solid reaction products were in a colored solution indicating that educts formed soluble compound(s). The solid products (crystals) were separated by hand and the homogeneity checked by XRD.

### *Structure determination*

The intensity data were collected using a STOE IPDS-2 (Imaging Plate Diffraction System) with Mo-$K_\alpha$ radiation at room temperature. The first structure was solved with direct methods using the program SHELXS-97[27] and the refinements were done against $F^2$ with SHELXL-97.[28] For all non-hydrogen atoms anisotropic displacement parameters were used. For compound **I** a numerical absorption correction was performed using X-Red and X-Shape from STOE (Min/max transmission: 0.6405/0.7832). The hydrogen atoms were positioned with idealized geometry and were refined using a riding model. The crystal (of **I**) investigated is very slightly non-merohedral twinned with a pseudo 2-fold axis as the twin element. Therefore, a twin refinement was performed (BASF parameter: 0.00387(19)). The second structure was solved with direct methods and structure refinement was performed using SHELXL-2013 [29]. All non-hydrogen atoms were refined isotropic. The data were corrected for absorption using X-Red and X-Shape from STOE. A numerical absorption correction was performed ($T_{min/max.}$: 0.6280, 0.7750). The C-H and N-H H atoms were positioned with idealized geometry and refined isotropic with $U_{iso}(H) = 1.2\ U_{eq}(C, N)$ using a riding model. The water H atoms could not be located but considered in the calculation of the molecular formula. The crystal investigated is also pseudo-merohedral twinned and thus, a twin refinement was performed (BASF parameter: 0.287(2)). Structural data have been deposited in the Cambridge Crystallographic Data Centre as publication no. CCDC 1017107 (**I**) and 1056063 (**II**). Copies of the data can be obtained, free of charge, on application to CCDC, 12 Union Road, Cambridge CB2 1 EZ, UK (mail: deposit@ccdc.ca.ac.uk).

### *EDX experiments*

Scanning electron microscopy investigations and energy dispersive X-ray analyses (EDX) were done with a Philips Environmental Scanning Electron Microscope ESEM XL30 equipped with an EDAX detector.

### *X-ray powder diffractometry*

The X-ray powder diffraction patterns were recorded on a STOE Stadi-P powder diffractometer (Cu-$K_{\alpha 1}$ radiation, $\lambda$ = 1.540598 Å, Ge monochromator) in transmission geometry.

### *Infrared spectroscopy*

MIR spectra (500-4000 cm$^{-1}$) were recorded with an ATI Mattson Genesis spectrometer. For the compound the absorptions located at 3213 (s, -$NH_2$ stretch), 3110 (m, -$NH_2$ stretch), 2929 (m, -$NH_2$ stretch), 2855 (m, -CH stretch, N-$CH_2$), 1629 (m, -C-N-H def.), 1573 (s, -$NH_2$ asym. def.), 1448 and 1402 (s, -CH def., N-$CH_2$), 1349 (s, -CH def.), 1130 (s, -CN stretch), 1047 (s, -CN stretch) cm$^{-1}$ can be assigned to the *trans*-1,2-diaminocyclohexane and at 513 cm$^{-1}$ the absorption of the disulfides is observed (Fig. S12, SI).

### *Raman spectroscopy*

Raman spectra were recorded with a Bruker IFS 66 Fourier transform Raman spectrometer (wavelength: 541.5 nm) in the region from 100 to 3500 cm$^{-1}$ (Fig. S13, SI).

### *UV/Vis spectroscopy*

UV/Vis spectroscopic investigations were carried out at room temperature using an UV-Vis-NIR two-channel spectrometer Cary 5 from Varian Techtron Pty., Darmstadt. The optical properties of the compound were investigated by analyzing the UV/Vis reflectance spectra of the powdered samples (with $BaSO_4$ powder used as reference material). The absorption data were calculated applying the Kubelka-Munk relation for diffuse reflectance data. The optical band gap was estimated to 1.0 eV (Fig. S14, SI).

### *Light driven photocatalytic experiment*

Photocatalytic reactions were carried out in a double-walled thermostatically controlled glass vessel that was loaded with 10 mg of the title compound, evacuated and back-filled with argon four times in order to remove other gases. Triethylamine (8 mL), distilled and degassed water (3 mL) and $[Ru(bpy)_3](PF_6)_2$ (1 mM) in acetonitrile (10 mL) were transferred via syringe. The mixture was stirred, set at 30 °C and the system was left to equilibrate for 15 min. The reaction was started by switching on the light source (300 W Xe lamp). An Agilent Technologies 7890A gas chromatograph with a 60/80 Carboxen 1000 (Supelco) column and a TCD was used to qualify the gas. The amount of hydrogen was quantified with an automatic burette. Differences in amount of produced hydrogen are due to different reaction conditions (see SI):

### *DFT calculations*

Quantum chemical calculations were performed within the framework of density functional theory (DFT). For structure optimizations, orbital decomposition and charge transfer analyses full potential local orbital and Gaussian type orbital (GTO) codes FPLO14[30] and CRYSTAL14[31] were applied. This allows for calculations on periodic structures and single molecules at the LDA, GGA,[32] and B3LYP functional approaches. FLPO treats Co-3d, 4s, 4p, 5s, 5p, and 4d, S-3s, 3p, and 3d, N-2s, 2p, 3s, 3p, and 3d, as well as H-1s, 2s, and 2p as valence, Co-3s and 3p, S-2s and 2p, and N-1s as semi-valence stats. Therein, the outer shells are optimized automatically at each SCF cycle. Convergence is considered at differences in total energy less than $10^{-7}$ H and Hellmann-Feynman forces less than $10^{-4}$ eV/Å. For direct space HOMO/LUMO, charge density, AIM (atoms in molecules) and ELF (electron localization function)[33] analyses with CRYSTAL98/14 and TOPOND97/13[34] all electron basis sets (N-8631d1G*, Co-86411d311G*, S-8631d1G*, and H-5111G) were optimized and tested for comparable performance in crystal and electronic structure prediction (see also [19,20]).

## Acknowledgements

Financial support by the State of Schleswig-Holstein and the DFG is gratefully acknowledged.

**Keywords:** $Co^{3+}$ compound, disulfide bridges, DFT, Hirshfeld surface, Photocatalyst

[1] a) W. S. Sheldrick, *Z. Anorg. Allg. Chem.* **2012**, *638*, 2401–2424; b) G. W. Drake, J. W. Kolis, *Coord. Chem. Rev.* **1994**, *137*, 131–178; c) M. Draganjac, T. B. Rauchfuss, *Angew. Chem. Int. Ed.* **1985**, *24*, 742–757.
[2] A. Müller, E. Diemann, *Adv. Inorg. Chem.* **1987**, *31*, 89–122.
[3] R. D. Adams, S. Miao, *Inorg. Chim. Acta* **2005**, *358*, 1401–1406.
[4] V. A. Uchtman, L. F. Dahl, *J. Am. Chem. Soc.* **1969**, *91*, 3756–3763.
[5] D. L. Stevenson, V. R. Magnuson, L. F. Dahl, *J. Am. Chem. Soc.* **1967**, *89*, 3727–3732.
[6] H. Brunner, N. Janietz, W. Meier, G. Sergeson, J. Wachter, T. Zahn, M. L. Ziegler, *Angew. Chem. Int. Ed.* **1985**, *24*, 1060–1061.
[7] R. J. Pleus, W. Saak, S. Pohl, *Z. Anorg. Allg. Chem.* **2001**, *627*, 250–253.
[8] H. Brunner, F. Leis, J. Wachter, M. Zabel, *J. Organomet. Chem.* **2001**, *628*, 39–45.
[9] M. Maruyama, J.-D. Guo, S. Nagase, E. Nakamura, Y. Matsuo, *J. Am. Chem. Soc.* **2011**, *133*, 6890–6893.
[10] C. Floriani, M. Fiallo, A. Chiesi-Villa, C. Guastini, *J. Chem. Soc., Dalton Trans.* **1987**, 1367–1376.
[11] M. Nishio, H. Matsuzake, Y. Mizobe, M. Hidai, *Angew. Chem. Int. Ed.* **1996**, *35*, 872–874.
[12] C. Bianchini, A. Meli, *Inorg. Chem.* **1987**, *26*, 1345–1346.
[13] a) T. Lazarides, T. McCormick, P. Du, G. Luo, B. Lindley, R. Eisenberg, *J. Am. Chem. Soc.* **2009**, *131*, 9192–9194; b) Y. Sun, J. Sun, J. R. Long, P. Yang, C. J. Chang, *Chem. Sci.* **2013**, *4*, 118–124.
[14] a) N. Pienack, S. Lehmann, H. Lühmann, M. El-Madani, C. Näther, W. Bensch, *Z. Anorg. Allg. Chem.* **2008**, *634*, 2323–2329; b) F. L. Jiang, X. Y. Huang, R. Cao, M. C. Hong, H. Q. Liu, *Acta Cryst. C* **1995**, *51*, 1275–1278.
[15] E. López-Torres, M. A. Mendiola, C. J. Pastor, *Inorg. Chem.* **2006**, *45*, 3103–3112.
[16] A. J. Blake, G. Reid, M. Schröder, *J. Chem. Soc., Dalton Trans.* **1994**, 3291.
[17] a) M. A. Spackman, D. Jayatilaka, *CrystEngComm* **2009**, *11*, 19–32; b) M. A. Spackman, J. J. McKinnon, *CrystEngComm* **2002**, *4*, 378–392; c) J. J. McKinnon, M. A. Spackman, A. S. Mitchell, *Acta Cryst. B* **2004**, *60*, 627–668; d) J. J. McKinnon, D. Jayatilaka, M. A. Spackman, *Chem. Commun.* **2007**, 3814–3816; e) M. A. Spackman, J. J. McKinnon, D. Jayatilaka, *CrystEngComm* **2008**, 377–388; f) M. J. Turner, J. J. McKinnon, D. Jayatilaka, M. A. Spackman, *CrystEngComm* **2011**, *13*, 1804–1813.
[18] P. J. Brown, K.-U. Neumann, A. Simon, F. Ueno, Ziebeck, K. R. A., *J. Phys. Cond. Mat.* **2005**, *17*, 1583–1592.
[19] J. Rothballer, F. Bachhuber, F. Pielnhofer, F. M. Schappacher, R. Pöttgen, R. Weihrich, *Eur. J. Inorg. Chem.* **2013**, *2013*, 248–255.
[20] O. Osters, T. Nilges, M. Schöneich, P. Schmidt, J. Rothballer, F. Pielnhofer, R. Weihrich, *Inorg. Chem.* **2012**, *51*, 8119–8127.
[21] a) J. M. Buriak, P. V. Kamat, K. S. Schanze, *ACS Appl. Mater. Interfaces* **2014**, *6*, 11815–11816; b) I. E. Wachs, S. P. Phivilay, C. A. Roberts, *ACS Catal.* **2013**, *3*, 2606–2611; c) S. E. Braslavsky, A. M. Braun, A. E. Cassano, A. V. Emeline, M. I. Litter, L. Palmisano, V. N. Parmon, N. Serpone, *Pure Appl. Chem.* **2011**, *83*, 931–1014; d) M. Schwarze, D. Stellmach, M. Schröder, K. Kailasam, R. Reske, A. Thomas, R. Schomäcker, *Phys. Chem. Chem. Phys.* **2013**, *15*, 3466–3472.
[22] P. Zhang, M. Wang, J. Dong, X. Li, F. Wang, L. Wu, L. Sun, *J. Phys. Chem. C* **2010**, *114*, 15868–15874.
[23] B. Shan, T. Baine, X. Ma, X. Zhao, R. H. Schmehl, *Inorg. Chem.* **2013**, *52*, 4853–4859.
[24] C. Kong, S. Min, G. Lu, *Int. J. Hydrogen Energy* **2014**, *39*, 4836–4844.
[25] Z. Yu, J. Meng, J. Xiao, Y. Li, Y. Li, *Int. J. Hydrogen Energy* **2014**, *39*, 15387–15393.
[26] Y. Zhu, Y. Xu, Y. Hou, Z. Ding, X. Wang, *Int. J. Hydrogen Energy* **2014**, *39*, 11873–11879.
[27] G. M. Sheldrick, *SHELXS-97, Program for the Solution of Crystal Structures, University of Göttingen, Göttingen (Germany)* **1997**.
[28] G. M. Sheldrick, *SHELXL-97, Program for the Refinement of Crystal Structures, University of Göttingen, Göttingen (Germany)* **1997**.
[29] G. M. Sheldrick, *SHELXL-2013, Program for the Refinement of Crystal Structures, University of Göttingen, Göttingen (Germany)* **2013**.
[30] K. Koepernik, H. Eschrig, *Phys. Rev. B* **1999**, *59*, 1743–1757.
[31] a) R. Dovesi, V. R. Saunders, C. Roetti, R. Orlando, C. M. Zicovich-Wilson, F. Pascale, B. Civalleri, K. Doll, N. M. Harrison, I. J. Bush et al., *CRYSTAL14 User's Manual*, Torino, 2014; b) R. Dovesi, R. Orlando, A. Erba, C. M. Zicovich-Wilson, B. Civalleri, S. Casassa, L. Maschio, M. Ferrabone, De La Pierre, Marco, P. D'Arco et al., *Int. J. Quantum Chem.* **2014**.
[32] J. P. Perdew, K. Burke, M. Ernzerhof, *Phys. Rev. Lett.* **1996**, *77*, 3865–3868.
[33] A. D. Becke, K. E. Edgecombe, *J. Chem. Phys.* **1990**, *92*, 5397–5403.
[34] a) C. Gatti, V. R. Saunders, C. Roetti, *J. Chem. Phys.* **1994**, *101*, 10686–10696; b) C. Gatti, S. Casassa, *TOPOND User's Manual*, *CNR-ISTM of Milano, Milano*, 2014.

# Supporting Information

## Two pseudopolymorphic star-shaped tetranuclear $Co^{3+}$ compounds with disulfide anions exhibiting two different connection modes and promising light-driven photocatalytic properties

Nicole Pienack, Henning Lühmann, John Djamil, Stefan Permien, Christian Näther, Sebastian Haumann, Richard Weihrich, Wolfgang Bensch*

### *Thermal decomposition - Transformation of II into I*

The phase transformation can be achieved by thermal decomposition. Fig. S1 shows the XRD powder patterns of compound **II** before and after heating to 150°C for 60h as well as the calculated patterns for both compounds.

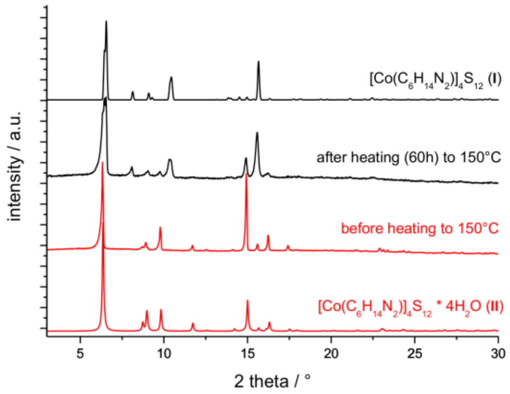

Fig. S1. XRD analysis of the title compounds after thermal decomposition.

### *Transformation of II into I*

The removal of the water molecules can be also reached by using $P_2O_5$. Fig. S2 shows the XRD powder patterns of compound **II** before and after treatment with $P_2O_5$ as well as the calculated patterns for both compounds.

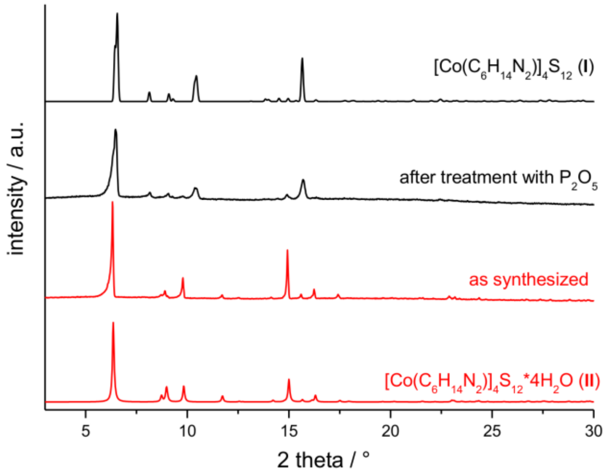

Fig. S2. Powder diffraction pattern of the title compounds after treatment with $P_2O_5$.

### *Stability tests before the hydrogen generation experiments*

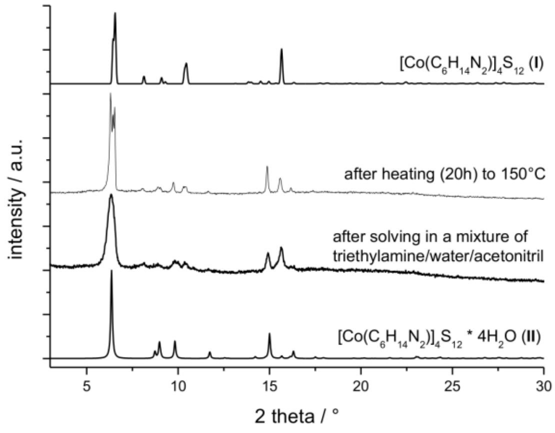

Fig. S3. Powder diffraction pattern of the title compound for stability tests.

## *Powder diffraction pattern of the title compounds*

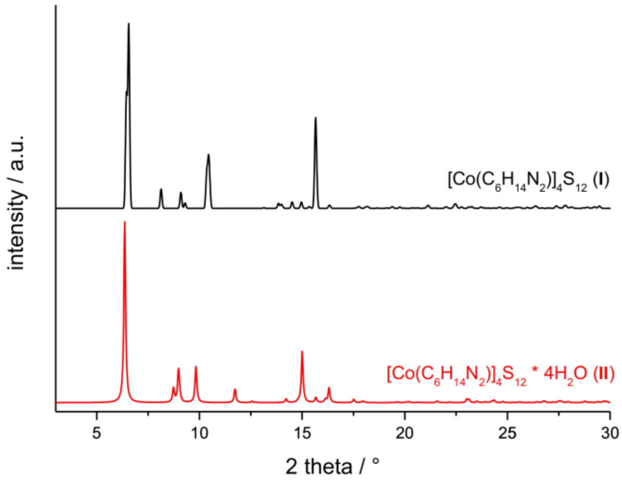

**Fig. S4. Powder diffraction pattern of compound I (top) and II (bottom).**

Tab. S1. Bond lengths (Å) and angles (°) of compound **I**.

| | | | |
|---|---|---|---|
| Co1 – S1 | 2.2271(4) | S1 – S5 | 2.1096(9) |
| Co1 – S4 | 2.2274(7) | S2 – S4 | 2.1244(10) |
| Co1 – S3 | 2.3174(7) | S3 – S7 | 2.0481(10) |
| Co1 – S8 | 2.3193(8) | S6 – S10 | 2.0429(12) |
| Co1 – N1 | 1.984(2) | S8 – S11 | 2.0401(12) |
| Co1 – N2 | 1.984(2) | S9 – S12 | 2.0371(11) |
| Co2 – S1 | 2.2269(7) | | |
| Co2 – S2 | 2.2424(7) | | |
| Co2 – S3 | 2.3027(7) | | |
| Co2 – S6 | 2.3207(8) | N1 – Co1 – N2 | 84.90(10) |
| Co2 – N3 | 1.975(2) | N1 – Co1 – S1 | 174.07(8) |
| Co2 – N4 | 1.981(2) | N2 – Co1 – S1 | 90.78(7) |
| Co3 – S5 | 2.2246(8) | N1 – Co1 – S4 | 93.09(7) |
| Co3 – S2 | 2.2428(8) | N2 – Co1 – S4 | 175.45(8) |
| Co3 – S9 | 2.3128(8) | S1 – Co1 – S4 | 91.51(3) |
| Co3 – S6 | 2.3189(8) | N1 – Co1 – S3 | 92.45(8) |
| Co3 – N5 | 1.978(2) | N2 – Co1 – S3 | 94.07(7) |
| Co3 – N6 | 1.982(3) | S1 – Co1 – S3 | 83.79(3) |
| Co4 – S5 | 2.2242(8) | S4 – Co1 – S3 | 90.09(3) |
| Co4 – S4 | 2.2397(7) | N1 – Co1 – S8 | 94.31(8) |
| Co4 – S9 | 2.3107(8) | N2 – Co1 – S8 | 93.38(7) |
| Co4 – S8 | 2.3307(8) | S1 – Co1 – S8 | 89.99(3) |
| Co4 – N7 | 1.978(2) | S4 – Co1 – S8 | 82.69(3) |
| Co4 – N8 | 1.999(2) | S3 – Co1 – S8 | 170.35(3) |
| | | N3 – Co2 – N4 | 84.76(9) |
| N3 – Co2 – S1 | 91.86(7) | N4 – Co2 – S1 | 175.01(7) |
| N3 – Co2 – S2 | 175.06(7) | N4 – Co2 – S2 | 92.26(7) |
| S1 – Co2 – S2 | 91.36(3) | N3 – Co2 – S3 | 94.48(7) |
| N4 – Co2 – S3 | 92.46(7) | S1 – Co2 – S3 | 84.14(3) |
| S2 – Co2 – S3 | 89.58(3) | N3 – Co2 – S6 | 92.83(7) |
| N4 – Co2 – S6 | 93.48(7) | S1 – Co2 – S6 | 90.34(3) |
| S2 – Co2 – S6 | 83.40(3) | S3 – Co2 – S6 | 170.97(3) |
| N5 – Co3 – N6 | 84.64(12) | N5 – Co3 – S5 | 175.27(9) |
| N6 – Co3 – S5 | 91.74(9) | N5 – Co3 – S2 | 92.41(9) |
| N6 – Co3 – S2 | 176.11(9) | S5 – Co3 – S2 | 91.33(3) |
| N5 – Co3 – S9 | 92.56(9) | N6 – Co3 – S9 | 94.90(8) |
| S5 – Co3 – S9 | 84.70(3) | S2 – Co3 – S9 | 87.77(3) |
| N5 – Co3 – S6 | 92.77(9) | N6 – Co3 – S6 | 94.14(8) |
| S5 – Co3 – S6 | 90.53(3) | S2 – Co3 – S6 | 83.44(3) |
| S9 – Co3 – S6 | 169.90(3) | N7 – Co4 – N8 | 83.91(9) |
| N7 – Co4 – S5 | 88.76(6) | N8 – Co4 – S5 | 172.25(8) |
| N7 – Co4 – S4 | 177.45(7) | N8 – Co4 – S4 | 96.31(8) |
| S5 – Co4 – S4 | 91.12(3) | N7 – Co4 – S9 | 94.24(7) |
| N8 – Co4 – S9 | 93.26(8) | S5 – Co4 – S9 | 84.76(3) |
| S4 – Co4 – S9 | 88.28(3) | N7 – Co4 – S8 | 95.29(7) |
| N8 – Co4 – S8 | 93.46(8) | S5 – Co4 – S8 | 89.71(3) |
| S4 – Co4 – S8 | 82.16(3) | S9 – Co4 – S8 | 168.87(3) |

Tab. S2. Bond lengths (Å) and angles (°) of compound **II.**

| | | | |
|---|---|---|---|
| Co1 – S1 | 2.298(3) | S1-S12 | 2.041(3) |
| Co1 – S2 | 2.290(2) | S2-S9 | 2.038(3) |
| Co1 – S3 | 2.230(2) | S3-S6 | 2.115(3) |
| Co1 – S4 | 2.227(2) | S4-S8 | 2.126(3) |
| Co1 – N11 | 1.983(7) | S5-S10 | 2.029(3) |
| Co1 – N12 | 1.974(7) | S7-S11 | 2.057(3) |
| Co2-S6 | 2.223(2) | | |
| Co2-S4 | 2.225(2) | N22-Co2-N21 | 84.9(3) |
| Co2-S2 | 2.311(2) | N22-Co2-S6 | 89.5(2) |
| Co2-S5 | 2.332(2) | N21-Co2-S6 | 173.8(2) |
| Co2-N22 | 1.959(7) | N22-Co2-S4 | 176.5(2) |
| Co2-N21 | 1.988(7) | N21-Co2-S4 | 93.9(2) |
| Co3-S8 | 2.229(2) | S6-Co2-S4 | 91.83(8) |
| Co3-S6 | 2.234(2) | N22-Co2-S2 | 93.7(2) |
| Co3-S7 | 2.291(2) | N21-Co2-S2 | 94.4(2) |
| Co3-S5 | 2.305(2) | S6-Co2-S2 | 88.73(8) |
| Co3-N31 | 1.981(7) | S4-Co2-S2 | 83.03(8) |
| Co3-N32 | 1.987(7) | N22-Co2-S5 | 94.9(2) |
| Co4-S8 | 2.220(2) | | |
| Co4-S3 | 2.224(2) | N12-Co1-N11 | 83.6(3) |
| Co4-S7 | 2.310(2) | N12-Co1-S4 | 175.2(2) |
| Co4-S1 | 2.317(2) | N11-Co1-S4 | 92.5(2) |
| Co4-N42 | 1.962(7) | N12-Co1-S3 | 92.5(2) |
| Co4-N41 | 1.969(7) | N11-Co1-S3 | 175.7(2) |
| N12-Co1-S2 | 94.0(2) | S4-Co1-S2 | 83.47(8) |
| N11-Co1-S2 | 93.6(2) | S3-Co1-S2 | 88.51(8) |
| N12-Co1-S1 | 94.7(2) | S4-Co1-S3 | 91.44(8) |
| N11-Co1-S1 | 94.6(2) | | |
| S4-Co1-S1 | 88.34(8) | N31-Co3-N32 | 84.5(3) |
| S3-Co1-S1 | 83.78(8) | N31-Co3-S8 | 91.6(2) |
| S2-Co1-S1 | 168.60(9) | N32-Co3-S8 | 176.0(2) |
| | | N31-Co3-S6 | 177.3(2) |
| N42-Co4-N41 | 85.2(3) | N32-Co3-S6 | 93.0(2) |
| N42-Co4-S8 | 175.4(2) | S8-Co3-S6 | 91.01(8) |
| N41-Co4-S8 | 90.8(2) | N31-Co3-S7 | 93.4(2) |
| N42-Co4-S3 | 92.6(2) | N32-Co3-S7 | 95.1(2) |
| N41-Co4-S3 | 176.6(2) | S8-Co3-S7 | 84.93(8) |
| S8-Co4-S3 | 91.50(8) | S6-Co3-S7 | 87.60(8) |
| N42-Co4-S7 | 93.3(2) | N31-Co3-S5 | 94.9(2) |
| N41-Co4-S7 | 94.5(2) | N32-Co3-S5 | 92.3(2) |
| S8-Co4-S7 | 84.67(8) | S8-Co3-S5 | 88.20(8) |
| S3-Co4-S7 | 88.16(8) | S6-Co3-S5 | 84.39(9) |
| N42-Co4-S1 | 94.8(2) | S7-Co3-S5 | 169.35(9) |
| N41-Co4-S1 | 94.2(2) | | |
| S8-Co4-S1 | 87.74(8) | | |

Tab. S3. Interatomic S···H distances (Å) indicating hydrogen bonding interactions for compound **I**.

| distances | | distances | |
|---|---|---|---|
| S1 ··· H-N2 | 2.9352(9) | S7 ··· H-N2 | 2.4508(12) |
| S1·····H-N3 | 2.9154(9) | S7·····H-N3 | 2.4236(11) |
| | | S7·····H-N6 | 2.6593(8) |
| | | S8 ··· H-N1 | 2.8826(7) |
| S3 ··· H-N2 | 2.8792(8) | S8·····H-N8 | 2.8882(7) |
| S3 ··· H-N3 | 2.8647(7) | S9·····H-N7 | 2.8579(11) |
| S3·····H-N4 | 2.9243(10) | S9·····H-N8 | 2.9574(14) |
| S4·····H-N3 | 2.6927(6) | S10·····H-N4 | 2.3888(10) |
| | | S10·····H-N5 | 2.3405(10) |
| S5 ··· H-N6 | 2.9326(9) | S11·····H-N1 | 2.4257(11) |
| S5 ··· H-N7 | 2.7924(9) | S11·····H-N8 | 2.4427(10) |
| S6·····H-N5 | 2.8286(7) | S12·····H-N6 | 2.4934(12) |
| S6 ··· H-N4 | 2.8666(8) | S12·····H-N7 | 2.4381(11) |

Tab. S4. Interatomic S•••H distances (Å) indicating hydrogen bonding interactions for compound **II**.

| distances | | distances | |
|---|---|---|---|
| S1 ··· H-N42 | 2.8772(1) | S9···H-N11 | 2.3821(1) |
| S1·····H-N12 | 2.8620(1) | S9···H-N21 | 2.4321(1) |
| S12···H-N42 | 2.4878(1) | S4···H-N21 | 2.9997(1) |
| S12···H-N12 | 2.4195(1) | S6···H-N22 | 2.8653(1) |
| S2···H-N11 | 2.8428(1) | S6···H-N31 | 2.8999(1) |
| S2···H-N21 | 2.8761(1) | S3···H-N31 | 2.6572(1) |
| S5···H-N22 | 2.8885(1) | S10···H-N22 | 2.5659(1) |
| S5···H-N32 | 2.8029(1) | S5···H-N32 | 2.3809(1) |
| S7···H-N31 | 2.8288(1) | S11···H-N31 | 2.4442(1) |
| S7···H-N41 | 2.8711(1) | S11···H-N41 | 2.5302(1) |
| O1···H-N22 | 2.164 | O3····H-N41 | 2.095 |

## DFT calculations

Structure optimizations were performed on the experimentally found crystal structure of **I** with a LCAO approach as implemented in CRYSTAL14, and on model molecule structures of **II** that contain $NH_3$ ligands (Ia, Fig. S5a) instead of the experimentally found bridged heterocycle ligands, and a simplified $NH_2$-$CH_2$-$CH_2$-$NH_2$ bridged ligand (Ib).

Tab. S5: Atomic distances from the DFT optimizations (LDA-FPLO, PBE-FPLO, PBE-CRYSTAL, and B3LYP-CRYSTAL calculations).

| | Co-N | Co-S5 | Co-S13 | S5-S7 | S13-S14 | N-H | S-H | S-H | N-C | C-C | C-H |
|---|---|---|---|---|---|---|---|---|---|---|---|
| Exp (I) | 1.975-1.999 | 2.227-2.242 | 2.318-2.331 | 2.110-2.124 | 2.037-2.048 | 0.90 | 2.34-2.43 | 2.72-3.00 | 1.49 | 1.51 | 0.98 |
| B3LYP | 1.986-2.000 | 2.23-2.24 | 2.31-2.33 | 2.12-2.13 | 2.04-2.06 | 0.93 | 2.24-2.38 | 2.67-2.99 | 1.49 | 1.53 | 1.00-1.01 |
| Model Ia | | | | | | | | | | | |
| PBE-FP | 2.005 | 2.200 | 2.321 | 2.161 | 2.063 | 1.03-1.05 | 2.21 | 2.78 | | | |
| LDA-FP | 1.941 | 2.151 | 2.257 | 2.148 | 2.045 | 1.03-1.07 | 2.10 | 2.69 | | | |
| B3-CRY | 1.992 | 2.264 | 2.330 | 2.112 | 2.068 | 1.03-1.07 | 2.02 | 2.68-2.72 | | | |
| Model Ib | | | | | | | | | | | |
| PBE-FP(C2v) | 1.998 | 2.204 | 2.314 | 2.170 | 2.069 | 1.02-1.06 | 2.18 | 2.74-2.77 | 1.48 | 1.52 | 1.10 |
| PBE-CRY | 1.980 | 2.190 | 2.290 | 2.155 | 2.069 | 1.02-1.07 | 2.07 | 2.68 | 1.50 | 1.53 | 1.10-1.11 |
| LDA-FP | 1.928 | 2.144 | 2.228 | 2.138 | 2.054 | 1.02-1.09 | 2.00 | 2.71 | 1.48 | 1.51 | 1.11 |
| B3-CRY | 1.984 | 2.258 | 2.317 | 2.113 | 2.072 | 1.01-1.06 | 2.12 | 2.73 | 1.49 | 1.53 | 1.10 |

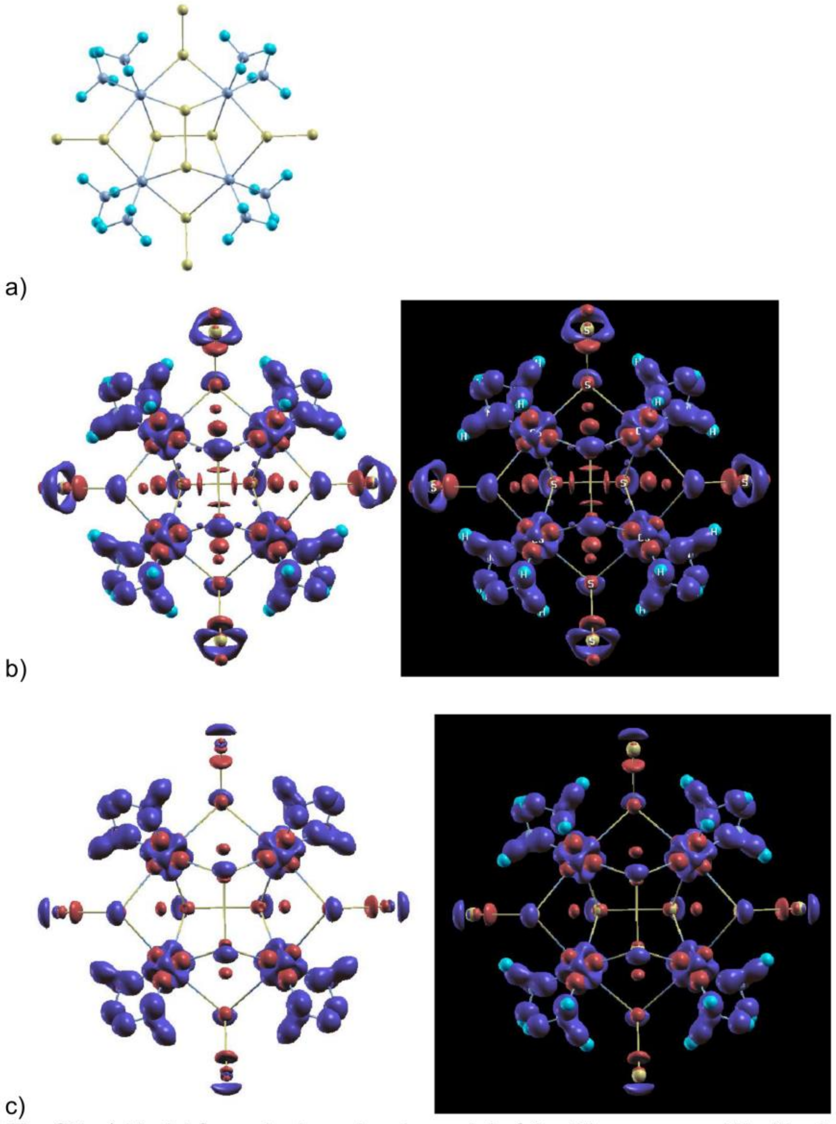

Fig. S5: a) Model for a single molecule model of the title compound **II** with atomic cores shown as balls for S (yellow), Co (blue), N (blue) and H (light blue), b, c) Charge difference plots at different iso-values to indicate charge accumulation (dark blue) and charge depletion (red) for compound **II** (a) compared to a superposition of atomic charge densities, without (left) and with (right).

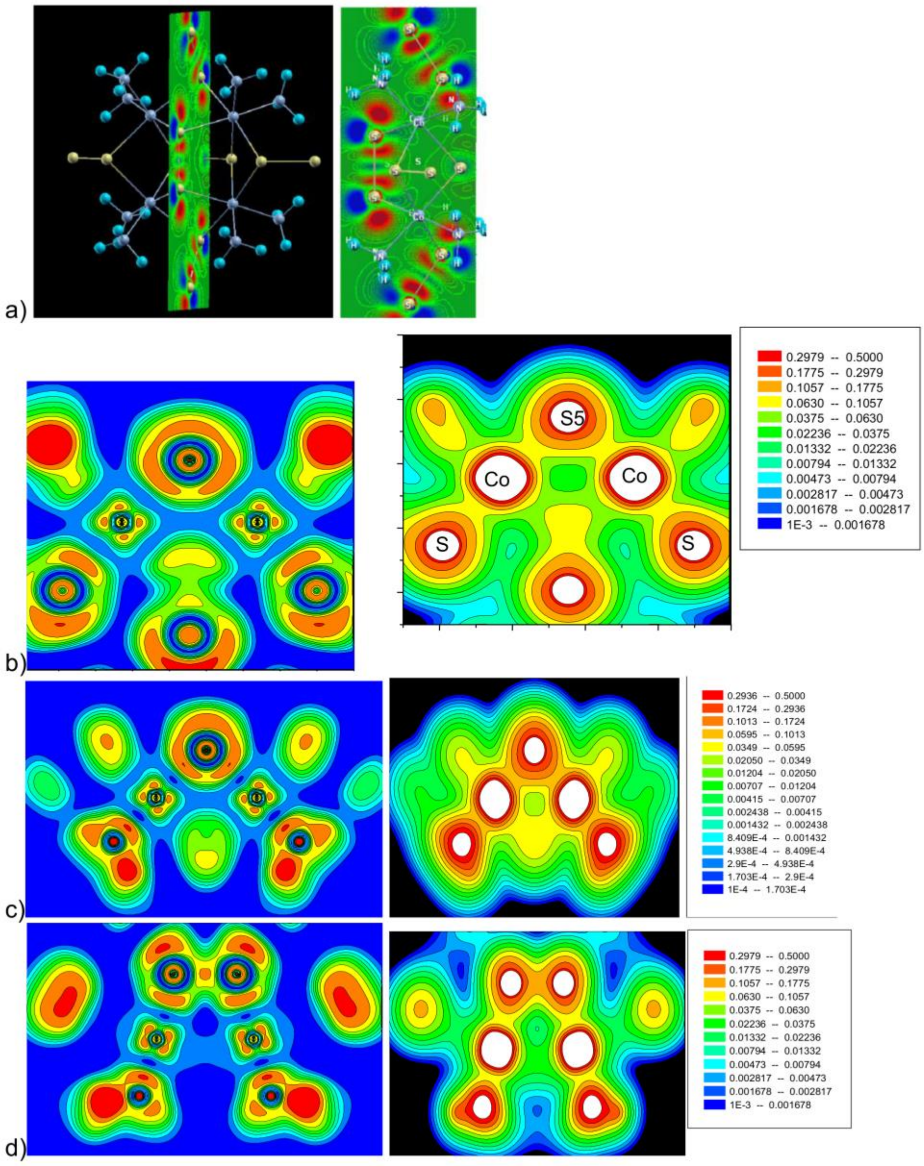
a)
b)
S5
Co
Co
S
S
0.2979 -- 0.5000
0.1775 -- 0.2979
0.1057 -- 0.1775
0.0630 -- 0.1057
0.0375 -- 0.0630
0.02236 -- 0.0375
0.01332 -- 0.02236
0.00794 -- 0.01332
0.00473 -- 0.00794
0.002817 -- 0.00473
0.001678 -- 0.002817
1E-3 -- 0.001678
c)
0.2936 -- 0.5000
0.1724 -- 0.2936
0.1013 -- 0.1724
0.0595 -- 0.1013
0.0349 -- 0.0595
0.02050 -- 0.0349
0.01204 -- 0.02050
0.00707 -- 0.01204
0.00415 -- 0.00707
0.002438 -- 0.00415
0.001432 -- 0.002438
8.409E-4 -- 0.001432
4.938E-4 -- 8.409E-4
2.9E-4 -- 4.938E-4
1.703E-4 -- 2.9E-4
1E-4 -- 1.703E-4
d)
0.2979 -- 0.5000
0.1775 -- 0.2979
0.1057 -- 0.1775
0.0630 -- 0.1057
0.0375 -- 0.0630
0.02236 -- 0.0375
0.01332 -- 0.02236
0.00794 -- 0.01332
0.00473 -- 0.00794
0.002817 -- 0.00473
0.001678 -- 0.002817
1E-3 -- 0.001678

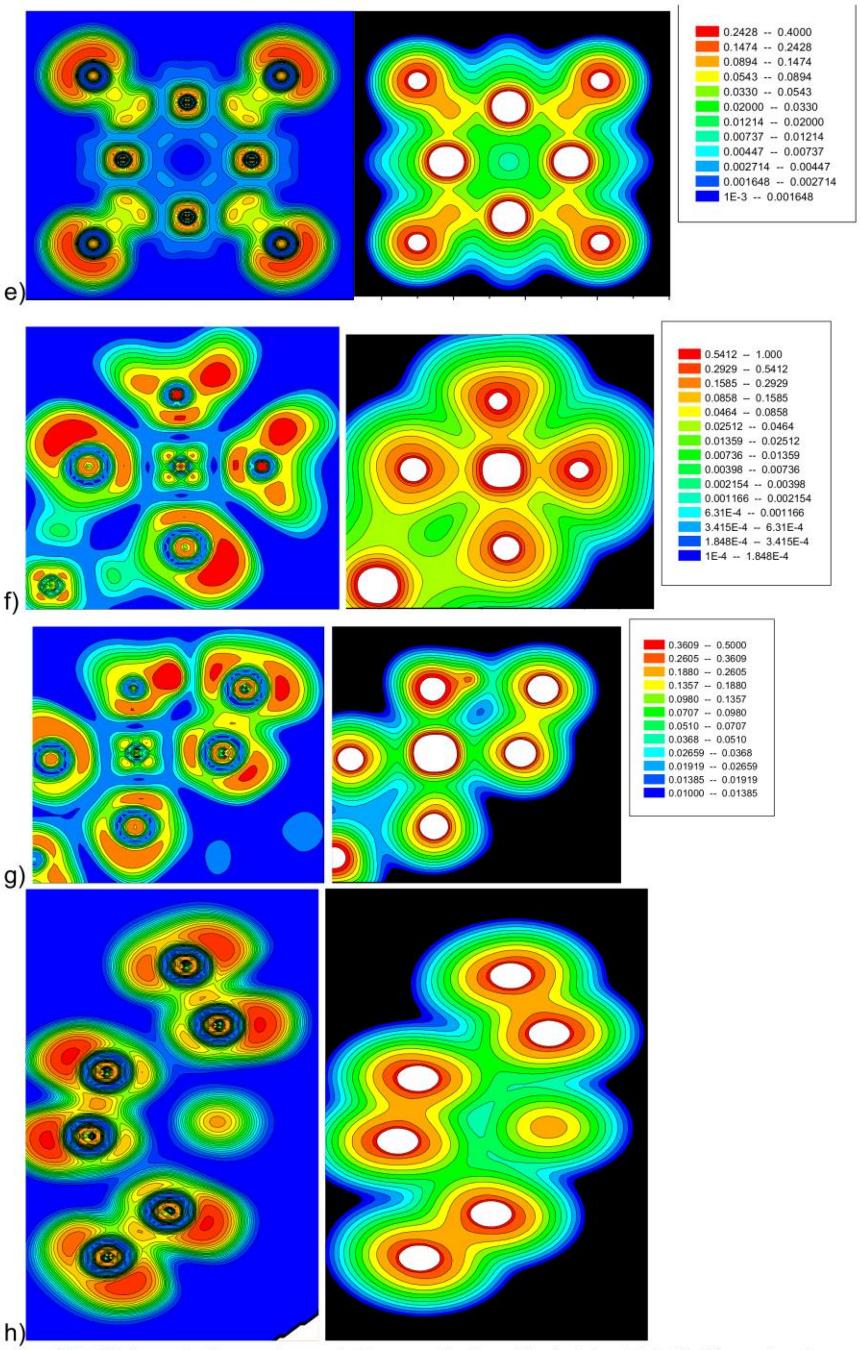

Fig. S6: Slide cuts through model Ia symbolized in (a) for ELF (left) and valence charge density (right) plots (a-h) for selected slices through b) S-Co-S5-Co-S, c) S-Co-S13-Co-S, d) $S_2$-brige with S-Co-S13-S14-Co-S, e) 4 Co atoms and terminal S2 units, f) [$CoS_2N_2$] square of the $CoS_4N_2$ octahedron, g) [$CoS_2N_2$] square of the $CoS_4N_2$ octahedron including one S9-S16 unit and the N-H-S bridge, h) the mirror plane of the model structure that contains terminal and bridging $S_2$ units.

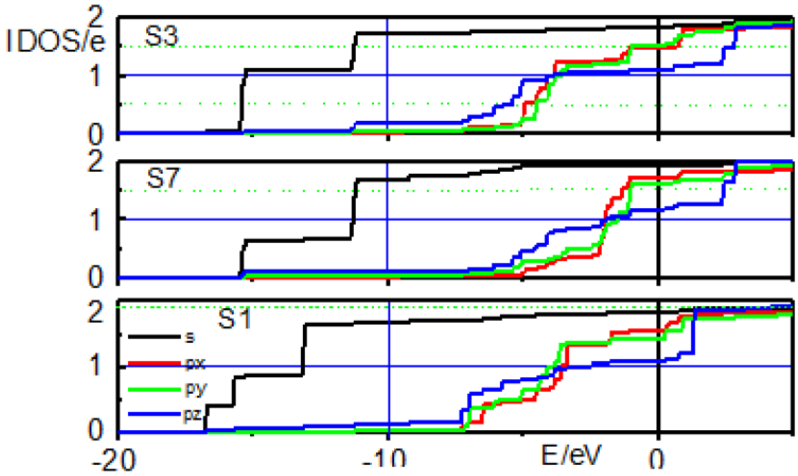

Fig. S7 b) Integrated orbital occupations (IDOS) (bottom).

### *Photocatalytic tests*

The stability of the title compound was proved by recovering the catalyst after the first run and applying it for a second run with new solvents and additives (Fig. S8). Kinetic studies of photocatalytic reactions are presented in Fig. S8 including the initial phase below. Additionally the catalyst was recovered after the first run and applied for a second run, where the same amount of hydrogen was produced. Note that differences in amount of produced hydrogen compared to the value reported in the manuscript are due to different reaction conditions (Fig. S9). The amount of catalyst was increased to 40 mg instead of 10 mg for increasing the amount of recovered catalyst. The concentration of catalyst clearly affects the photocatalytic activity. Being a dark/black solid, the title compound itself may interact with the incident light by absorption. Thus the sensitizer $[Ru(bpy)_3](PF_6)_2$ and the title compound are competing for light absorption. According to that a higher loading of catalyst causes less light absorption of the sensitizer. The data presented in this work have been already corrected against background contribution (acetonitrile, triethylamine, water, $[Ru(bpy)_3](PF_6)_2$). Nevertheless uncorrected data including reference experiment in the absence of the catalyst are displayed below (Fig. S10).

The XRD powder pattern confirms the stability of the title compound during the photocatalytic reaction und demonstrates that the 'structural properties' appear (nearly) unchanged (Fig. S11).

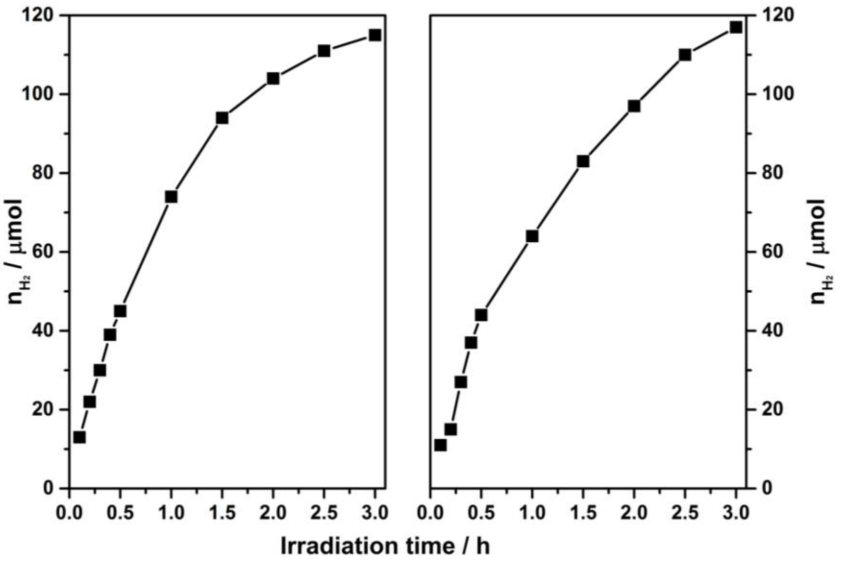

Fig. S8: Photocatalytic hydrogen evolution of first (left) and second (right) run.

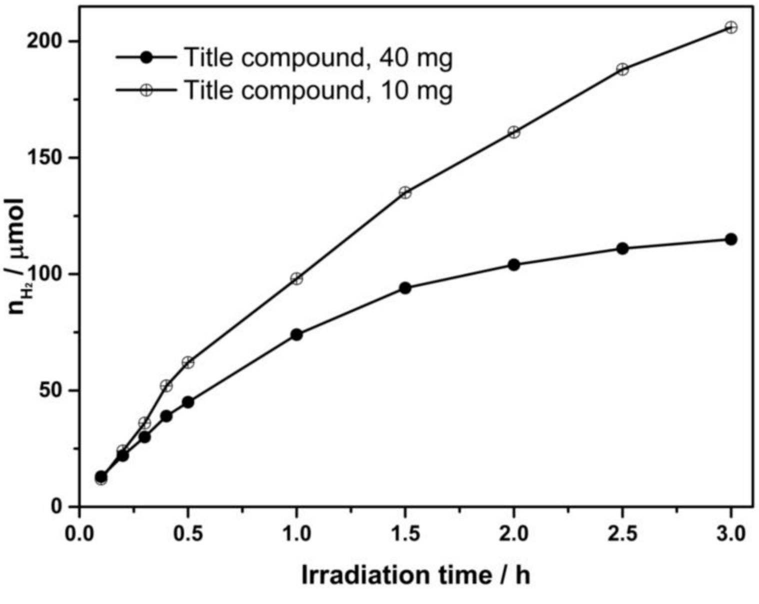

Fig. S9: Photocatalytic hydrogen evolution applying 40 mg and 10 mg of title compound.

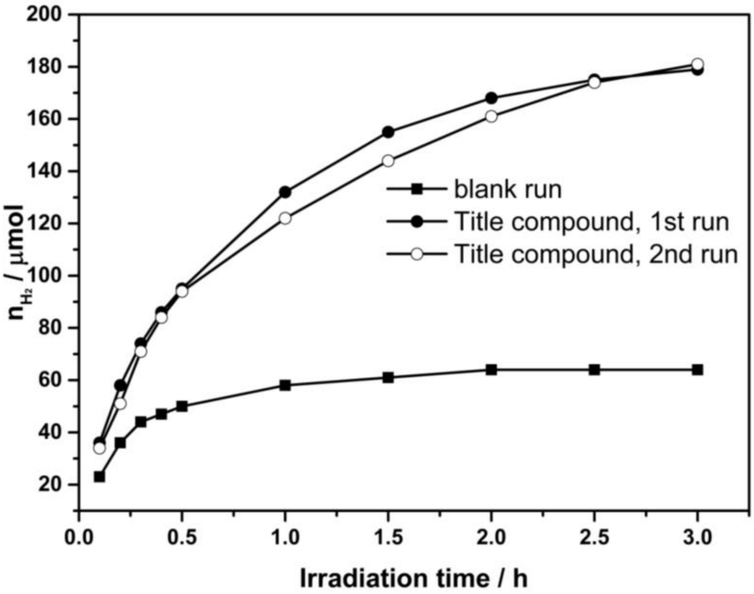

Fig. S10: Photocatalytic hydrogen evolution of title compound (not corrected) and reference experiment in the absence of catalyst respectively.

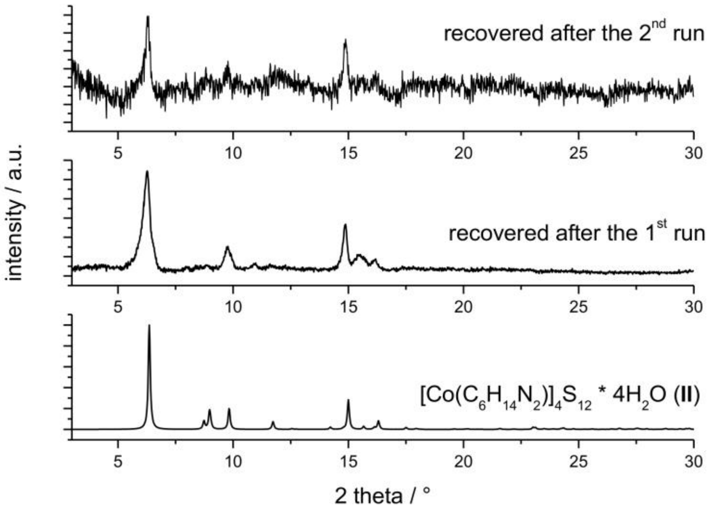

Fig. S11. XRD powder pattern of the compound before and after the photocatalytic tests.

***Infrared spectroscopy***

MIR spectra (500-4000 $cm^{-1}$) were recorded with an ATI Mattson Genesis spectrometer. For the title compound the absorptions located at 3213 (s, $-NH_2$ stretch), 3110 (m, $-NH_2$ stretch), 2929 (m, $-NH_2$ stretch), 2855 (m, -CH stretch, $N-CH_2$), 1629 (m, -C-N-H def.), 1573 (s, $-NH_2$ asym. def.), 1448 and 1402 (s, -CH def., $N-CH_2$), 1349 (s, -CH def.), 1130 (s, -CN stretch), 1047 (s, -CN stretch) $cm^{-1}$ can be assigned to the *trans*-1,2-diaminocyclohexane and at 513 $cm^{-1}$ the absorption of the disulfide modes is observed.

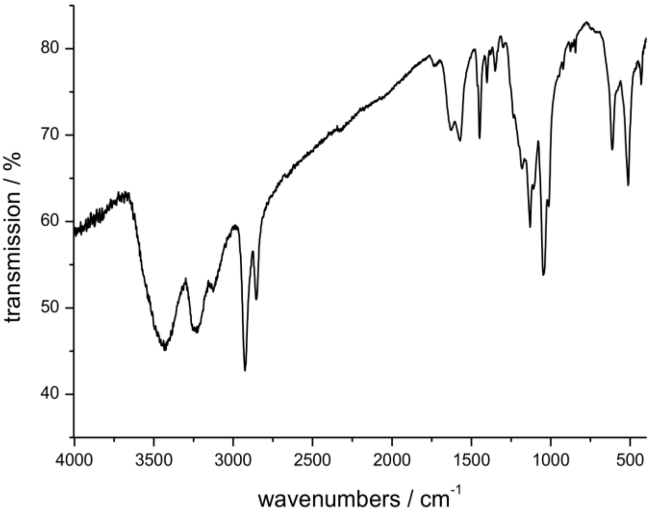

Fig. S12. MIR spectrum of the title compound **I**.

***Raman spectroscopy***

Raman spectra were recorded with a Bruker IFS 66 Fourier transform Raman spectrometer (wavelength: 541.5 nm) in the region from 100 to 3500 cm$^{-1}$. The spectrum and the assignment are presented in the supporting information.

The Raman spectrum is shown in Fig. S3. The resonances of the disulfide modes are found between 400 and 520 cm$^{-1}$,[1] but are often located around 500 cm$^{-1}$ respectively at 497 cm$^{-1}$ for the title compound **I**. The Co-S bond lengths vary between 2.3316(6) and 2.3355(7) Å and the signals observed in the spectra are slightly shifted to 280 and 267 cm$^{-1}$.[2] Deformation vibrations occur below 200 cm$^{-1}$, but a detailed assignment is not unambiguous due to resonances for lattice vibrations.

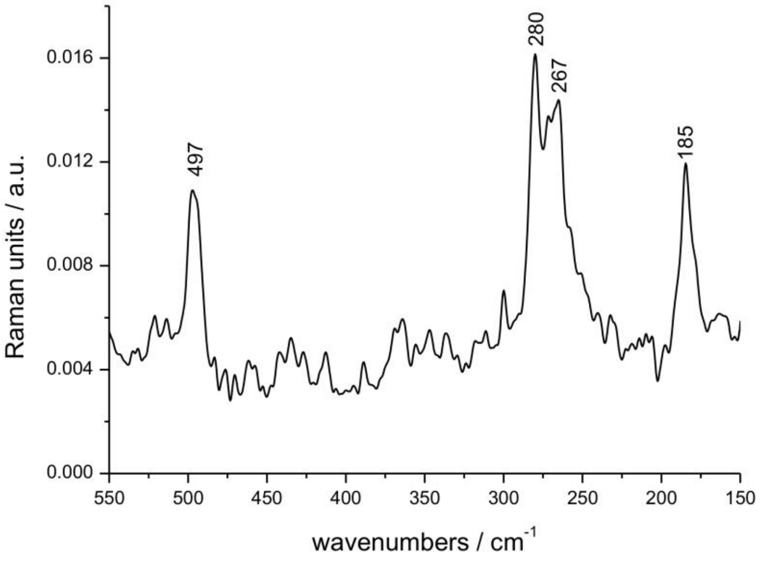

Fig. S13. Raman spectrum of the title compound **I**. Important modes are labeled.

### *UV/Vis spectroscopy*

UV/Vis spectroscopic investigations were carried out at room temperature using an UV-Vis-NIR two-channel spectrometer Cary 5 from Varian Techtron Pty., Darmstadt. The optical properties of the compound were investigated by analyzing the UV/Vis reflectance spectra of the powdered samples (with $BaSO_4$ powder used as reference material). The absorption data were calculated applying the Kubelka-Munk relation for diffuse reflectance data. The optical band gap was estimated to 1.0 eV (Fig. S14).

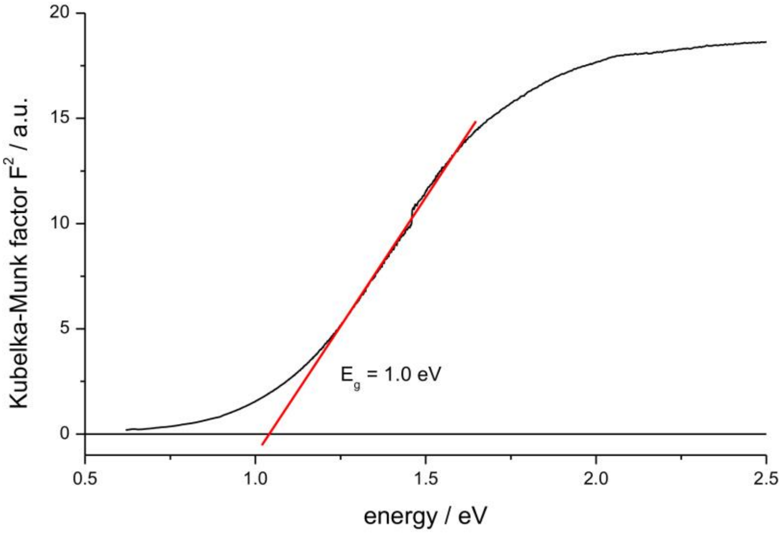

Fig. S14. Determination of the optical band gap of UV/Vis data applying the Kubelka-Munk theory.

## References

[1] G. Socrates, *Infrared and Raman Characteristic Group Frequencies: Tables and Charts* **2004**(3rd Edition), John Wiley & Sons; 3. Edition, Chichester, New York, Weinheim, Toronto, Brisbane, Singapore.

[2] K. Kanamori, S. Ino, Y. Mizuno, I. Kanesake, K. Kawai, J. Hidaka, *Bull. Chem. Soc. Jpn.* **1989**, *62*, 2375–2378.

# 5 Zusammenfassende Diskussion

Die Herstellung und Charakterisierung neuartiger $MoS_2$-Cokatalysatoren für die lichtgetriebene $H_2$-Entwicklung bildete das Hauptziel dieser Arbeit. Dabei standen besonders der Einfluss der chemischen Zusammensetzung sowie die Rolle der mikrostrukturellen Eigenschaften im Fokus der Untersuchungen. Durch den Zusatz von Kohlenstoff wurde die chemische Zusammensetzung von $MoS_2$ modifiziert. Dies erfolgte durch Einsatz unterschiedlicher organischer Thiomolybdate. Der C-Gehalt wurde auf einfachem Wege über den thermischen Abbau von $(R_4N)_2MoS_4$ (R = $-H_4$ ($C_0$), $-CH_3$ ($C_1$), $-C_3H_7$ ($C_3$), $-C_6H_{13}$ ($C_6$)) und $[(C_6H_5)_4P]_2MoS_4$ gesteuert. Je nach C-Gehalt des Precursors resultierten Produkte mit variablem C-Anteil, d.h. das C-reichste Edukt lieferte das C-reichste Produkt. Der C-Gehalt ließ sich auch über die Zersetzungstemperatur steuern und nahm mit zunehmender Zersetzungstemperatur im Molybdänsulfid ab. Im Gegensatz dazu waren C-reichere Produkte (Ausnahme: $C_3$) bei einer gegebenen Temperatur schwefelärmer und der S-Gehalt wurde mit zunehmender Zersetzungstemperatur erhöht. Der C-Gehalt wurde auch durch mechanische Beimischung von Graphen bzw. rußartigem Kohlenstoff zum Ausgangsstoff $C_0$ eingestellt. C-freie nanoskalige Molybdänsulfide wurden auch über den thermischen Abbau von $(NH_4)_2MoS_4$ in Abhängigkeit von der Temperatur und der Zersetzungsatmosphäre synthetisiert. Unterschiede im S-Gehalt wiesen nur die Zersetzungsserien, welche in $N_2$ hergestellt wurden auf. Bei geringeren Temperaturen als 350 °C lag ein S-Überschuss vor und ab 550 °C wurde stöchiometrisches $MoS_2$ gebildet. Thermische Zersetzungen in Formiergas dagegen generierten im Temperaturbereich von 200 bis 850 °C Molybdänsulfide mit einem Mo:S Verhältnis von 1:2. Besonders interessant sind die Abbauprodukte von $[(C_6H_5)_4P]_2MoS_4$, welche intakte organische Baueinheiten in Form von $[(C_6H_5)_4P]_2S$ und bei einer niedrigeren Zersetzungstemperatur zusätzlich noch $Ph_3PS$ enthalten.

Neben der chemischen Zusammensetzung wurden in den Produkten besonders die strukturellen Eigenschaften verändert. Alle Produkte sind nanoskalig und durch ausgeprägte strukturelle Fehlordnungen/Defekte charakterisiert. Der thermische Abbau von alkylhaltigen Thiomolybdaten lieferte Produkte mit kürzeren $MoS_2$-Schichtlängen und geringerer Stapelung der $MoS_2$-Schichten mit steigendem C-

Anteil in dem Edukt. Des Weiteren wurde in allen Nanokompositen die Anwesenheit von unkorrelierten $MoS_2$-Monoschichten gefunden. Zusätzlich sind die $MoS_2$-Schichten oft verbogen und die Materialien weisen turbostratische Fehlordnung auf. Der Einfluss der Temperatur und der Atmosphäre auf die Produkte des thermischen Abbaus von $(NH_4)_2MoS_4$ wurde bei der Analyse der strukturellen Eigenschaften deutlich. Oberhalb von T = 250 °C setzte die Bildung von 2H-$MoS_2$ ein, dessen Kristallinität mit steigender Zersetzungstemperatur zunahm. Dabei wurde $MoS_2$ in $H_2/N_2$-Atmosphäre bei niedrigeren Temperaturen erhalten im Vergleich zur Reaktion in $N_2$. Zu den thermischen Abbauprodukten der alkylhaltigen Thiomolybdate vergleichbare mikrostrukturelle Eigenschaften wie gebogene und gegeneinander verdrehte $MoS_2$-Schichten sind Charakteristika dieser Produkte. Die Zersetzung von $[(C_6H_5)_4P]_2MoS_4$ erfolgte bei zwei unterschiedlichen Temperaturen (250 °C und 350 °C). Bei der niedrigeren Temperatur resultierte ein Molybdänsulfid mit einem signifikant vergrößerten $MoS_2$-Schichtabstand, welcher durch die *in situ* Bildung von $Ph_3PS$ verursacht wird, welches zwischen die $MoS_2$-Schichten hineinragt. Im Gegensatz dazu wurde bei der höheren Zersetzungstemperatur ein Molybdänsulfid mit geringfügiger aufgeweitetem $MoS_2$-Schichtabstand und unkorrelierten $MoS_2$-Monoschichten erhalten. Alternativ zu den thermischen Abbaureaktionen wurde $MoS_2$-Volumenmaterial in einer Hochenergiekugelmühle in Abhängigkeit von der Zeit behandelt, so dass $MoS_2$-Nanopartikel erhalten wurden. Durch diese Behandlung wurden bei identischer chemischer Zusammensetzung die strukturellen Eigenschaften verändert. Mit zunehmender Behandlungsdauer änderte sich das Aspektverhältnis und die Stapelfehlerdichte sowie die Anzahl gebogener Schichten nahm zu. Bei der Behandlung nahm die Zahl gestapelter $MoS_2$-Schichten schneller ab als die Schichtlänge.

Die mit den verschiedenen Syntheserouten synthetisierten Materialien waren ausnahmslos aktivere Cokatalysatoren verglichen mit $MoS_2$-Volumenmaterial. Die Variation der chemischen Zusammensetzung von $MoS_2$ durch C-Zusätze führte zu einer Verbesserung der katalytischen Aktivität. Ein direkter Zusammenhang zwischen C-Gehalt und der entwickelten Menge an $H_2$ konnte für Produkte des thermischen Abbaus nicht einfach hergestellt werden, da sowohl die chemische Zusammensetzung als auch zusätzlich die strukturellen Eigenschaften deutlich variierten. Mechanisch beigemengter Kohlenstoff zu dem Ausgangsstoff $C_0$ in Form von Graphen oder russartigem Kohlenstoff bewirkte eine mengenunabhängige

Verbesserung der Molybdänsulfidkatalysatoren. Die Verwendung von $MoS_2$-Cokatalysatoren mit Dimensionen im nm-Bereich hat ebenfalls die katalytische Eigenschaft verbessert, was besonders bei den mechanisch behandelten $MoS_2$-Proben beobachtet werden konnte. In Abhängigkeit des Aspektverhältnisses und der Dichte von $MoS_2$-Kanten nahm die katalytische Aktivität bei der lichtgetriebenen Wasserstoffgenerierung zu. Diese Beobachtung bestätigt Vermutungen, dass die katalytisch aktiven Zentren an den Kanten von $MoS_2$ lokalisiert sind.

In dieser Arbeit wird dargestellt, wie auf einfachem synthetischem Weg die chemische Zusammensetzung und die strukturellen Eigenschaften in $MoS_2$ in einem weiten Bereich verändert werden können. Der Einfluss dieser Eigenschaften macht sich bei den fotokatalytischen Untersuchungen zur Wasserstoffgenerierung deutlich bemerkbar, so dass C-Zusätze oder die Veränderung der Partikelgröße die katalytische Aktivität positiv beeinflussen.

Im Rahmen der Arbeit wurden auch fotokatalytische Untersuchungen an anderen Übergangsmetallsulfiden sowie –oxiden durchgeführt. Die meisten Proben haben sich dabei als viel versprechende Cokatalysatoren erwiesen.

# 6 Literaturverzeichnis

[1] F. R. Pazheri, M. F. Othman, N. H. Malik, *Renew. Sustain. Energy Rev.* **2014**, *31*, 835–845.

[2] N. R. Moheimani, D. Parlevliet, *Renew. Sustain. Energy Rev.* **2013**, *27*, 494–504.

[3] D. Boehme, J. Nick-Leptin, **2013**, *Erneuerbare Energien in Zahlen*, zu finden unter http://www.erneuerbare-energien.de/die-themen/datenservice/erneuerbare-energien-in-zahlen/.

[4] S. Bilgen, *Renew. Sustain. Energy Rev.* **2014**, *38*, 890–902.

[5] V. V. Tyagi, N. A. A. Rahim, N. A. Rahim, J. A. /L. Selvaraj, *Renew. Sustain. Energy Rev.* **2013**, *20*, 443–461.

[6] L. Carrette, K. A. Friedrich, U. Stimming, *ChemPhysChem.* **2000**, *1*, 162–193.

[7] C. Descorme, P. Gallezot, C. Geantet, C. George, *ChemCatChem..* **2012**, *4*, 1897–1906.

[8] A. E. Lutz, R. W. Bradshaw, J. O. Keller, D. E. Witmer, *Int. J. Hydrog. Energy* **2003**, *28*, 159–167.

[9] H. Dau, C. Limberg, T. Reier, M. Risch, S. Roggan, P. Strasser, *ChemCatChem.* **2010**, *2*, 724–761.

[10] A. Fujishima, K. Honda, *Nature* **1972**, *238*, 37–38.

[11] A. Kudo, Y. Miseki, *Chem. Soc. Rev.* **2009**, *38*, 253–278.

[12] F. E. Osterloh, *Chem. Mater.* **2008**, *20*, 35–54.

[13] X. B. Chen, S. H. Shen, L. J. Guo, S. S. Mao, *Chem. Rev.* **2010**, *110*, 6503–6570.

[14] A. A. Ismail, D. W. Bahnemann, *Sol. Energy Mater. Sol. Cells* **2014**, *128*, 85–101.

[15] F. Fresno, R. Portela, S. Suarez, J. M. Coronado, *J. Mater. Chem. A* **2014**, *2*, 2863–2884.

[16] M. Kitano, M. Hara, *J. Mater. Chem.* **2010**, *20*, 627–641.

[17] K. Maeda, K. Domen, *J. Phys. Chem. Lett.* **2010**, *1*, 2655–2661.

[18] H. Bannwarth, B. P. Kremer, A. Schulz, *Basiswissen Physik, Chemie Und Biochemie*, Springer, Berlin Heidelberg, **2007**.

[19] J. Yang, D. Wang, H. Han, C. Li, *Acc. Chem. Res.* **2013**, *46*, 1900-1909.

[20] J. K. Nørskov, T. Bligaard, A. Logadottir, J. R. Kitchin, J. G. Chen, S. Pandelov, U. Stimming, *J. Electrochem. Soc.* **2005**, *152*, J23–J26.

[21] B. Hinnemann, P. G. Moses, J. Bonde, K. P. Jorgensen, J. H. Nielsen, S. Horch, I. Chorkendorff, J. K. Norskov, *J. Am. Chem. Soc.* **2005**, *127*, 5308–5309.

[22] S. Trasatti, *J. Electroanal. Chem. Interfacial Electrochem.* **1972**, *39*, 163–184.

[23] T. F. Jaramillo, K. P. Jorgensen, J. Bonde, J. H. Nielsen, S. Horch, I. Chorkendorff, *Science* **2007**, *317*, 100–102.

[24] J. K. Norskov, J. Greeley, T. F. Jaramillo, J. Bonde, I. B. Chorkendorff, *Nat. Mater.* **2006**, *5*, 909–913.

[25] P. Sabatier, *Berichte Dtsch. Chem. Ges.* **1911**, *44*, 1984–2001.

[26] Y. Xu, M. A. A. Schoonen, *Am. Mineral.* **2000**, *85*, 543–556.

[27] Y. Y. Gurevich, Y. V. Pleskov, *Semicond. Semimet.* **1983**, *19*, 255–328.

[28] A. Galinska, J. Walendziewski, *Energy Fuels* **2005**, *19*, 1143–1147.

[29] Q. J. Xiang, J. G. Yu, M. Jaroniec, *J. Am. Chem. Soc.* **2012**, *134*, 6575–6578.

[30] K. Hara, K. Sayama, H. Arakawa, *Appl. Catal. Gen.* **1999**, *189*, 127–137.
[31] A. Iwase, A. Kudo, *J. Mater. Chem.* **2010**, *20*, 7536–7542.
[32] J. Kiwi, M. Gratzel, *Nature* **1979**, *281*, 657–658.
[33] K. Hashimoto, T. Kawai, T. Sakata, *Chem. Lett.* **1983**, 709–712.
[34] S. Min, G. Lu, *J. Phys. Chem. C* **2012**, *116*, 25415–25424.
[35] K. Maeda, M. Eguchi, W. J. Youngblood, T. E. Mallouk, *Chem. Mater.* **2008**, *20*, 6770–6778.
[36] R. R. Chianelli, M. H. Siadati, M. P. De la Rosa, G. Berhault, J. P. Wilcoxon, R. Bearden, B. L. Abrams, *Catal. Rev.* **2006**, *48*, 1–41.
[37] C. W. Scheele, *Sämtliche Physische Und Chemische Werke*, D. S. F. Hermstädt, Niederwalluf/Wiesbaden, **1971**, 185-200.
[38] U. S. Geological Survey, **2013**, *Mineral Commodity Summaries 2013*, zu finden unter http://minerals.usgs.gov/minerals/pubs/mcs/2013/mcs2013.pdf.
[39] R. G. Dickinson, L. Pauling, *J. Am. Chem. Soc.* **1923**, *45*, 1466–1471.
[40] R. E. Bell, R. E. Herfert, *J. Am. Chem. Soc.* **1957**, *79*, 3351–3354.
[41] F. Wypych, R. Schollhorn, *J. Chem. Soc.-Chem. Commun.* **1992**, 1386–1388.
[42] J. A. Wilson, A. D. Yoffe, *Adv. Phys.* **1969**, *18*, 193–335.
[43] K. K. Kam, B. A. Parkinson, *J. Phys. Chem.* **1982**, *86*, 463–467.
[44] A. Splendiani, L. Sun, Y. Zhang, T. Li, J. Kim, C.-Y. Chim, G. Galli, F. Wang, *Nano Lett.* **2010**, *10*, 1271–1275.
[45] Mattheis.Lf, *Phys. Rev. B* **1973**, *8*, 3719–3740.
[46] R. Coehoorn, C. Haas, R. A. Degroot, *Phys. Rev. B* **1987**, *35*, 6203–6206.
[47] H. Tributsch, *Z. Naturforschung Sect. - J. Phys. Sci.* **1977**, *32*, 972–985.
[48] A. E. van Arkel, *Recl. Trav. Chim. Pays-Bas* **1926**, *45*, 437–444.
[49] T. Weber, J. C. Muijsers, H. J. M. C. vanWolput, C. P. J. Verhagen, J. W. Niemantsverdriet, *J. Phys. Chem.* **1996**, *100*, 14144–14150.
[50] T. P. Prasad, E. Diemann, A. Muller, *J. Inorg. Nucl. Chem.* **1973**, *35*, 1895–1904.
[51] J. L. Brito, M. Ilija, P. Hernandez, *Thermochim. Acta* **1995**, *256*, 325–338.
[52] H. W. Wang, P. Skeldon, G. E. Thompson, *J. Mater. Sci.* **1998**, *33*, 3079–3083.
[53] A. Leist, S. Stauf, S. Loken, E. W. Finckh, S. Ludtke, K. K. Unger, W. Assenmacher, W. Mader, W. Tremel, *J. Mater. Chem.* **1998**, *8*, 241–244.
[54] G. L. Frey, S. Elani, M. Homyonfer, Y. Feldman, R. Tenne, *Phys. Rev. B* **1998**, *57*, 6666.
[55] N. Berntsen, T. Gutjahr, L. Loeffler, J. R. Gomm, R. Seshadri, W. Tremel, *Chem. Mater.* **2003**, *15*, 4498–4502.
[56] R. Wei, H. Yang, K. Du, W. Fu, Y. Tian, Q. Yu, S. Liu, M. Li, G. Zou, *Mater. Chem. Phys.* **2008**, *108*, 188–191.
[57] K. Hu, X. Hu, Y. Xu, X. Pan, *React. Kinet. Mech. Catal.* **2010**, *100*, 153–163.
[58] M. Nath, A. Govindaraj, C. N. R. Rao, *Adv. Mater.* **2001**, *13*, 283–286.
[59] P. D. Fleischauer, *Thin Solid Films* **1987**, *154*, 309–322.
[60] E. Gourmelon, O. Lignier, H. Hadouda, G. Couturier, J. C. Bernede, J. Tedd, J. Pouzet, J. Salardenne, *Sol. Energy Mater. Sol. Cells* **1997**, *46*, 115–121.
[61] R. Bichsel, F. Levy, *J. Phys. Appl. Phys.* **1986**, *19*, 1809.
[62] J. Shi, D. Ma, G.-F. Han, Y. Zhang, Q. Ji, T. Gao, J. Sun, X. Song, C. Li, Y. Zhang, Q. Ji, T. Gao, J. Sun, X. Song, C. Li, Y. Zhang, X.Y. Lang, Y. Zhang, Z. Liu., *ACS Nano* **2014**, *8*, 10196–10204.
[63] H. S. S. Ramakrishna Matte, A. Gomathi, A. K. Manna, D. J. Late, R. Datta, S. K. Pati, C. N. R. Rao, *Angew. Chem. Int. Ed.* **2010**, *49*, 4059–4062.
[64] K.-G. Zhou, N.-N. Mao, H.-X. Wang, Y. Peng, H.-L. Zhang, *Angew. Chem. Int. Ed.* **2011**, *50*, 10839–10842.

[65] S. Z. Butler, S. M. Hollen, L. Cao, Y. Cui, J. A. Gupta, H. R. Gutiérrez, T. F. Heinz, S. S. Hong, J. Huang, A. F. Ismach, E. Johnston-Halperin, M. Kuno, V. V. Plashnitsa, R. D. Robinson, R. S. Ruoff, S. Salahuddin, J. Shan, L. Shi, M. G. Spencer, M. Terrones, W. Windl, J. E. Goldberger, *ACS Nano* **2013**, *7*, 2898–2926.

[66] A. K. Geim, I. V. Grigorieva, *Nature* **2013**, *499*, 419–425.

[67] J. N. Coleman, M. Lotya, A. O'Neill, S. D. Bergin, P. J. King, U. Khan, K. Young, A. Gaucher, S. De, R. J. Smith, I. V. Shvets, S. K. Arora, G. Stanton, H.-Y. Kim, K. Lee, G. T. Kim, G. S. Duesberg, T. Hallam, J. J. Boland, J. J. Wang, J. F. Donegan, J. C. Grunlan, G. Moriarty, A. Shmeliov, R. J. Nicholls, J. M. Perkins, E. M. Grieveson, K. Theuwissen, D. W. McComb, P. D. Nellist, V. Nicolosi, *Science* **2011**, *331*, 568–571.

[68] P. Joensen, R. F. Frindt, S. R. Morrison, *Mater. Res. Bull.* **1986**, *21*, 457–461.

[69] R. F. Frindt, *J. Appl. Phys.* **1966**, *37*, 1928–1929.

[70] E. Benavente, M. A. Santa Ana, F. Mendizabal, G. Gonzalez, *Coord. Chem. Rev.* **2002**, *224*, 87–109.

[71] Y. F. Zhao, Y. X. Zhang, Z. Y. Yang, Y. M. Yan, K. N. Sun, *Sci. Technol. Adv. Mater.* **2013**, *14*, 043501.

[72] B. Radisavljevic, A. Radenovic, J. Brivio, V. Giacometti, A. Kis, *Nat. Nanotechnol.* **2011**, *6*, 147–150.

[73] Q. H. Wang, K. Kalantar-Zadeh, A. Kis, J. N. Coleman, M. S. Strano, *Nat. Nanotechnol.* **2012**, *7*, 699–712.

[74] W. O. Winer, *Wear* **1967**, *10*, 422–452.

[75] F. J. Clauss, in *Solid Lubr. Self-Lubr. Solids* (Ed.: F.J. CLAUSS), Academic Press, **1972**, 75–112.

[76] E. Furimsky, *Catal. Rev.* **1980**, *22*, 371–400.

[77] G. C. A. Schuit, B. C. Gates, *AIChE J.* **1973**, *19*, 417–438.

[78] A. N. STARTSEV, *Catal. Rev.* **1995**, *37*, 353–423.

[79] T. R. Thurston, J. P. Wilcoxon, *J. Phys. Chem. B* **1999**, *103*, 11–17.

[80] Y. Tan, K. Yu, T. Yang, Q. Zhang, W. Cong, H. Yin, Z. Zhang, Y. Chen, Z. Zhu, *J. Mater. Chem. C* **2014**, *2*, 5422–5430.

[81] D. Merki, X. Hu, *Energy Environ. Sci.* **2011**.

[82] Y. Yan, B. Xia, Z. Xu, X. Wang, *ACS Catal.* **2014**, *4*, 1693–1705.

[83] L. S. Byskov, J. K. Nørskov, B. S. Clausen, H. Topsøe, *J. Catal.* **1999**, *187*, 109–122.

[84] J. V. Lauritsen, M. V. Bollinger, E. Lægsgaard, K. W. Jacobsen, J. K. Nørskov, B. S. Clausen, H. Topsøe, F. Besenbacher, *J. Catal.* **2004**, *221*, 510–522.

[85] P. Raybaud, J. Hafner, G. Kresse, S. Kasztelan, H. Toulhoat, *J. Catal.* **2000**, *189*, 129–146.

[86] W. I. Choi, B. C. Wood, E. Schwegler, T. Ogitsu, *J. Phys. Chem. C* **2013**, *117*, 21772–21777.

[87] Y. Min, G. He, Q. Xu, Y. Chen, *J. Mater. Chem. A* **2014**, *2*, 2578–2584.

[88] L. Yang, D. Zhong, J. Zhang, Z. Yan, S. Ge, P. Du, J. Jiang, D. Sun, X. Wu, Z. Fan, S. A. Dayeh, B. Xiang, *ACS Nano* **2014**, *8*, 6679-6985.

[89] U. Maitra, U. Gupta, M. De, R. Datta, A. Govindaraj, C. N. R. Rao, *Angew. Chem.* **2013**, *125*, 13295-13299.

[90] X. Zong, H. J. Yan, G. P. Wu, G. J. Ma, F. Y. Wen, L. Wang, C. Li, *J. Am. Chem. Soc.* **2008**, *130*, 7176–7177.

[91] J. V. Lauritsen, J. Kibsgaard, S. Helveg, H. Topsoe, B. S. Clausen, E. Laegsgaard, F. Besenbacher, *Nat. Nano* **2007**, *2*, 53–58.

[92] C. D. Putnam, M. Hammel, G. L. Hura, J. A. Tainer, *Q. Rev. Biophys.* **2007**, *40*, 191–285.

[93] O. Glatter, O. Kratky, *Small Angle X-Ray Scattering*, Academic Press Inc, London, **1982**.

[94] H. P. Klug, L. E. Alexander, *X-Ray Diffraction Procedures*, John Wiley And Sons, New York, London, Sidney, **1966**.

[95] A. Guinier, *X-Ray Diffraction*, W. H. Freeman And Company, San Francisco, **1963**.

[96] C. J. Tassone, **2014**, *Small Angle X-Ray Scattering*, zu finden unter http://www-ssrl.slac.stanford.edu/conferences/workshops/sxst2014/documents/tassone_christopher_saxs_06042014.pdf.

[97] M. C. Biesinger, B. P. Payne, A. P. Grosvenor, L. W. M. Lau, A. R. Gerson, R. S. C. Smart, *Appl. Surf. Sci.* **2011**, *257*, 2717–2730.

[98] P. Atkins, J. de Paula, *Atkin’s Physical Chemistry*, Oxford, Oxford, **2006**.

[99] C. R. Brundle, C. A. J. Evans, S. Wilson, *Encyclopedia of Materials Characterization*, Butterworth-Heinemann, Stoneham, **1992**.

[100] J. H. Scofield, *J. Electron Spectrosc. Relat. Phenom.* **1976**, *8*, 129–137.

[101] J. F. Moulder, W. F. Stickle, P. E. Sobol, K. D. Bomben, *Handbook of X-Ray Photoelectron Spectroscopy*, Perkin Elmer Eden Prairie, MN, **1992**.

[102] K. Madeja, K. Lühder, *Wiss. Z. Ernst-Moritz-Arndt-Univ. Greifswald Math-Natwiss Reihe* **1986**, 23–28.

# Danksagung

Die vorliegende Arbeit wurde am Institut für Anorganische Chemie der Christian-Albrechts-Universität zu Kiel angefertigt.

An dieser Stelle möchte ich mich bei den Institutsangehörigen für die vielseitige Unterstützung bedanken.

Besonders bedanke ich mich bei Prof. Dr. Wolfgang Bensch für die Bereitstellung des interessanten Themas und für seine Diskussions- und Hilfsbereitschaft bei wissenschaftlichen Problemstellungen. Ein Dank geht auch an die gesamte Arbeitsgruppe für ein kollegiales Arbeitsklima. Besonders möchte ich dabei ‚Team Nano' (Svenja Harm, Philipp Breuninger, Markus Krengel, Sebastian Mangelsen, Felix Niefind, Stefan Permien, Michael Poschmann, Björn Reimer, David Westfal) für die erfrischende Arbeitsatmosphäre und die gute Zusammenarbeit danken. An dieser Stelle sei außerdem den Studenten gedankt, die meine Arbeit in Form von Praktika und Bachelorarbeiten unterstützt haben.

Bedanken möchte ich mich bei den Kooperationspartnern, ohne die diese Arbeit nicht zustande gekommen wäre. Das sind Uschi Cornelissen, Stefanie Pehlke und Jaqueline Pick (Raman, IR, Elementaranalyse), Dr. Antje Reher, Dr. Nele Reimer, Jana Timm und Dr. Christian Stoltenberg ($N_2$-Gas Sorption), Dr. Helge Reinsch (Kraftfeldrechnungen), Mao Deng, Prof. Dr. Lorenz Kienle, Dr. Ulrich Schürmann und Dr. Andriy Lotnyk (TEM), Laura Dura, Dr. Torsten Beweries und Dr. Sven Hansen (fotokatalytische Messungen), Prof. Dr. Leo van Wüllen (FK-NMR), Prof. Dr. Paul Heitjans und Dr. Andre Düvel (Kugelmühle), Dr. Sabine Rosenfeldt und Prof. Dr. Achim Förster (SAXS), Prof. Dr. Wolfgang Grünert und Dr. Ilya Sinev (XPS), Udo Bauer, Christian Papp, Hans-Peter Steinrück (XPS).

Bedanken möchte ich mich darüber hinaus bei den ‚Chemikern' aus meinem Semester für eine denkwürdige Studienzeit in Kiel.

Julia Klempert danke ich für ihre Geduld, ihr Verständnis und den Rückhalt, den sie mir stets gibt und gegeben hat. Abschließend bedanke ich mich bei meinen Eltern und meinen Geschwistern für die permanente Unterstützung.

# Eidesstattliche Erklärung

Die vorliegende Dissertation wurde am Institut für Anorganische Chemie der Christian-Albrechts-Universität zu Kiel unter Anleitung von Herrn Prof. Dr. W. Bensch angefertigt. Hiermit versichere ich, John Djamil, an Eides statt, dass ich die vorliegende Arbeit selbständig, abgesehen von der Beratung durch meinen wissenschaftlichen Lehrer und nur unter Verwendung der angegebenen Hilfsmittel angefertigt habe. Die Dissertation wird ausschließlich an dieser Stelle zur Promotion vorgelegt. Einen weiteren Promotionsversuch habe ich weder an dieser noch an einer anderen Hochschule unternommen.

Kiel, 18.08.2015 John Djamil